UNIVERSITY OF CALIFORNIA

Los Angeles

Theoretical Modeling of the High Temperature Helium Embrittlement in Structural Alloys

A dissertation submitted in partial satisfaction of the

requirements for the degree Doctor of Philosophy

in Engineering

by

Jamal Nasser Al-Hajji

1985

TABLE OF CONTENTS

ACKNOWLEDGMENTS

I would like to thank the members of my dissertation committee: Professor Mohamed Abdou, Professor Amos Norman, Professor David Okrent, Professor Rakesh Savin, and Professor Nasr Ghoniem. Professor Ghoniem, who served as my committee chairman, was especially helpful. His encouragement, guidance, and enthusiasm have been a constant source of motivation.

I would like to thank Mr. C. Wassilew and Dr. D. Kaletta (Kernforschungszentrum, Karlsruhe, W. Germany), and Drs. R. Bullough and J. Mathews (United Kingdom Atomic Energy Authority, Harwell, Oxfordshire, England), for providing me with the opportunity to join their research staff during my trip to Europe. I am particularly grateful to Mr. C. Wassilew for many useful discussions and for the access to his valuable experimental data.

I would like to thank Joan George for an excellent job editing and typing the manuscript.

I am indebted to Kuwait University and the Kuwait Government for providing me with the opportunity to continue my graduate studies. Professor Abbas Marafi was especially helpful.

I also would like to thank the staff of the Kuwait University Office in Washington, D.C. for their help and support. In particular I would like to thank Kristine Aulenbach for all her help.

VITA

October 17, 1956:	Born, Kuwait
1979:	B. S., University of California, Santa Barbara
1980:	Awarded a scholarship from Kuwait University to continue graduate studies
1982:	M. S. in Engineering, University of California, Los Angeles
1983:	Engineer Degree, University of California, Los Angeles
1983-1985:	Ph. D. in Nuclear Engineering, University of California, Los Angeles
Jan.-April 1984:	Research Assistant, Kernforschungszentrum, Karlsruhe, W. Germany
April-June 1984:	Research Assistant, United Kingdom Atomic Energy Authority, Harwell, Oxfordshire, England

PUBLICATIONS

J. N. Alhajji and N. M. Ghoniem, "The Simultaneous Formation of Both Vacancy and Interstitial Loops Under Irradiation," American Nuclear Society Transactions, 41-42 (1982) 251.

N. M. Ghoniem, J. Alhajji and F. A. Garner, "Hardening of Irradiated Alloys Due to the Simultaneous Formation of Vacancy and Interstitial Loops," Effects of Radiation on Materials: Eleventh Conference, ASTM-STP-782, H. R. Brager and J. S. Perrin, Eds., American Society for Testing and Materials (1982) 1054-1072.

N. M. Ghoniem, J. N. Alhajji and D. Kaletta, "The Effect of Helium Clustering on Its Transport to Grain Boundaries," to be pub. J. Nucl. Mater. (1985).

ABSTRACT OF THE DISSERTATION

Theoretical Modeling of the High Temperature
Helium Embrittlement in Structural Alloys

by

Jamal Nasser Al-Hajji

Doctor of Philosophy in Nuclear Engineering
University of California, Los Angeles, 1985
Professor Nasr M. Ghoniem, Chair

Modeling the high temperature helium embrittlement problem in non-fissile materials during neutron irradiation and charged particle bombardment is the primary objective of this dissertation. The model describes the helium embrittlement phenomenon as a sequence of four steps. First, helium clustering in the matrix is modeled using rate theory. This is followed by modeling the transport of helium to grain boundaries. The third step in this work describes the role of helium and stress in the nucleation of cavities at grain boundaries, emphasizing the role of precipitates and triple-point junctions. The last step deals with the growth and coalescence of grain boundary cavities, until fracture is achieved by cavity-cavity interlinkage.

The model shows that in the absence of irradiation, grain boundary sliding plays a significant role in nucleating cavities at grain boundary obstacles such as precipitates. In addition, it is shown that such cavities are not spherical but are lenticular in shape. However, helium is shown to play a larger role in the nucleation of cavities at grain boundaries as compared to applied stress. Helium can result in orders of magnitude increase in the density of grain boundary bubble nuclei, as opposed to the influence of the applied stress alone. However, the density reaches a steady state once the injected helium reaches ~ 10 appm in steels. Both helium and stress drive cavity nucleation, which occurs extremely fast and is not rate controlling in the high temperature fracture phenomenon. The growth behavior of these cavities determines the life of reactor structural alloys. Comparisons of the model with available experimental data show good agreement over a wide range of conditions.

It is concluded that the helium embrittlement phenomenon can be mitigated by increasing the matrix and grain boundary precipitate density. Matrix precipitates are very efficient traps for helium while grain boundary precipitates can reduce secondary grain boundary dislocation climb distance, and hence reduce the rate of vacancy emission from such dislocations. A new explanation of the resistance of high martensitic steels to helium embrittlement is given in the dissertation.

CHAPTER I

INTRODUCTION

A detailed knowledge and understanding of the mechanical behavior of fuel elements or fusion reactor components for a wide range of temperatures, stress states, and irradiation conditions is essential for the reliable prediction of their performance during normal operation as well as off-normal situations. Of all the mechanical properties, fracture and loss of ductility under irradiation are least understood. The problem of loss of ductility at high temperatures after neutron irradiation due to the introduction of helium has been known since the early 1960s [1]. This problem has been termed "helium embrittlement." In order to gain some insight into this problem, it is appropriate to look at the fracture map and how it is altered due to irradiation.

1. FRACTURE AND IRRADIATION

The fracture behavior can be shown by a plot such as Fig. 1 [2]. Here the regions of the fracture phenomena are shown on a plot of stress as a function of temperature, normalized to the shear modulus and melting temperature, respectively. The main purpose of fracture maps is to illustrate trends and general effects.

If we focus our attention on the low stress levels and high temperatures ($T/T_m > 0.4$), characteristics of creep tests, fracture is usually intergranular in nature. This is clearly shown in Fig. 1. "W"-type cracks refer to wedge-shaped cracks generally initiated at triple-point junctions. At higher temperatures and lower stress levels, "R"-type grain boundary cavities appear. These cavities are usually associated

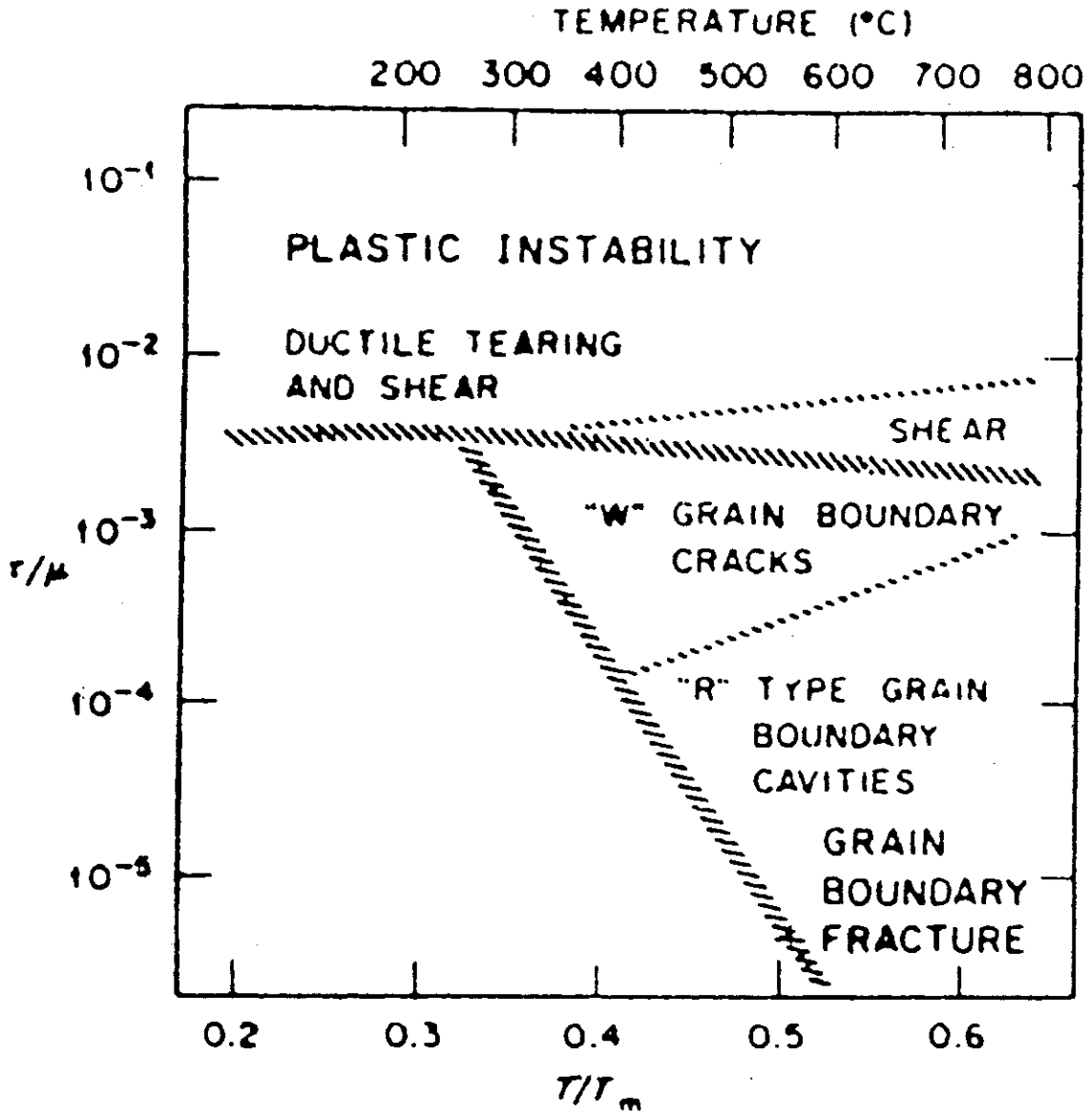

Figure 1. Fracture map of austenitic stainless steel before irradiation [2]. Reprinted with the permission from Radiation Effects in Breeder Reactor Structural Materials, edited by M.L. Bleiberg and J.W. Bennett, 1977, The Metallurgical Society of AIME, 420 Commonwealth Drive,Warrendale, PA 15086, USA

with second phase particles present at grain boundaries. Surface diffusion acts to lower their surface energy by spheroidization.

Figure 2 shows how irradiation alters the fracture map. The region of grain boundary cavitation extends over a larger range of temperature and stress. The map clearly shows that irradiation results in a degradation of grain boundaries at high temperatures due to enhanced cavitation of grain boundaries. This enhanced cavitation is a result of helium presence at grain boundaries. Once helium is present in the cavities, they are termed helium bubbles. The stress-enhanced growth of helium bubbles in grain boundaries at high temperatures ($T/T_m > 0.4$), is the primary cause of the phenomenon of helium embrittlement.

2. SOURCES OF HELIUM

The most relevant parameter to high temperature helium embrittlement is, of course, helium. Helium is generated by neutron irradiation in reactors via (n,α) nuclear reactions. In thermal or mixed-spectrum fission reactors with sufficient high flux of thermal neutrons, nickel and boron play an important role in generating helium while in future fusion reactors, a much wider spectrum of alloys play a significant role in helium production. A discussion of the role of the various isotopes in helium generation follows.

2.1. The Role of Nickel

Thermal or mixed spectrum fission reactors with sufficient high flux of thermal neutrons create high amounts of helium in nickel

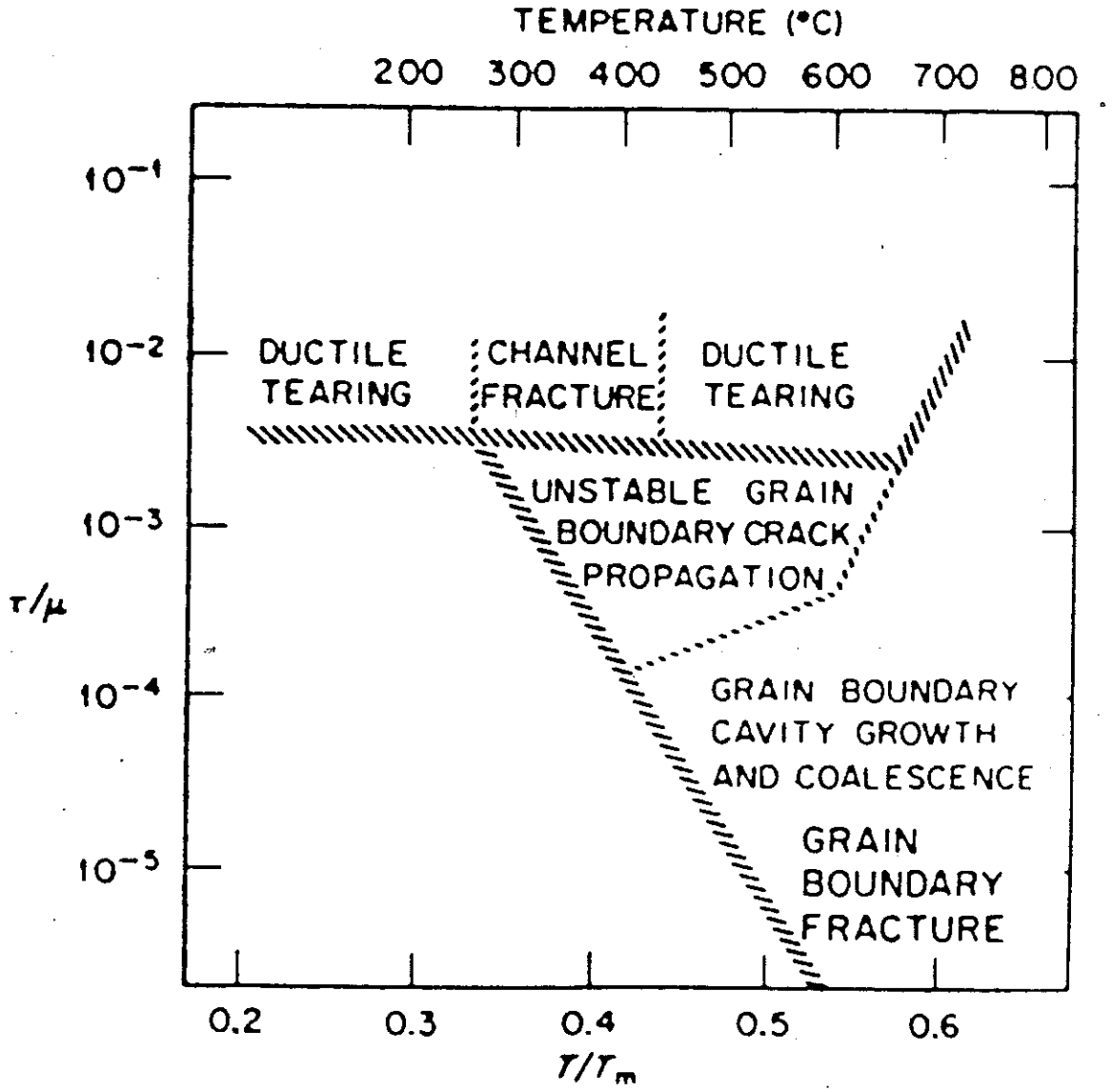

Figure 2. Fracture map of austenitic stainless steel after irradiation to high fast neutron fluences (5×10^{22} n/cm^2,E > 0.1 MeV) [2]. Reprinted with the permission from Radiation Effects in Breeder Reactor Structural Materials, edited by M.L. Bleiberg and J.W. Bennett,1977, The Metallurgical Society of AIME, 420 Commonwealth Drive , Warrendale, PA 15086, USA

containing alloys because of a special two-step nuclear reaction with thermal neutrons (n_{th}) and ^{58}Ni:

$$^{58}Ni(n_{th},\gamma)^{59}Ni \quad ; \qquad ^{59}Ni(n_{th},\alpha)^{56}Fe \quad .$$

So, reactors with a high amount of thermal neutrons like the High Flux Isotope Reactor (HFIR) generate about 2200 appm helium in stainless steel in the first year, together with about 30 dpa [3]. This is a very high helium generation rate. However, the nickel content is important only within the presence of thermal neutrons. For fast fission and fusion reactors, where the thermal neutron flux is small, the nickel double-capture sequence is not important.

2.2. The Role of Boron

Besides the nickel isotopes ^{58}Ni and ^{59}Ni, there exists another isotope of an element which is present in many austenitic steels and which has a very high cross section for transmutation into helium via a nuclear reaction with thermal neutrons:

$$^{10}B + n \rightarrow 2\alpha + {}^{3}T \quad ,$$
$$^{10}B + n \rightarrow \alpha + {}^{7}_{3}Li \quad .$$

Boron is added to steels to improve hot workability and decrease the tendency of grain boundary cracking at high temperature [4]. Boron is known to increase grain boundary precipitation, e.g., $M_{23}(C,B)_6$. Grain boundary precipitates are believed to play a significant role in reducing grain boundary sliding which is closely tied to intergranular cavity nucleation [4]. However, helium production by boron transmutation, though small, can play a more serious role due to the tendency of the

boron to segregate at or near grain boundaries at high temperatures. As a result, the helium created by the ^{10}boron isotope is concentrated in the vicinity of the grain boundaries. Thus it produces its drastic embrittling effect.

2.3. Helium Production in Fusion Reactors

The fundamental reaction to consider in D-T fueled fusion plasmas is

$$ {}^{2}_{1}D + {}^{3}_{1}T \rightarrow {}^{4}_{2}He + {}^{1}_{0}n(14\ MeV) \quad . $$

There are several concepts of magnetically confined plasma devices that are being studied today, [e.g., Reversed Field Pinches (RFP), mirrors, and tokamaks]. All of these rely on magnetic fields to constrain the trajectory of the D^+, T^+, and He^{++} ions to achieve fusion conditions. Another approach to fusion is to compress deuterium and tritium to very high densities and temperatures with high intensities of charged particles or laser light. Such a mechanism holds the plasma together long enough for more energy to be released than was invested in the compression. For this reason it is called the inertial confinement approach.

In all of these devices there are three major forms of radiation emitted from the plasma that could reach the reaction chamber first wall. These forms are: photons, energetic particles, and neutrons. Part of the energetic particles are actually helium ions and their impingement on the first wall is a direct helium source into the first wall. Neutrons from the D-T reaction are highly energetic (14 MeV) and interact with the first wall in various ways, such as the normal (n,γ) reactions which cause some elements to be transmuted to others. In

addition, the higher energy neutrons can produce gaseous atoms via (n,p) and (n,α) reactions. Of the two types of transmutant atoms, solid or gaseous, it has been generally observed that gaseous atoms can have the greater effect on the mechanical behavior of a metallic system. This is because only a few atomic parts per million of helium in alloys such as 316 stainless steel at elevated temperatures can produce a significant degradation in mechanical properties [5].

Perhaps the best way to understand why the production of helium atoms in a fusion environment is so much larger than that in a fission environment is to examine the energy dependence of the (n,α) cross section. The total helium production cross section for metallic systems like Al, V, 316 SS, Nb, Ti, and Mo for fusion neutron (14 MeV) are 2-3 orders of magnitude higher than those associated with fission neutrons which are born in the 1-2 MeV region [6]. This readily shows that helium production rates in fusion reactors will be much higher than in fission facilities. The amount of helium generated in different materials in different reactors is given in Table 1.

TABLE 1. The helium production rates for various materials.

Material	appm He/Yr		
	Fusion[a]	EBR-II	HFIR
Austenitic SS (316)	105	13.8	4000
Vanadium	39.6	0.9	0.47
Molybdenum	33	1.8	3
Aluminum	223	16.3	18

[a](wall loading 1 MW/m^2)[7]

3. DEGRADATION OF DUCTILITY BY HELIUM AND ITS IMPACT ON FUSION AND FISSION REACTORS

The ability of materials to deform freely without fracture is drastically affected in many structural alloys by helium. This effect was even observed for as low as 0.4 appm helium [8]. The work of Lovell [9] illustrates that both the rupture times and rupture strains can be reduced by a factor of ten or more due to the introduction of a few appm helium.

Current design philosophy in the liquid metal fast breeder reactor (LMFBR) program for the fuel cladding is that at least 0.5% uniform elongation should be available beyond the yield point. Helium can severly reduce the ductility of the cladding and clad failure might occur prematurely during transient overpower accidents as well as steady-state operation. However, the LMFBR can operate with a few failed elements, whereas a fusion reactor probably cannot operate with as much as one major leak. As a matter of fact, higher levels of ductility will be required for fusion reactor components [7]. It has been suggested by Kulcinski [7] that at least a 1% level of uniform elongation will be required for safe operation of a fusion reactor. It has been shown by Bloom et al. [5] that 10 appm helium (much lower than a fusion environment) can render ductility loss to levels below 1%. Such embrittlement levels can jeopardize the future of fusion reactors.

4. THE SIGNIFICANCE OF MODELING THE HELIUM EMBRITTLEMENT PROBLEM

Although extensive experimental research has been done by scientists since the 1960s to understand high temperature fracture under irradiation (e.g., [1,5,8,9]), there remain many unanswered questions.

The mode of fracture has been proven by many studies which unanimously point at the stress-enhanced nucleation and growth of helium bubbles in grain boundaries at high temperatures. But these experimental studies (reviewed in Chapter II) have not satisfactorily answered many questions. The following aspects are still open for discussion: (a) The influence of material parameters; (b) The dependence of the microstructure and composition on the amount of helium at grain boundaries; (c) The reasons behind the reduced embrittling effect of helium in ferritics as compared to austenitic steels; (d) The reasons behind the increased embrittling effect of helium at low strain rates; and (e) The dependence of embrittlement on the damage rate, helium generation rate, the total helium concentration, stress, and temperature. Thus, no prediction of the mechanical properties such as time to fracture and fracture strain are yet possible for a given material with given experimental parameters. Even if such laws do exist, their applicability is quite limited and their value lies in providing an insight to an overall trend.

This thesis represents a comprehensive attempt to model high temperature fracture. High temperature fracture under irradiation is not an isolated phenomenon, but it is rather closely tied to high temperature fracture in general. Both phenomena wre considered in the present model. Modeling fracture phenomena under irradiation will enable scientists to extrapolate beyond the experimental capabilities and provide an insight into future designs. A good example of this situation is the expected high radiation damage to the first wall in a fusion reactor. It is expected that few thousands of atomic parts per million of helium will be generated in the first wall, as well as a significant amount of

dpa's over the wall operation time [6,7]. Hence, helium embrittlement effects will be of much more importance to fusion reactor materials, however it will be difficult to assess the extent of the embrittlement without experimental simulation of the fusion reactor environment with respect to radiation damage. Facilities like HFIR cannot provide high dpa rates to simulate the fusion environment while facilities like EBR-II fall quite short as far as high helium generation is concerned. It is clear that fusion reactor environment simulation is difficult and the role of modeling of such an environment is quite important in providing an insight into the extent of embrittlement which will be encountered by the first wall.

REFERENCES

[1] R. S. Barnes, "Embrittlement of Stainless Steels and Nickel-Based Alloys at High Temperature Induced by Neutron Irradiation," Nature (London), 206 (1965) 1307.

[2] M. L. Grossbeck, J. O. Stiegler and J. J. Holmes, "Effects of Irradiation on the Fracture Behavior," Proc. Int. Conf. on Radiation Effects in Breeder Reactor Structural Materials, AIME, Scottsdale, 1977, p. 95.

[3] T. A. Gabriel, B. L. Bishop and F. W. Wiffen, Oak Ridge National Laboratory Report ORNL TM-6361 (1979).

[4] T. M. Williams and K. Gott, "The Effects of Initial Boron Content and Distribution on Helium Bubble Populations and the Stress Rupture Properties Exhibited by Irradiated Type 316 Austenitic Steel," J. Nucl. Mater., 95 (1980) 265.

[5] E. E. Bloom and F. W. Wiffen, "The Effects of Large Concentrations of Helium on the Mechanical Properties of Neutron-Irradiated Stainless Steel," J. Nucl. Mater., 58 (1975) 171.

[6] G. L. Kulcinski, M. Abdou, and D. G. Doran, "Comparison of Displacement and Gas Production Rates in Current Fission and Future Fusion Reactors," in Proc. Conf. on Properties of Reactor Structural Alloys After Neutron or Particle Irradiation, Am. Soc. Testing Mater., Gatlinburg, TN, June 1974, ASTM-STP-570, p. 329.

[7] G. L. Kulcinski, "Fusion Reactors: Their Challenge to Materials Scientists," Contemp. Phys., 20 (4), (1979) 417.

[8] D. Matlock and W. Nix, "Effects of Helium on the High-Temperature Creep and Fracture Properties of Ni-6%W," J. Nucl. Mater., 56 (1975) 145.

[9] A. J. Lovell, "Postirradiation Creep of Annealed Type 316 Stainless Steel," Nucl. Tech., 16 (1972) 323.

CHAPTER II

REVIEW OF EXPERIMENTAL AND THEORETICAL RESEARCH ON HELIUM EMBRITTLEMENT

In order to identify the key physical mechanisms of helium effects and to develop theoretical models, a review of fundamental findings of experiments is indispensable. This is particularly important here since the thesis is a theoretical modeling of these physical mechanisms. The review of fundamental experimental findings will be followed by a review of early attempts of scientists to model the various physical mechanisms. This review will actually set the path for the comprehensive model which is implemented in this thesis. This will be discussed in the latter part of this chapter.

1. DEGRADATION OF THE DUCTILITY OF STRUCTURAL ALLOYS BY HELIUM

The ability of materials to deform freely without fracture is drastically affected in many structural alloys by helium. It was observed by Matlock and Nix [1] that the embrittling effect of helium does occur for as little as 0.4 appm. The work of Lovell [2] illustrates that both the rupture times and rupture strain can be reduced by a factor of 10 or more due to the introduction of a few appm helium. This is shown in Fig. 1. Figure 1 compares the creep rupture properties of unirradiated AISI 316 SS with ones tested after reactor irradiation. The irradiation temperature was in the same range as the test temperature. The figure clearly shows that the introduction of helium represents a weakening effect which causes premature fracture. The key physical mechanism which caused premature fracture was identified as

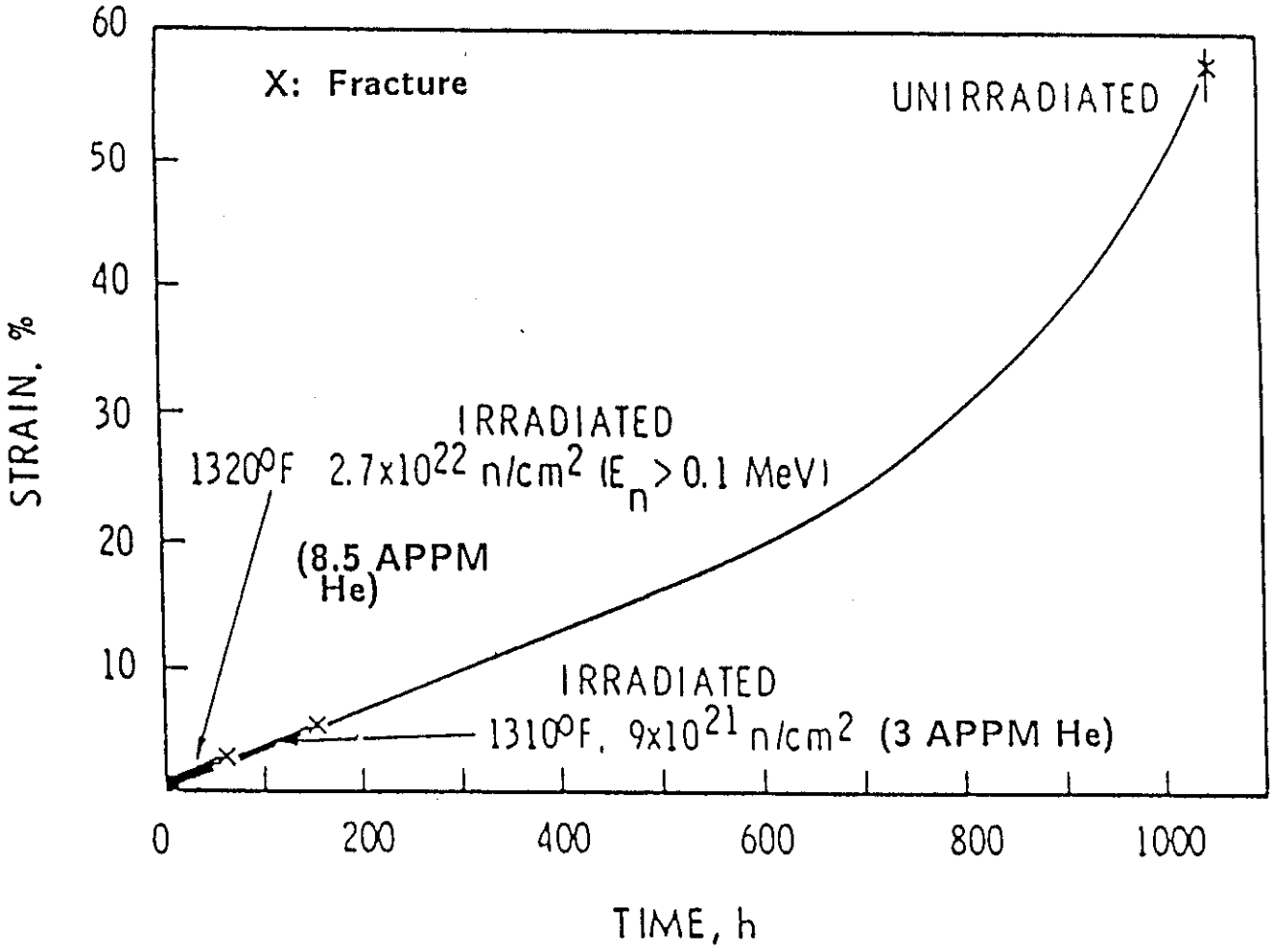

Figure 1. Effect of pre-irradiation on the 1400°F creep curve, at 69 MPa of AISI 3/6 SS (after Lovell [2]). Reprinted with permission from the American Nuclear Society, 555 North Kensington Ave, La Grange Park, Illinois, 60525.

enhanced cavity nucleation at grain boundaries due to the introduction of helium. The growth and coalescence of these cavity nuclei are blamed for the premature fracture.

To gain a good understanding of the temperature range over which helium exercises its detrimental effect, the work of DeVries et al. [3], is quite valuable. This is shown in Fig. 2. where the total elongation values of irradiated specimens are plotted against testing temperature from 723° to 1023°K, together with the data band for reference unirradiated specimens tested at strain rates ranging from 6×10^{-6} to 6 S^{-1}. From this figure the onset of embrittlement can be observed at a temperature of about 750°K. The fracture strain values decrease with increasing helium content over the temperature range of 723° to 923°K. In the temperature range of 923° to 1023°K, an apparent recovery of ductility is observed. The recovery of ductility is due to the increased helium bubble mobility with temperature in this temperature range.

The strain rate dependence of helium embrittlement has been thoroughly investigated by DeVries et al. [3], over the range of $\dot{\varepsilon}$ from 10^{-7} to 10 S^{-1} at temperatures from 723° to 1023°K. The fracture strains are plotted in Fig. 3. The hatched bands illustrate the difference between the two helium levels in the specimens. The largest reduction of fracture strain, as a result of the embrittlement effect due to irradiation (i.e., helium content), is observed at the lowest strain rates (i.e., creep regime). However, at very high strain rates there is a large region, depending on the helium content, in which the pre-irradiation has no effect on the rupture elongation. The reason for these observed differences on strain rate is the fact that the bubble

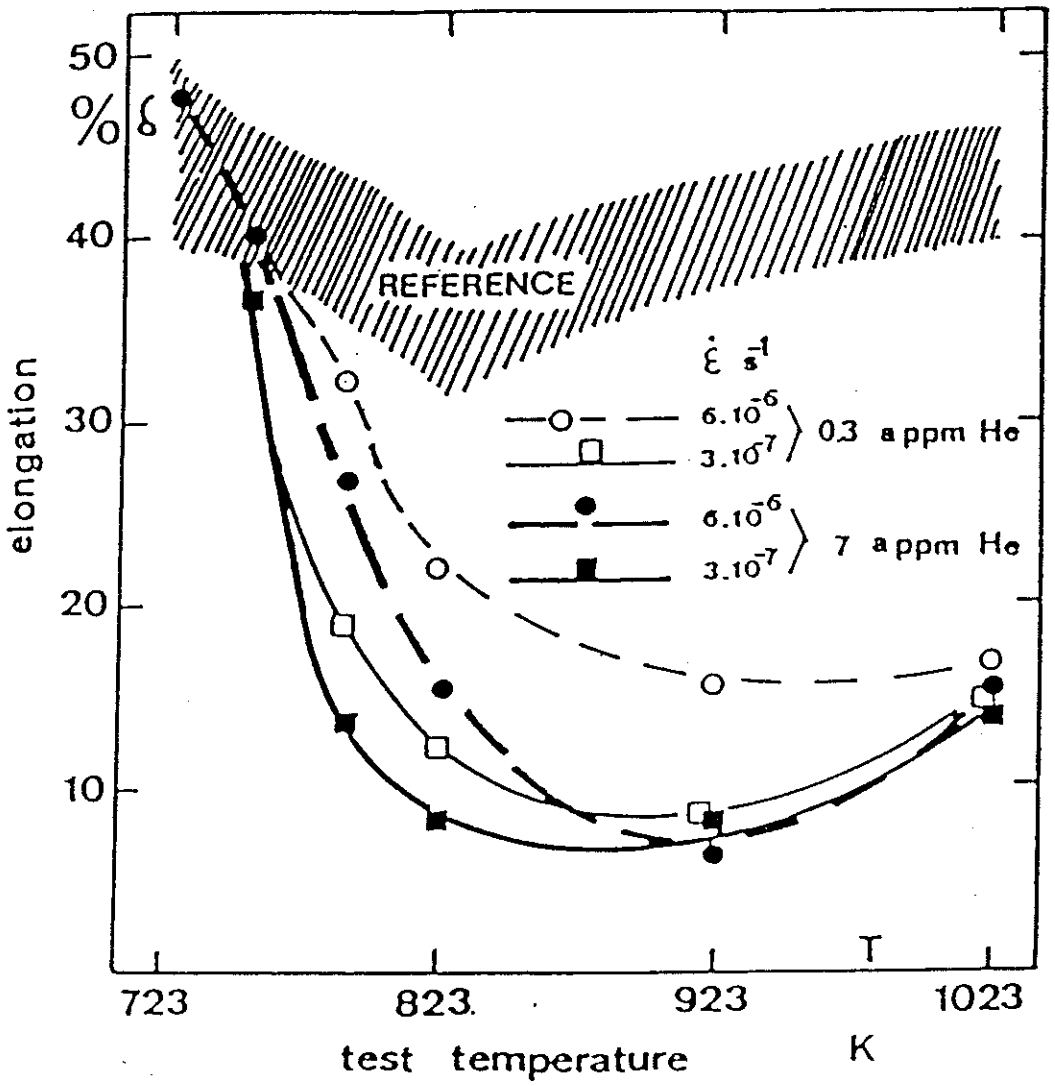

Figure 2. Increase of helium embrittlement at increasing temperature for DIN 1.4948 stainless steel (De Vries et al. Ref. [3]). Copyright, ASTM, 1916 Race Street, Philadelphia, PA, 19103. Reprinted with permission.

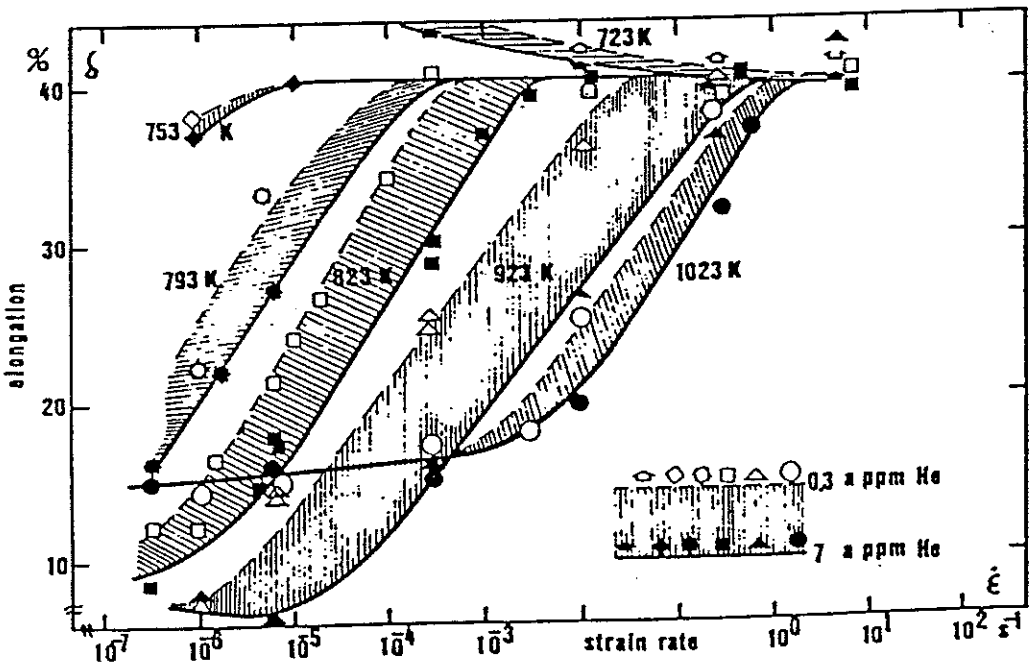

Figure 3. Influence of strain rate, temperature, and helium content on post-irradiation total elongation of stainless steel DIN 1.4946 SS (De Vries et al. Ref. [3]). Copyright, ASTM, 1916 Race Street, Philadelphia, PA, 19103. Reprinted with permission.

microstructure needs time to develop its detrimental effects, because bubble nucleation and growth are diffusion controlled processes.

2. HELIUM EMBRITTLEMENT OF FERRITIC VERSUS AUSTENITIC STEELS

The traditional structural alloys for LMFBR have been austenitic stainless steels or nickel base alloys. In recent years, however, ferritic or highly tempered martensitic stainless steels have been under serious consideration as alternative materials for fission as well as fusion applications. Ferritics appear to exhibit a certain degree of resistance to high temperature helium embrittlement [4]. This is clearly shown in Fig. 4. The figure compares the ductility of the martensitic steel 1.4914 with that of the austenitic 1.4970 in the cold-worked and aged condition after irradiation. For this comparison, specimens with similar helium content of 90 appm were used. The difference in the ductility behavior between the two steels is clearly recognizable. The ductility of the austenitic steels decrease significantly with increasing rupture life because of the growing efficiency of helium embrittlement with a decreasing deformation rate. In contrast, the ductility of the martensitic steel shows only a mild dependence on the deformation rate. It can be concluded, therefore, that the martensitic steel has a high resistance to helium embrittlement. Explanations of this phenomenon are limited and will be discussed later in Chapter VI.

3. COMPARISON OF NEUTRON (REACTOR) AND IMPLANTATION RUPTURE DATA

To experimentally study the helium embrittlement effect in proposed fusion first wall materials, one has to simulate the fusion reactor

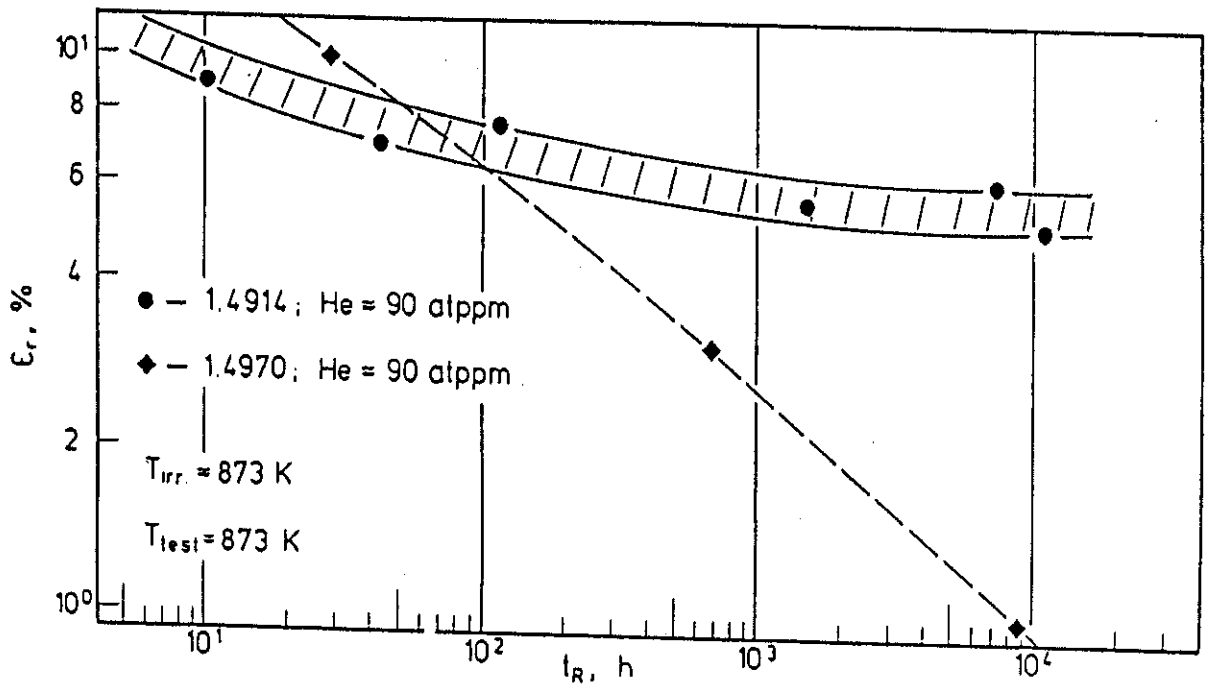

Figure 4. Comparison of the ductility between the irradiated steels 1.4914 and 1.4970. After C. Wassilew [4]. Courtesy of the Institute of Metals, 1 Carlton House Terrace, London, SW1Y 5DB, England.

environment in conjunction with a test mode to measure mechanical properties. Mechanical properties can be measured during reactor irradiation (in-pile) or during α implantation (in-beam). This situation represents an ideal testing environment. However, difficulties in experimental setups to accommodate the radiation environment and mechanical properties testing simultaneously have driven scientists to pre-irradiate or pre-implant specimens, followed by the mechanical test. It is quite important that irradiation/implantation temperature is the same as the test temperature.

A collection of creep rupture times t_R versus applied stress σ on specimens of a T_i-stabilized austenitic stainless steel DIN 1.4970 SS, irradiated with neutrons (in-pile as well as out-of-pile) and helium implanted (in-beam as well as pre-implanted) is presented in Fig. 5 [5]. The figure clearly shows that out-of-pile measurements have a very strong stress dependence of t_R ($t_R \sim \sigma^m$), whereas in-pile/in-beam measurements exhibit a mild stress dependence on t_R. This contradiction cannot be easily rationalized but rather it is due to a combination of various phenomena such as the absence of radiation damage in post-implantation/post-irradiation testing and how it affects the microstructure, helium re-solution, and the creep rate.

4. THEORETICAL MODELS

As mentioned earlier, the mechanism of high temperature helium embrittlement is the unstable growth of grain boundary helium bubbles under the influence of stress. Electron microscopy (TEM and SEM) have shown (see Refs. [4,6]) that grain boundaries perpendicular to the applied stress are affected preferentially. Therefore, all proposed

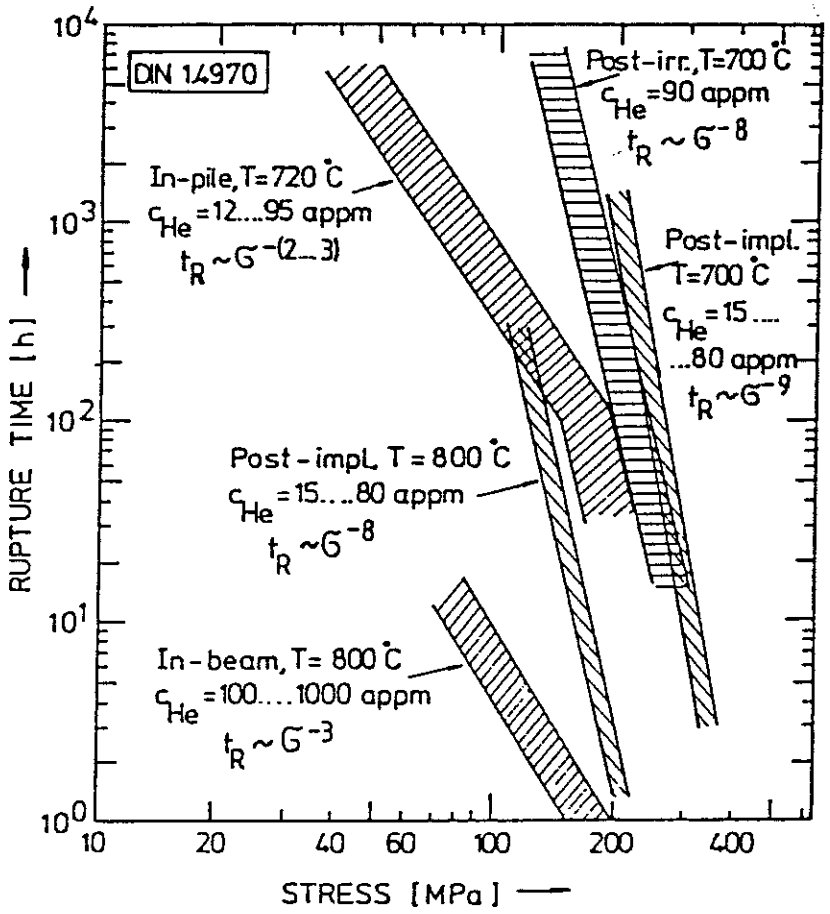

Figure 5. Comparison of the stress dependencies of the creep rupture times of DIN 1.4970 SS tested in various conditions. After Shroeder [5]. Copyright Gordon and Breach, Science Publishers Inc., 50 W. 23 Street, New York, N.Y., 10010. Reprinted with permission.

models focus on the nucleation and growth of such bubbles. A summary of key theoretical models is represented as a flowchart (Figs. 6 and 7). The discussion of previous work in this area is given below.

4.1. Theoretical Models of Creep Fracture In the Absence of Irradiation

4.1.1. Cavity Growth by Vacancy Diffusion. Hull and Rimmer [7] were the first investigators to treat the problem of grain boundary cavity growth, which has been identified earlier by Balluffi and Seigle [8] as the mode of high temperature creep fracture. Hull and Rimmer calculated the growth rate of cavities by making a number of assumptions which may be listed as follows:

1. Vacancies could be produced at grain boundaries in sufficient numbers to allow cavity growth, and that an equilibrium exists between the vacancy concentration and the local stress.

2. The vacancy fluxes are described by diffusion theory.

3. Rapid surface diffusion maintains spherical cavity surfaces.

4. The normal boundary stress immediately adjacent to the cavity is maintained at a value equal to $2\gamma/R$ where γ is the surface tension and R is the cavity radius.

5. The boundary is divided into square unit cells, each associated with a cavity.

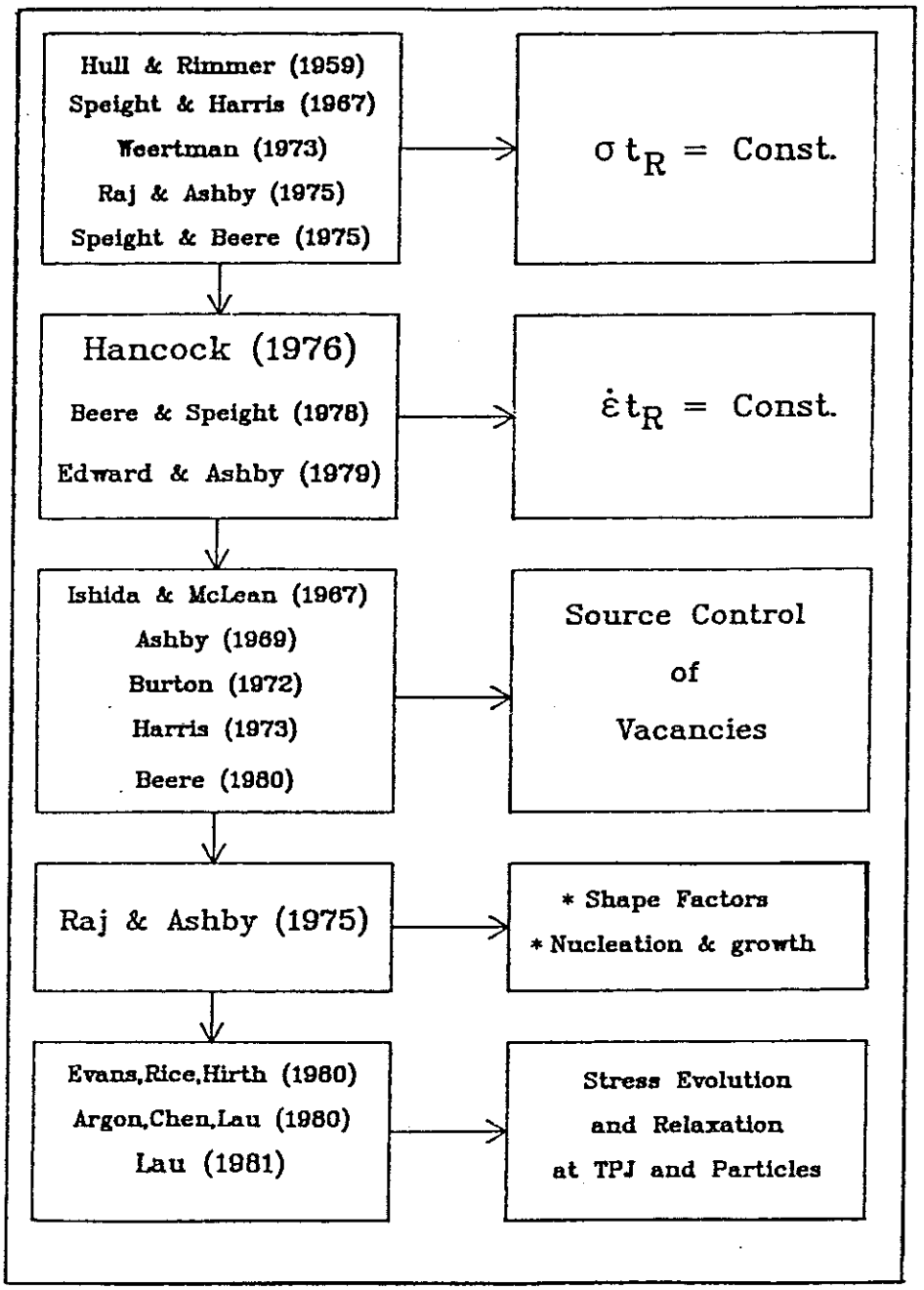

Figure 6. The significant theoretical model contributions in high temperature creep in the last three decades.

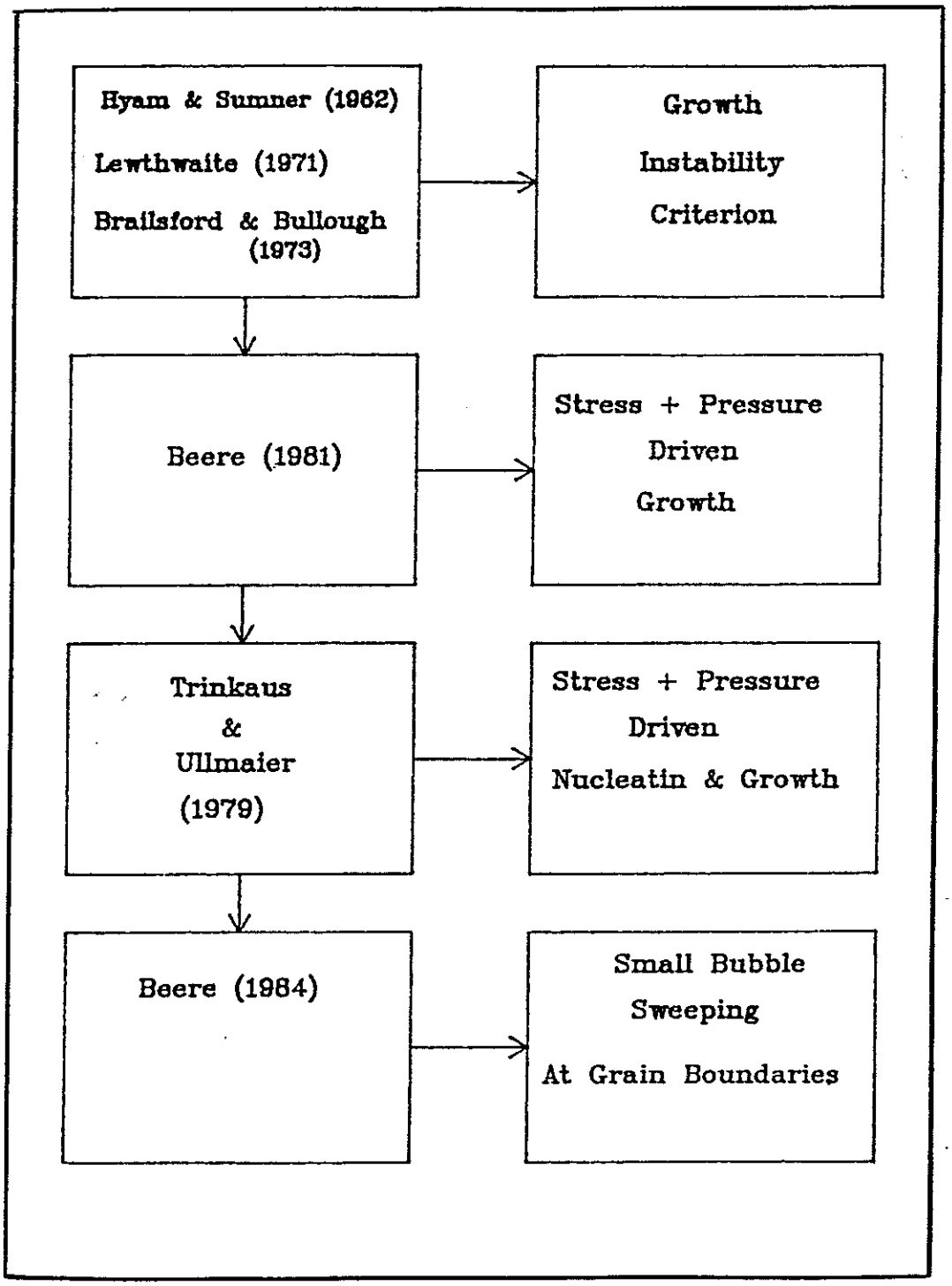

Figure 7. The significant theoretical contributions analyzing the helium embrittlement phenomenon.

The combination of circular and square geometries leads to an inconvenient mathematical form for the growth rate. Since then many authors [9-12] have recalculated the growth rate by assuming circular geometry in the boundary plane for both the cavity and the collection area of vacancies. This greatly simplified the calculation and gives a simple analytical form. However, the diffusion growth model predicts a time to rupture t_R, inversely proportional to the applied stress. That is

$$t_R \propto \frac{1}{\sigma} \quad . \tag{1}$$

In addition, the diffusional growth model overpredicts the growth rate of cavities by many orders of magnitude. Experimental evidence (e.g., [13]) has shown the rupture time takes the form

$$t_R \propto \frac{1}{\sigma^n} \quad , \tag{2}$$

or

$$t_R \propto \frac{1}{\dot{\varepsilon}} \quad . \tag{3}$$

where $\dot{\varepsilon}$ is the creep rate. This relationship has been termed the Monkman-Grant relationship.

4.1.2. Theoretical Models Predicting the Monkman-Grant Relationship. Hancock [14] presented the first model which results in a Monkman-Grant-type relationship. The problem was modeled as large-scale growth of a single cylindrical hole in an incompressible viscous solid under a biaxial state of stress. The model showed that the initial hole-growth rate for an elastic or viscous solid behaves as

$$\frac{dR}{dt} = R\dot{\varepsilon} \quad , \tag{4}$$

where R is the radius of the hole. Integrating the previous equation results in a Monkman-Grant-type relationship. Edward and Ashby [15] have also considered cavity growth by power-law creep alone. Their model leads directly to the Monkman-Grant relationship. However, both models resulted in an overestimate of the time and strain to fracture, and predict values for the Monkman-Grant constant which are too large.

Beere and Speight [16] have suggested that the discrepancies between the growth models and the Monkman-Grant relationship can be resolved. They suggested that the voids, when small, grow by diffusion which is driven by local stresses, which in turn are fixed by the power-law creep of the surrounding grains. This is illustrated in Fig. 8. The size of the diffusion zone depends on the distance matter can diffuse outward from the void in a time scale which is dictated by the strain rate. In turn, this coupled growth model has two limits: (1) At low applied stress, the extent of the creep region becomes vanishingly small so that b tends to c. The void growth is then entirely controlled by diffusion and hence a Hull-and-Rimmer-type growth model is applicable. (2) At sufficiently high rates, the diffusion zone becomes very small and b approaches a. The void growth is then controlled by plastic deformation and their model reduces to the one derived by Hancock [14] for the growth of a spherical hole in a viscous solid without a vacancy flux.

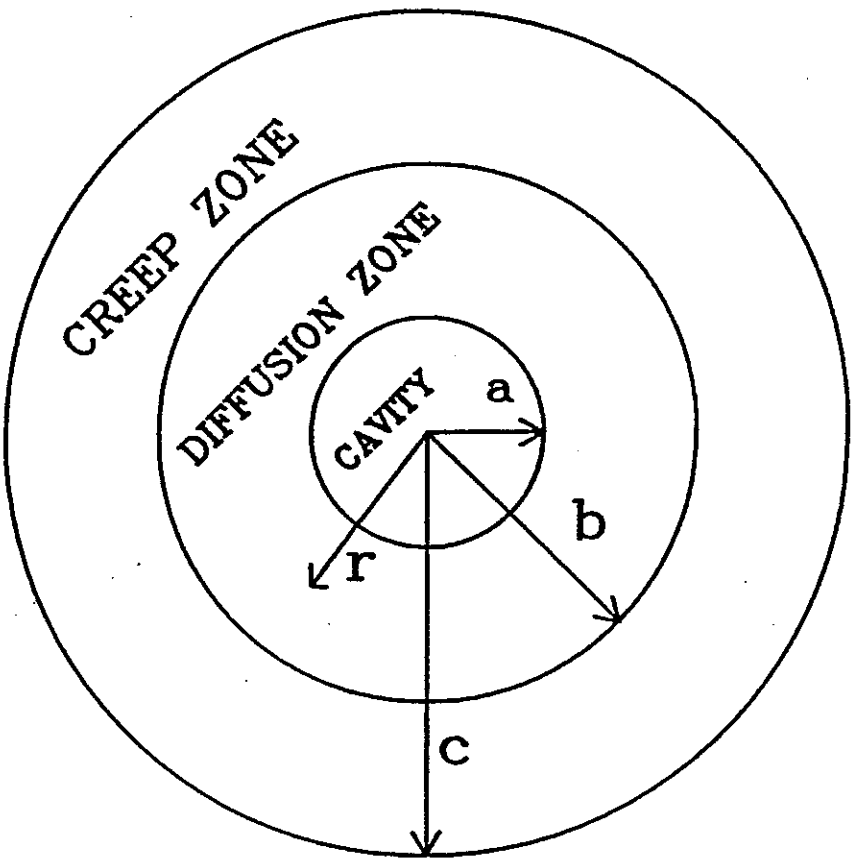

Figure 8. Beere and Speight's model of creep cavitation by vacancy diffusion in plastically deforming solid [16]

4.1.3. Cavity Growth Models to Account for the Source of Vacancies. Grain boundary cavity growth is a process which involves the creation of vacancies in ample quantitles. Hull-and-Rimmer-type growth models [7,9-12] always assumed that boundaries can supply such vacancies without exhaustion. However, many studies have shown that grain boundaries are not a perfect source of vacancies (e.g., Balluffi [17], Greenwood [18], and Gleiter [19]). Several models have been proposed to describe the inhibition of vacancy creation at grain boundaries. Ashby [20] proposed that vacancies are created at moving dislocations in the boundary. The motion of such dislocations can be impeded by particles and cannot proceed unless the Orowan stress is exceeded. Dislocation passage leaves a dislocation loop around the particle, blocking any additional dislocation passage. Burton [21] proposed that for a continued dislocation motion in the grain boundary, the loop must climb in the particle matrix interface. Harris [22] proposed a similar mechanism which has been termed loop punching. However, the kinetics of these processes are at present not well understood.

Ishida and McLean [23] have suggested that the vacancy source may be controlled by dislocation creep. Dislocations moving in the matrix were considered to enter the boundary and migrate in the boundary by a combination of climb and glide. Vacancies are created during climb and migrate to the cavities. Cavity growth can actually be controlled by the supply of dislocations. Beere [24] suggested an extension of this model which has been quantified by assuming dislocations to climb, on average, a distance equal to the interparticle spacing before reentering the lattice. Beere's model produces a cavity growth rate given by

$$\frac{dV}{dt} \sim \frac{\pi^2}{4} L^2 \lambda \dot{\varepsilon} \quad , \tag{5}$$

where L is the cavity half spacing and λ is the dislocation climb distance which is assumed to be equal to the interparticle half spacing. In a later publication, Beere [25] has suggested that overall the growth rates can be computed by considering grain boundary diffusion to act independently of the plastic growth by dislocation creep. However, when grain boundary diffusion is appreciably the faster of the two mechanisms, the growth rate might be determined by the dislocation source control of vacancies. This will be discussed further in Chapter VI.

4.1.4. Nucleation of Cavities at Second-Phase Particles in Grain Boundaries. During the last decade, metallurgists (e.g., [11,26]) adapted the classical nucleation theory to make it applicable to stress-driven nucleation of cavities at grain boundaries. Earlier applications of classical nucleation theory [11] did not satisfactorily explain the nucleation phenomenon. The link between grain boundary particles and cavity nucleation was established earlier (1951) by Servi and Grant [27]. Their experimental work has shown that in the absence of any grain boundary obstacles, no creep cavities were present. Harris [28] had suggested that stress concentrations at inclusions and triple points could lead to void nucleation. However, Raj and Ashby [11] speculated that cavities are not nucleated spherical but are lenticular in shape, and asserted that grain boundary particles are preferable sites for thin cavities. This actually enters classical nucleation theory as a shape factor and it reduces the nucleation energy barrier and enhances the

nucleation rate. This will be discussed in detail in Chapter III. The Raj and Ashby [11] contribution, in addition to the introduction of the shape factor in classical nucleation theory, is the introduction of a compounded model in which the nucleation and the growth rates are integrated sequentially to calculate the time to fracture.

The other approach to bridge the gap between classical nucleation theory and the observed nucleation behavior is the one suggested by Harris [28]. That is, stress concentration at boundary precipitates is a key mechanism in cavity nucleation. Raj [29] analyzed the role of sliding with elastic accommodation in building up stress concentrations at precipitates, ledges, and triple-point junctions. In addition, the role of diffusional and power-law creep accommodation, which serves to relieve such stress concentrations, is also included in the analysis.

The issue of stress concentration at grain boundary inclusions and triple-point junctions due to sliding received considerable attention by Lau [30]. The finite element method was used to calculate the stress concentration factors associated with grain boundary inclusions in a power-law creeping material. The numerical results are given in Chapter III. Evans, Rice, and Hirth [31] have presented a fairly complete model of stress evolution and relaxation at triple-point junctions. Argon, Chen, and Lau [32] presented a model which coupled grain boundary sliding and the stress evolution and relaxation at triple-point junctions and precipitates. However the model was not suitable for the description of the nucleation phenomenon.

Although a large number of attempts have been made to model cavity nucleation at grain boundary precipitate, no model has attempted to explain cavity nucleationa at boundaries perpendicular to the applied

stress. Fracture at high temperatures occurs along perpendicular boundaries to the applied stress. However, preferred nucleation occurs on boundaries parallel to the applied stress, since the stress singularity is most severe at obstacles along such boundaries. In the next chapter, a comprehensive model will be presented to describe the nucleation phenomenon of cavities in the absence of irradiation.

Figure 7 is a flowchart of the theoretical efforts on high temperature creep fracture.

4.2. Theoretical Modeling of Helium Embrittlement

4.2.1. The Effect of Stress on the Growth of Helium Bubbles. The growth models of cavities lying on grain boundaries perpendicular to the direction of the applied stress are applicable to the growth of helium bubbles located on such boundaries. However, two aspects of the void analysis needed changing: the stability criterion and the vacancy concentration at the bubble surface during growth. In the absence of irradiation, the stability criterion for a spherical cavity is given by

$$\sigma = \frac{2\gamma_s}{R_o} \quad , \tag{6}$$

where γ_s is the cavity surface energy. However, an analogous criterion for gas-filled bubbles in mechanical equilibrium with the solid was deduced by Hyam and Sumner [33]. Essentially, the gas pressure and the applied stress cooperate to enlarge the bubble and the growth starts if, and only if, the bubble is unstable due to the fact that the radius of the bubble has already reached its critical value ($R > R_{crit}$) for a

given applied stress. This can be explained quantitatively as follows: If m is the number of gas atoms in the bubble and γ is the surface tension, then

$$m = \frac{4}{3} \pi R_o^2 \left(\frac{2\gamma_s}{kT}\right) \quad , \tag{7}$$

where k is the Boltzmann's constant and T is the absolute temperature.

The mechanical equilibrium no longer holds when the stress σ, assisted by the gas pressure P, is applied. It follows then, that a change in R takes place and

$$\sigma + P = \frac{2\gamma_s}{R} \quad . \tag{8}$$

Applying the gas law PV = mkT, it results in

$$\sigma = \frac{2\gamma_s}{R} \left(1 - \frac{R_o^2}{R^2}\right) \quad . \tag{9}$$

This equation is then the criterion for stability and it reaches a maximum when $R = \sqrt{3}\, R_o$, i.e.,

$$\sigma_c = \frac{4\sqrt{3}}{9} \frac{\gamma_s}{R_o} \quad . \tag{10}$$

The moment $\sigma > (4/3\sqrt{3})\ (\gamma/R_o)$, stability is lost and growth starts. The Hyam and Sumner [33] instability criterion is applicable in the post-irradiation state. Brailsford and Bullough [34] have derived a similar instability growth relation which is applicable during irradiation. The Brailsford and Bullough criterion for unstable growth is given by

$$\sigma_c = \frac{2}{3}\left[\frac{32\pi\ \gamma_s^3}{9m(t)\ kT}\right]^{1/2} \quad , \tag{11}$$

where m(t) is the increasing number of gas atoms within a bubble with time. Both the Hyam and Sumner and the Brailsford and Bullough criteria are applicable only to spherical cavities, however Lewthwaite [35] has shown that such criteria can be modified to apply to lenticular shaped bubbles.

Another fact that may be considered at this moment is the vacancy concentration and interstitial concentration at the bubble surface. It is shown [36] that the internal pressure reduces the vacancy and interstitial concentrations at the bubble surface. Beere [25] has included this effect in an overall growth model to study helium embrittlement.

4.2.2. Theoretical Treatments of Bubble Nucleation at Grain Boundaries. Lane and Goodhew [37] have attempted to model bubble nucleation behavior at grain boundaries. The model can be described qualitatively as follows. Implanted helium atoms diffuse rapidly, by an interstitial mechanism, until they are trapped at a lattice defect or at a grain boundary. Helium atoms, encountering the interface of the boundary, will become bound to it. Although helium atoms are bound to the interface of the boundary, they are free to diffuse in two dimensions within the boundary plane until they encounter other helium atoms. Two helium atoms were considered a stable bubble nucleus. Helium bubbles are nucleated until newly arrived helium atoms are more likely to reach an existing nucleus than another single gas atom. These assumptions

resulted in a simple analytical form describing bubble nucleation at grain boundaries. However, the model is strongly dependent upon the helium arrival rate at grain boundaries. In their model, it was assumed to be constant and was measured experimentally at the end of irradiation. In Chapter IV it will be shown that it is not constant and it is strongly dependent on the irradiation conditions as well as material parameters.

4.2.3. The Growth of Sub-Critical Bubbles on Grain Boundaries. Recently it has been suggested by Beere [38] that small pre-existing bubbles situated at grain boundaries can be swept by secondary grain boundary dislocations during their climb process. This bubble motion induced by dislocations results in bubbles continuously impinging and coalescing. This process actually aids bubbles in reaching their critical size. However, the process is limited to high temperatures and small bubbles and isn't applicable to the helium embrittlement regime.

4.2.4. Trinkaus and Ullmaier Model of Helium Embrittlement. Rather than reviewing the details of the Trinkaus and Ullmaier model, it is more important to mention the key features of their model.

1. The model essentially focuses at the grain boundary area and the associated damage caused by cavity nucleation and growth.
2. It is assumed in the model that cavities nucleate solely at grain boundary precipitates and classical nucleation theory is implemented to describe the nucleation phenomenon.

3. In addition, it is assumed that all helium generated ends up in grain boundary cavities and results in highly pressurized cavities. The high pressure represents the driving force for subcritical embryos to overcome the nucleation energy barrier.

4. The growth law for the gas-filled bubble is formulated in a manner similar to that applied by Hull and Rimmer [7] to grain boundary voids. The Hull and Rimmer growth law essentially accounts for growth by vacancy diffusion.

Although the model is fairly recent, it is far from complete and fell short from describing all the physics involved in the problem of helium embrittlement. Our viewpoint is summarized in the following:

1. The model focuses at the grain boundary region. However, the helium embrittlement phenomenon extends beyond the grain boundary. Helium which is generated homogeneously throughout the material (except for the isolated case of boron) and the associated irradiation damage is a prerequisite to helium embrittlement. Together, they reshape the microstructural features of the matrix (i.e., matrix bubble nucleation and growth) and control the amount of helium escaping to the grain boundary.

2. The model assumes that grain boundary cavities nucleate solely at the precipitates. However, experiments (e.g., Ref. [37]) have shown that helium results in a large homogeneous bubble

density at grain boundaries. This can seriously degrade the grain boundaries.

3. In the model, it is assumed that all the helium generated ends up at grain boundary precipitate bubbles. Helium is known to form homogeneous bubbles within the grains and only a fraction resides at grain boundaries.

4. If the helium balance has been done for the model, there will not be enough cavity pressure to drive cavity nucleation if classical nucleation theory is utilized.

5. The model assumes that the diffusional growth of grain boundary cavities is the sole mechanism of growth, while it is a very well established fact [25] that other growth mechanisms can operate independently, such as plastic growth of cavities by dislocation creep [13-15].

The brief rebuttal to the Trinkaus and Ullmaier model is only intended to show the need for a more comprehensive model to correctly account for the various physical processes involved in helium embrittlement. The goal of this thesis is to establish such a model. An overall description is given below.

4.2.5. The Current Model. Figure 9 is a flowchart of our proposed model to describe the helium embrittlement phenomenon. The model can be summarized as follows:

1. The creep stress is responsible for cavity nucleation at precipitates. Grain boundary sliding does occur at high temperatures under the action of the applied stress and will result in high stress concentrations at precipitates and triple-point junctions. The stress amplification, if used in classical nucleation theory, results in observed nucleation rates.

2. Neutron irradiation or ion implantation will result in the introduction of helium in the specimen along with displacement damage. Helium atoms can reside in an interstitial position, a substitutional position, or in a cluster/bubble of helium and vacancies. The remaining helium escapes the body of the grain and ends up at the grain boundary. The model utilizes rate theory to describe the different helium reactions which will lead to its clustering. A simple expression to describe the flux of helium to grain boundaries can be derived following the theory of sink strengths.

3. Once the flux of helium to the grain boundary is known, the homogeneous bubble structure at grain boundaries is estimated by utilizing rate theory.

4. The growth behavior of grain boundary cavities is described by considering a detailed growth model [25] which takes growth by

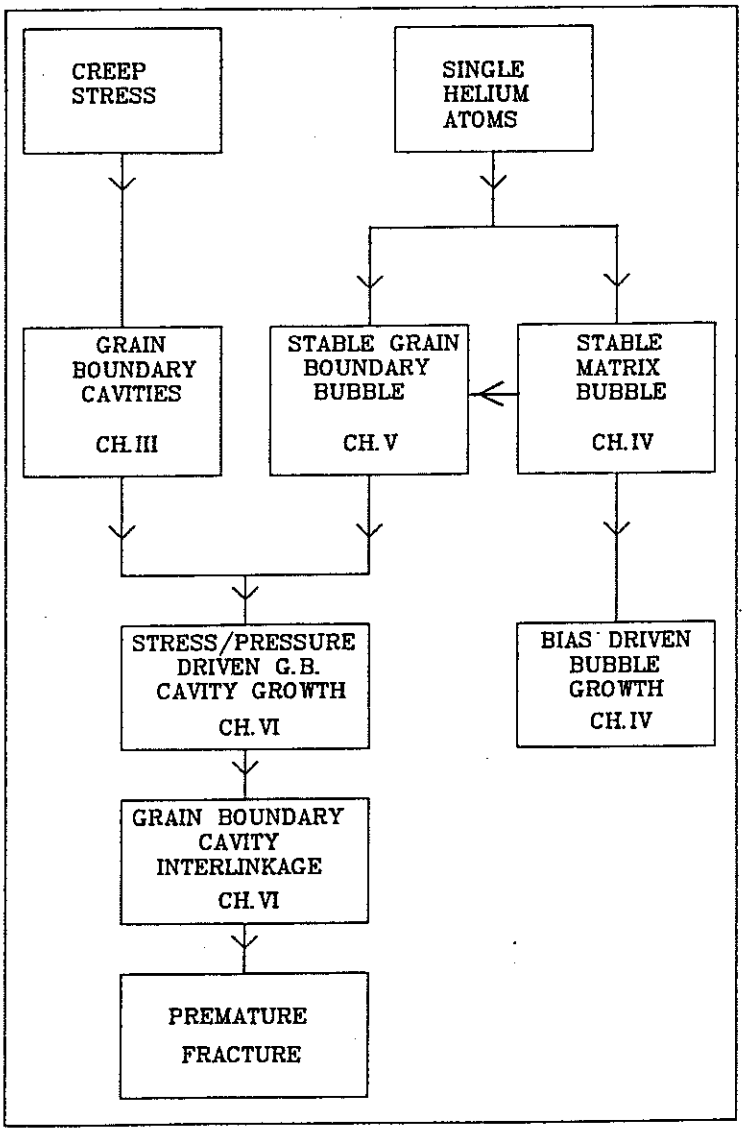

Figure 9. A flowchart of the current model of helium embrittlement.

the grain boundary vacancy-diffusion mode to act independently of growth by plastic deformation. However, plastic deformation results in dislocations entering the boundary and will act as a source of vacancies. Dislocations entering the boundary climb, on the average, a distance equal to the precipitate half spacing. Precipitates act as obstacles to dislocation climb and hence limit the supply of vacancies at grain boundaries.

5. The cavities will grow under the action of stress by the various growth mechanisms until the boundary can no longer support the load and premature fracture occurs readily.

REFERENCES

[1] D. K. Matlock and W. D. Nix, "Effects of Helium on the High-Temperature Creep and Fracture Properties of Ni-6%W," J. Nucl. Mater., 56 (1975) 145.

[2] A. J. Lovell, "Post-Irradiation Creep of Annealed Type 316 Stainless Steel," Nucl. Tech., 16 (1972) 323.

[3] M. I. de Vries, B. van der Schaaf, H. U. Staal and J. D. Elen, "Effects of Neutron Irradiation and Fatigue on Ductility of Stainless Steel DIN 1.4948," in Proc. 9th Intl. Symp. on Effects of Radiation on Structural Materials, Am. Soc. Testing Mater., Richland, WA, 1978, ASTM-STP-683, p. 477.

[4] C. Wassilew, "Influence of Helium Embrittlement on Post-Irradiation Creep Rupture Behaviour of Austenitic and Martensitic Stainless Steels," in Proc. of Int. Conf. on Mechanical Behaviour and Nuclear Applications of Stainless Steel at Elevated Temperatures, The Metals Society, Varese, Italy, 1981, p. 172.

[5] H. Schroeder, "High Temperature Embrittlement of Metals by Helium," Radiat. Eff., 78 (1983) 297.

[6] A. A. Sagües, H. Schroeder, W. Kesternich and H. Ullmaier, "The Influence of Helium on the High Temperature Mechanical Properties of an Austenitic Stainless Steel," J. Nucl. Mater., 78 (1978) 289.

[7] D. Hull and D. E. Rimmer, "The Growth of Grain Boundary Voids Under Stress," Philos. Mag., 4 (1959) 673.

[8] R. W. Balluffi and L.L. Seigle, "Effect of Grain Boundaries Upon Pore Formation and Dimensional Changes During Diffusion," Acta Metall., 3 (1955) 170.

[9] M. V. Speight and J. E. Harris, "The Kinetics of Stress-Induced Growth of Grain-Boundary Voids," Met. Sci. J., 1 (1967) 83.

[10] J. Weertman, "Hull-Rimmer Grain Boundary Void Growth Theory — A Correction," Scripta. Metall., 7 (1973) 1129.

[11] R. Raj and M. F. Ashby, "Intergranular Fracture at Elevated Temperature," Acta Metall., 23 (1975) 653.

[12] M. V. Speight and W. Beere, "Vacancy Potential and Void Growth on Grain Boundaries," Met. Sci. J., 9 (1975) 190.

[13] F. C. Monkman and N. J. Grant, Proc. ASTM, 56 (1956) 593.

[14] J. W. Hancock, "Creep Cavitation Without Vacancy Flux," Met. Sci. J., 10 (1976) 319.

[15] G. H. Edward and M. F. Ashby, "Intergranular Fracture During Power-Law Creep," Acta Metall., 27 (1979) 1505.

[16] W. Beere and M. V. Speight, "Creep Cavitation by Vacancy Diffusion in Plastically Deforming Solid," Met. Sci. J., 12 (1978) 172.

[17] R. W. Balluffi, "High Angle Grain Boundaries as Sources or Sinks for Point Defects," in Proc. Sem. on Grain-Boundary Structure and Kinetics, ASM Materials Science, Milwaukee, WI, Sept. 15-16, 1979 (ASM, Metals Park, OH, 1980).

[18] G. W. Greenwood, "Grain Boundaries as Vacancy Sources and Sinks," in Vacancies '76, (The Metals Society, London, 1977) 141.

[19] H. Gleiter, "The Interaction of Point Defects, Dislocations and Two-Dimensional Defects with Grain Boundaries," in Progress in Materials Science, J. W. Christian, P. Haasen and T. B. Massalski, Eds., Chalmers Anniv. Vol. (Pergamon Press, New York, 1981), p. 125.

[20] M. F. Ashby, "On Interface Reaction Control of Nabarro Herring Creep and Sintering," Scripta Metall., 3 (1969) 837.

[21] B. Burton, "On the Mechanisms of the Inhibition of Diffusional Creep by Second Phase Particles," Mater. Sci. and Eng., 11 (1973) 337.

[22] J. E. Harris, "The Inhibition of Diffusion Creep by Precipitates," Met. Sci. J., 7 (1973) 1.

[23] Y. Ishida and D. McLean, "The Formation and Growth of Cavities in Creep," Met. Sci. J., 1 (1967) 171.

[24] W. Beere, "Inhibition of Intergranular Cavity Growth in Precipitate Hardened Materials," J. Mater. Sci., 15 (1980) 657.

[25] W. Beere, "Theoretical Treatment of Creep Cavity Growth with Application to Embrittlement by Inert Gas," Res Mechanica, 2 (1981) 189.

[26] R. Raj, "Nucleation of Cavities at Second Phase Particles," Acta Metall., 26 (1978) 995.

[27] I. Servi and N. J. Grant, "Creep and Stress Rupture Behavior of Aluminum as a Function of Purity," Trans. AIME, 191 (1951) 909.

[28] J. E. Harris, "Nucleation of Creep Cavities in Magnesium," Trans. Metall. Soc. AIME, 233 (1965) 1509.

[29] R. Raj, "Crack Initiation in Grain Boundaries Under Conditions of Steady-State and Cyclic Creep," J. Eng. Mater. Technol. 98 (Trans. ASME, April 1976) 132.

[30] C. W. Lau, "Dominant Singularity and Finite Element Analyses of Plane-Strain Stress Fields in Creeping Alloys with Sliding Grain Boundaries," Ph.D. thesis, Massachusetts Institute of Technology (1981).

[31] A. G. Evans, J. R. Rice, and J. P. Hirth, "Suppression of Cavity Formation in Ceramics: Prospects for Superplasticity," J. Amer. Ceram. Soc., 163 (7-8) (1980) 368.

[32] A. S. Argon, I. W. Chen and C. W. Lau, "Intergranular Cavitation in Creep: Theory and Experiments," in Creep-Fatigue-Environment Interactions, R. M. Pelloux and N. S. Stoloff, Eds., (AIME, New York, 1980) 46.

[33] E. D. Hyam and G. Sumner, in Proc. Symp. on Radiation Damage in Solids, Vol. 1, International Atomic Energy Agency, Venice, 1962 (IAEA, Vienna, 1962) 323.

[34] A. D. Brailsford and R. Bullough, "The Stress Dependence of High Temperature Swelling," J. Nucl. Mater., 48 (1973) 87.

[35] G. W. Lewthwaite, "On the Growth of Inert Gas Bubbles Subjected to Stress," J. Nucl. Mater., 42 (1972) 235.

[36] D. R. Olander, Fundamental Aspects of Nuclear Reactor Fuel Elements, NTIS TID-26711-P1, (Nat. Tech. Info. Serv., Springfield, VA, 1976).

[37] P. L. Lane and P. J. Goodhew, "Helium Bubble Nucleation at Grain Boundaries," Philos. Mag. A, 48, (1983) 965.

[38] W. Beere, "The Growth of Sub-Critical Bubbles on Grain Boundaries," J. Nucl. Mater., 120 (1984) 88.

[39] H. Trinkaus and H. Ullmaier, "A Model for the High-Temperature Embrittlement of Metals Containing Helium," Philos. Mag. A, 39 (5) (1979) 563.

CHAPTER III

STRESS-CONTROLLED CAVITY NUCLEATION AT GRAIN BOUNDARY PARTICLES AND TRIPLE-POINT JUNCTIONS

1. INTRODUCTION

Over the past decade, a number of theoretical and experimental investigations have addressed the question of cavity nucleation at grain boundaries [1-4]. For example, Raj and Ashby [3] developed a kinetic model of classical heterogeneous nucleation by vacancy clustering at interfaces between precipitate particles and grain boundaries. Their work revealed that cavity nucleation is in fact stress controlled. However, the discrepancy between observed nucleation rates and those predicted by classical nucleation theory led to a widely accepted belief that cavities are mainly nucleated at grain boundary particles or irregularities, where high stress concentrations develop.

Although the main theme of the dissertation is helium embrittlement, there exist situations in which most of the helium is trapped in the matrix and little, if any, helium can end up at grain boundaries (Chapter IV). However, the fracture mode at high temperatures continues to be by a stress-driven growth of voids at boundaries orthogonal to the applied stress. The distinction between void nucleation by helium and stress has to be made. A theory for helium-driven nucleation is given in Chapter V. For the case of stress-driven nucleation, the classical nucleation theory which was founded by Gibbs [5] is implemented in this chapter.

During the last decade, metallurgists [3,4,6] have developed the classical nucleation theory to be applicable to stress-driven nucleation

of cavities. However, theoretical analysis did not explain many aspects of the observed nucleation phenomena. In 1951, a pioneering experiment by Servi and Grant [7] showed that in the absence of any grain boundary obstacles, no creep cavities were present. This led to speculations that stress concentrations are present at grain boundary particles and triple-point junctions [3,8]. Although the existence of an accentuated stress at grain boundary obstacles which opposes sliding is an established fact, no nucleation calculation has yet linked the two phenomenona of stress concentration and cavity nucleation.

In addition, the phenomenon of cavity nucleation at boundaries transverse to the applied stress needs to be explained. Although fracture occurs at orthogonal boundaries to the applied stress, nucleation calculation (e.g., [1-4]) has always been carried out at inclined boundaries [1].

In this Sections 2 and 3, a review of nucleation theory is presented which includes basic energy barrier calculations to illustrate the need for the presence of a stress concentration. In the literature [3], nucleation rates have been used to illustrate the need for the presence of stress concentration. However, energy barrier calculations are much more appropriate. Energy barrier calculations rather than nucleation calculations have also been carried out to illustrate that cavities can never be nucleated with a spherical shape, but should be lenticular.

In Section 4, a review of the source of stress concentrations at boundary obstacles and triple-point junctions is given. That section also includes some time constants which characterize stress evolution and relaxation at obstacles. Although a form of these characteristic

times is given in the literature [9], it is shown here that the loading times of stress can be derived using Maxwell's visco-elastic model. The characteristic loading time of stress at triple-point junctions derived here is quite similar to that which is derived using diffusion conservation equations [9]. The application of Maxwell's model to derive the characteristic loading time of stress at triple-point junctions is a different approach from that given by Argon [9].

In Section 5, nucleation calculations are presented. Stress pulse calculations are carried out at various boundary orientations are utilized in the nucleation calculations. Such calculations are the first to be presented in the literature. The combined model gives a first quantified explanation of cavity nucleation at what seems to be orthogonal boundaries. It is shown that localized disturbances on the orthogonal boundaries can actually explain cavity nucleation at such boundaries. It is also shown in the present work that if localized disturbances are present, they will be sufficient to produce enough stress accentuations to result in cavity nucleation. Another concept has been added to that of localized sliding which is that sliding occurs intermittently. This intermittency of sliding can explain experimental observations that cavity nucleation occurs throughout the creep experiment [10]. Finally, in Section 6 discussions and conclusions are presented.

In summary, this chapter presents the first comprehensive model linking stress evolution at grain boundary obstacles and cavity nucleation. In the present work, many ambiguous concepts such as cavity nucleation at orthogonal boundaries are clarified. In addition, the

model shows the importance of the intermittency of sliding even at boundaries orthogonal to the applied stress.

2. NUCLEATION OF CAVITIES

At elevated temperatures of $\sim 0.6\ T_m$ and medium applied stresses of $\sim 10^{-3}\ \mu$ (μ is the shear modulus), grain boundary cavities are nucleated by diffusional transfer of atoms from grain boundary precipitate surfaces into the grain boundary. This results in the formation of a vacancy cluster, which is large enough to overcome the shrinkage tendency under the action of surface energy forces. The local tensile traction plays a considerable role in aiding cavity embryos to grow through a size range where growth is energetically unstable.

2.1. Thermodynamics of Cavity Nucleation

If C_{max} is the maximum number of potential nucleation sites on a grain boundary per unit area, then the number of critical nuclei per unit area is given by [11]

$$C_c = C_{max} \exp(-\Delta G_c/kT) \quad , \tag{1}$$

where ΔG_c is the change in Gibbs free energy due to the introduction of cavities on the stressed boundary, k is Boltzmann constant, and T is the temperature. The change in the total Gibbs free energy ΔG of a local system due to the introduction of a cavity is given by

$$\Delta G = \Delta G_s + \Delta G_\sigma + \Delta G_e \quad . \tag{2}$$

The three terms on the right-hand side of Eq. (2) are: (1) the energy change due to the introduction of a cavity surface ΔG_s (positive); (2) the work done by the local stress due to the displacement resulting from the formation of a cavity ΔG_σ (negative); and (3) the released elastic strain energy over the cavity volume which has been previously occupied by highly strained matter ΔG_e (negative).

The energy change due to changes in surface and interface areas is given by

$$\Delta G_s = \gamma_s F_s r^2 - \gamma_B F_B r^2 \quad , \tag{3}$$

where r is the radius of curvature, γ_s and γ_B are the surface energies of the cavity and the boundary, respectively, and F_s and F_B are geometrical factors which are discussed in the next section. The work done by the local stress is

$$\Delta G_\sigma = \sigma_L F_v r^3 \quad , \tag{4}$$

where σ_L is the local normal traction and F_v is another geometrical factor which is also discussed in the next section. The elastic energy change ΔG_e is simply the released elastic energy which was contained in the cavity volume, and is given by

$$\Delta G_e = \frac{\sigma_L^2}{2E} F_v r^3 \quad . \tag{5}$$

Comparing Eqs. (4) and (5) and realizing that $E >> \sigma_L$, we realize that $\Delta G_\sigma >> \Delta G_e$. We can therefore safely ignore ΔG_e. Recalling Eq. (2), the following expression is obtained for the total energy:

$$\Delta G = -r^3 F_v \sigma_L + r^2(\gamma_s F_s - \gamma_B F_B) \quad . \tag{6}$$

Equation (6) shows that the barrier to nucleation is the interfacial free energy of the cluster matrix interface ΔG_s. As shown in Fig. 1, ΔG for the formation of a cavity embryo has two components ΔG_s which is positive and ΔG_σ which is negative. ΔG_σ is proportional to r^3. For physical constants in Eq. (6), ΔG_s increases more rapidly than the decrease in ΔG_σ when r is very small; the opposite occurs at relatively large values of r. When the contribution ΔG_σ is first able to prevent ΔG_s from further increasing ΔG, $\partial(\Delta G)/\partial r = 0$. The radius at which this occurs is termed r_c, the critical radius; the corresponding ΔG is termed ΔG_c, the free energy of formation for the critical nucleus. However, even though further increases in r occur with a decrease in ΔG, not until r corresponds to $\Delta G_c - kT$ is the cluster safe against loss of vacancies through destabilizing thermal fluctuations. The back and forth thermal fluctuations can be accounted for by using the Zeldovich factor [12]. This is presented in Section 2.2. below.

In order to find the ΔG_c, the geometrical shape factors need to be defined as well as the equilibrium between surface tension forces at the junction. This is treated in the next section.

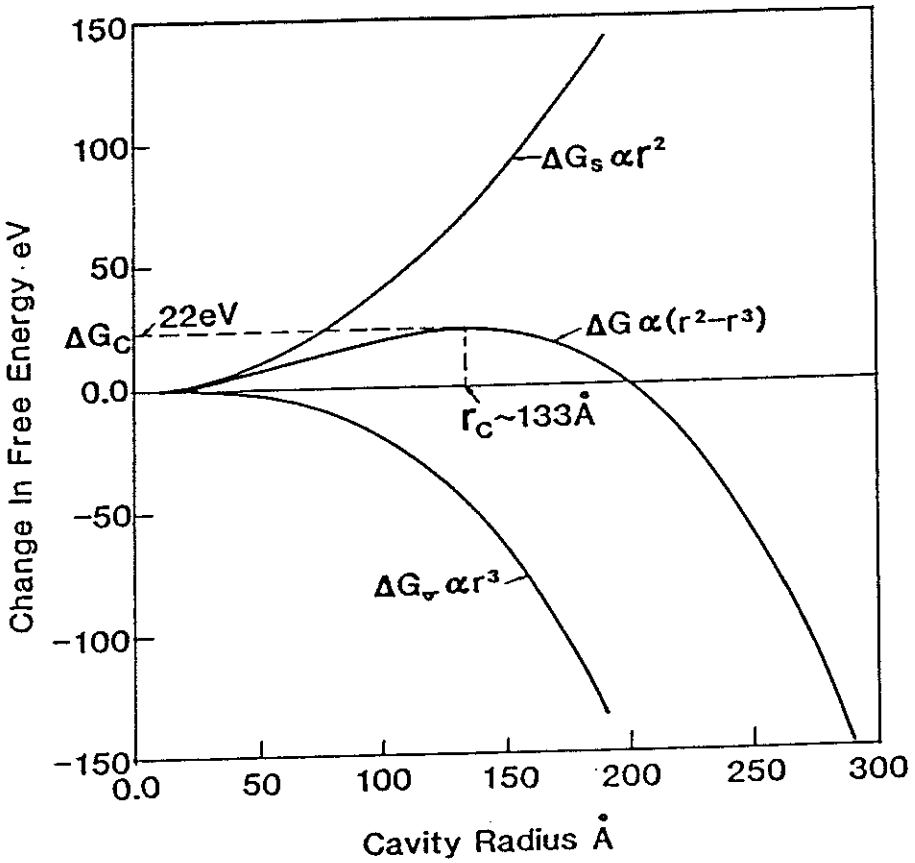

Figure 1. Variation of free energy for embryo formation with cavity radius for an applied stress of 300 MPa and a volume shape factor value of 0.01 .

2.2. Nucleation Kinetics

The kinetics of cavity nucleation is adequately described by the current density of cavity embryos from subcritical to supercritical in size space. The number of supercritical nuclei formed per second is C_c times the time-dependent probability of adding one vacancy to the critical nucleus P_v. P_v can be derived from the jump frequency of a vacancy, which is related to the boundary self-diffusion coefficient, and from the probability of finding a vacancy at the perimeter of the critical embryo. This has been derived by Trinkaus and Ullmaier [13], and we will use their result

$$P_v \simeq 2\pi D_b \delta/\Omega \quad . \tag{7}$$

An additional term, the Zeldovich factor, needs to be included in Eq. (1) which takes into account the back and forth thermal fluctuations between the subcritical and supercritical regimes [12]. This is given in [11] by

$$Z = \left(48\pi F_v \gamma_s^3 \, kT/\sigma_L^4\right)^{-1/2} \quad . \tag{8}$$

Including Eqs. (7) and (8) into Eq. (1), one finds the nucleation rate for nucleation at precipitate sites is given by

$$\dot{C} = C_{max}\left(\frac{\pi}{3F_v\gamma_s^3 \, kT}\right)^{1/2} \frac{1}{2} \sigma_L^2 \, D_b \delta \, \exp\left(-\frac{\Delta G_c}{kT}\right) \quad . \tag{9}$$

Equation (9) does not account for the fact that once a cavity is nucleated its site is no longer available for any additional nucleation. An additional probabilistic factor needs to be included to account for the ever decreasing number of available nucleation sites. This is given by

$$P_s = \frac{C_{max} - C}{C_{max}} \quad . \tag{9a}$$

This factor has been neglected in the literature. Including Eq. (9a) into Eq. (9) gives

$$\dot{C} = (C_{max} - C)\left[\left(\frac{\pi}{12F_v\gamma_s^3\ kT}\right)^{1/2} \sigma_L^2\ D_b\delta\ \exp\left(-\frac{\Delta G_c}{kT}\right)\right] \quad . \tag{9b}$$

If we denote all terms within the large brackets by A(t), then we can rewrite the equation as

$$\frac{dC}{dt} = (C_{max} - C)\ A(t) \quad . \tag{9c}$$

The term A(t) is a complex function of time since the local stress is a complex function of time as it is influenced by the diffusional flow of matter. Equation (9c) is subject to the initial condition that at $t = 0$, $C = 0$.

Solving Eq. (9c) results in

$$C = C_{max}\left[1 - e^{-\int A(t)\ dt}\right] \quad . \tag{9d}$$

Cavity nucleation calculations are carried out utilizing the complex time dependence of the local stress.

Inspecting Eq. (9b), we notice two values which have been the center of controversy, σ_L and F_v. The stresses necessary for nucleation are found to be about 30 times greater than the applied stresses at which nucleation still occurs [14]. Another school of thought [1] argues that such high stress concentrations cannot be reached due to the instantaneous stress relaxation by diffusional flow of matter. It has also been argued [1,4] that cavities assume thin, crack-type shapes. Such shapes help cavities reach equilibrium without the need for the existance of stress concentrations.

In the next section, we develop expressions for cavity geometries and their corresponding shape factors. The final part of the next section is aimed at finding an expanded expression for ΔG_c.

3. VOID GEOMETRIES AND THERMODYNAMIC CONSIDERATIONS

3.1. Void Geometries

Cavities assume different shapes depending on whether they are formed at two-grain junctions, triple-point junctions, or at the interface of inclusions present in grain boundaries. The different possible shapes are shown in Fig. 2. The voids which form at inclusion-free grain boundaries are common in the presence of irradiation [15]. This is treated in detail in Chapter V. Cavities which are of type D are the most commonly observed during creep experiments in the absence of external effects such as irradiation [10].

If we focus our attention on a type A cavity, it is expected that the equilibrium geometry of the cavity in the presence of an interfacial

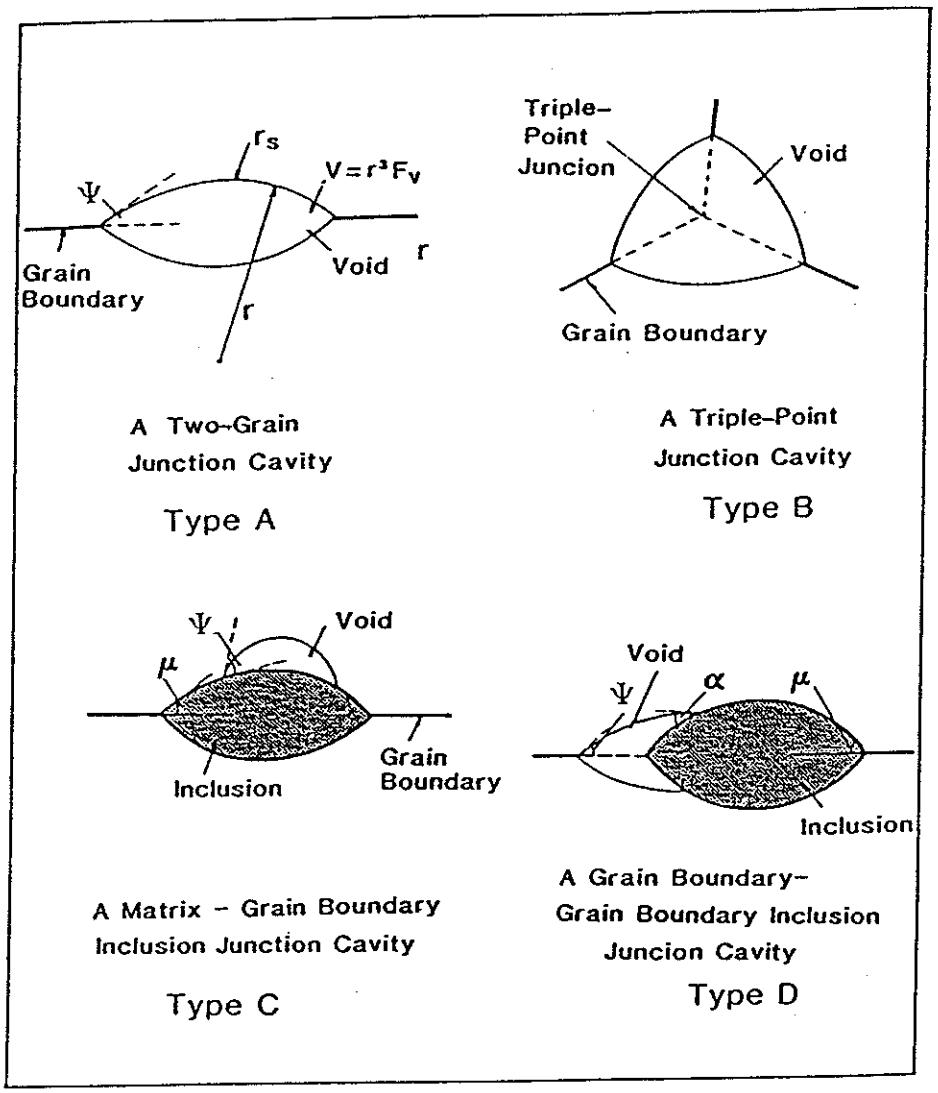

Figure 2. Different grain boundary cavity orientations.

stress is lenticular with an apex angle 2Ψ. This shape is a result of local equilibrium governed by the vacancy chemical potential at the curved free surface and the stressed boundary [16]. These cavities are constrained by local equilibrium at the apex, governed by the free energy of the free surface and the free energy of the boundary that it replaces. Thus, the apex angle is governed by

$$2\gamma_s \cos\Psi = \gamma_B \quad , \tag{10a}$$

or

$$\Psi = \cos^{-1}(\gamma_B/2\gamma_s) \quad . \tag{10b}$$

If we define V as the cavity volume, S as its surface area and B as the grain boundary area that it occupies, we can express such quantities in terms of r and Ψ. In general

$$V = r^3 F_v(\Psi) \quad , \tag{11a}$$

$$S = r^2 F_s(\Psi) \quad , \tag{11b}$$

$$B = r^2 F_B(\Psi) \quad . \tag{11c}$$

The shape factors depend upon the cavity type. They have been calculated for various cavity geometries by Clemm and Fisher [17]. For a cavity of type A, the dependence of the shape factors on Ψ are

$$F_v(\Psi) = \frac{2}{3}\pi(2 - 3\cos\Psi + \cos^3\Psi) \quad , \tag{12a}$$

$$F_S(\Psi) = 4\pi(1 - \cos\Psi) \quad , \tag{12b}$$

$$F_B(\Psi) = \pi \sin^2\Psi \quad . \tag{12c}$$

At the limit of $\Psi = \pi/2$, Eqs. (11) and (12) give shape factors appropriate for a sphere:

$$F_v\left(\frac{\pi}{2}\right) = \frac{4}{3}\pi \quad , \tag{13a}$$

$$F_S\left(\frac{\pi}{2}\right) = 4\pi \quad , \tag{13b}$$

$$F_B\left(\frac{\pi}{2}\right) = \pi \quad . \tag{13c}$$

On the other hand, as Ψ decreases to zero, the geometric properties of a penny-shaped disc are:

$$V = 0 \quad , \tag{14a}$$

$$B = \pi r_D^2 \quad , \tag{14b}$$

where r_D is the radius of the circle of intersection of the cavity with the boundary, and it is related to r by

$$r_D = r \sin\Psi \quad . \tag{14c}$$

The overall trend is illustrated in Fig. 3. A calculated example of the actual cavity shape change as functions of F_v is shown in Fig. 4.

3.2. Thermodynamic Considerations

The critical radius r_c at which ΔG reaches a maximum and the magnitude of this maximum ΔG_c can now be calculated using Eqs. (6), (10a), and (12). Based upon the definitions of shape factors, Eq. (6) can now be written as

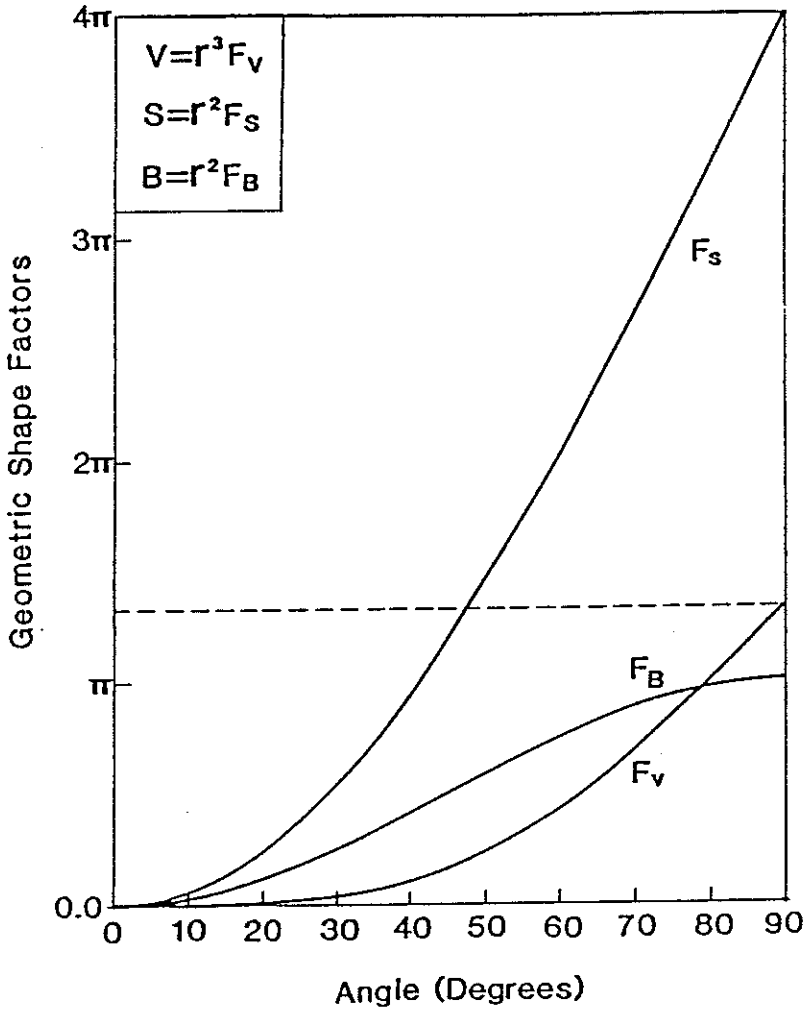

Figure 3. Geometrical shape factors trend as a function of the dihedral angle.

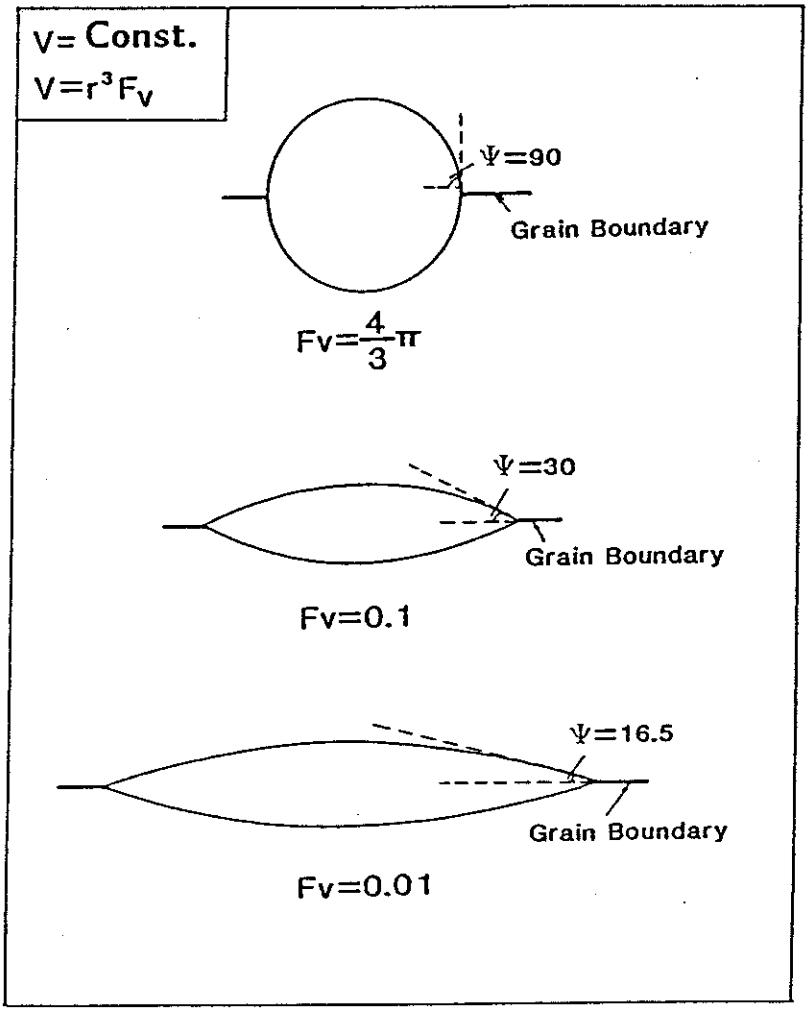

Figure 4. The actual cavity shape changes as a function of the volumetric shape factor F_v.

$$\Delta G = -r^3\left[\frac{2\pi}{3}\left(2 - 3\cos\Psi + \cos^3\Psi\right)\right]\sigma_L$$

$$+ r^2\left\{\gamma_s[4\pi(1 - \cos\Psi)] - 2\pi\gamma_s \cos\Psi \sin^2\Psi\right\} \quad , \tag{15}$$

or

$$\Delta G = (-r^3\sigma_L + 3r^2\gamma_s)F_V \ . \tag{16}$$

Now imposing the condition $\partial(\Delta G)/\partial r = 0$ results in the general result which is applicable to all types of cavity configurations

$$r_c = \frac{2\gamma_s}{\sigma_L} \quad , \tag{17}$$

$$\Delta G_c = \frac{r_c^3 F_V \sigma_L}{2} \quad , \tag{18a}$$

thus

$$\Delta G_c = 4\gamma_s^3 F_V/\sigma_L^2 \quad . \tag{18b}$$

Figure 1 shows calculated ΔG versus cavity radius for a shape factor of 0.01, and applied stress of 300 MPa and a typical surface energy of 2 J/m^2. The figure reveals that even in the presence of a relatively high local stress, the barrier to nucleation stands at 22.13 eV and it is expected that nucleation is impossible. If we examine Eqs. (18a and 18b) they show that there are three possible ways to reduce the energy barrier to nucleation: (1) the cavities must be extremely thin (reducing F_v); (2) the local stress has to reach extremely high values; or (3) a combination of the first two. Figure 5 illustrates that if the local stress is 100 MPa, the shape factor should be in the neighborhood of 10^{-4}, otherwise nucleation will be impossible. Such extreme values of F_v have been suggested by Reidel [1] and Raj and Ashby [4]. The

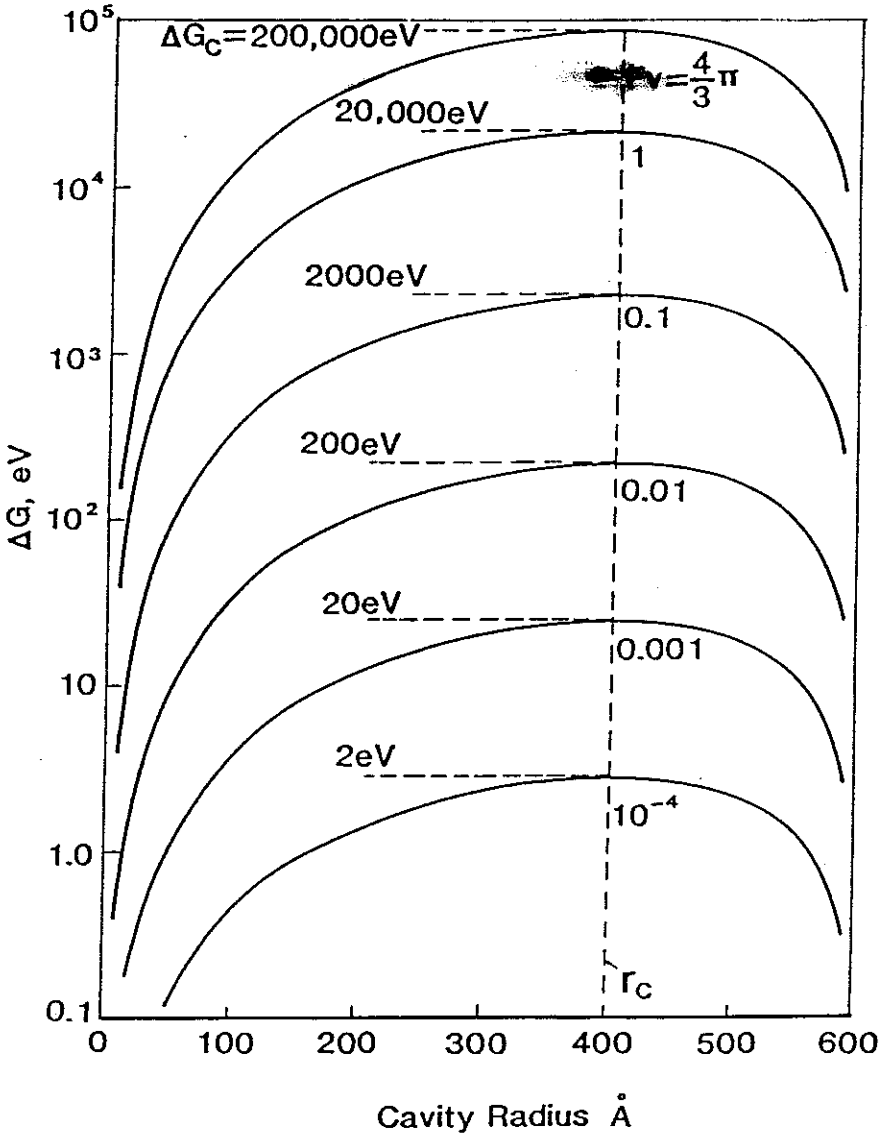

Figure 5. The formation energy dependence of the volumetric shape factor for a typical creep test stress of 100 MPa.

other possibility is that stress concentrations have to be present at inclusions and triple points in order for void nucleation to proceed [6,18, 19]. Figure 6 shows that the critical free energy for cavity formation varies significantly as a function of the local stress. The figure clearly illustrates that a stress-concentration mechanism has to be present in order to make nucleation possible (typical engineering stresses under creep are ~ 100-200 MPa). The shape factor value of about 0.01 has been adopted as reasonable by many investigators [4,13]. However, other investigators [20] asserted that F_v has a value of ~ 0.3 according to their experimental observations. This shows an uncertainty in the actual value of F_v. The next section will deal with stress-concentration evolution at preferred sites at the grain boundaries. This will then be followed by nucleation calculations which incorporate the stress concentration factors as well as various possible shape factors.

4. STRESS CONCENTRATIONS AT PARTICLES AND TRIPLE-POINT JUNCTIONS

4.1. Introduction

The principles behind the presence of stress concentrations at rigid particles embedded in an elastic matrix have been pioneered by Goodier [21]. For the purposes of calculations, it was assumed by Goodier that the solid surrounding the inclusion is infinite in extent and subjected to a uniformly applied stress far away from the particle. It was also assumed that the solid has ideal properties of elasticity, isotropy, and homogeneity. The calculations revealed that in simple tension, a perfectly rigid spherical inclusion intensifies the tension

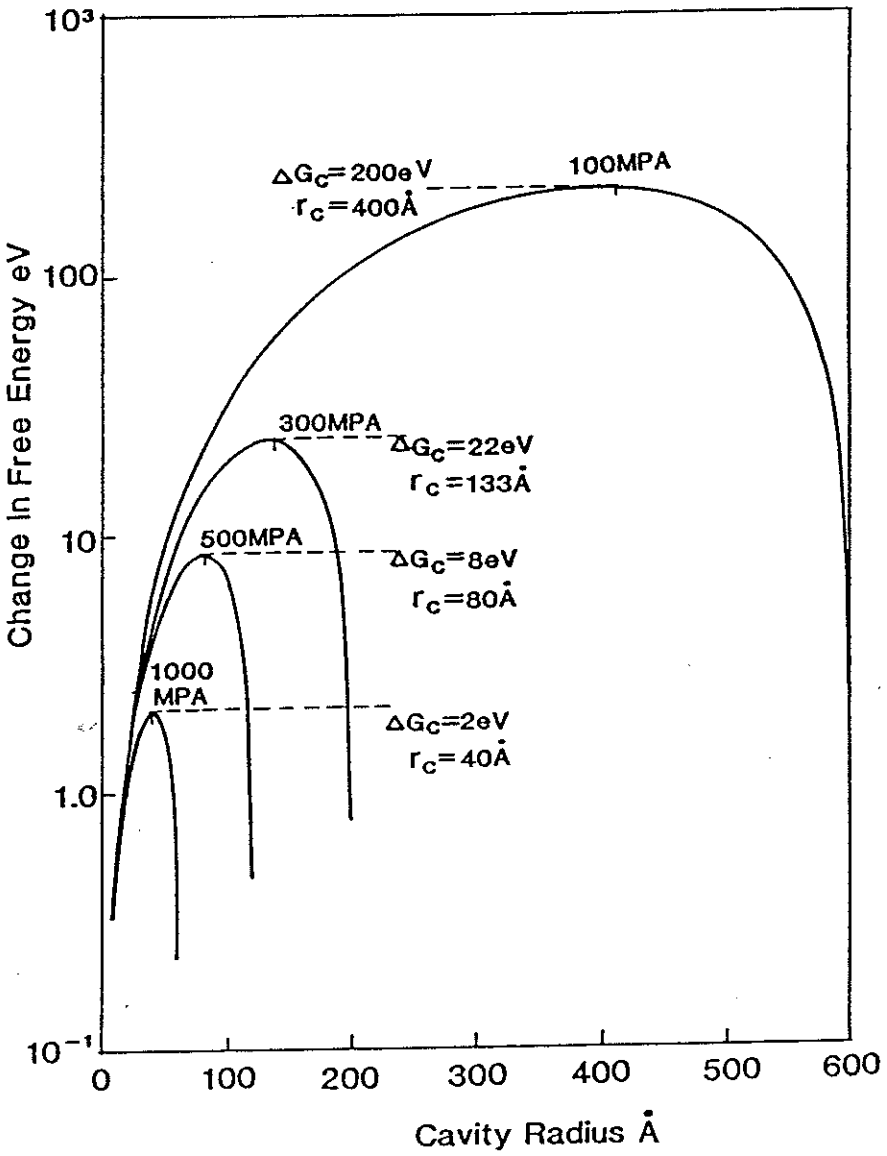

Figure 6. The formation energy dependence of the local creep stress for a shape factor value of 0.01.

stress (Fig. 7) in the same direction as the applied tensile stress σ. The magnitude of this intensification at the "pole" is given by

$$\sigma_{pole} = \left(\frac{2}{1 + \nu} + \frac{1}{4 - 5\nu}\right)\sigma_{applied} \quad . \tag{19}$$

However, the tension at the "equator" is the same direction is reduced to

$$\sigma_{equator} = \left(\frac{\nu}{1 + \nu} - \frac{5\nu}{8 - 10\nu}\right)\sigma_{applied} \quad , \tag{20}$$

where ν is the Poisson's ratio. For stainless steel, where the Poisson's ratio is about 1/3, the stress at the pole is about $2\sigma_{applied}$ and at the equator, it is compressive and has a value of $\sigma_{applied}/9$.

The magnitude of the stress concentrations, as calculated by Goodier [21], are not really significant in reducing the free energy of formation to a reasonable value. However, if particles are present at sliding grain boundaries, stress concentrations approaching the ideal cohesive strength limit will be present at particle faces. This has been shown by Lau [22] as well as Reidel [1]. The next section will deal with grain boundary sliding and the stress concentration at particles and triple-point junctions. That will be followed by simple models in which the time dependence of such stress will be incorporated. The reason for such time dependence is the fact that at high temperature, matter motion occurs to relieve such stress concentrations. Before proceeding to the next subsection, it is reasonable to present a simplified picture of stress concentration at triple-point junctions.

Triple-point junction stress concentration is closely related to the tensile stress concentration of a single mode II penny-shaped crack

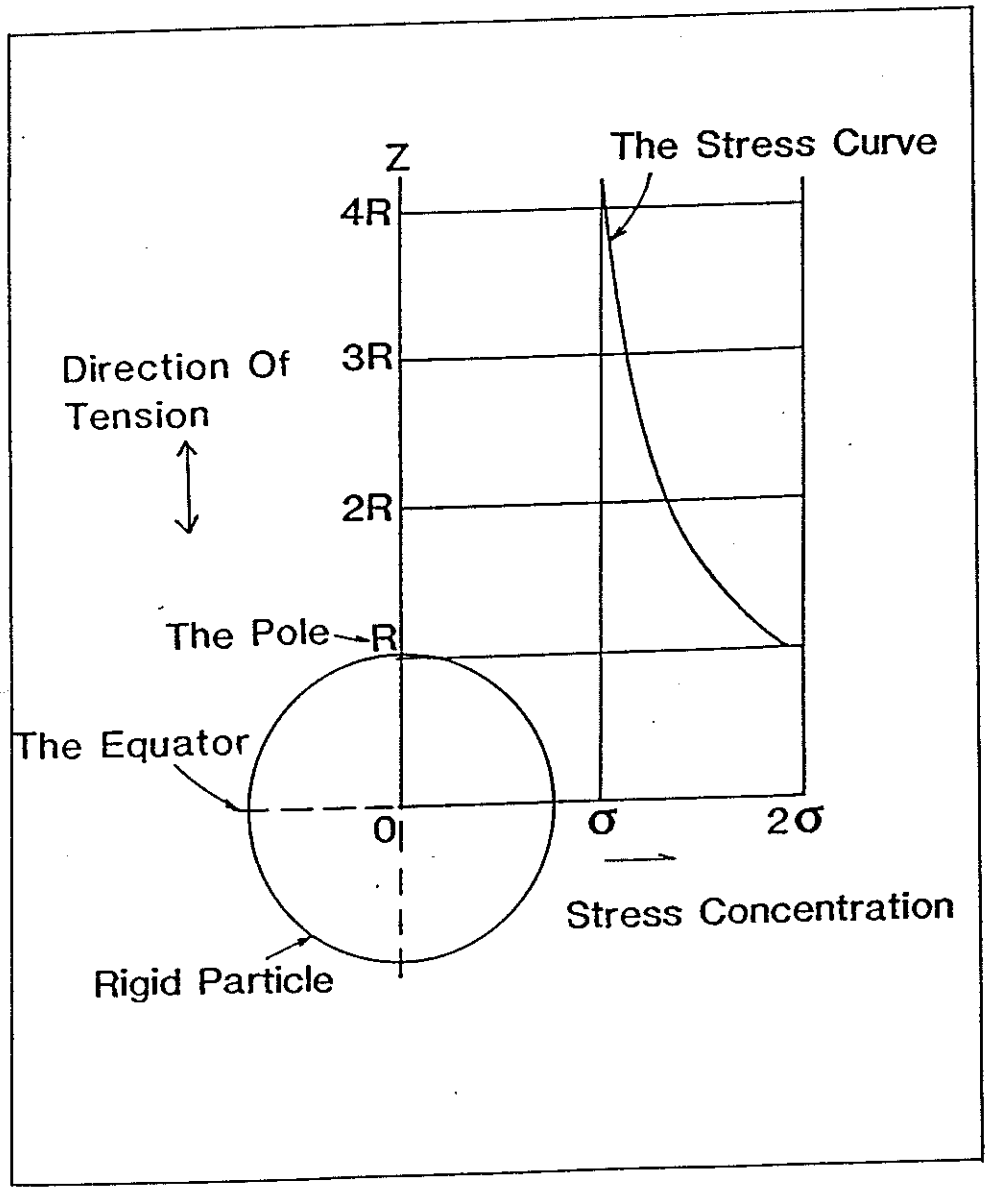

Figure 7. Stress concentraion at the "pole" of a rigid particle embedded in an elastic matrix (after Goodier[21]

loaded by a shear stress (Fig. 8). The solution of such a crack has been presented by Lawn and Wilshaw [23]. The crack tip stress is given by

$$\sigma_{\theta\theta} = \frac{K_{II}}{(2\pi x)^{1/2}} [-3 \sin(\theta/2) \cos^2(\theta/2)] \quad , \tag{21a}$$

where

$$K_{II} = \frac{\sigma}{2} \left(\frac{\pi}{2} \frac{d}{\sqrt{3}}\right)^{1/2} \quad , \tag{21b}$$

and x is the distance measured from the crack tip. Evaluating Eq. (21) for $\theta = 30^0$, gives the following crack tip tensile stress

$$\sigma_{\theta\theta}(\theta=30^0) = 0.14\sigma \sqrt{d/x} \quad . \tag{22}$$

Equation (22) will be compared to the magnitude of stress concentration at triple-point junctions as evaluated in detail by Lau [22] using the finite element method.

4.2. Grain Boundary Sliding and Stress Concentration

"At all temperatures, the shearing resistance of grain boundaries is apparently less than the shearing resistance of individual grains themselves." This statement was made in 1941 by Zener [24]. He also asserted that the variation of the boundary internal friction with temperature and with grain size indicates that at low stress levels, the individual grains behave elastically and slip comparatively readily over one another. However, a polycrystalline specimen under a constant stress cannot of course continue to creep indefinitely merely by slipping at grain boundaries. It was pointed out by Schumacher [25] that

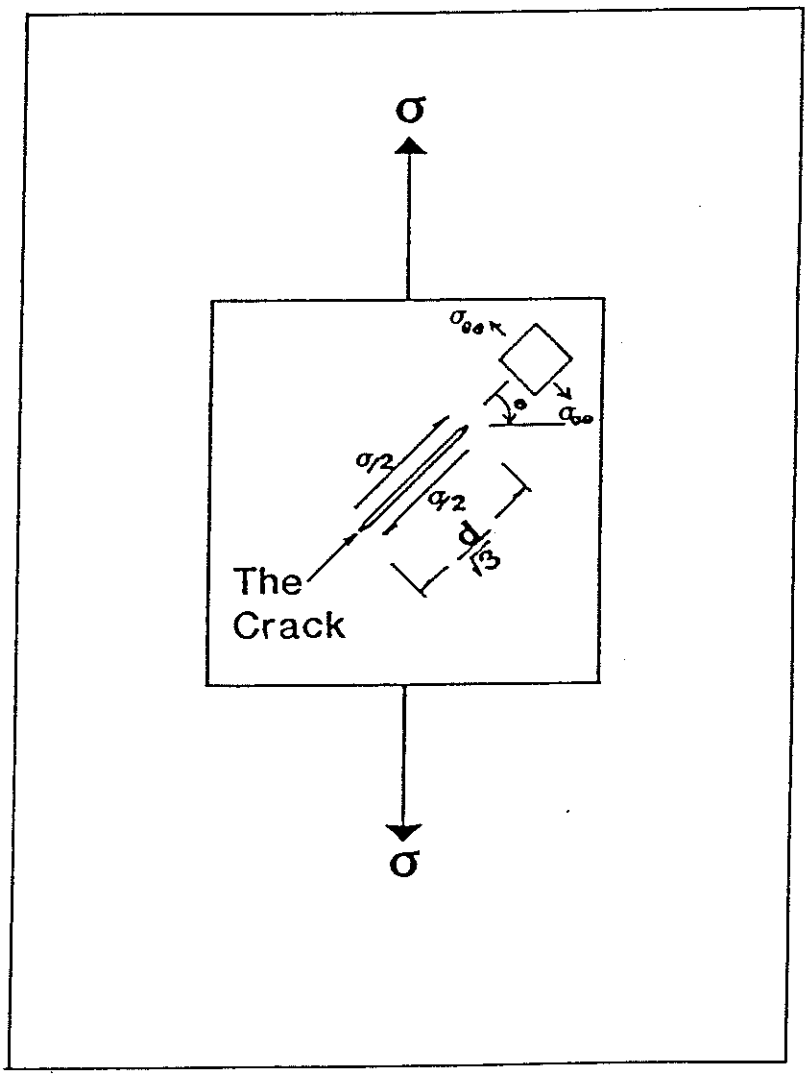

Figure 8. Mode II crack loaded by a shear stress.

grains form a self-locking system. Before further discussion of this locking mechanism, it is important to clarify the meaning of the viscous behavior of the boundaries. By viscous behavior, it is implied that the rate of shear strain across grain boundaries is proportional to the shear stress across them. There can, however, be no relative motion with respect to the grain triple-point junctions. Such junctions serve, so to speak, as keys which limit the relative displacement of adjacent grains but give rise to a substantial stress concentration at such junctions.

This locking action of the grain junctions may be best understood by considering the simple model suggested by Zener [26]. If we look at a completed jigsaw puzzle subjected to a tensile stress, and if the edges of each piece are well greased so that no shear stress can exist across the boundary of any two adjacent pieces, such a jigsaw puzzle will not pull apart under the action of a tensile stress. As may readily be seen, it will not fall apart because of the locking action of the corners of the individual pieces. If we examine in detail the stress system surrounding a triple-point junction, we will see that it is similar to that of a mode II penny-shaped crack loaded by shear. Before examining such a stress system, it is a reasonable stage to look at the stress concentration at grain boundary particles since they act as obstacles to sliding.

4.3. Stress Singularities at Grain Boundary Particles and Triple-Point Junctions

Figure 9 is a simple picture of blocked motion of a sliding boundary by the presence of a particle. If we denote the particle spacing as L and its diameter by p, a simple force balance gives

$$\tau L^2 = \sigma_p \, p^2/2 \quad , \tag{23a}$$

$$\sigma_p = 2(L/p)^2 \, \tau \quad . \tag{23b}$$

Such a particle stress is quite substantial and can explain the fact that obstacles at sliding boundaries are preferential sites for cavity nucleation. Reidel calculations [1] show that in the absence of any diffusional flow, the average stress on the particle should therefore be of the order of $\sigma_p \simeq \tau(L/p)^2$.

C. W. Lau [22] made calculations of the stress-concentration factors associated with grain boundary inclusions and triple-point junctions in a power-law creeping material using the finite element technique. His work shows that a singularity develops at the particle apex (Fig. 10a) which is of the form

$$\sigma_{\theta\theta} = \frac{K_p}{x^{\lambda_p}} \quad . \tag{24}$$

Similarly, for a triple-point junction (Fig. 10b)

$$\sigma_{\theta\theta} = \frac{K_{TPJ}}{x^{\lambda_{TPJ}}} \quad , \tag{25}$$

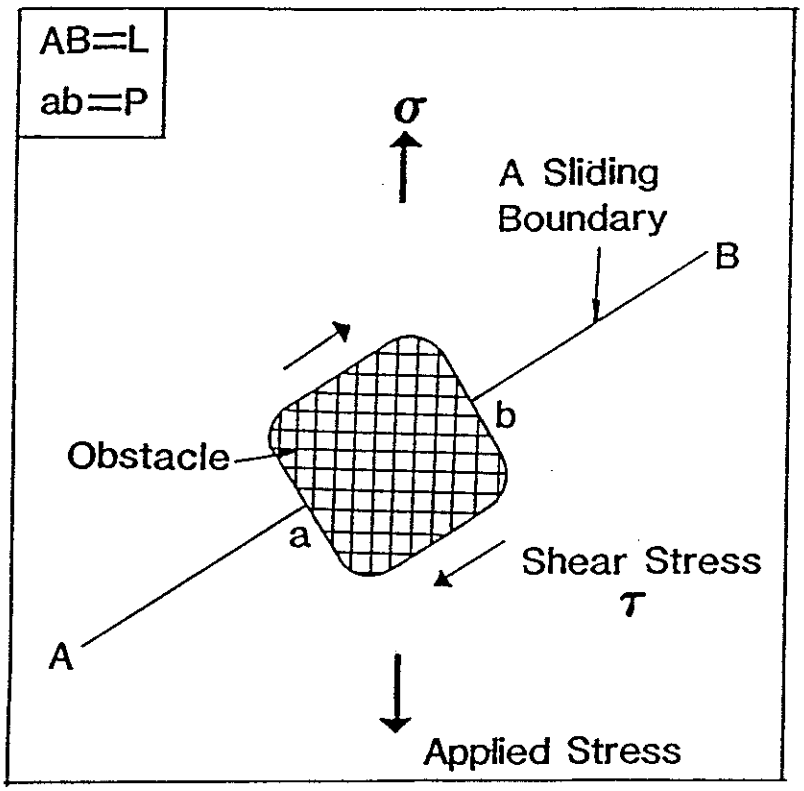

Figure 9. A grain-boundary sliding motion is hindered by the presence of a particle.

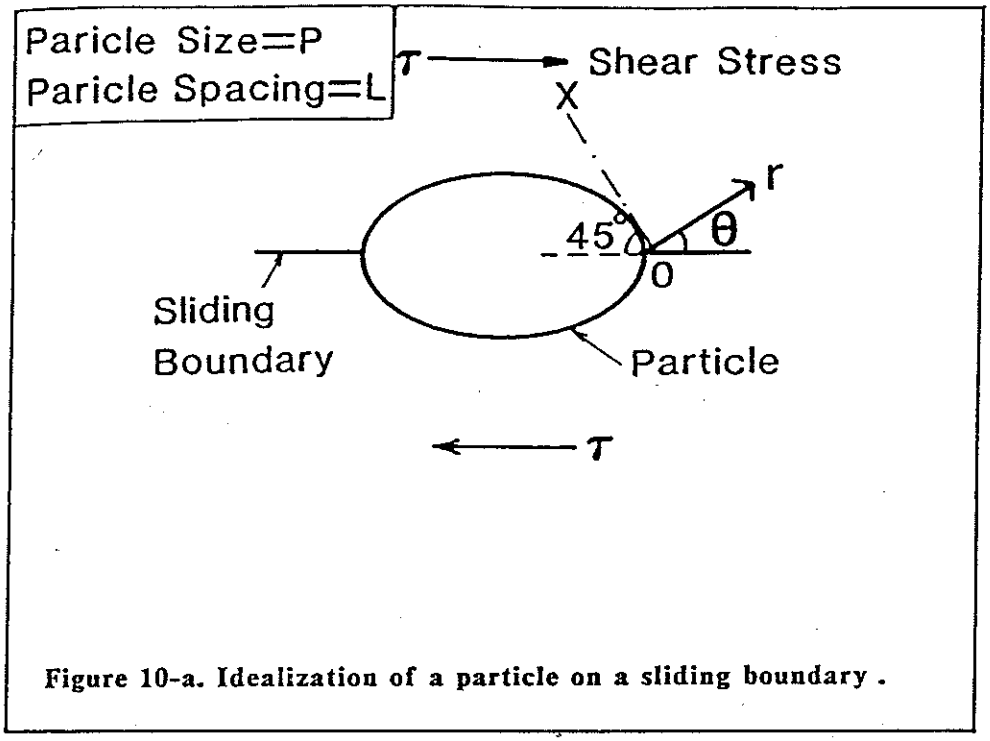

Figure 10-a. Idealization of a particle on a sliding boundary .

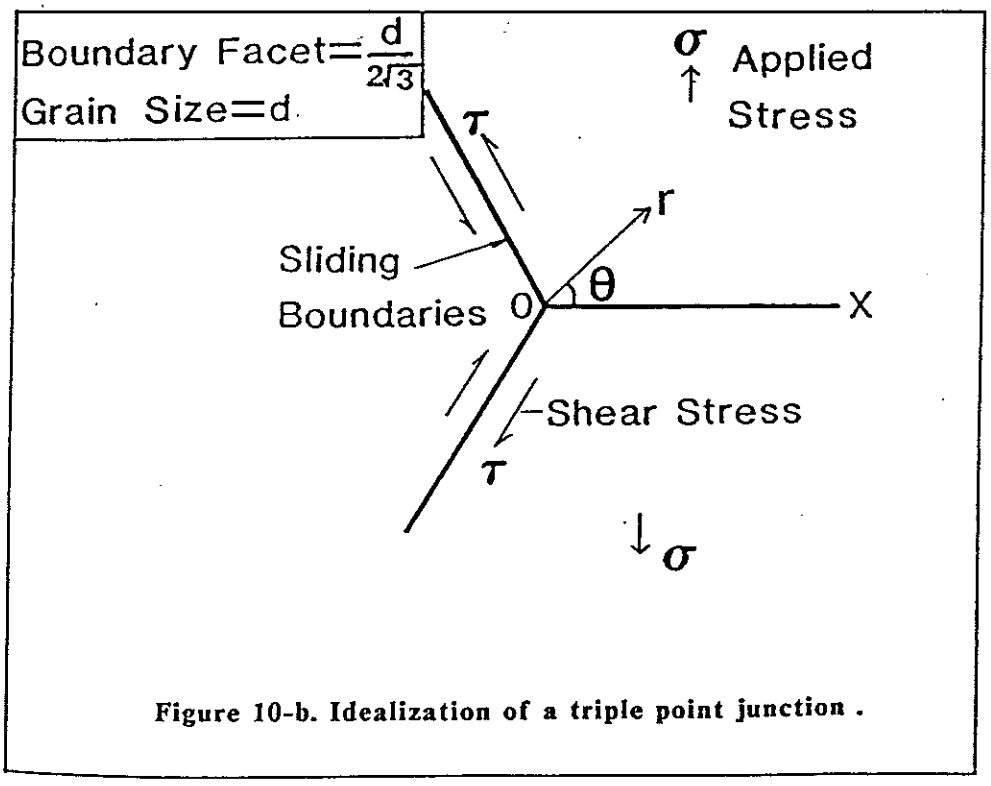

Figure 10-b. Idealization of a triple point junction .

where K_p and K_{TPJ} are the generalized stress-intensity factors, x is the distance along the inclined particle interface (ox) or the boundary orthogonal to the applied stress (ox), λ_p and λ_{TPJ} are the range exponents and are a function of the creep exponent m. These are shown in Table 1.

TABLE 1. The range exponents vs the creep exponents as were calculated by Lau [22].

m (creep exponent)	λp	λ_{TPJ}
1	0.456	0.449
2	0.299	0.312
3	0.225	0.231
4	0.181	0.182
5	0.152	0.15
6	0.131	0.128
7	0.115	0.112
8	0.103	0.099
9	0.093	0.089
10	0.085	0.081

The stress-singularity factors are given by

$$K_p(\Theta=45^0) = 2C_1(m)(1 - \lambda_p)\, f(p/\sqrt{2})^{\lambda_p}\, \tau \quad , \tag{26}$$

and

$$K_{TPJ}(\Theta=0^0) = \frac{3}{2}\, C_2(m)(1 - \lambda_{TPJ})(d/2\sqrt{3})^{\lambda_{TPJ}}\, \sigma \quad , \tag{27}$$

where f is the areal fraction of the boundary covered by the particles and C_1 and C_2 are given by

$$C_1(m) = 0.689 + 0.039(m - 3) \quad , \tag{28}$$

$$C_2(m) = 0.613 - 0.01(m - 3) \quad . \tag{29}$$

If we substitute Eqs. (26)-(29) into Eqs. (24) and (25), the strength of the singularity can be obtained quite simply. The results from Lau's model [22] are shown in Fig. 11.

Evaluating Eq. (25) for m = 1, we obtain

$$\sigma_{\theta\theta}/\sigma = 0.3(d/x)^{0.449} \quad . \tag{30}$$

Now comparing Eq. (30) to Eq. (22), we notice a great deal of resemblance. The strength of the singularity as calculated by Lau [22] for m = 1 is about twice as large which can be rationalized by the fact that at triple-point junctions we have two sliding faces which result in a singularity twice as large as that due to a mode II penny-shaped crack loaded by shear.

4.4. A Time-Dependent Model for Stress Loading and Relaxation at Particles on Sliding Boundaries

4.4.1. Characteristic Time for Boundary Relaxation. As shown in Fig. 12, we view the boundary with particles of size p and spacing L as a series of short cracks of length (L - p) spaced a distance L apart, containing a viscous medium of thickness δ and viscosity η given by Ashby [27]

$$\eta = \frac{kT}{8\delta D_b} \quad . \tag{31}$$

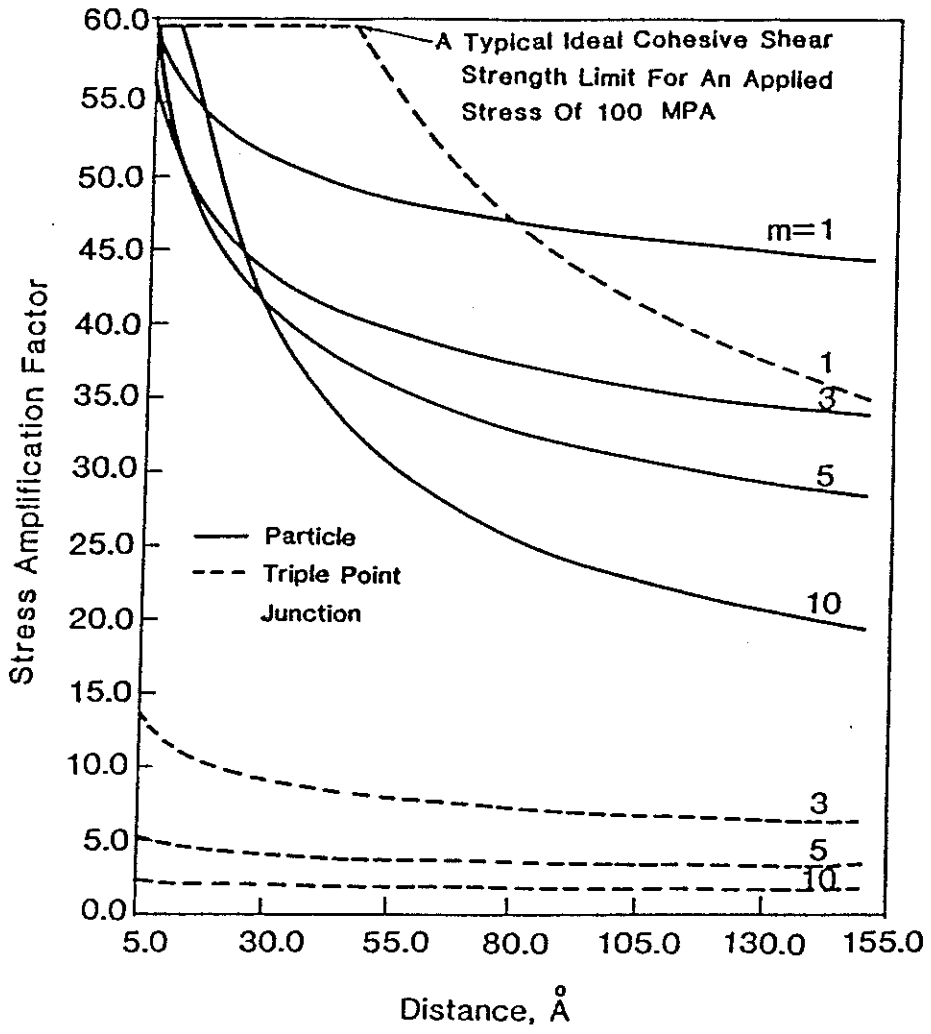

Figure 11. The strength of the singularity at particle apexes and triple point junctions due to sliding boundaries. The grain size is 50 microns , the particle spacing is 0.21 microns and the particle size is 0.03 microns.

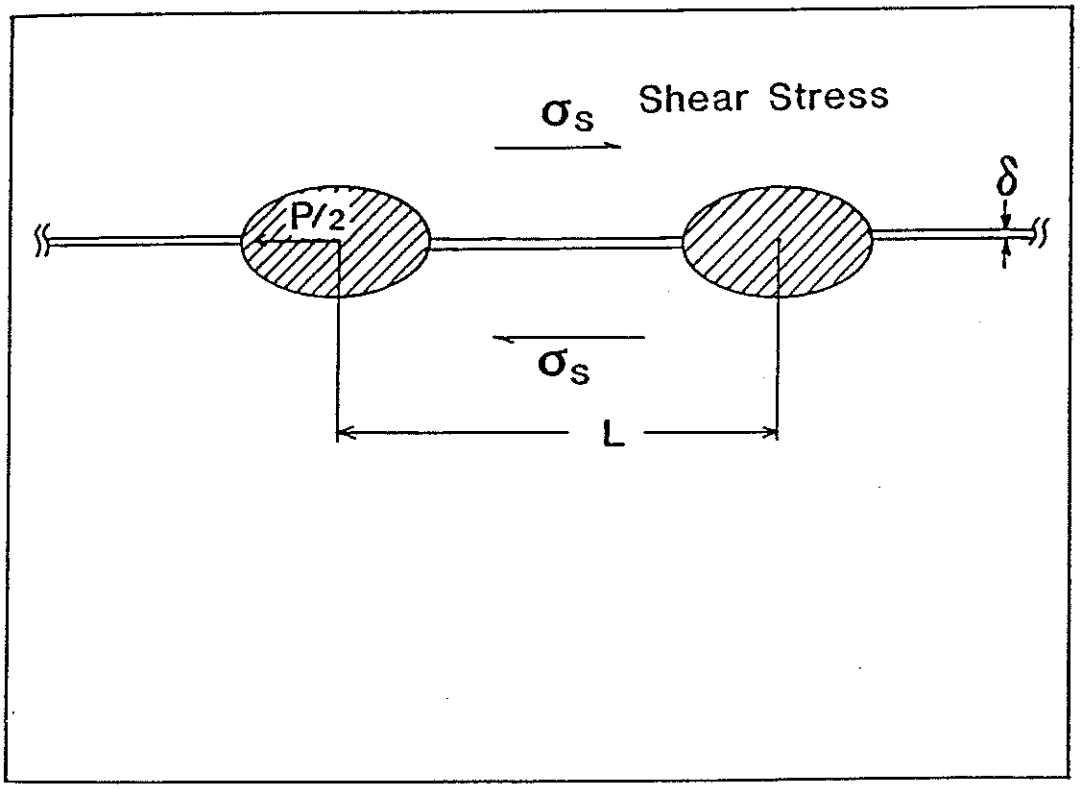

Figure 12. A model for boundary relaxation as a series of cracks of length L separated by ligamants of length P .

The elastic stiffness K_L of the crack faces to a shear stress σ_s is given by [28]

$$K_L = \frac{d\sigma_s}{du} = \frac{\pi G}{L} \frac{1}{\cosh^{-1}\{1/\cos[\pi(1 - p/L)/2]\}} \quad , \tag{32}$$

where u is the relative displacement across the crack faces, G is the shear modulus and inverse cosh term account for crack-crack interaction and will be denoted by $\beta(p/L)$. In order to understand the time dependence of the viscoelastic behavior of the grain boundary, we utilize Maxwell's viscoelastic model [29] which is formed by a spring and a dashpot in series as shown in Fig. 13.

Here a sudden strain u_t is induced and kept constant. Its magnitude is only dependent upon the elastic component since the dashpot acts as a rigid body under the initial application of stress. With the passage of time, the viscous component undergoes strain. This must be accompanied by a contraction of the elastic component, if the overall strain is to remain fixed, which causes a decrease in the stress. This can be represented as follows:

1. The dashpot is perfectly viscous and the rate of extension is directly proportional to the stress. Thus

$$\sigma_s = \eta \frac{\dot{u}}{\delta} \quad , \tag{33a}$$

$$u = \frac{\sigma_s t}{\eta} \delta \quad . \tag{33b}$$

2. The behavior of the spring is given by

$$\sigma_s = K_L u \quad . \tag{34}$$

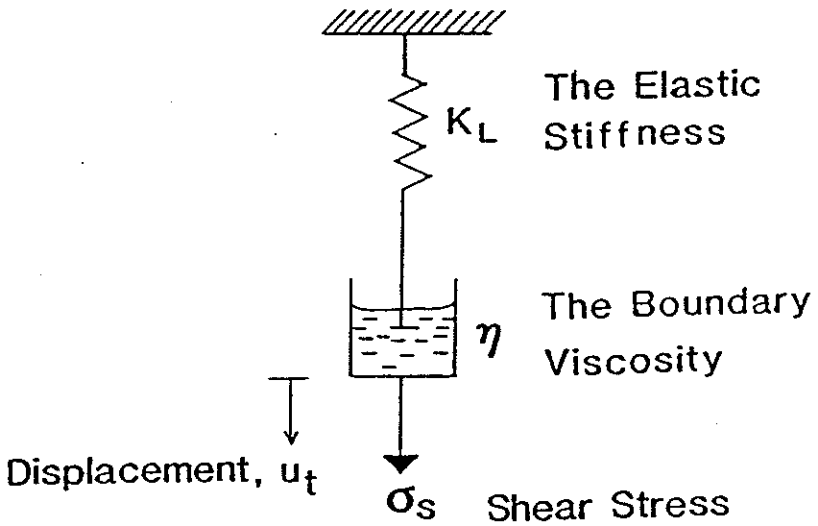

Figure 13. The viscoelastic model for particle stress loading .

Thus, the total strain under stress is simply given by

$$u_t = \frac{\sigma_s}{K_L} + \frac{\sigma_s t}{\eta}\,\delta \quad . \tag{35}$$

In terms of rates,

$$\frac{du_t}{dt} = \frac{1}{K_L}\frac{d\sigma_s}{dt} + \frac{\sigma_s \delta}{\eta} \quad . \tag{36}$$

Here it is assumed that both K_L and η are rate independent. However, at any time u_t is constant and hence $du_t/dt = 0$. Therefore Eq. (6) is simply

$$\frac{\dot{\sigma}_s}{K_L} + \frac{\sigma_s}{\eta}\,\delta = 0 \quad . \tag{37}$$

This immediately gives the shear stress relaxation across the grain boundary

$$\sigma_s = \sigma_{so}\exp(-t/\tau_{BR}) \quad , \tag{38}$$

where σ_{so} is the initial homogeneous shear stress and τ_{BR} is the characteristic time for boundary relaxation. That is

$$\tau_{BR} = \frac{\eta L}{\pi G \delta}\,\beta(p/L) = \frac{kTL}{8b\pi\delta D_b G}\,\beta(p/L) \quad , \tag{39}$$

where $\beta(p/L) = \cosh^{-1}\{1/[\cos(\pi/2)](1-P/L)\}$.

4.4.2. Diffusional Relaxation of the Stress Concentration at Particles. The analysis here is limited to the elastic-diffusion problem. Since stress is quite localized at the faces of the particles and grain

boundary, diffusion should be quite effective in smoothing the stress disturbances. This problem has already been solved in the literature by Koeller and Raj [30]. For very rigid particles (shear modulus ~ β)

$$\tau_{R,BDIFF} \simeq \frac{L^3 kT}{G\delta D_b \Omega} \quad . \tag{40}$$

Now if we use the usual criteria for a changeover from boundary to volume diffusion ($D_b \delta \rightarrow LD_v$), as it is usually done in the literature (i.e., Raj and Ashby [31]), we have

$$\tau_{R,VDIFF} \simeq \frac{L^2 kT}{GD_v \Omega} \quad . \tag{41}$$

The method used is that where the authors start with a non-uniform distribution of the normal traction at the interface at which the chemical potential of atoms is defined. Then the diffusive flow from the gradient of this potential is obtained. This calculation takes into account the continuous traction change as matter is transported.

This expression is very analagous to that of characteristic relaxation times for the triple point (to be discussed next) and just modifying the characteristic distance over which an even matter plating occurs ($L \rightarrow d$).

4.4.3. Stress Buildup and Relaxation at Particles. The simplest description of stress loading and unloading is provided by a phenomenological visco-elastic model which yields an expression given by [32]

$$\sigma_p(t) = (\tau_o - \tau^*) \exp(-t/\tau_L)$$

$$+ (\tau^* - \tau_\infty) \exp(-t/\tau_R) + \tau_\infty \quad , \tag{42}$$

where τ_L and τ_R represent the loading and relaxation times, respectively. For all practical purposes

$$\tau_\infty = \tau_o = \sigma_{applied}/2 \quad , \tag{43a}$$

and

$$\tau^* = \tau_o/f \quad , \tag{43b}$$

where

$$f = (p/L)^2 \quad , \tag{43c}$$

which is the fractional area of the boundary occupied by particles and τ_R which will be used (volume/grain boundary diffusion controlled) is the one that is most efficient in smoothing out the singularity.

4.5. A Time-Dependent Model for Stress Loading and Relaxation at Triple-Point Junctions

4.5.1. Characteristic Times for Stress Loading at Triple-Point Junctions Due to Sliding of Grain Boundaries.

Figure 14 shows a boundary with particles of size p and spacing L. We can view the boundary as having an enhanced viscosity due to the presence of particles. This resistance to sliding varies according to the mode of accommodation. Viscosity expressions for diffusive accommodation have been derived by Raj and Ashby [33] and are given by

$$\eta_{B-DIFF} = \frac{\delta}{8} \frac{kT}{\Omega} \frac{p^4}{L^2} \frac{1}{\delta D_b} \quad , \tag{44}$$

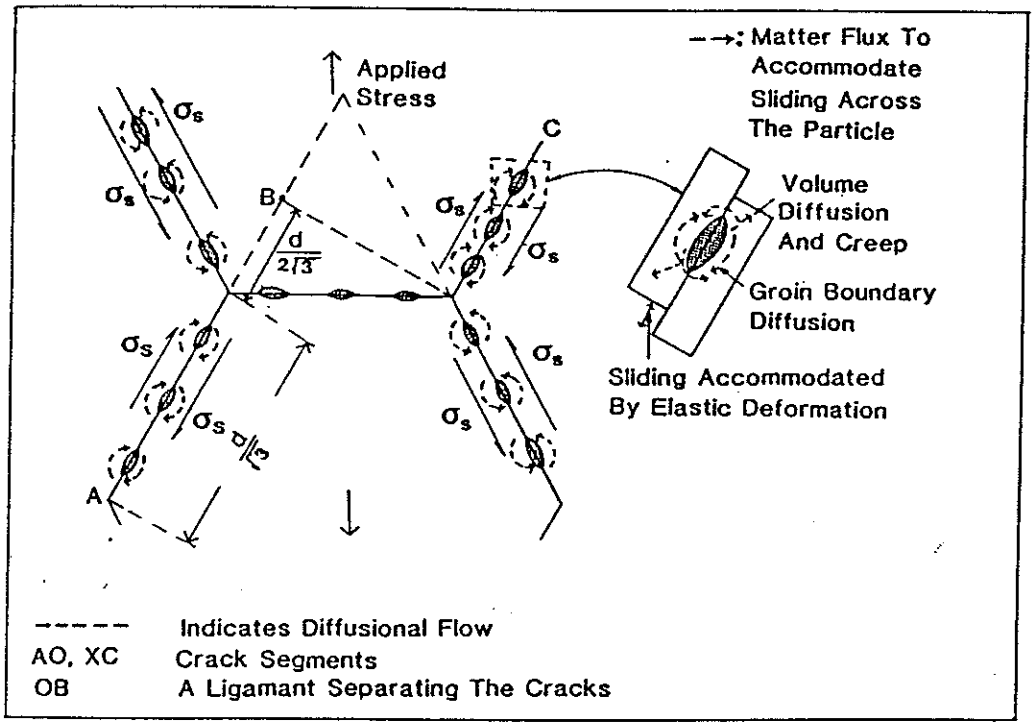

Figure 14. A model for triple point junction stress loading .

$$\eta_{V\text{-}DIFF} = \frac{\delta}{8}\frac{kT}{\Omega}\frac{p^4}{L^2}\frac{5}{D_v p} \quad . \tag{45}$$

It is easy to realize that each viscosity leads to a different loading time at the triple-point junction. However, the viscosity which leads to the shortest loading time will be used in our analysis. The elastic stiffness K_{TPJ} of the grain faces to a shear stress σ_s can be calculated utilizing Eq. (32) and modeling all grain boundaries as a series of cracks of length $d/\sqrt{3}$ separated by ligaments of thickness $d/2\sqrt{3}$, as shown in Fig. 14 represented by A and B, respectively. Thus,

$$K_{TPJ} = \frac{d\sigma_s}{dv} = \frac{\pi G\sqrt{3}}{d\beta(1/2)} \quad , \tag{46}$$

where $\beta(1/2) = 0.9$ and v is the relative displacement. Analogous to Eq. (39), the characteristic time for stress loading $\tau^{TPJ}_{L\text{-}DIFF}$ is thus given by

$$\tau^{TPJ}_{L\text{-}DIFF} = \frac{0.9\ d\eta}{\pi\sqrt{3}\ \delta G} \quad , \tag{47}$$

or explicity

$$\tau^{TPJ}_{L\text{-}GBDIFF} = \frac{d}{50G}\frac{kT}{\Omega}\frac{p^4}{L^2}\frac{1}{\delta D_b} \quad , \tag{48a}$$

$$\tau^{TPJ}_{L\text{-}VDIFF} = \frac{d}{10G}\frac{kT}{\Omega}\frac{p^3}{L^2}\frac{1}{D_v} \quad . \tag{48b}$$

The viscoelastic model used in this derivation is simply the Maxwell model, which is shown in Fig. 15. During this time, $\tau^{TPJ}_{L\text{-}DIFF}$ represents

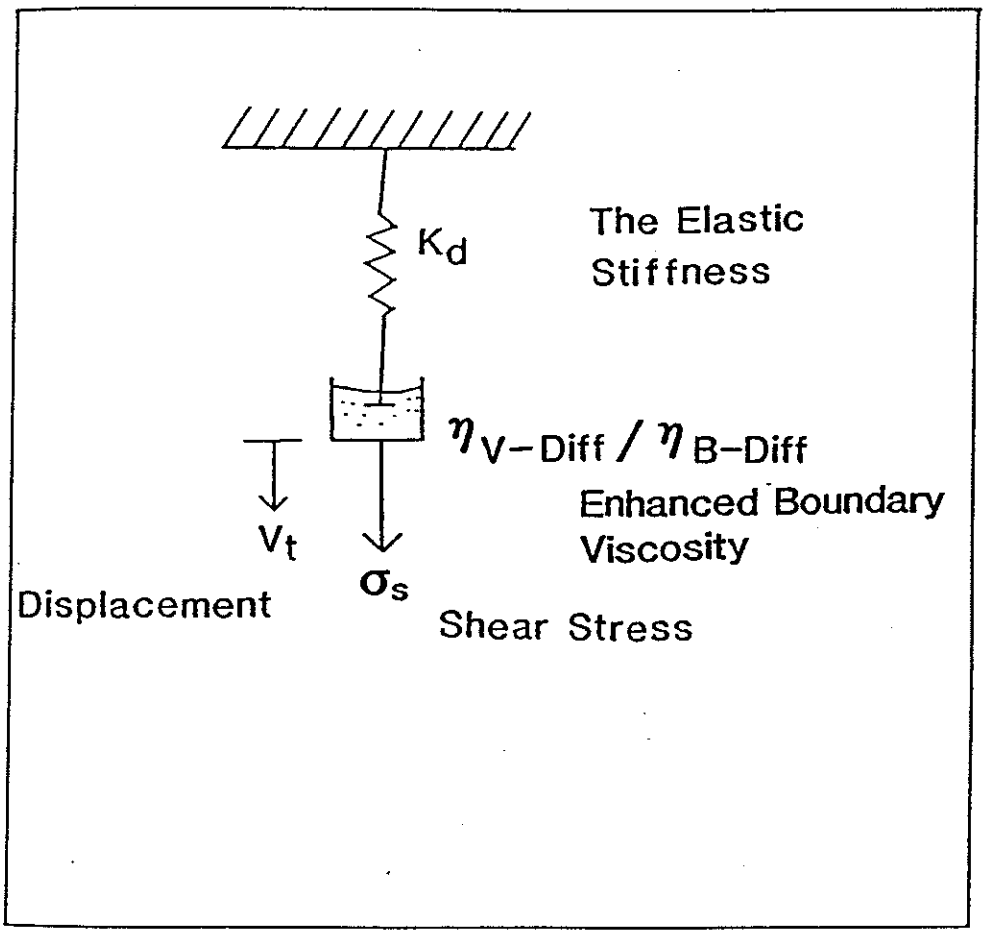

Figure 15. The viscoelastic model for triple point junction stress loading .

a characteristic time for stress buildup at the grain boundary triple-point junctions.

4.5.2. Diffusional Relaxation of the Stress Singularity at Triple-Point Junctions. At this stage, it is clear that grain boundary sliding generates a singularity at triple points (Fig. 16). We will assume here that grains respond in a linear elastic manner to stress buildup, in response to boundary sliding. For all practical purposes, Evans, Rice and Hirth [8] used the solution for the tensile stress concentration of a single mode II penny-shaped crack loaded by the shear stress $\sigma_\infty/2$ to study the time-dependent behavior of the stress singularity. In the absence of any diffusional flow, Eq. [22] can be applied and can be rewritten as

$$\sigma_{TPJ} = K_c/\sqrt{x} \quad , \tag{49}$$

where $K_c = \sqrt{d}\ \sigma_\infty/7.5$.

Now, let δ be the effective thickness of the grain boundary and J be the number of atoms diffusing along the grain boundary per unit time, per unit thickness into the plane of the diagram. Mass conservation requires that

$$\Omega \frac{\partial J}{\partial x} + \frac{\partial \delta}{\partial t} = 0 \quad . \tag{50}$$

Further, the linearized law of diffusion is

$$\Omega J = - \frac{D_b \delta}{kT} \frac{\partial}{\partial x} (-\Omega\sigma) \quad . \tag{51}$$

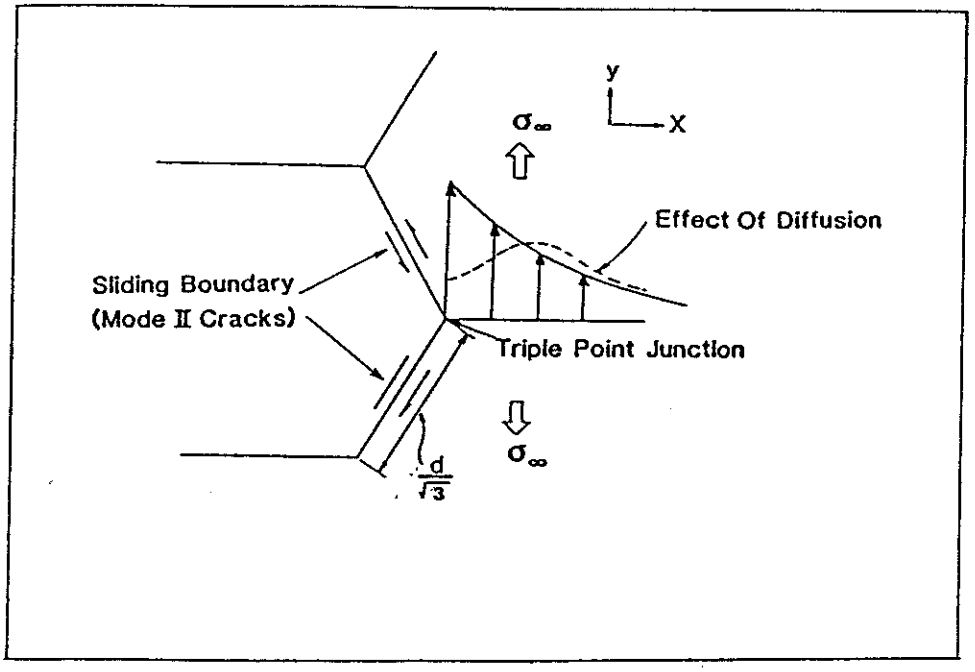

Figure 16. Evans,Rice and Hirth model [8] for diffusional relaxation of stress at triple point junctions.

It has to be realized in the previous equation that $-\Omega\sigma$ is essentially the chemical potential per atom. Combining the previous two equations yields

$$(D_b \delta\Omega/kT) \frac{\partial^2 \sigma}{\partial x^2} + \frac{\partial \delta}{\partial t} = 0 \quad . \tag{52}$$

The solution for Eq. (52) is given by [8].

$$\sigma(x,t) = \frac{K_c}{(\alpha t)^{1/6}} f\left[x/(\alpha t)^{1/3}\right] \quad , \tag{53}$$

where

$$\alpha = GD_b \delta\Omega/2(1 - \nu)kT \quad ,$$

and

$$f(z) = \sqrt{2/\pi} \int_0^\infty \left\{\exp(-u^6)\left[\cos(u^2 z) + \sin(u^2 z)\right]\right\} du \quad .$$

The function f(z) approaches $1/\sqrt{z}$ at large z. This will result in realizing that the classical elastic stress distribution for a relatively short time remains unperturbed at a relatively large distance away from the triple-point junction. That is $\sigma(x,t) = K_c/\sqrt{x}$, which is Eq. (49). While if z is equal to zero (when x = 0, it is the triple-point junction), f(0) = 0.74 and hence

$$\sigma(0,t) = 0.74\ K/(\alpha t)^{1/6} \quad , \tag{54}$$

or in an expanded form

$$\sigma(0,t) = \frac{1}{9} \sigma_\infty \left[\frac{(1 - \nu)kTd^3}{GD_b \delta\Omega t}\right]^{1/6} \quad , \tag{55}$$

if we recall that

$$\tau_{R,TPJ} = \frac{(1 - \nu)kTd^3}{GD_b \delta\Omega} \quad , \tag{56}$$

Eq. (55) can be written as

$$\sigma(0,t) = \frac{1}{9}\,\sigma_\infty \left(\frac{\tau_{R,TPJ}}{t}\right)^{1/6} \quad . \tag{57}$$

4.5.3. Stress Buildup and Relaxation at Triple-Point Junctions. We have already derived an expression for stress relaxation in the vicinity of triple-point junctions. However, this expression does not take into account any loading time. Introducing in this case a characteristic exponential loading time into our model, the following expression results for the normal stress at the intersection

$$\sigma_{TPJ} = \sigma_\infty \left\{1 + \left[1 - \exp\left(-\frac{t}{\tau_L^{TPJ}}\right)\right]\frac{1}{9}\left(\frac{\tau_R^{TPJ}}{t}\right)^{1/6}\right\} \quad . \tag{58}$$

In this expression, τ_L^{TPJ} is the fastest mode of triple-point loading time (either by volume or grain boundary diffusion).

4.6. Stress Pulse Calculations

Figure 17 shows that the overall time dependence of stress evolution at triple-point junctions is much slower than that at particle interfaces. The reason behind this is that the time dependence of the stress concentration at triple-point junctions is characterized by a wide spectrum of relaxation times; small relaxation times controlling

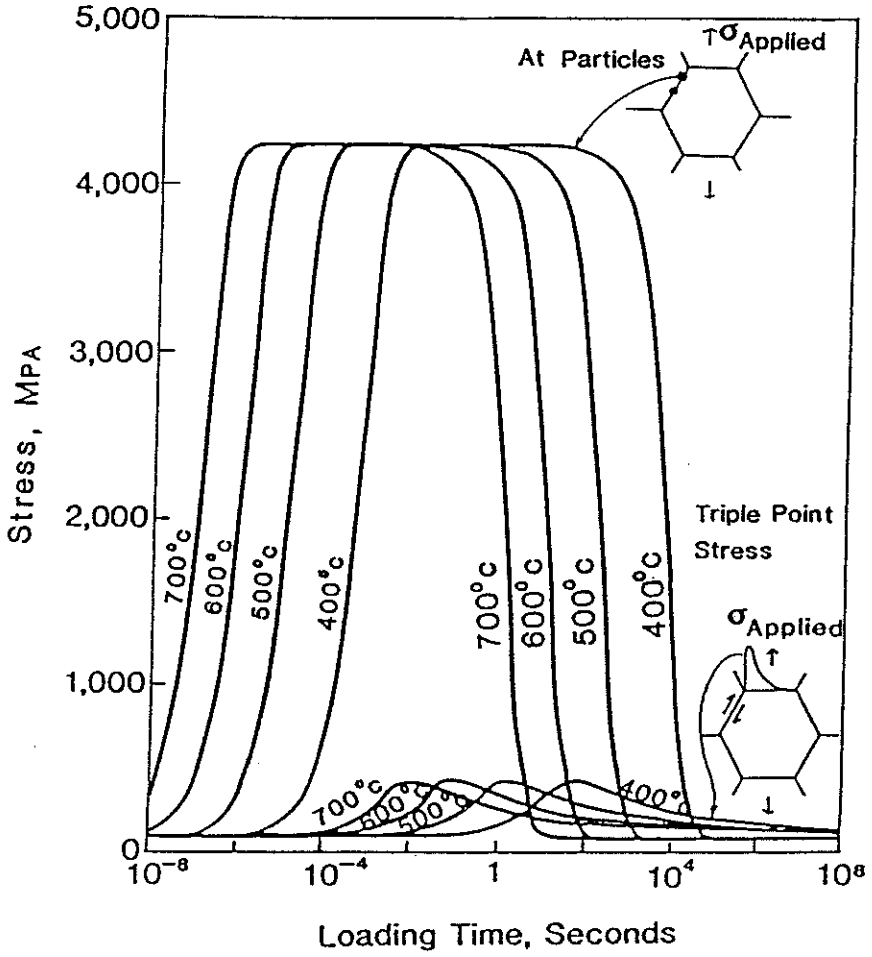

Figure 17. Stress loading and relaxation at particles and triple point junctions for an applied stress of 100 MPa , a grain size of 50 microns , a particle size of 0.03 microns and spacing of 0.21 microns.

the early stages and large ones controlling the late stages [8]. This is in contrast with stress relaxation times of particles in which diffusional matter flow needs only to occur over short distances in order to relieve the stress.

Figure 17 further reveals that the duration of the stress pulse becomes quite short at higher temperatures. At lower temperatures, the triple-point junction stress becomes quite persistent for a reasonably long time. This can explain the observed triple-point cracking at temperatures below about 400°C [34], since persistent stress concentration at triple-point junctions leads to crack initiation.

Figure 18 demonstrates the magnitude of the stress pulse at particles located at boundaries of various inclinations. Particles at boundaries which are parallel to the direction of applied stress will suffer the most severe stress pulse in contrast to particles at boundaries which are orthogonal.

The stress pulses shown in Figs. 17 and 18 will be used later in nucleation calculations.

5. NUCLEATION CALCULATIONS AND DISCUSSIONS

It has been experimentally observed (e.g., [10]) that high temperature fracture occurs due to the nucleation and growth of cavities along grain boundaries which are most perpendicular to the applied stress. However, two experimental studies directed toward understanding cavity nucleation at high temperatures (Dyson, Loveday, and Rodgers [35], and Kikuchi, Shiozawa, and Weertman [36]) showed the surprising result that most nucleated cavities have formed on grain boundaries which are parallel to the maximum principal stress axis. However, the experiment by

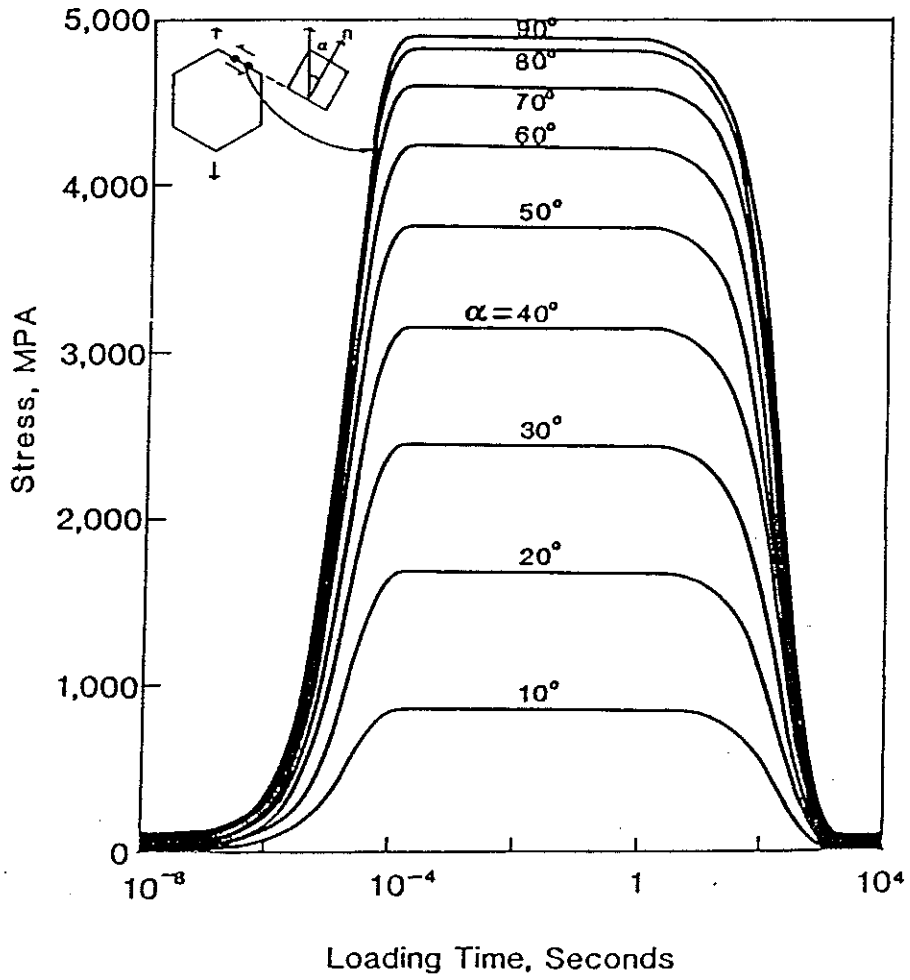

Figure 18. Stress loading and relaxation of particles at various inclined boundaries . The applied stress is 100 MPa , the particle size is 0.03 microns with a spacing of 0.21 microns and the temperature is 500 C .

Dyson et al. [35] also showed that preferential cavity growth occurred during subsequent tensile creep. Those cavities on parallel boundaries either remained constant in size or diminished while those on boundaries which were orthogonal to the applied stress axis grew relatively quickly. This behavior of cavity growth can be misleading in the sense that it can be mistaken for preferential nucleation on orthogonal boundaries to the applied stress and subsequent fracture along these boundaries. Figure 19 shows a schematic of the fundamental findings of Dyson et al. [35] which have been overlooked most often in the literature. The figure illustrates that inclined boundaries tend to host the majority of cavity nuclei population, while orthogonal boundaries host a small fraction of the population. However, the cavity population on orthogonal boundaries tends to experience preferential growth during the course of the creep test until fracture. Chen and Argon [10] have experimentally observed a $\sin^2(\alpha)$-type distribution for large cavities. The subject of cavity growth will be treated in Chapter VI.

Stress concentrations at particles present on orthogonal boundaries due to the difference in rigidity between the particles and the matrix as was calculated by Goodier [21], was not significant to produce reasonable nucleation rates. In order to bridge the gap, a localized grain boundary sliding has to be present on orthogonal boundaries which will result in a localized high stress concentration at particles. Grain boundaries are hardly ever flat. This has been asserted by Ashby [27]. When the boundary is stressed, a certain degree of sliding occurs until a particle is encountered which gives rise to a fairly high stress concentration. This process of localized sliding should occur in principle throughout the creep test in response to various deformation

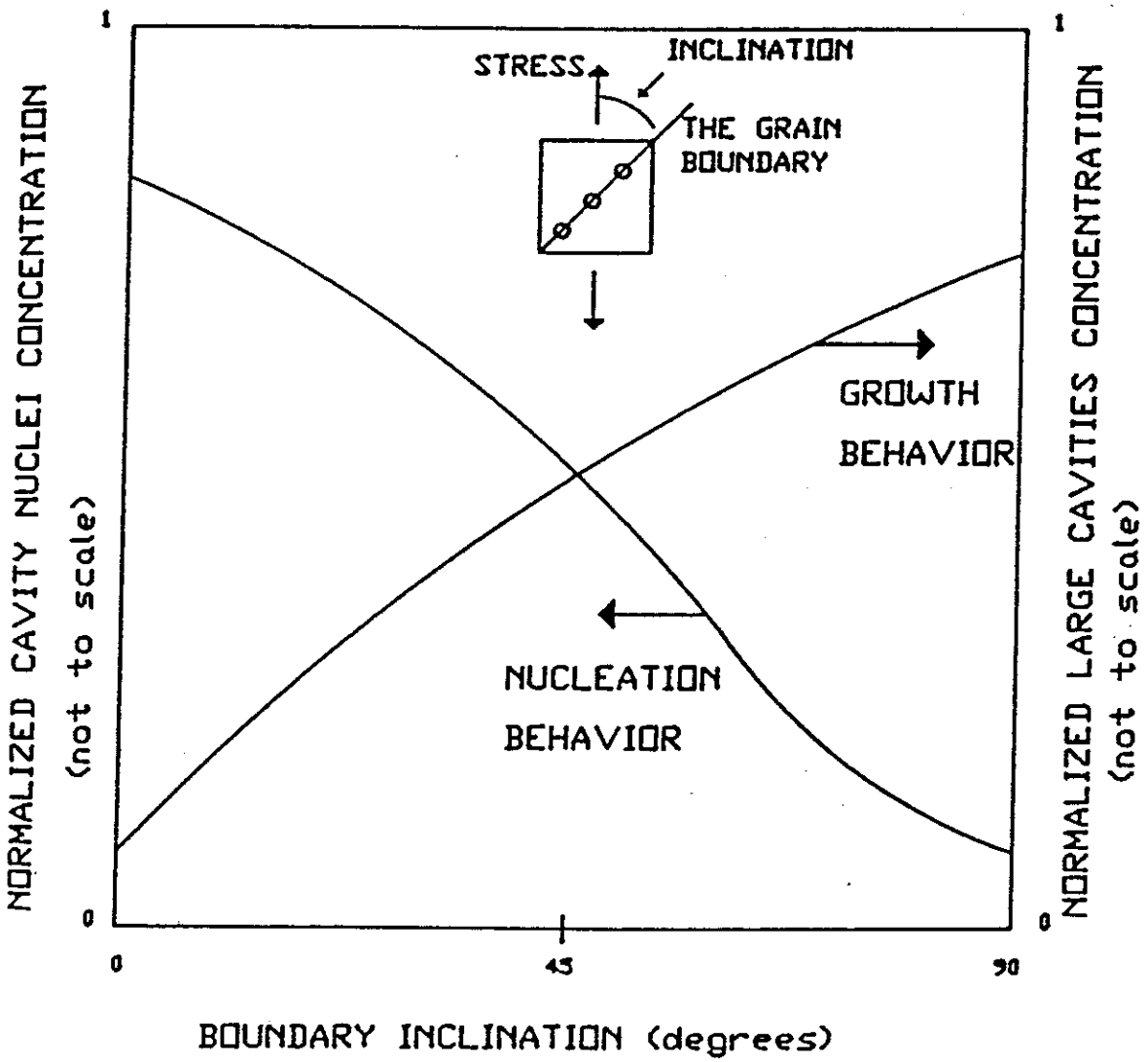

Figure 19. A schematic illustrating the angular distribution of cavitated grain boundaries during a typical tensile creep test (condensation of work in reference [34]).

processes such as unpinning of grain boundaries, triple-point cracking, stress relaxation in neighboring sliding regions, triple-point migration, etc. [37].

In order to model nucleation at orthogonal boundaries which exhibit localized irregularities, it will be assumed that a boundary exhibits localized sliding due to deviations from orthogonality by about 10 deg to 20 deg. The stochasticity of the process is not treated here. Figure 20 shows that the nucleation rate is the highest along boundaries which are parallel to the applied stress and decreases sharply as boundaries tend toward orthogonality. At orthogonal flat boundaries, nucleation is essentially nonexistant. The nucleation pulse essentially follows the stress pulse behavior and the nucleation pulse is terminated once the stress pulse has elapsed. At 600°C, the nucleation pulse lasts ~ 100 sec. If the nucleation rate is high, all possible nucleation sites will be filled up by cavities. If the nucleation rate is low, cavity nucleation will occur throughout the creep experiment following the course of stress concentration buildup and relaxation in response to localized sliding which should occur intermittently.

Figure 21 shows that nucleation is virtually impossible for large volumetric shape factors ($F_v > 0.02$). This asserts the idea that cavities possess a lenticular rather than spherical shape during the course of nucleation. The figure also illustrates that the actual value of F_v may be constrained by the limit $0.01 < F_v < 0.001$, for consistency with experimental observations.

It is very important to examine the temperature dependence of the nucleation process. This is shown in Fig. 22. The figure shows that the nucleation rate is the highest at 700°C and decreases as the

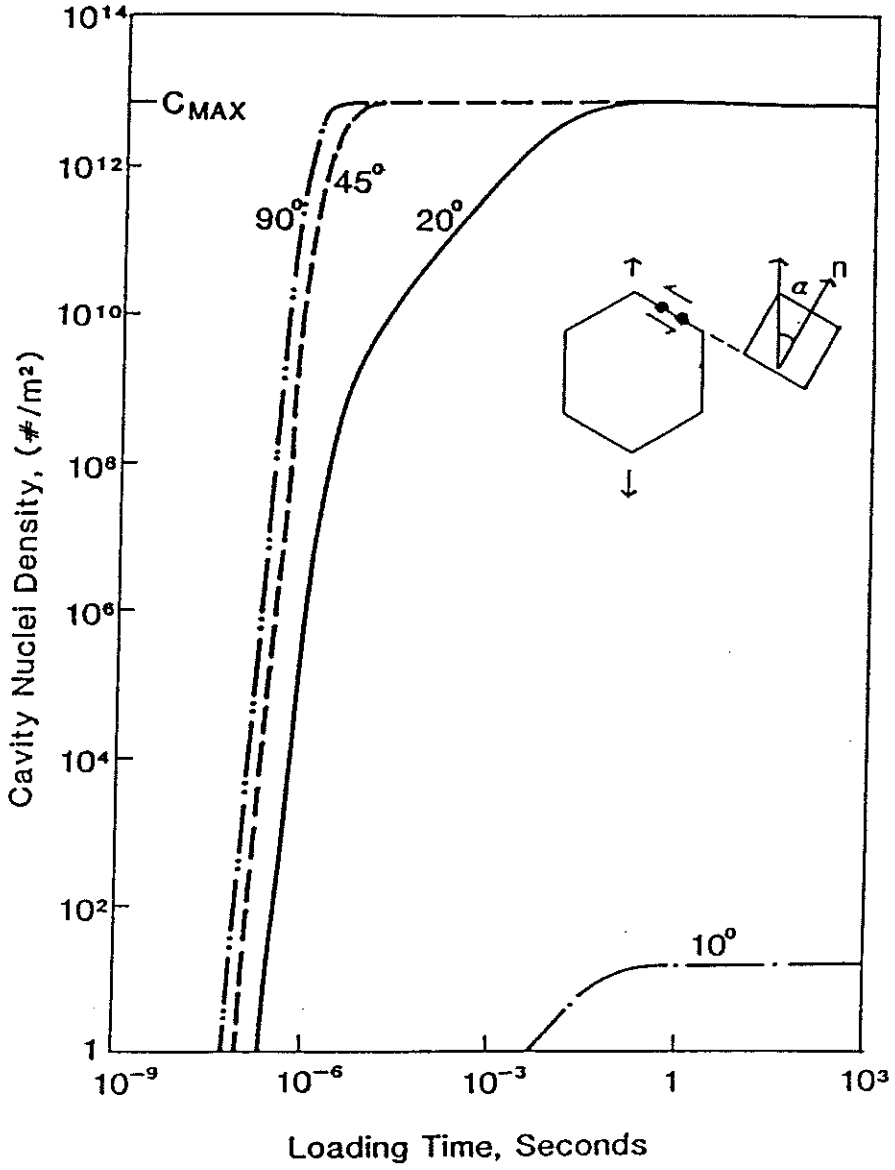

Figure 20. Cavity nuclei density at boundaries of various inclination at 600 °C and F_v value of 0.01 as a result of a single sliding pulse . The applied stress is 100 MPa.

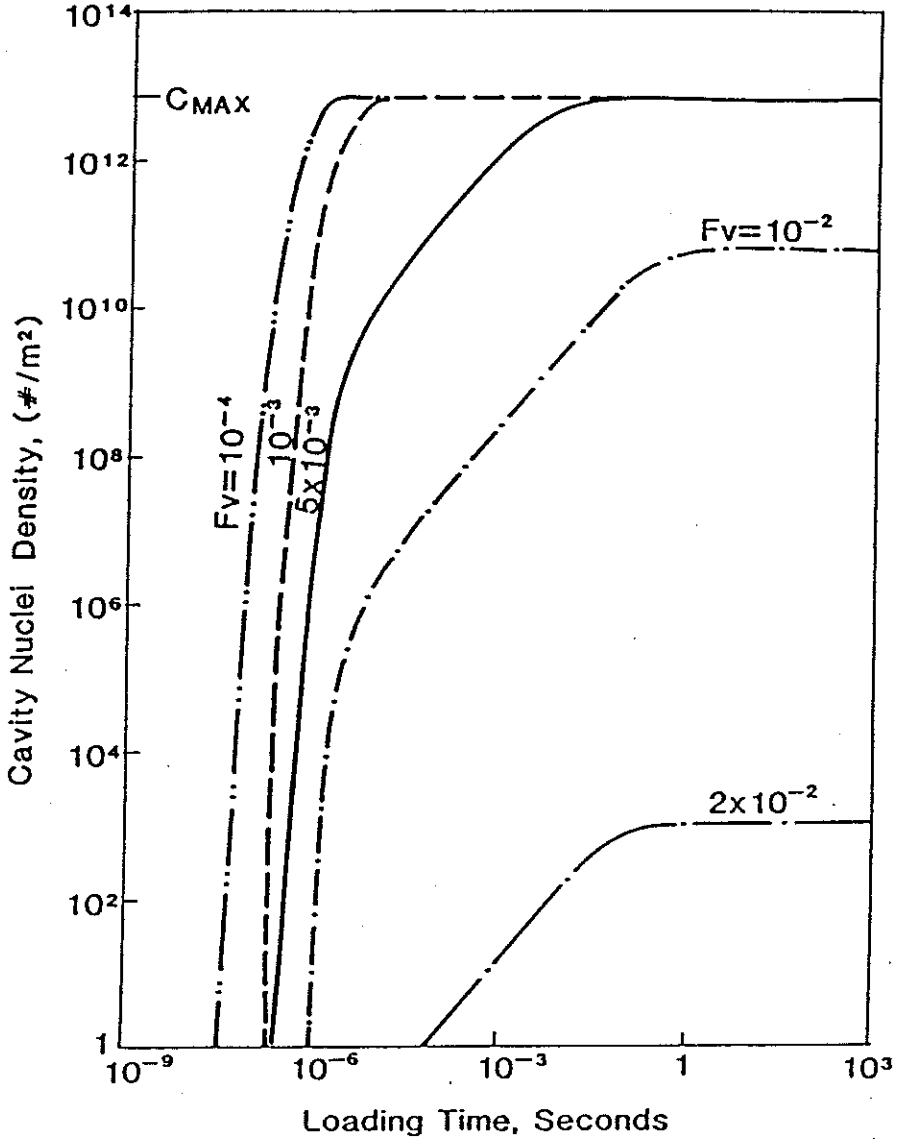

Figure 21. Cavity nuclei density for various values of F_v at 600 °C, a boundary inclination of 15 degrees and an applied stress of 100 MPa.

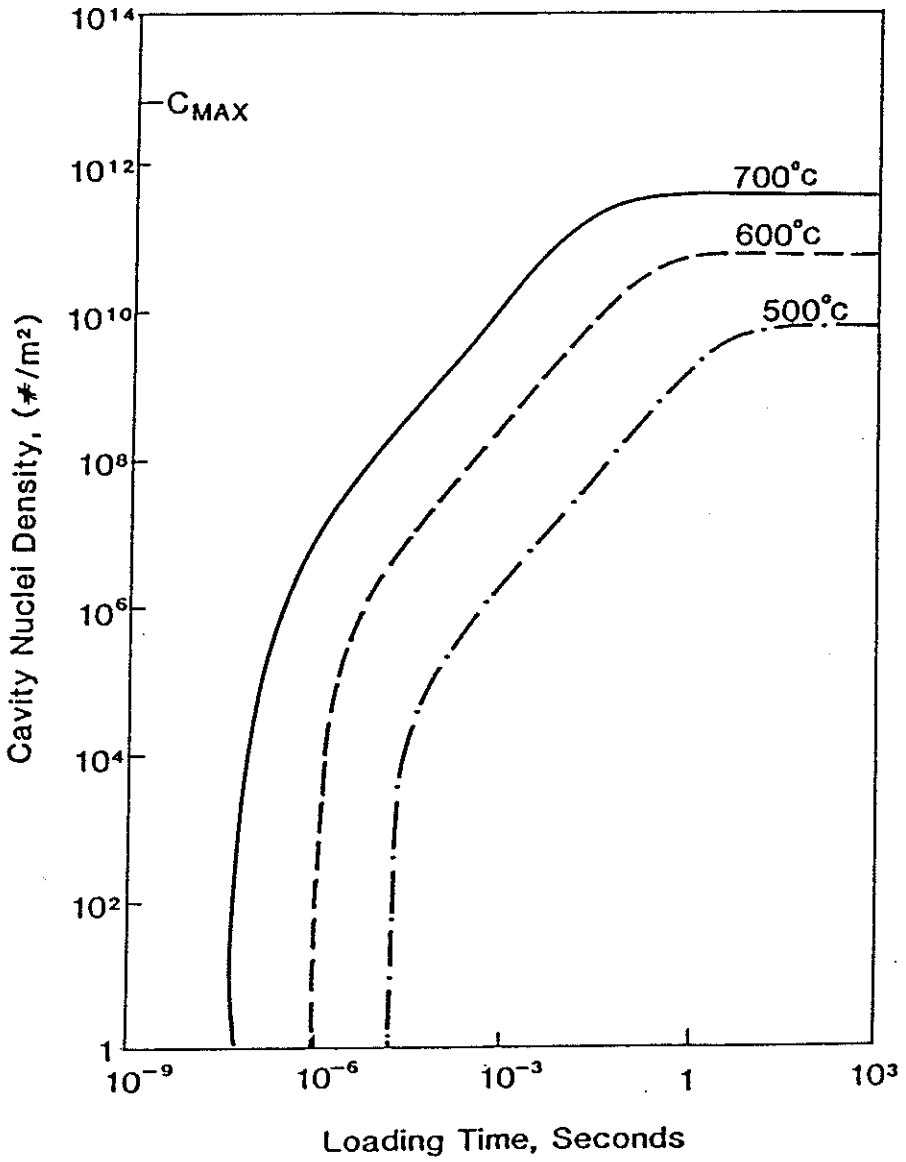

Figure 22. Cavity nuclei density as a function of temperature for an F_v value of 0.01 and a boundary inclination of 15 degrees and an applied stress of 100 MPa.

temperature decreases. The behavior actually translates into more extensive nucleation at higher temperatures. This is consistent with the experimental observations presented by Argon [9]. The figure also shows another important result: the duration of the nucleation pulse is sharply curtailed at high temperatures. The basic reason for this behavior is that stress relaxation is faster at high temperatures due to the more extensive atom motion. At lower temperatures, the duration of the stress pulse will be large; however, the nucleation rate is too low to produce significant cavitation. The low cavitation at lower temperatures can be linked to the high thermal barrier to nucleation at lower temperatures.

Experimental observations by Chen and Argon [10] showed that more extensive nucleation occurs near triple-point junctions. As was shown in the previous section, high stress concentration exists at triple-point junctions and prevails for a relatively long period of time. This stress results in an enhanced sliding rate past grain boundary irregularities and results in high stress concentrations at neighboring particles. The relaxation of stress concentration at neighboring particles is a part of the relaxation process of the triple-point stress concentration. The relaxation of the triple-point stress concentration is a very slow one which can be attributed simply to the large distance over which uniform atom plating has to occur. Figure 23 shows that the neighborhood of a triple-point junction suffers a more extensive cavitation. This is consistant with results presented in the literature [10]. If we now examine Fig. 17 again, it shows that at a temperature which is too low to result in any significant nucleation (~ 400°C), the triple-point stress concentration prevails for an extensive period of time and

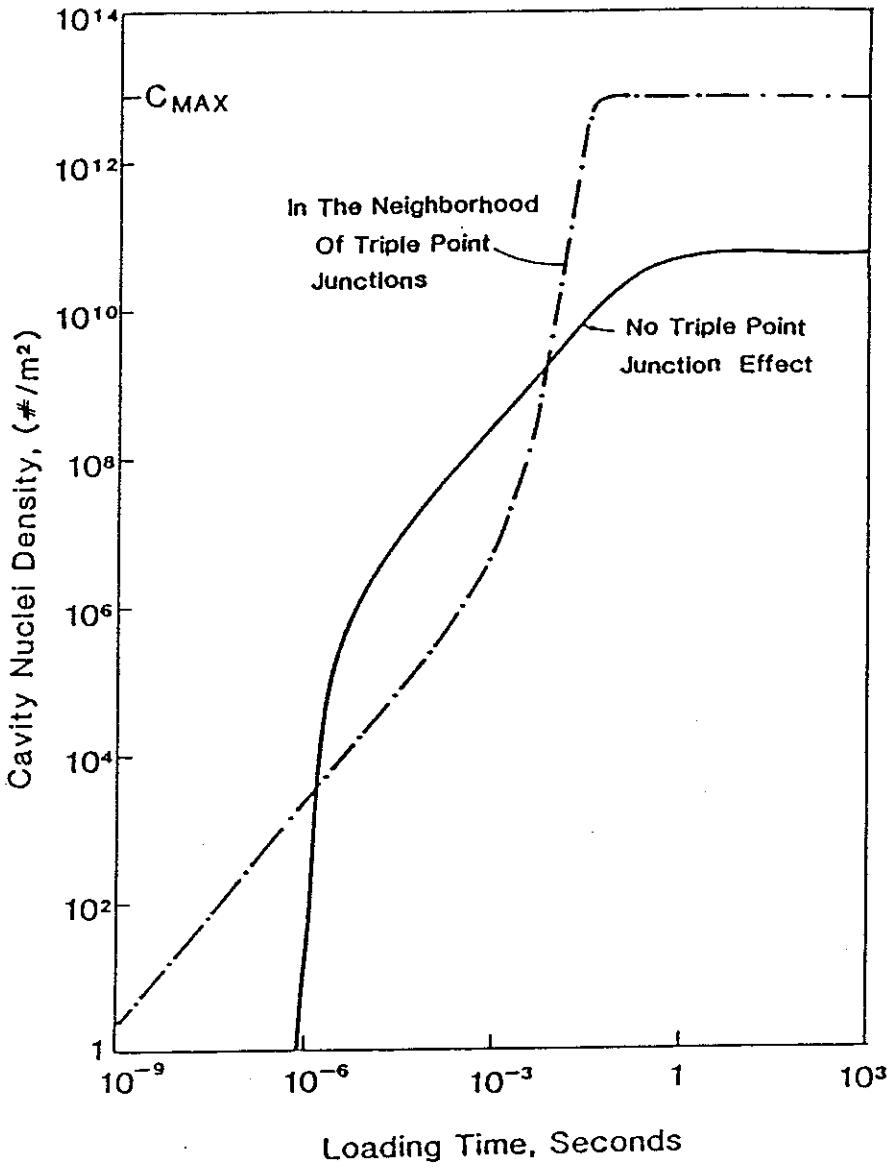

Figure 23. Cavity nuclei density in the neighborhood of a triple point junction and at a distance far from the triple point. The applied stress is 100 MPa at 600 ^{o}C and F_v=0.01.

can result in the opening of a crack at the triple point by decohesion. One can conclude that triple-point cracking can be due to decohesion at lower temperatures; but at higher temperatures, cavitation near the triple point plays a major role in opening such a crack.

6. CONCLUSIONS

1. Classical nucleation theory can be utilized to study creep cavitation as was suggested by Aaronson and Lee [38].

2. Nucleated cavities are not spherical but are lenticular in shape and possess a shape factor of less than 0.01. This translates into a dihedral angle of at most 17.0 deg. Lenticular-shaped cavities have been observed by Chen and Argon [10].

3. Grain boundary sliding and obstacles at sliding boundaries such as particles and ledges are basic ingredients and in their absence, cavity nucleation is virtually impossible. In the absence of grain boundary particles, no cavities were observed by Servi, et al. [7] during a creep test.

4. Cavity nucleation is most probable on those boundaries which are parallel to the maximum principal stress axis and least probable on orthonganal boundaries to such a stress. This is consistant with experimental observations [35] and [36].

5. Cavity nucleation rate at triple-point junctions is higher than those regions which are far away from triple points. This is consistant with observations by Chen and Argon [10].

6. Enhanced cavity nucleation at triple points is responsible for triple-point crack nucleation at high temperatures ($T > 600°C$) [10], while at lower temperatures ($\sim 400°C$) simple decohesion of the boundary at triple-point junctions due to a persistent stress concentration results in such a crack nucleation [34].

7. Cavity nucleation rate is highest at elevated temperatures and decreases as the temperatures is lowered, which is also consistent with the data presented by Argon [14]. However, the period of the nucleation pulse decreases significantly as the temperature increases.

8. Future studies should look at the idea of localized intermittent sliding at orthogonal boundaries to the maximum principal stress.

9. Cavity nucleation at low temperature is not possible unless geometrical shape factors as low as 10^{-4} are used. This has been suggested by Reidel [1].

REFERENCES

[1] H. Reidel, "Cavity Nucleation at Particles on Sliding Grain Boundaries. A Shear Crack Model for Grain Boundary Sliding in Creeping Polycrystals," Acta Metall., 32 (1984) 313.

[2] A. S. Argon, "Intergranular Cavitation in Creeping Alloys," Scripta Metall., 17 (1983) 5.

[3] R. Raj, "Nucleation of Cavities at Second Phase Particles in Grain Boundaries," Acta Metall., 26 (1978) 995.

[4] R. Raj and M. F. Ashby, "Intergranular Fracture at Elevated Temperature," Acta Metall., 23 (1975) 653.

[5] I. J. W. Gibbs, On the Equilibrium of Heterogeneous Substances, Collected Works, Vol. 1, (Longmanns, Green and Co., New York, 1928).

[6] W. Pavinich and R. Raj, "Fracture at Elevated Temperature," Metall. Trans. A, 8A (1977) 1917.

[7] I. Servi and N. J. Grant, "Creep and Stress Rupture Behavior of Aluminum as a Function of Purity," Trans. AIME, 191 (1951) 909.

[8] A. G. Evans, J. R. Rice and J. P. Hirth, "Suppression of Cavity Formation in Ceramics: Prospects for Superplasticity," J. Am. Ceram. Soc., 63 (7-8), (1980) 368.

[9] A. S. Argon, I. W. Chen, and C. W. Lau, "Intergranular Cavitation in Creep: Theory and Experiments," in Creep-Fatigue-Environment Interactions, R. M. Pelloux and N. S. Stoloff, Eds. (AIME, New York, 1980) 46.

[10] I. W. Chen and A. S. Argon, "Creep Cavitation in 304 Stainless Steel," Acta Metall., 29 (1981) 1321.

[11] M. H. Yoo and H. Trinkaus, "Crack and Cavity Nucleation at Interfaces During Creep," Metall. Trans. A, 14A (1983) 547.

[12] J. B. Zeldovich, J. Exp. Theor. Phys., 12 (1942) 525.

[13] H. Trinkaus and H. Ullmaier, "A Model for the High Temperature Embrittlement of Metals Containing Helium," Philos. Mag., 39 (1979) 563.

[14] A. S. Argon, "Mechanisms and Mechanics of Fracture in Creeping Alloys," Recent Advances in Creep and Fracture of Engineering Materials and Structures, B. Wilshire and D. R. J. Owen, Eds. (Pineridge Press, Swansea, 1982) pp. 1-52.

[15] P. Batfalsky and H. Schroeder, "Helium Bubble Microstructure in Stainless Steel Implanted Under Various Conditions," J. Nucl. Mater., 122&123 (1984) 1475.

[16] C. Herring, "Surface Tension as a Motivation for Sintering," The Physics of Powder Metallurgy, W. E. Kingston, Ed. (McGraw-Hill, New York, 1951) 143.

[17] P. J. Clemm and J. C. Fisher, "The Influence of Grain Boundaries on the Nucleation of Secondary Phases," Acta Metall., 3 (1955) 70.

[18] J. E. Harris, "Nucleation of Creep Cavities in Magnesium," Trans. Metall. Soc. AIME, 233 (1965) 1509.

[19] F. W. Crossman and M. F. Ashby, "The Non-Uniform Flow of Polycrystals by Grain Boundary Sliding Accommodated by Power Law Creep," Acta Metall., 23 (1975) 425.

[20] A. L. Chang and M. L. Bleiberg, "Grain Boundary Cavitation Theory for Post Irradiation Tensile Ductility in Nimonic PE 16, Part I - Diffusion Controlled Model," Ward Topical Report WARD-AD-3045-12, (1980) 259.

[21] J. N. Goodier, "Concentration of Stress Around Spherical and Cylindrical Inclusions and Flaws," J. Appl. Mech., 55 (1933) 39.

[22] C. W. Lau, "Dominant Singularity and Finite Element Analysis of Plane-Strain Stress Fields in Creeping Alloys with Sliding Grain Boundaries," Ph.D. thesis, Massachusetts Institute of Technology, 1981.

[23] B. R. Lawn and T. R. Wilshaw, Fracture of Brittle Solids (Cambridge University Press, London, 1975).

[24] C. Zener, "Theory of the Elasticity of Polycrystals with Viscous Grain Boundaries," Phys. Rev., 60 (1941) 906.

[25] E. E. Schumacher, "Discussion on Creep and Recrystalization of Lead," Trans. AIME, 143 (1941) 176.

[26] C. Zener, "The Micro-Mechanism of Fracture," presented at a Seminar on the Fracturing of Metals, American Society for Metals, Chicago, 1948, p. 3.

[27] M. F. Ashby, "Boundary Sliding and Diffusional Creep," Surface Sci., 31 (1972) 498.

[28] H. Tada, P. C. Paris and G. R. Irwin, The Stress Analysis of Cracks Handbook (Del Research Corp., Hellertown, PA, 1973) 7.1.

[29] R. M. Caddell, Deformation and Fracture of Solids (Prentice-Hall, Inc., Englewood Cliffs, NJ, 1980).

[30] R. C. Koeller and R. Raj, "Diffusional Relaxation of Stress Concentration at Second Phase Particles," Acta Metall., 26 (1978) 1551.

[31] R. Raj and M. F. Ashby, "Grain Boundary Sliding and Diffusional Creep," Metall. Trans. A, 2A (1971) 1113.

[32] M. H. Yoo and H. Trinkaus, to be published (1985).

[33] R. Raj and M. F. Ashby, "Grain Boundary Sliding and the Effects of Particles on its Rate," Metall. Trans. A, 3A (1972) 1937.

[34] A. Evans, "Deformation and Failure Caused by Grain Boundary Sliding and Brittle Cracking," Acta Metall., 28 (1980) 1155.

[35] B. F. Dyson, M. S. Loveday and M. J. Rodgers, "Grain Boundary Cavitation Under Various States of Applied Stress," Proc. R. Soc. London, Ser. A, 349 (1976) 245.

[36] M. Kikuchi, K. Shiozawa and J. R. Weertman, "Void Nucleation in Astroloy: Theory and Experiments," Acta Metall., 29 (1981) 1747.

[37] N. J. Grant and A. W. Mullendore, Eds. Deformation and Fracture at Elevated Temperatures (M.I.T. Press, Cambridge, MA, 1965).

[38] H. I. Aaronson and J. K. Lee, "The Kinetic Equation of Solid-Solid Nucleation Theory," in Lectures on the Theory of Phase Transformation, H. I. Aaronson, Ed. (Metall. Soc. AIME, New York, 1975).

CHAPTER IV

HELIUM CLUSTERING AND TRANSPORT TO GRAIN BOUNDARIES

1. INTRODUCTION

When helium atoms are introduced into a solid, either by implantation or by nuclear reactions, they tend to be insoluble. Like other noble gases, the closed electronic structure of helium results in segregation. Because of this insolubility, there is a great tendency for helium atoms to be trapped on vacancies, impurity atoms, or other helium atoms [1-13].

The introduction of helium into structural materials by nuclear reactions results in a general degradation of their properties. In fast breeder reactors, as well as anticipated fusion reactors, helium generation can lead to volumetric swelling and high temperature embrittlement of structural components. It has been shown by numerous experiments [14-27] that even small amounts of helium can lead to a severe loss of ductility. Creep rupture lifetime of structural materials can therefore be drastically reduced at high temperature. Failure creep ductilities on the order of less than 1% have been reported [26]. This is essentially an indication of helium transport to grain boundaries causing its weakening.

It has also been experimentally demonstrated that the location of helium production is of strategic importance [27]. Steels with a small amount of boron have shown low ductility when boron precipitates near the grain boundary. Experiments have shown that when boron atoms are uniformly distributed throughout the matrix (e.g., by thermomechanical heat treatments), the loss of ductility is not so great [27].

The problem of high temperature helium embrittlement is critical for fast breeder core and vessel structural materials. If fusion reactor first walls are operated at temperatures above 500°C for steels, helium embrittlement can also be a limiting design factor. It is therefore technologically important to address this problem. During the past two decades there has been a significant effort to understand and solve this phenomenon [14-27] and a great degree of understanding has been achieved. From a theoretical standpoint, the presence of helium in grain boundary cavities has been shown to result in growth instabilities that reduce the rupture lifetime [28-30]. For these treatments, however, the presence of helium inside grain boundary cavities was always assumed. For example, Trinkaus and Ullmaier [29] assumed a constant gas pressure inside growing grain boundary cavities, while Bullough, Hayns and Harries [30] assumed a simple form of gas arrival to grain boundary cavities. Even with the greater understanding of helium effects on grain boundary cavitation, there still seem to be two weak links: (1) the method of helium transport to grain boundaries and (2) poor understanding of the process of grain boundary cavity nucleation.

The migration of single gas atoms to grain boundaries is complicated by the fact that there are competing matrix processes that may hinder helium transport to boundaries. Helium atoms, which predominantly migrate by an interstitial mechanism, can be trapped at precipitate interfaces, vacancies, or in vacancy-helium clusters.

In this chapter, a rate theory based model has been developed to study of helium migration from the matrix to the grain boundary. Helium atoms are produced in the lattice in one of the following ways:

1. Nuclear reactions or by direct implantation. This source produces a uniform distribution of helium atoms in the matrix

2. Displacement damage (dynamic re-solution). When helium atoms are trapped, collision cascades or direct collisions with the primary particle (neutron or ion) can displace them again into the lattice. This is an internal source of helium atoms that is also uniform over space.

3. Localized sources. In this case, when elements such as boron are segregated near grain boundaries, a high localized source of helium is introduced. However, the burnup of boron atoms due to neutron absorption reactions leads to a transient helium source.

The first source of helium is dominant for short times, while the third is transient and relevent only for the case of neutron irradiation. The transient time scale for the third mechanism is on the order of $(\sigma_a \phi)^{-1}$, where σ_a is a spectral-averaged boron neutron absorption cross section, and ϕ is the neutron flux. It will be shown later that the second mechanism is the most dominant for times longer than the time required to achieve about 1 dpa.

In the following sections a theory for helium clustering and transport to grain boundaries by single gas atom motion is developed.

Section 2 deals with the rate theory of helium clustering and transport. The results of calculations are presented in Section 3 and conclusions follow in Section 4. The symbols and their units are given in the Nomenclature.

2. THEORY OF HELIUM CLUSTERING AND TRANSPORT TO GRAIN BOUNDARIES

In the present theoretical treatment, "localized" or "time dependent" helium sources are not included. In principle, the present work can be extended to allow for these inhomogenieties. Other important space or time inhomogenieties can be due to the nature of irradiation. The production of vacancies, self interstitials and helium are stochastic processes, since they are involved in collision cascades. Therefore, certain reactions between those primary species can be influenced by the time/space distribution of the production source. There is some progress in this area [31-33], however, the conclusions are not yet formulated in a way to include in a rate theory type approach. It is therefore assumed that defect reactions are homogeneous in both space and time.

If the external helium generation rate is given by G^{He}_{ext} (first mechanism), the internal helium generation rate by G^{He}_{int}, and the displacement damage rate by G, then the total fractional helium concentration is $G^{He}_{ext}t$, where t is time and the total fractional helium displacement rate (internal source) is therefore

$$\text{internal helium source rate} = G^{He}_{int} = G^{He}_{ext}tG \quad . \qquad (1)$$

For this source rate to exceed the external rate of helium introduction.

$$G_{ext}^{He} \tau G \geq G_{ext}^{He} \quad . \tag{2}$$

Therefore, the time required to achieve this condition is on the order of

$$\tau \geq G^{-1} \quad . \tag{3}$$

Of course, this is a simplified argument, and the exact value of τ will depend on the strength of the interaction between displacement damage and helium atoms [34]. However, it illustrates the point that the time required to achieve this condition is not very long if the gas resolution rate is the same as the displacement damage rate.

In addition to single gas atom migration to grain boundaries, helium can also be transported in migrating bubbles. In this case, bubbles can move by a variety of mechanisms and transfer helium atoms with them. Once a helium atom is trapped in a vacancy, it forms a substitutional atom until other gas atoms or vacancies react with it. If that happens, a vacancy-helium complex is said to be formed. Such a vacancy-helium complex can grow in principle by one or all of the following three processes: (1) it can accept newly created, injected, or re-dissolved gas atoms; (2) it can accept vacancies either by producing nearby Frenkel pairs in the low temperature regime ($T < 0.3\ T_m$, where T_m is the melting temperature in Kelvin) or by absorbing excess radiation-produced vacancies at high temperatures; and (3) it can migrate until it coalesces with other bubbles. The first two mechanisms are likely to operate in the presence of irradiation, while the last can proceed under irradiation as well as under post-irradiation conditions. Since in this case bubble migration is the rate-controlling step for bubble growth,

bubble coalescence occurs only in the high temperature regime, i.e., above 0.5 T_m [35].

The driving force for bubble migration can be either the Brownian motion in the absence of temperature or stress gradients, or sweeping by moving dislocations. In the first case bubble migration is random while in the latter cases it is directed up the gradient. Bubble motion practically stops when the bubble radius becomes large (~ 100 nm), or when restoring forces occur. A simple mechanism of delay is the self-pinning of bubbles by their own stress fields. This may occur when the internal gas pressure is so high as to plastically deform the surrounding matrix. Recently, gas pressures indicating solid-state conditions have been measured for aluminum and nickel [36]. Important pinning centers for bubbles are the dislocations with a restoring force assumed to be constant, precipitates, and grain boundaries with forces increasing linearly with bubble radius [35].

The term bubble used here applies to a gas-filled cavity with a diameter above the resolution limit of the transmission electron microscope (~ 1.0 nm). Below this limit, the bubble is considered to be a vacancy-helium cluster. Although different theoretical mechanisms exist for bubble re-solution, experimental observations suggest that bubbles are highly stable defects. Possible re-solution processes are:

1. Re-solution or shrinkage by gas-displacement events.

2. Re-solution of small bubbles due to Ostwald ripening by vacancy or helium emission.

3. Absorption of bubbles by others during coalescence.

Direct observations of fission gas bubble re-solution have been reported [37]. Therefore, dynamic re-solution for helium bubbles in metals is considered to exist as well. Bubble growth by Ostwald ripening has been proposed [35], but experimental evidence is still missing. From both post-irradiation annealing experiments and irradiation experiments, the disappearance of small bubbles due to coalescence has been concluded. Bubble-growth observations versus time-growth exponent α larger than 3, when a power-law ($r \sim t^{1/\alpha}$) is applied, have been attributed to coalescence growth [35]. Theoretically, however, it could be shown that any growth exponent between 1.5 and 6 can be achieved under irradiation independent of the net flux of helium to bubbles [35]. Thus, it seems to be questionable, whether the growth mechanism represented by the α value can be concluded from a simple power-law growth behavior.

The mode of cavity nucleation is important to discuss here. Recent stability line analyses [38,39] have shown that there are two general modes of cavity nucleation. The first mode, driven by helium gas, which has been termed "spontaneous" nucleation, is dominant for high helium to dpa ratios (> 5). The second mode is what is termed stochastic nucleation by the condensation of vacancies on themselves or residual impurities. This occurs at low helium to dpa ratios. However, spontaneous nucleation is the only mode considered here.

2.1. Rate Equations

The appropriate rate equations are given for the following species: (1) unoccupied vacancies, (2) self-interstitial atoms, (3) interstital helium atoms, (4) substitutional helium atoms, (5) di-interstitial helium atom clusters, (6) di-helium single vacancy clusters, (7) bubble nuclei containing three helium atoms, and (8) large bubbles containing m helium atoms. Equations for the average bubble size, the average number of helium atoms in a bubble, and the amount of helium absorbed on grain boundaries are also developed. For the case of the existence of matrix precipitates, it is assumed that one helium bubble is associated with each precipitate. Therefore, an equation describing the average precipitate bubble radius and another equation for the average number of helium atoms in a bubble are included. The following are equations for the fractional concentrations of various species:

1. Unoccupied Vacancies.

$$\frac{dC_v}{dt} = fG + E^h_{gv}C_{gv} + bGC_{gv} - \alpha C_v C_i - R_{g,v}C_g C_v - R_{v,s}C^v_s C_v$$

$$- R_{v,2g}C_v C_{2g} - R_{v,gv}C_v C_{gv} - R_{v,2gv}C_v C_{2gv} - R_{v,*}C_v C^* \quad . \quad (4)$$

2. Self Interstitials.

$$\frac{dC_i}{dt} = fG - \alpha C_v C_i - R_{i,gv}C_i C_{gv} - R_{i,s}C_i C^i_s$$

$$- R_{i,2gv}C_i C_{2gv} - R_{i,*}C_i C^* \quad . \quad (5)$$

3. Interstitial Helium.

$$\frac{dC_g}{dt} = G_H + E^h_{gv} C_{gv} + bGC_{gv} + R_{i,gv} C_i C_{gv} + m_1 bGC_b + bGM_{gb} + bGM_{ppt}$$

$$+ 2R_{i,2gv} C_i C_{2gv} + E^h_{2gv} C_{2gv} + 3bGC^*_{} + R_{i,*} C_i C^* + 2(2bG)C_{2g}$$

$$+ 2bGC_{2gv} - R_{g,b} C_g C_b - R_{g,v} C_g C_v - 2R_{g,g} C_g^2 - R_{g,gv} C_g C_{gv}$$

$$- R_{g,2gv} C_g C_{2gv} - R_{g,gb} C_g C_{gb} - R_{g,*} C_g C^* - R_{g,2g} C_g C_{2g}$$

$$- R_{g,ppt} C_{ppt} C_g \quad . \tag{6}$$

4. Substitutional Helium.

$$\frac{dC_{gv}}{dt} = R_{g,v} C_g C_v + E^h_{2gv} C_{2gv} + 2bGC_{2gv}$$

$$- C_{gv} \left(E^h_{gv} + bG + R_{i,gv} C_i + R_{g,gv} \right) \quad . \tag{7}$$

5. A Cluster of Two Helium Atoms and One Vacancy.

$$\frac{dC_{2gv}}{dt} = R_{g,gv} C_g C_{gv} + 3bGC^*_{} + R_{v,2g} C_v C_{2g} - R_{g,2gv} C_g C_{2gv}$$

$$- 2bGC_{2gv} - E^h_{2gv} C_{2gv} - R_{i,2gv} C_i C_{2gv} \quad . \tag{8}$$

6. Di-Interstitial Helium Clusters.

$$\frac{dC_{2g}}{dt} = R_{g,g}\, C_g^2 - R_{v,2g}\, C_v\, C_{2g} - R_{g,2g}\, C_g\, C_{2g} - 2bGC_{2g}$$

$$+ R_{i,*}\, C_i\, C^* - E_{2g}^h\, C_{2g} \quad . \tag{9}$$

7. Bubble Nucleus.

$$\frac{dC^*}{dt} = R_{g,2gv}\, C_g\, C_{2gv} + R_{g,2g}\, C_g\, C_{2g} - R_{g,*}\, C_g\, C^*$$

$$- R_{v,*}\, C_v\, C^* - R_{i,*}\, C_i\, C^* - 3bGC^* \quad . \tag{10}$$

8. Matrix Bubble Concentration.

$$\frac{dC_b}{dt} = \frac{4}{m_1} R_{g,*}\, C_g\, C^* + \frac{3}{m_1} R_{v,*}\, C_v\, C^* \quad . \tag{11}$$

9. Average Number of Gas Atoms in a Matrix Bubble.

$$\frac{dm_1}{dt} = R_{g,b}\, C_g - bGm_1 \quad . \tag{12}$$

10. Average Matrix Bubble Radius.

$$\frac{dR}{dt} = \frac{1}{R}\left(D_v C_v - D_i C_i - D_v C_v^e\left\{\exp\left[\frac{\Omega}{kT}\left(\frac{2\gamma_b}{R} - p_1\right)\right] - 1\right\}\right) \quad . \tag{13}$$

11. Grain Boundary Gas.

$$\frac{dM_{gb}}{dt} = R_{g,gb}\, C_g - bGM_{gb} \quad . \tag{14}$$

12. Average Precipitate Bubble Radius.

$$\frac{dR_{pb}}{dt} = (R_{pb}^2 + r_p^2)^{-1/2}\left(D_v C_v - D_i C_i - D_v C_v^e\{\exp[\frac{\Omega}{kT}(\frac{2\gamma_b}{R_{pb}} - p_2)] - 1\}\right) \quad . \tag{15}$$

13. Total Gas on Precipitates.

$$\frac{dM_{ppt}}{dt} = R_{g,ppt} C_{ppt} C_g - bGM_{ppt} \quad . \tag{16}$$

While the definitions of various symbols are given in the Nomenclature section, a description for the basis of the previous equations is given here. The general forms of the previous reactions are: displacement damage G, thermal emission E, radiation re-solution bG (b is re-solution parameter), and reactions between type A and type B mobile species $R_{A,B}C_AC_B$. The first four equations are given for the primary reacting species: vacancies, self interstitials, and helium atoms. The difference between the present equations for C_v and C_i and the conventional ones is that clustering reactions with helium atoms in the conservation equations are added. Since it is assumed that gas atoms force cavity nucleation, equations for two gas atoms (single vacancy) and for a di-interstitial helium cluster are included. It was shown that di-interstitial helium clusters are unstable at high temperature due to the low binding energy [40], and that their contribution to cavity formation is limited to the low temperature regime. A cluster of two helium atoms and one or no vacancies is still not the critical nucleus size, since backward reaction rates can be strong. Therefore, it is assumed that the critical nucleus size is a cluster of three gas atoms and some

vacancies (need not be exactly determined). This defines the early clustering part of the process. Another larger group of bubbles is then introduced with a concentration C_b. The formation of these bubbles is achieved either by a vacancy or helium atom impingement on the critical nucleus. For helium gas atom conservation, the gas-nucleus reaction rate is scaled by a factor of $4/m_1$, and the vacancy-nucleus reaction rate by a factor of $3/m_1$. These are the ratios of the number of gas atoms in the reaction to the average number of gas atoms in the large size bubble group. With this, the zeroth moment of the size distribution is conserved (total number of helium atoms). Section 2.3 will clarify this concept further.

2.2. Reaction Rates

Four basic fequencies in the clustering system are introduced. α is the frequency of self-interstitial reaction, β is the frequency of helium gas reaction, γ is the frequency of vacancy reaction and δ is the radiation re-solution frequency. These are given by:

$$\alpha = 48\ \nu_i \exp\left(-E_i^m/kT\right) \quad , \quad s^{-1} \quad , \tag{17}$$

$$\beta = 48\ \nu_g \exp\left(-E_g^m/kT\right) \quad , \quad s^{-1} \quad , \tag{18}$$

$$\gamma = 48\ \nu_v \exp\left(-E_v^m/kT\right) \quad , \quad s^{-1} \quad , \tag{19}$$

$$\delta = bG \quad , \quad s^{-1} \quad . \tag{20}$$

Also, basic thermal emission probabilities are given by the Boltzmann factors:

$$e_1 = \exp\left(-E_{vh}^B/kT\right) \quad , \tag{21}$$

$$e_2 = \exp(-E^B_{v,2h}/kT) \quad , \tag{22}$$

$$e_3 = \exp(-E^B_{v,b}/kT) \quad , \tag{23}$$

$$e_4 = \exp(-E^f_v/kT) \quad , \tag{24}$$

$$e_5 = \exp(-E^B_{2g}/kT) \quad . \tag{25}$$

The binding energies E^B_{vh}, $E^B_{v,2h}$, E^B_{2g} are determined from experiments or computer lattice calculations. The vacancy-bubble binding energy $E^B_{v,b}$ is evaluated from the work done in emitting a vacancy as follows:

$$E^B_{v,b} = E^f_v + \Delta w \quad , \tag{26}$$

$$\Delta w = -\left(\frac{2\gamma_b}{R} - P_1\right)\Omega \quad , \tag{27}$$

where Δw is the work done by the change in surface area and in compressing the gas. The gas pressure p_1 is determined by using the Van der Waal's equation of state for helium, i.e.

$$p_1 = \frac{m_1 kT}{\left(\frac{4}{3}\pi R^3 - m_1 B\right)} \quad . \tag{28}$$

For high gas pressures at small radii, a virial expansion is used. The following parameters are also used in our calculations:

Vacancy-diffusion coefficient = $D_v = (a^2/48)\gamma$;

Self-interstitial diffusion coefficient = $D_i = (a^2/48)\alpha$;

Diffusion-control combinatorial factor for bubbles
$= \varepsilon = (4\pi/48)(R/a)$;

Equivalent dispersed vacancy sink concentration = C_s^v;

Equivalent dispersed interstitial sink concentration = C_s^i;

Equivalent grain boundary sink concentration = C_{GB}.

The last three parameters are given by:

$$C_s^v = \left(\frac{a^2}{48}\right)\left(Z_v\rho + 4\pi RC_b/\Omega + 4\pi R_p^e N_p\right) \quad , \tag{29}$$

$$C_s^i = \left(\frac{a^2}{48}\right)\left(Z_i\rho + 4\pi RC_b/\Omega + 4\pi R_p^e N_p\right) \quad , \tag{30}$$

$$C_{GB} = \left(\frac{a^2}{8d}\right)\left(Z\rho + 4\pi RC_b/\Omega + 4\pi R_p^e N_p\right)^{1/2} \quad . \tag{31}$$

where

$$R_p^e = \sqrt{r_p^2 + R_{pb}^2} \quad , \tag{32}$$

is the effective bubble-precipitate pair radius [Eq. (15) and Ref. [41]]. Equations (29) and (30) are standard rate theory expressions for distributed sink strenghts, and Eq. (31) is discussed in Section 2.4.

With the previous notations, the reaction rates for the various processes can take on a simplified form. In the following, it is assumed that the basic combinatorial number is 48, and that the combinatorial number with a cluster containing n particles is simply 48 n. The subject of combinatorial number calculations for small size clusters

has been extensively discussed in the literature, with no conclusive results. Combinatorial numbers between 48 and 500 have been used for point defect recombination [42,43]. However, recent Monte Carlo simulations by Fastenau [44] show a monotonic increase in the combinatorial number with n, depending on the sink density and capture criteria. Therefore it is assumed that this dependence is ~ 48n for n = 1, 2, and 3 only. For larger clusters, the conventional diffusion-limited reaction rates are adopted. Table 1 lists expressions for the various elementary reaction rates. A discussion on the grain boundary loss term is given in Section 2.4.

Now the previous set of rate equations can be re-written in the following form:

$$\frac{dC_v}{dt} = fG + (\beta e_1 + \delta)C_{gv} - [\alpha C_i + \beta C_g + \gamma(C_s^v + C_{gv} + 2C_{2g} + 2C_{2gv} + 3C^*)]C_v \quad , \tag{33}$$

$$\frac{dC_i}{dt} = fG - (C_v + C_{gv} + 2C_{2gv} + 3C^* + C_s^i)\alpha C_i \quad , \tag{34}$$

$$\frac{dC_g}{dt} = G_H + (\beta e_1 + \delta + \alpha C_i)C_{gv} + (\beta e_2 + 2\delta)C_{2gv} + 3(\delta + \alpha C_i)C^* + 4\delta C_{2G} + 4\alpha C_i C_{2gv} + m\delta C_b + \delta M_{gb} + \delta M_{ppt} - (\varepsilon C_b + C_v + 4C_g + C_{gv} + 2C_{2gv} + 2C_{2g} + C_{GB} + \varepsilon_{ppt} C_{ppt})\beta C_g \quad , \tag{35}$$

TABLE 1. Elementary reaction rates.

	Reactions	Emissions
Interstitial	Recombination = α	
	Distributed Sink = $R_{i,s}C_s^i = \alpha C_s^i$	
	$R_{i,gv} = \alpha$	
	$R_{i,*} = 3\alpha$	
Vacancy	Distributed Sink = γC_s^v	$D_v C_v \exp[\frac{\Omega}{kT}(\frac{2\gamma}{R} - p_1)] = a^2\gamma e_3$
	$R_{v,2g} = 2\gamma$	$D_v^e C_v = a^2\gamma e_4$
	$R_{v,*} = 3\gamma$	
	$R_{v,gv} = \gamma$	
	$R_{v,2gv} = 2\gamma$	
Helium Gas	$R_{g,v} = \beta$	$E_{g,v}^h = \beta e_1$
	$R_{g,b} = \varepsilon\beta$	$E_{2g,v}^h = \beta e_2$
	$R_{g,g} = 2\beta$	$E_{2g}^h = \beta e_5$
	$R_{g,gv} = \beta$	
	$R_{g,2gv} = 2\beta$	
	$R_{g,2g} = 2\beta$	
	$R_{g,*} = 3\beta$	
	$R_{g,gb} = C_{GB}\beta$	

$$\frac{dC_{gv}}{dt} = \beta C_g C_v + (\beta e_2 + 2\delta)C_{2gv} - (\beta e_1 + \beta C_g + \delta + \alpha C_i)C_{gv} \quad , \tag{36}$$

$$\frac{dC_{2gv}}{dt} = \beta C_g C_{gv} + 3\delta C^* + 2\gamma C_v C_{2g} - (2\beta C_g + 2\delta + \beta e_2 + 2\alpha C_i)C_{2gv} \quad , \tag{37}$$

$$\frac{dC_{2g}}{dt} = 2\beta C_g^2 + 3\alpha C_i C^* - (2\gamma C_v + 2\beta C_g + 2\delta)C_{2g} \quad , \tag{38}$$

$$\frac{dC^*}{dt} = 2(C_{2gv} + C_{2g})\beta C_g - 3(\beta C_g + \gamma C_v + \alpha C_i + \delta)C^* \quad , \tag{39}$$

$$\frac{dC_b}{dt} = (12/m_1)\beta C_g C^* + (9/m_1)\gamma C_v C^* \quad , \tag{40}$$

$$\frac{dm_1}{dt} = \varepsilon\beta C_g - \delta m_1 \quad , \tag{41}$$

$$\frac{dR}{dt} = \left(\frac{a^2}{R}\right)[\gamma C_v - \alpha C_i - \gamma(e_3 - e_4)] \quad , \tag{42}$$

$$\frac{dM_{ppt}}{dt} = \varepsilon_{ppt}\beta C_{ppt} C_g - \delta M_{ppt} \quad , \tag{43}$$

$$\frac{dM_{gb}}{dt} = \beta C_{GB} C_g - \delta M_{gb} \quad , \tag{44}$$

$$\frac{dR_{pb}}{dt} = \frac{a^2}{\sqrt{R_{pb}^2 + r_p^2}}[\gamma C_v - \alpha C_i - \gamma(e_3' - e_4)] \quad , \tag{45}$$

where e_3' is calculated for a precipitate bubble in a similar way to e_3.

2.3. Gas Conservation

For the previous system of equations to have a realistic solution, total helium gas content should be conserved. In this case, the total amount of injected gas should be accounted for in various clusters, in

bubbles, on precipitates, and on grain boundaries. This means that the following equation must be satisfied:

$$M_t = G_H t = C_g + C_{gv} + 2C_{2gv} + 3C^* + m_1 C_b + M_{ppt} + M_{gb} \quad . \quad (46)$$

The time derivative of this equation gives:

$$G_H = \frac{dC_g}{dt} + \frac{dC_{gv}}{dt} + 2\frac{dC_{2gv}}{dt} + 2\frac{dC_{2g}}{dt} + 3\frac{dC^*}{dt} + m_1\frac{dC_b}{dt} + C_b\frac{dm_1}{dt} + \frac{dM_{ppt}}{dt} + \frac{dM_{gb}}{dt} \quad . \quad (47)$$

The right-hand side of Eq. (47) is composed of time derivatives of various cluster concentrations. Using Eqs. (35) through (41), and Eqs. (43) and (44), it can be easily shown that the conservation equation (47) is strictly satisfied. At this stage, the fraction of total injected gas that ends up on the grain boundaries can be simply calculated by using:

$$f_{gb} = \frac{M_{gb}}{G_H t} \quad . \quad (48)$$

2.4. Grain Boundary Helium Flux

The amount of helium arriving at the grain boundary is dependent upon the matrix sink for helium. During the early stages of irradiation, matrix precipitates and bubbles are not the dominant sink and one must take into account all other helium sinks (vacancies and small size clusters). The amount of helium going to grain boundaries will be small during this phase, however. Now, suppose that helium diffuses in a medium of distributed sink strength k^2. And suppose also that the grain

boundary is a perfect helium sink. The diffusion equation is then given by:

$$D_g \nabla^2 C_g + G_g - k^2 D_g C_g = \frac{\partial C_g}{\partial t} \quad , \tag{49}$$

where

$$k^2 = 4\pi R C_b/\Omega + 4\pi R_p^e N_p + Z\rho + \sum(\text{small cluster sinks}) \quad . \tag{50}$$

Equation (49) may be solved analytically for cases where the helium gas diffusion coefficient D_g, the gas generation rate G_g, and the sink concentration k^2 are all constants and not functions of time or space. An eigenfunction solution results in a time-series representation [45]. For a time-dependent variation of D_g, G_g, and k^2, Wood and Matthews [46] developed a variational method for the calculation of grain boundary gas flow. For our purposes, it is sufficient to adopt the steady-state solution given by Brailsford and Bullough [47]. The following simple expression is therefore used for the "equivalent" grain boundary sink strength:

$$C_{GB} = \frac{a^2 k}{8d} \quad . \tag{51}$$

2.5. "Constrained" and "Unconstrained" Cavity Growth Modes

Due to the fact that vacancy-gas reactions have been included in these analyses, not all of the vacancies will be readily available for cavity growth by excess vacancy absorption. Normally when there are only two reacting species, vacancies and interstitials, the presence of a dislocation bias toward interstitials ensures a larger vacancy flux to be absorbed at cavities. The growth rate of cavities is directly related to the magnitude of dislocation bias in this case. This growth

behavior can be described as an unconstrained cavity growth mode. A new situation is encountered when helium atoms are included in this delicate balance process. In one form or another, vacancies and interstitials eventually recombine, except for some biased interstitials that end up preferentially on dislocations. The cavity growth is therefore dictated by the amount of interstitials absorbed, which has an equivalent net number of vacancies in cavities. When helium gas preferentially reacts with vacancies, some vacancies are then immobilized and therefore will not be available for cavity growth. If vacancy-helium reactions are significant (i.e., the number of substitutional helium atoms is a large fraction of the total vacancy population), a larger flux of self-interstitials may arrive at the cavity inhibiting its growth. If this is the case, cavities can only grow by the absorption of helium atoms and not by an excess vacancy flux. This is a very slow growth process since helium atoms absorbed in the cavity have to produce their own Frenkel pairs due to the excessive cavity pressure. The growth behavior in this case can be described as constrained as opposed to the unconstrained growth mode. In the following, an analytical condition for the predominance of one of these modes of growth is derived.

Suppose now that quasi-steady-state conditions have been achieved by the previous system of equations. In this case, the vacancy and interstitial equations can be described by:

$$\frac{dC_v}{dt} = 0 = fG - \alpha C_v C_i - \gamma C_v C_s^v - \beta C_g C_v \quad , \tag{52}$$

$$\frac{dC_i}{dt} = 0 = fG - \alpha C_v C_i - \alpha C_i C_s^i \quad . \tag{53}$$

In Eqs. (52) and (53), all vacancy sinks are combined into the C_s^v term, and all equivalent intersitial sinks into the C_s^i term. Notice that in these equations there is one non-symmetric reaction rate, which is the reaction rate of helium gas with vacancies. Subtracting Eq. (52) from (53), and re-arranging, it can be easily shown that:

$$\frac{\gamma C_v}{\alpha C_i} = \frac{(C_s^i/C_s^v)}{[1 + (\beta C_g/\gamma C_s^v)]} \quad . \tag{54}$$

For unconstrained cavity growth [Eq. (42)], $\gamma C_v/\alpha C_i$ must be greater than unity. Since $\langle Z_i \rangle = C_s^i/C_s^v$, where $\langle Z_i \rangle$ is the average system bias, then the unconstrained growth condition is expressed as

$$\langle Z_i \rangle > \left(1 + \frac{\beta C_g}{\gamma C_s^v}\right) \quad . \tag{55}$$

If $\langle Z_i \rangle$ is expressed as

$$\langle Z_i \rangle = 1 + \Delta Z_i \quad , \tag{56}$$

then, the unconstrained growth condition is

$$\langle \Delta Z_i \rangle > \frac{\beta C_g}{\gamma C_s^v} \quad . \tag{57}$$

Cavity growth can therefore be constrained until this condition is satisfied. In other words, the conversion condition from constrained to unconstrained growth is achieved when:

$$\text{(vacancy-sink reaction rate)} > \langle \Delta Z_i \rangle \times \text{(vacancy-helium reaction rate)} \quad . \tag{58}$$

Equation (58) is the necessary condition for the conversion process.

3. RESULTS OF CALCULATIONS

3.1. Influence of Clustering on Single Gas Atom Transport to Grain Boundaries

During the early stages of irradiation, helium is generated as an interstitial atom but is soon trapped when vacancies become available. The concentration of untrapped helium is never very high. This trapping eventually leads to the formation of bubbles from substitutional helium. The results of calculations for ion-irradiation conditions are presented first. This is intended to simulate a study conducted by Argonne using dual-ion beam irradiation at a nominal temperature of 625°C on type 316 stainless steel [48]. The displacement damage rate is 3×10^{-3} dpa/sec, and the helium/dpa ratio is 5. While the re-solution parameter b has been set = 1, and the dislocation bias factor to $\langle Z_i \rangle = 1.2$, the remainder of material parameters are the standard values for 316 stainless steel and are given in Table 2. The sensitivity of the calculations to input parameters is discussed later in this section.

The influence of matrix clustering on the transport of helium atoms to grain boundaries is shown in Figs. 1 and 2. Figure 1 shows the concentrations of single vacancies C_v, self interstitials C_i, interstitial helium C_g, substitutional helium C_{gv}, as well as bubbles C_B. It is shown that the time structure of C_v and C_i is little affected by the presence of helium. However, the absolute magnitude of the vacancy

TABLE 2. Standard material parameters for 316 stainless steel.

Notation	Parameter	Value	Units	Ref.
a	Lattice parameter	3.63	Å	1
k	Boltzmann's constant	8.617×10^{-5}	eV/K	
ρ	Dislocation density	3×10^{10}	cm/cm^2	
d	Grain diameter	3×10^{-3}	cm	2
E_i^m	Migration energy of single interstitials	0.2	eV	3
E_g^m	Migration energy of interstitial helium	0.2	eV	
E_v^m	Migration energy of single vacancy	1.4	eV	3
E_{vh}^B	Detrapping energy of a sustitutional helium	2.4	eV	39
$E_{v,2h}^B$	Detrapping energy of a Sub-He-He	3.5	eV	39
E_{2g}^B	Detrapping energy of di-interstitial helium	0.79	eV	4
E_v^F	Formation energy of a vacancy	1.6	eV	3
E_i^F	Formation energy of an interstitial	4.08	eV	3
γ_b	Surface energy	6.24×10^{14}	eV/cm^2	3
ν_i	Interstitial vibration frequency	5×10^{13}	sec^{-1}	5
ν_g	Helium vibration frequency	5×10^{13}	sec^{-1}	
ν_v	Vacancy vibration frequency	5×10^{12}	sec^{-1}	6
r_p	Precipitate radius	10^{-6}	cm	
N_p	Precipitate number density	10^{10}	cm^{-3}	
B	Van der Waals' constant	1.75×10^{-23}		6
b	Re-solution parameter	1		
Z_i	Bias factor of interstitials	1.2		
Ω	Atomic volume	1.1958×10^{-23}	cm^3	8

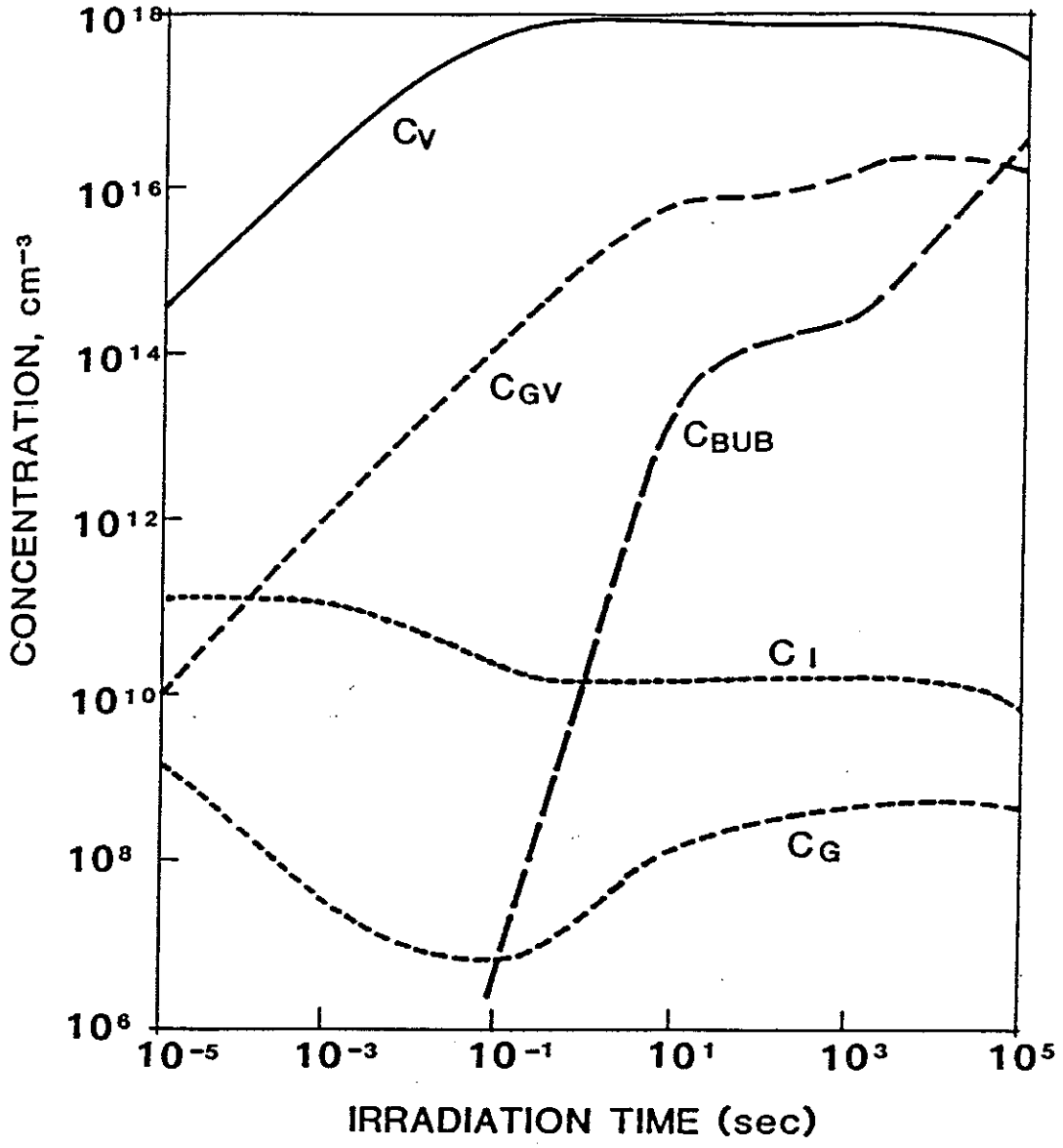

Figure 1. The evolution of clusters and bubble concentrations as a function of irradiation time. Irradiation condition is dual ion beam with a He (appm) to dpa ratio of 5 and damage rate of 3×10^{-3} dpa/sec at 625°C.

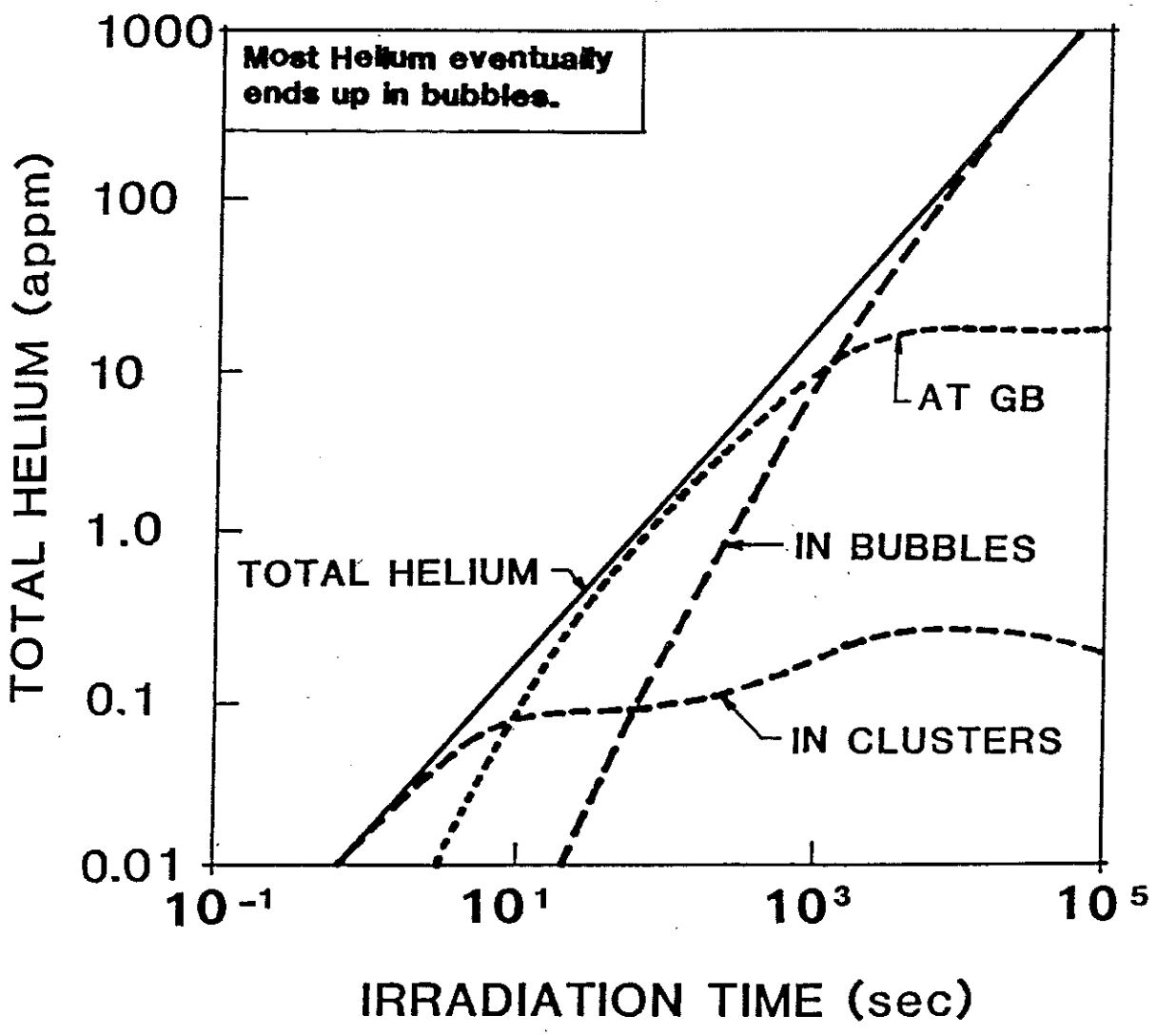

Figure 2. Helium distribution between the different traps in the material. The irradiation condition is a He(appm)/dpa equal to 5 at a $3x10^{-3}$ dpa/sec at 625 C.

concentration in this case is less than the corresponding case without the interaction with helium gas. After a short period of irradiation time ($t > 0.1$ sec), more helium is produced by displacement reactions leading to a second peak in the interstitial helium concentration around 10 sec, as can be seen in Fig. 1. The system comes to near dynamic equilibrium in about 1000 sec (few dpa's). Figure 2 shows the distribution of helium in clusters, bubbles, and grain boundaries as a function of time. By definition, vacancy-helium clusters are those containing three helium atoms or less, while bubbles contain more than three helium atoms. Since the helium injection rate is constant, the total amount of helium is linear in time. During early irradiation times (< 0.01 dpa), most of the injected helium resides in small helium-vacancy clusters. These are converted to bubbles at a higher dose, as shown in Fig. 2. The largest proportion of helium ends up in matrix bubbles at doses greater than about 10 dpa. It is observed that during the early stages of irradiation helium is contained in small clusters. Later, a large proportion goes to grain boundaries. However, the matrix bubble concentration becomes significant when the fraction of helium at grain boundaries is only a few percent of total injected helium.

3.2. Comparison with Experiments

Figures 3 and 4 demonstrate the sensitivity of cavity evolution parameters to variations in the re-solution rate. In Fig. 3, a higher re-solution rate is shown to result in continuous cavity nucleation without saturation of the total number density. Low re-solution parameters (below 0.1) lead to saturation of the cavity number density after a short transient time. On the other hand, higher re-solution

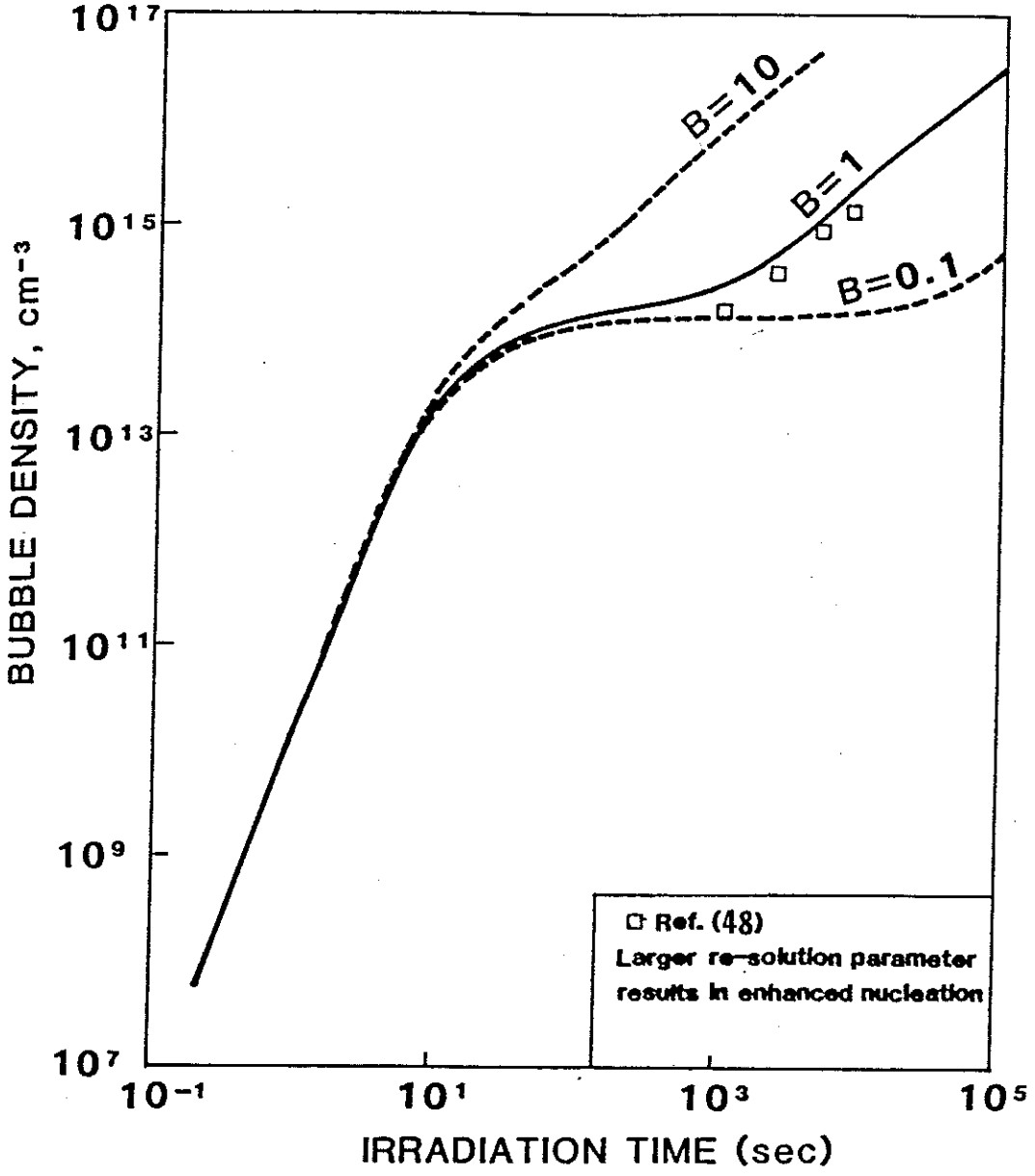

Figure 3. The effect of re-solution parameter on the bubble concentration for dual ion beam irradiation at 625°C. The He(appm)/dpa is 5 and the damage rate is 3×10^{-3} dpa/sec. (Data from ref.[48])

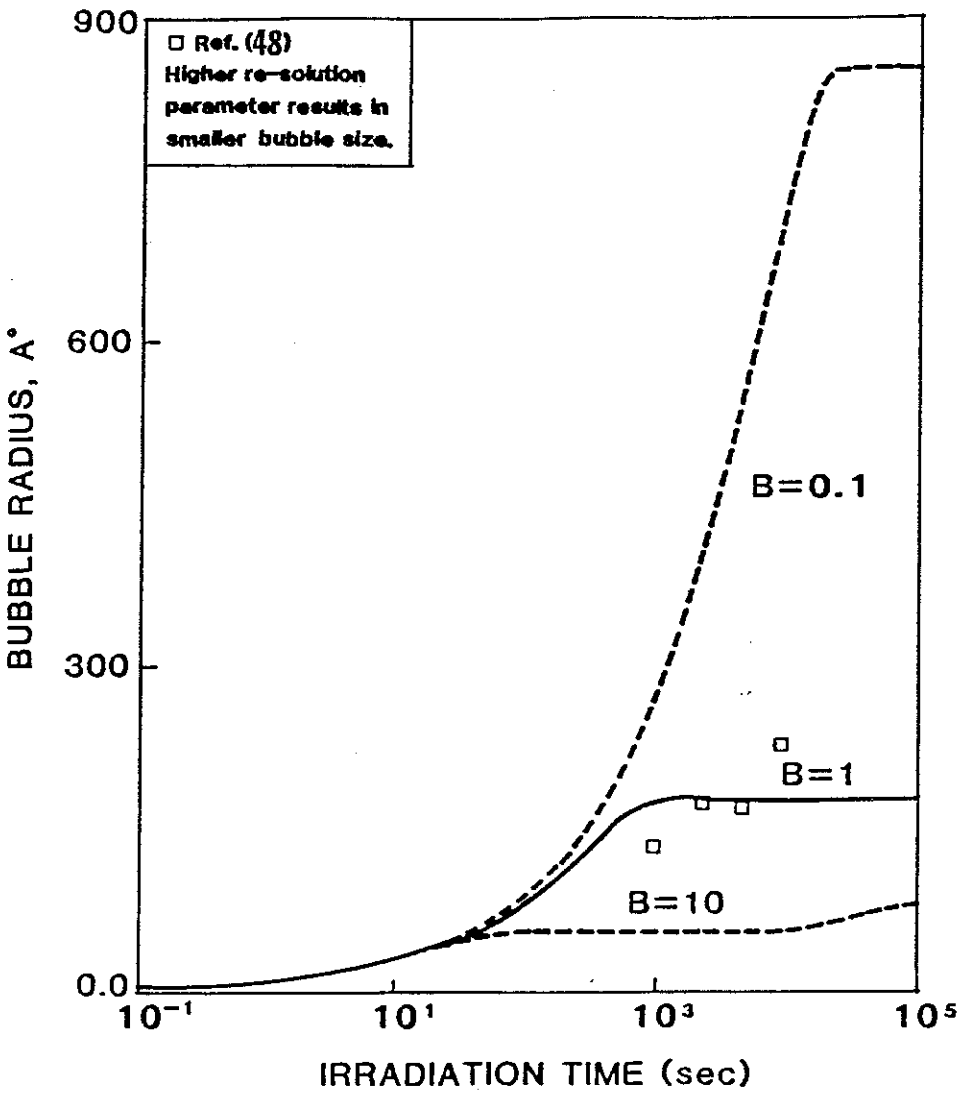

Figure 4. The effect of re-solution parameter on the bubble growth for dual ion beam irradiation at 625°C. The He(appm)/dpa is 5 and the damage rate is $3x10^{-3}$ dpa/sec. (Data from ref.[48])

parameters result in continuous cavity nucleation. The exact value of the re-solution parameter is actually a function of the PKA energy and the cavity radius [49]. This refinement is not included in the present analysis. The effects of helium re-solution on the average matrix bubble radius is shown in Fig. 4. A larger re-solution parameter leads to a higher concentration of substitutional helium, and hence to constrained cavity growth.

The influence of the bias factor Z_i on the microstructural parameters is demonstrated in Fig. 5. The reasonable variation in Z_i shows that the model results come in agreement with experiments. The point to note in Fig. 5 is the fast buildup of total cavity density. Cavity nucleation is shown to be a fast physical process. However, trailing nucleation may still persist beyond this fast phase, as illustrated in Fig. 6. The nucleation current, J, is shown as a function of irradiation time for extreme parametric conditions. It is interesting to note that nucleation during the early parts of irradiation (below ~ 0.01 dpa) is totally insensitive to parametric variations and is primarily dependent upon helium and dpa generation rates. Generated helium is immediately trapped in free vacancies or by small vacancy-helium clusters. This behavior is similar to the concept of a nucleation pulse as described by Trinkaus [40]. Trailing nucleation may still proceed at a slower rate, dictated by irradiation conditions, for a long time. Cavity number density may therefore increase by a crucial few orders of magnitude over the period of irradiation. It is therefore emphasized that this mechanism is a dynamic nucleation mechanism for cavity formation. Such dynamic nucleation can be continuous throughout irradiation if the re-solution rate is high, as demonstrated in Fig. 6.

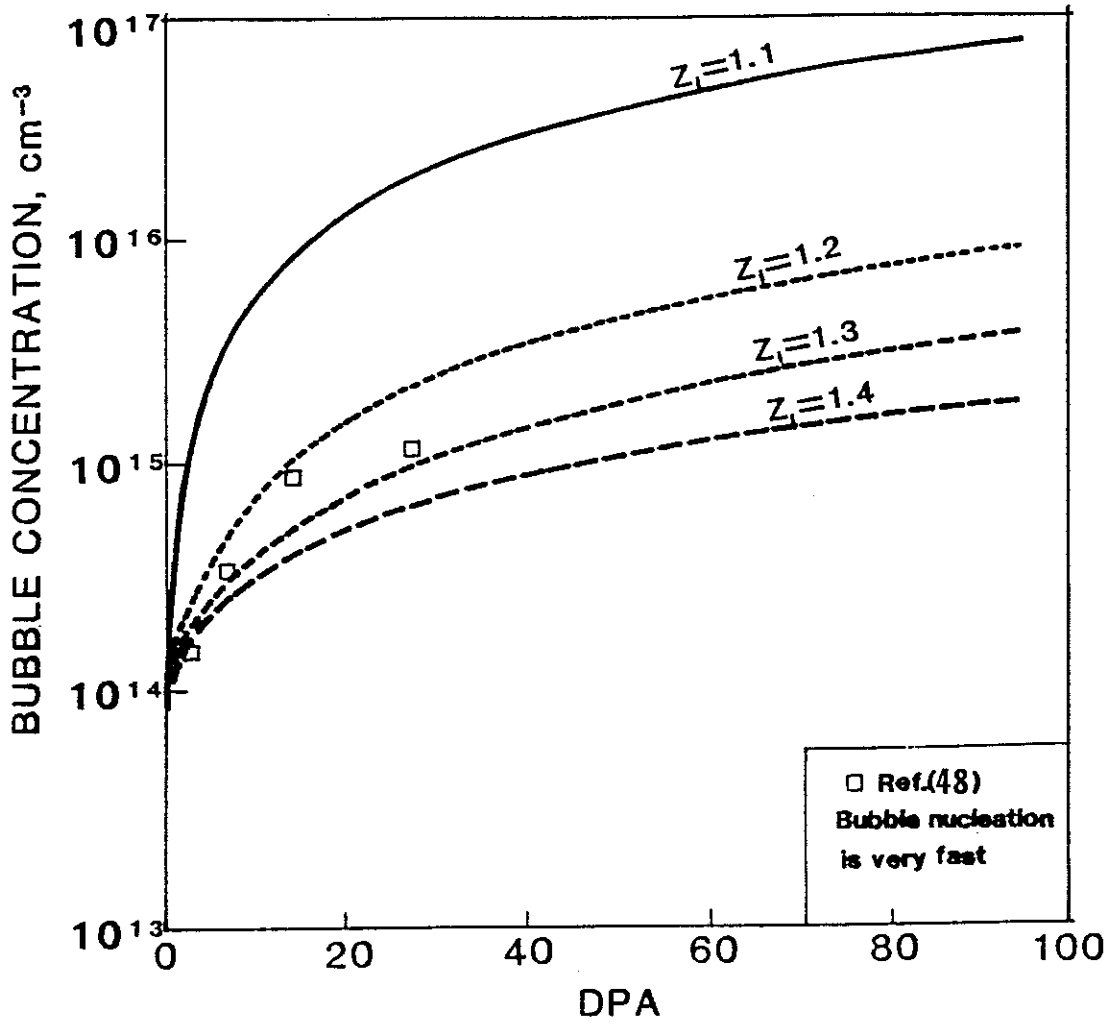

Figure 5. The number density of bubbles is strongly affected by the interstitial bias factor Z_i. The irradiation condition is 1.5×10^{-2} appm/sec and a He(appm)/dpa of 5 at 625°C. (Data from ref.[48])

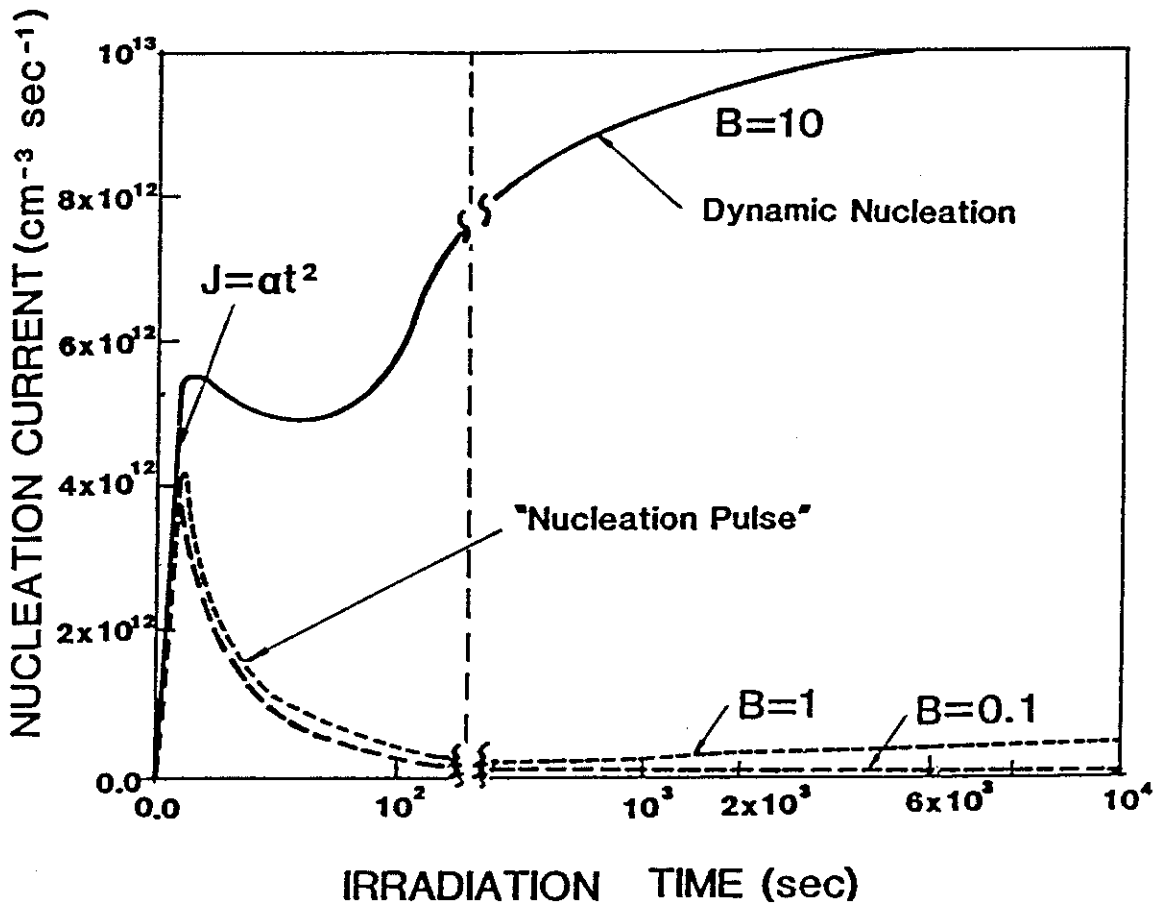

Figure 6. The nucleation behaviour of bubbles under irradiation for various values of the re-solution parameter.

A comparison of calculations with HFIR data [50] is shown in Figs. 7 and 8. The high cavity densities in HFIR experiments may be an indication of the dominance of dynamic re-solution, as well as constrained growth as described earlier. A comparison of this data with EBR-II data shows that cavity densities are orders of magnitude higher due to the profound influence of helium on nucleation.

3.3. Effects of Pre-Existing Matrix Precipitates and Grain Size on Grain Boundary Helium Gas

One practical idea to prevent grain boundary cavity nucleation, and hence mitigate helium embrittlement, is to trap the helium on matrix precipitates (e.g., [26]). This idea has been implemented in the development of titanium-modified stainless steels that are resistant to helium embrittlement. This section describes the results of the present model regarding precipitate effects on helium trapping. Figure 9 shows the results of such calculations for a simulation of the Argonne experiment. The figure shows the grain boundary gas content (appm), for a total amount of 150 appm injected helium, as a function of the matrix precipitate concentration (cm^{-3}). It is shown that the amount of grain boundary gas is an insensitive function of the matrix precipitate concentration below ~ 10^{12} precipitate/cm^3. The precipitates were assumed here to be spherical and of an average size R_p = 100 Å. The amount of gas finally residing at the grain boundaries decreases sharply as the precipitate density is increased (above 10^{11} cm^{-3}). However, even at relatively moderate densities (10^{14} cm^{-3}), few ppm helium still escape to the grain boundary. Figure 10 shows helium bubble densities in the matrix at precipitates, as well as the total density. Homogeneous

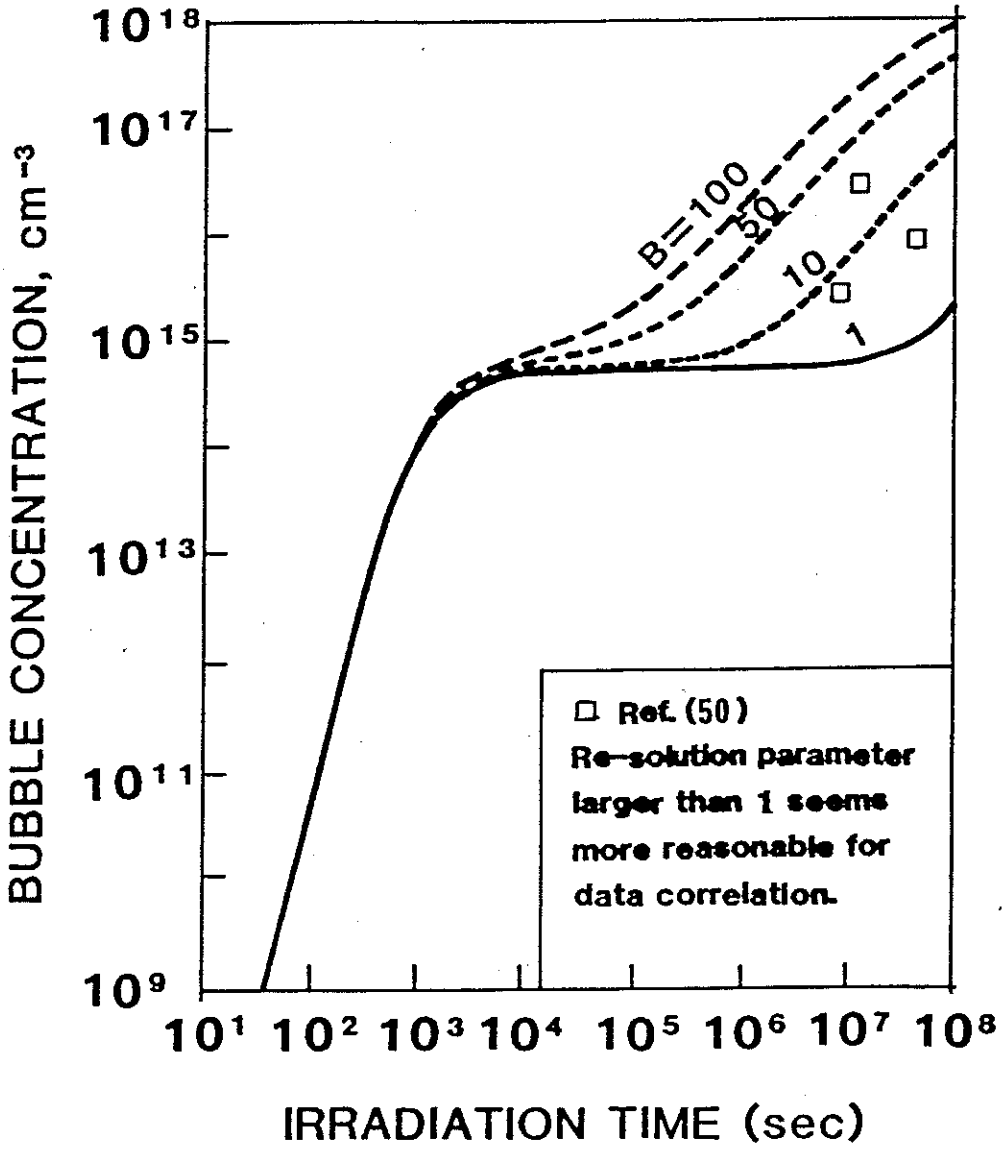

Figure 7. The effect of re-solution parameter on the bubble concentration for HFIR irradiation at 467°C. The He(appm)/dpa is 69 and the helium implantation rate is 6.9×10^{-5} appm/sec. (Data from ref.[50])

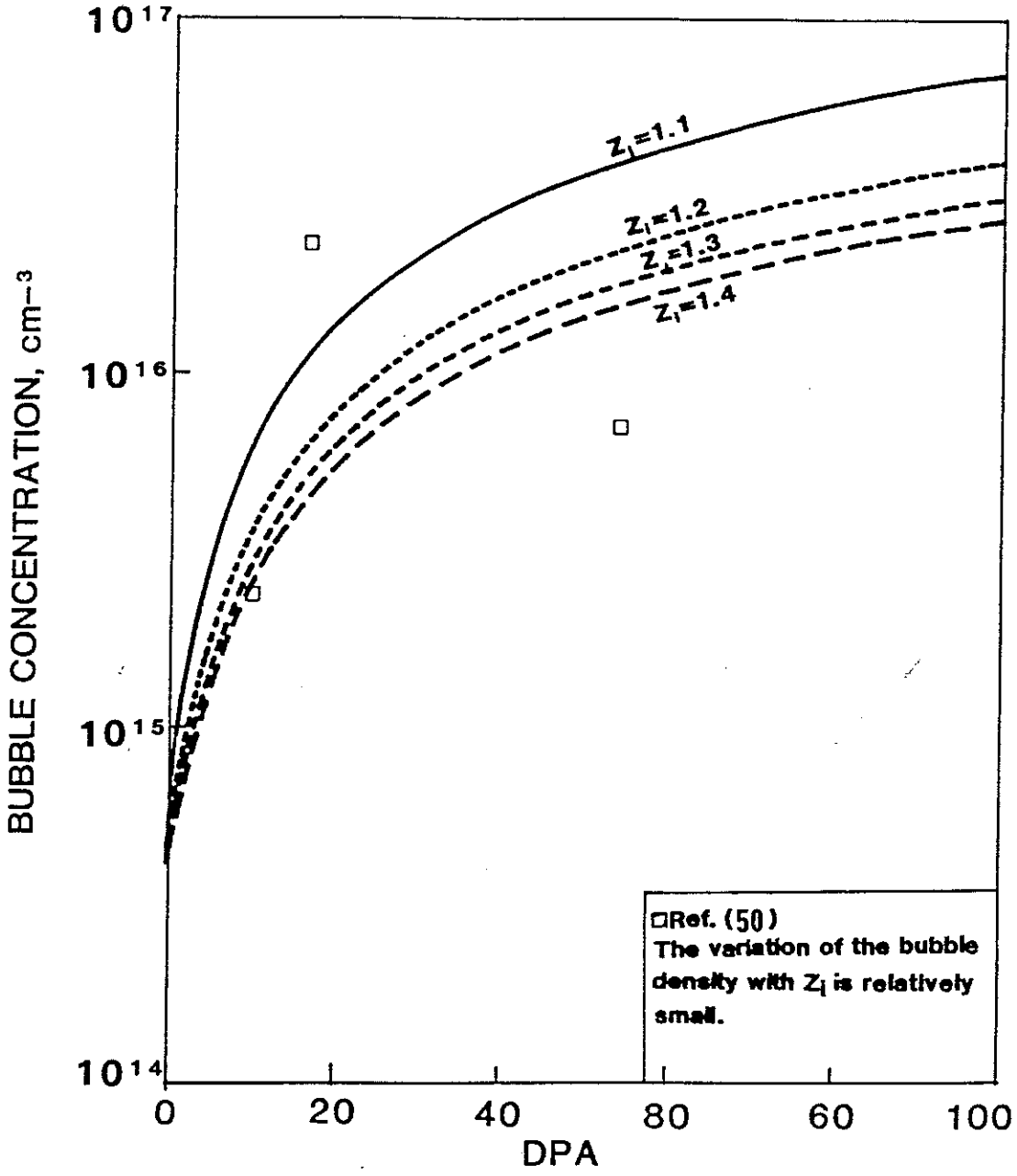

Figure 8. The dependence of the bubble density on the bias factor as a function of DPA for HFIR condition at 467°C. a re-solution parameter of 10 is used in this case. (Data from ref.[50])

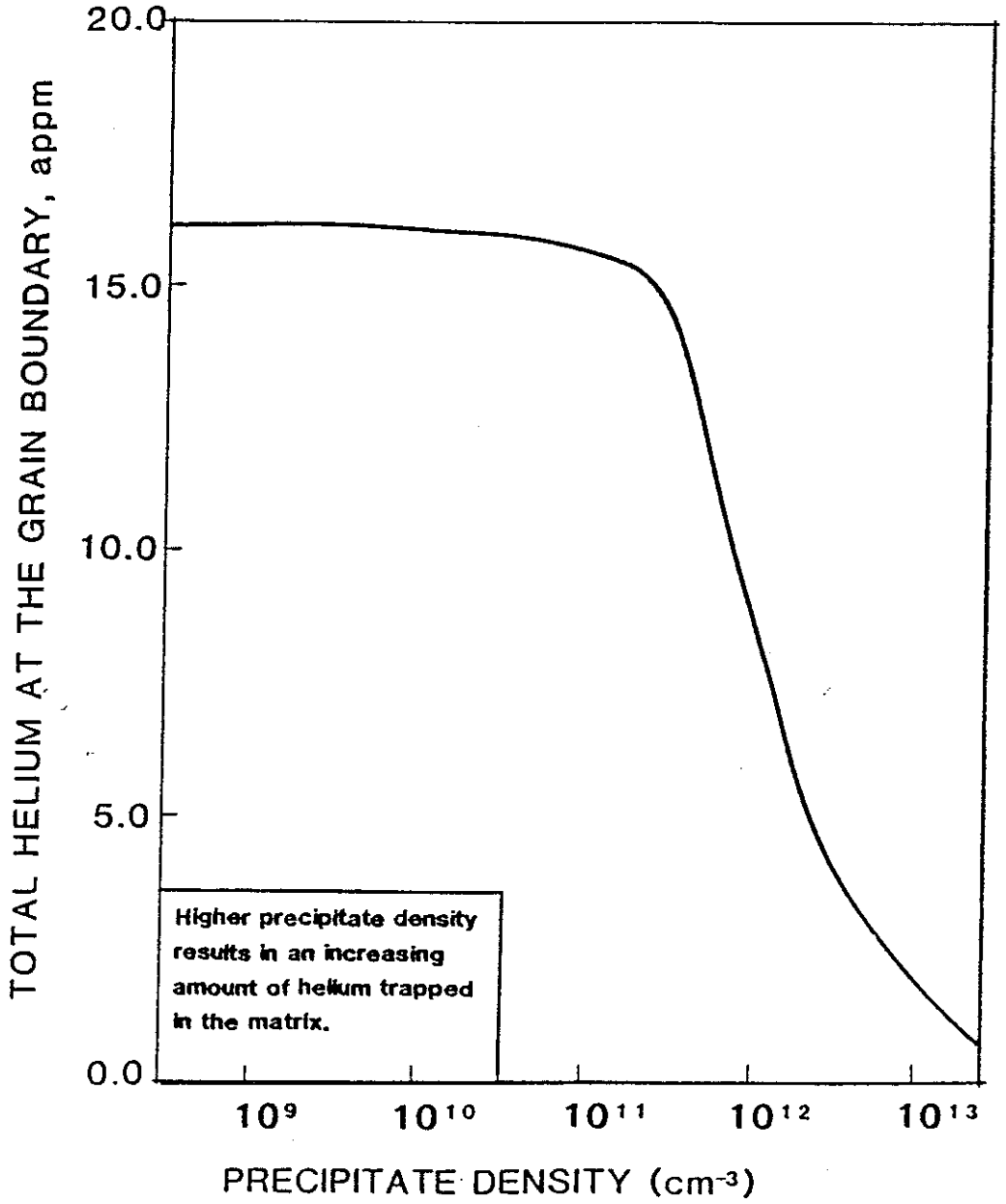

Figure 9. The effect of matrix precipitates density on the amount of helium at the grain boundary. Total injected helium is 150 appm at 625°C.

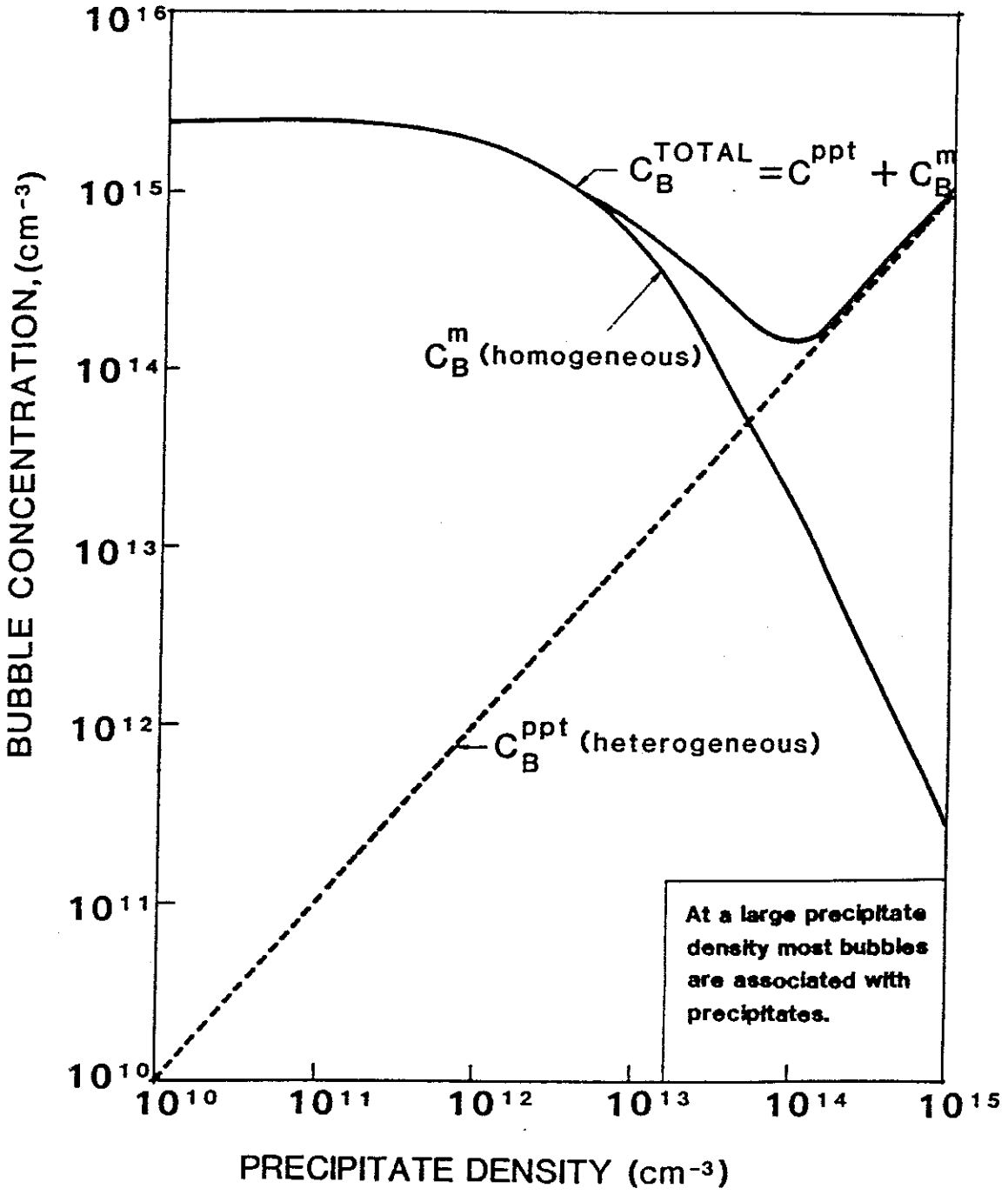

Figure 10. The effect of matrix precipitates density on the bubble concentration. The total injected helium is 150 appm at 625°C.

nucleation of matrix cavities is reduced by the heterogeneous nucleation of cavities at precipitates.

Figure 11 shows grain boundary helium content (appm) as a function of grain diameter (micrometers), for a total injected helium of 150 appm. The grain boundary gas is a strong function of grain diameter in the range of 10-50 micrometers. It decreases sharply from about 1/3 of total injected helium for a grain diameter of 15 μm, to roughly 1/30 of injected helium at a diameter of 60 μm, and then saturates thereafter. A moderate grain diameter of 30-60 μm is shown to be sufficient for reducing grain boundary helium trapping. Larger grain sizes do not result in a considerable improvement. The amount of helium per unit surface area is also shown on the same figure. It is shown that this quantity, which determines grain boundary bubble density, is relatively insensitive to grain size. Precipitates have been quantitatively shown to result in a reduction in the amount of helium trapped at grain boundaries. However, for practical precipitate densities few appm of helium may still reside at grain boundaries. Increasing matrix precipitates is therefore concluded to be more effective in reducing helium embrittlement than increasing grain size.

4. CONCLUSIONS

In this chapter, it was shown that the model gives a reasonable agreement with available data on matrix helium-filled cavity nucleation and growth. This investigation demonstrates the effects of several

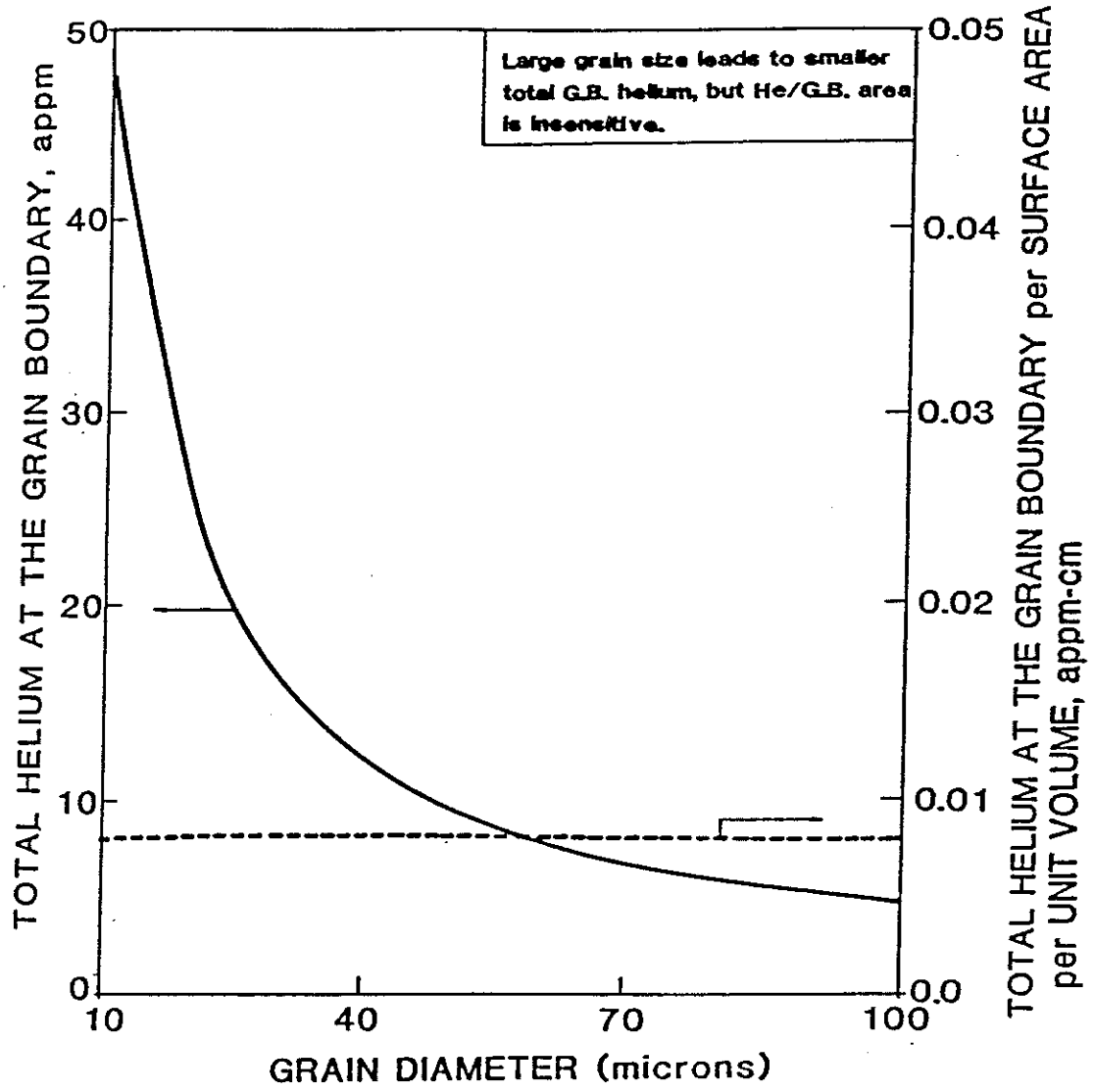

Figure 11. The influence of grain size on the amount of gas at the grain boundary. The total injected helium is 150 appm at 625°C.

physical mechanisms that are significant in interpreting experiments and furthering theory development. The following points are concluded:

1. The injection of helium gas into the solid, either via nuclear reactions or by implantation, cannot be separated from the question of vacancy mobility. It has been shown that large helium concentrations lead to the immobilization of a large fraction of vacancies, which in turn leads to a constrained mode of cavity growth provided that the cavities or clusters are immobile.

2. Helium gas re-solution due to the interaction of displacement damage with gas-filled cavities is a process of prime importance to cavity re-nucleation. At high re-solution rates, dynamic nucleation is a continuous process throughout irradiation.

3. Theoretical models and experiments are both needed to determine the effects of re-solution.

4. The external source of helium injection can be less important compared to internal helium sources due to gas re-solution effects on gas arrival rates at grain boundaries.

5. During early irradiation, helium gas is trapped in small vacancy clusters. A large fraction of gas migrates to grain boundaries until matrix cavity nucleation is complete. When this is achieved, the majority of introduced gas resides in bubbles and a small percentage arrives at grain boundaries. It

may be impossible therefore to completely suppress helium from reaching grain boundaries.

6. In order for matrix precipitates to act as effective helium traps, their density must be high ($> 10^{13} - 10^{14}$ cm^{-3}).

NOMENCLATURE

Symbol	Description	Units
a	Lattice parameter	(cm)
B	Van der Waals' constant	(~ 1)
b	Re-solution parameter	(at/at)
C_b	Matrix bubble concentration	(at/at)
C_g	Interstitial helium concentration	(at/at)
C_{gb}	Equivalent grain boundary sink concentration	(at/at)
C_{gv}	Substitutional helium concentration	(at/at)
C_{2g}	Di-interstitial helium cluster concentration	(at/at)
C_{2gv}	Concentration of a cluster containing 2-helium atoms and one vacancy	(at/at)
$C_{i,v}$	Interstitial/vacancy concentration	(at/at)
C_s^i	Equivalent dispersed self-interstitial sink concentration	(at/at)
C_s^v	Equivalent dispersed vacancy sink concentration	(at/at)
C_{ppt}	Matrix precipitates concentration	(at/at)
C^*	Bubble embryo concentration	(at/at)
C_v^e	Equilibrium vacancy concentration	(at/at)
d	Grain diameter	(cm)
$D_{v,i}$	Diffusion coefficient of vacancies/interstitials	(cm^2s^{-1})
e_1	Thermal emission probability from a substitutional helium	
e_2	Thermal emission probability from a vacancy-di-helium cluster	
e_3	Thermal emission probability from a bubble	
e_4	Thermal formation probability for a vacancy	
e_5	Dissociation probability for a di-gas atom cluster	
e_3'	Thermal emission probability from a precipitate bubble	

$E^h_{g,v}$	Emission rate constant of a helium atom from a substitutional helium	(1/sec)
$E^h_{2g,v}$	Emission rate constant of a helium from a di-helium single vacancy cluster	(1/sec)
E^h_{2g}	Emission rate constant of a helium from a di-helium cluster	(1/sec)
E^B_{vh}	Binding energy of a substitutional helium	(eV)
$E^B_{v,2h}$	Binding energy for a vacancy and a di-helium	(eV)
E^B_{2g}	Binding energy for a di-helium	(eV)
$E^B_{v,b}$	Binding energy for a vacancy and a bubble	(eV)
E^f_v	Vacancy formation energy	(eV)
f	Fraction of vacancies surviving cascade instantaneous recombination	
f_{gb}	Fraction of total gas at the grain boundary	
G	Frenkel-pair generation rate	(dpa/sec)
G_H	Helium atom generation rate	(at/at/sec)
G^{he}_{int}	Internal He generation rate	(at/at/sec)
G^{He}_{ext}	External He generation rate	(at/at/sec)
J_g	Flux of helium to the grain boundary	(at/at/sec)
K	Boltzmann's Constant	(eV/K)
$m_{1,2}$	Number of gas atoms in a matrix bubble/precipitate bubble	
M_{gb}	Total number of gas atoms at the grain boundary	
M_{ppt}	Total number of gas atoms at precipitates	
M_p	Matrix precipitate density	($1/cm^3$)
$P_{1,2}$	Pressure in a matrix bubble/precipitate bubble	(eV/cm^3)
R	Radius of a matrix bubble	(cm)
R_{pb}	Radius of a precipitate bubble	(cm)
r_p	Radius of a precipitate	(cm)
R^e_p	Equivalent radius of a bubble-precipitate pair	(cm)

$R_{g,v}$	Reaction rate between single helium and a vacancy	(1/sec)
$R_{v,s}$	Reaction rate between vacancies and the equivalent vacancy sink	(1/sec)
$R_{v,2g}$	Reaction rate between vacancies and a di-helium cluster	(1/sec)
$R_{v,gv}$	Reaction rate between vacancies and a substitutional helium	(1/sec)
$R_{v,2gv}$	Reaction rate between vacancies and a di-gas single vacancy cluster	(1/sec)
$R_{v,*}$	Reaction rate between vacancies and a critical bubble nucleus	(1/sec)
$R_{i,2gv}$	Reaction rate between interstitials and a di-gas single vacancy cluster	(1/sec)
$R_{i,*}$	Reaction rate between interstitials and a critical bubble nucleus	(1/sec)
$R_{i,s}$	Reaction rate between interstitials and the equivalent interstitial sink	(1/sec)
$R_{i,gv}$	Reaction rate between self interstitials and a substitutional helium cluster	(1/sec)
$R_{g,b}$	Reaction rate between interstitial helium and bubbles	(1/sec)
$R_{g,v}$	Reaction rate between interstitial gas atoms and single vacancies	(1/sec)
$R_{g,g}$	Reaction rate between interstitial gas atoms	(1/sec)
$R_{g,gv}$	Reaction rate between interstitial gas atoms and substitutional helium clusters	(1/sec)
$R_{g,2gv}$	Reaction rate between interstitial gas and a di-gas single vacancy cluster	(1/sec)
$R_{g,gb}$	Reaction rate between interstitial gas and the equivalent grain goundary	(1/sec)
$R_{g,2g}$	Reaction rate between interstitial gas and di-gas atom clusters	(1/sec)
$R_{g,*}$	Reaction rate between interstitial gas and a critical bubble nucleus	(1/sec)
$R_{g,ppt}$	Reaction rate between interstitial gas atoms and precipitates	(1/sec)

t	Time	(sec)
T	Temperature	(°K)
Z	Line dislocation bias factor for helium gas	
Z_i	Line dislocation bias factor for self-interstitials	
Z_v	Line dislocation bias factor for vacancies	
ρ	Line dislocation density	(cm/cm^3)
Ω	Atomic volume	(cm^3)
γ_b	Bubble surface tension	(eV/cm^2)
α	Frequency factor for recombination	
β	Frequency factor for helium	
γ	Frequency factor for vacancies	
δ	Re-solution frequency	(1/sec)
ε	Diffusion-control combinatorial factor for bubbles	

REFERENCES

[1] M. I. Baskes, C. L. Bisson and W. D. Wilson, "Calculations of the Trapping and Migration of Vacancies and Nickel Self-Interstitials in the Presence of Rare Gases and Dislocations," J. Nucl. Mater., 83 (1979) 139.

[2] G. Carter, D. G. Armour, S. E. Donnelly, D. C. Ingram and R. P. Webb, "The Injection of Inert Gas Ions into Solids: Their Trapping and Escape," presented at Harwell Consultants Symposium, Oxfordshire, England, October 1979, p. 83.

[3] G. Farrell and W. A. Grant, "Radiation Damage in Tungsten. Its Influence on the Trapping and Subsequent Thermal Desorption of Helium," Radiat. Eff., 3 (1970) 249.

[4] R. H. J. Fastenau, A. van Veen, P. Penning and L. M. Caspers, "Monte Carlo Simulation of the Interaction of Interstitial Helium, Selfinterstitials, and Vacancies with Vacancies or Vacancy Clusters," Phys. Status Solidi A, 47 (1978) 577.

[5] J. E. Inglesfield and J. B. Pendry, "Energy of Helium Dissolved in Metals," Philos. Mag., 34 (2), (1976) 205.

[6] D. L. Johnson and J. R. Cost "Characterization and Behavior of Atomic Helium in Niobium," in Proc Conf. on Defects and Defect Clusters in B.C.C. Metals and their Alloys, National Bureau of Standards, Gathersburg, MD, August 1973, p. 279.

[7] G. R. Odette, P. J. Maziasz and J. A. Spitznagel, "Fission-Fusion Correlations for Swelling and Microstructure in Stainless Steels: Effect of the Helium to Displacement Per Atom Ratio," J. Nucl. Mater., 103&104 (1981) 1289.

[8] D. B. Poker and J. M. Williams, "Low-Temperature Release of Ion-Implanted Helium from Nickel," Appl. Phys. Lett., 40 (1982) 851.

[9] J. Roth, S. T. Picraux, W. Eckstein, J. Bottiger and R. Behrisch, "Temperature Dependence of He Trapping in Niobium," J. Nucl. Mater., 63 (1976) 120.

[10] W. Schilling, "Diffusion of Helium in Metals," presented at Yamada V Conference on Point Defects, Tokyo, Japan, Oct. 1981.

[11] F. A. Smidt, Jr. and A. G. Pieper, "Helium Mobility and Bubble Formation in Type 316 Stainless Steel, Aluminum and Vanadium," in Proc. Conf. on the Properties of Reactor Structural Alloys After Neutron or Particle Irradiation, Am. Soc. Testing Mater., Gatlinburg, TN, June 1974, ASTM-STP-570, p. 352.

[12] W. D. Wilson and C. L. Bisson, "Rare Gás Complexes in Tungsten," Radiat. Eff., 22 (1974) 63.

[13] N. M. Ghoniem, S. Sharafat, J. M. Williams and L. K. Mansur, "Theory of Helium Transport and Clustering in Materials Under Irradiation," J. Nucl. Mater., 117 (1983) 96.

[14] H. Böhm, H. Hauck, W. Leo and C. Wassilew, "Postirradiation Creep-Rupture Properties of Austenitic Stainless Steel and Nickel-Base Alloys," J. Nucl. Mater., 33 (1969) 343.

[15] G. J. C. Carpenter and R. B. Nicholson, "High-Temperature Embrittlement of Metals by Rare Gase Bubbles," in Proc. Conf. on the Radiation Damage in Reactor Materials, Vol II., International Atomic Energy Agency, Vienna, June 1969, p. 383.

[16] K. D. Closs and L. Schäfer, "In-Pile Stress Rupture Strength of Three Stabilized Austenitic Stainless Steels," in Proc. Conf. on the Effects of Radiation on Substructure and Mechanical Properties

of Metals and Alloys, Am. Soc. Testing Mater., Los Angeles, CA, June 1972, ASTM-STP-529, p. 460.

[17] T. Furuta, S. Kawasaki and R. Nagasaki, "The Effect of Cold Working on Creep Rupture Properties for Helium-Injected Austenitic Stainless Steel," J. Nucl. Mater., 47 (1973) 65.

[18] K. R. Garr, D. Kramer, C. G. Rhodes and A. G. Pard, "Helium Embrittlement of Incoloy 800," J. Nucl. Mater., 28 (1968) 230.

[19] M. Kangilaski, F. T. Zurey, J. J. Perrin and R. A. Wullaert, "Relationship of Microstructure to Embrittlement In Irradiated Stainless Steel At Elevated Temperatures," J. Nucl. Mater., 39 (1971) 117.

[20] R. L. Klueh and J. M. Vitek, "The Resistance of 9 Cr-1 MoVNb and 12 Cr-1 MoVW Steels to Helium Embrittlement," J. Nucl. Mater., 117 (1983) 295.

[21] D. Kramer, H. R. Brager, C. G. Rhodes and A. G. Pard, "Helium Embrittlement in Type 304 Stainless Steel," J. Nucl. Mater., 25 (1968) 121.

[22] G. R. Odette, "A Model for In-Reactor Stress Rupture of Austenitic Stainless Steel," J. Nucl. Mater., 122&123 (1984) 435.

[23] A. A. Sagüés, H. Schroeder, W. Kesternich and H. Ullmaier, "The Influence of Helium on the High Temperature Mechanical Properties of an Austenitic Stainless Steel," J. Nucl. Mater., 78 (1978) 289.

[24] H. Shiraishi, N. Nagata and R. Watanabe, "Effects of Pre-Irradiation Treatment and Minor Composition Modification on Neutron Irradiation Embrittlement of 316 Stainless Steel," J. Nucl. Mater., 87 (1979) 157.

[25] H. Trinkaus, "On the Modeling of the High-Temperature Embrittlement of Metals Containing Helium," J. Nucl. Mater., 118 (1983) 39.

[26] H. Schroeder, W. Kesternich and H. Ullmaier, "Helium Effects on the Creep and Fatigue Resistance of Austenitic Stainless Steels at High Temperatures," Nucl. Eng. Des/Fusion., 2 (1984) 65.

[27] D. R. Harries, A. C. Roberts, G. T. Rogers, J. D. H. Hughes and M. Dewey, "Role of Boron in the High-Temperature Irradiation Embrittlement of Austenitic Steel," in Proc. Conf. on the Radiation Damage in Reactor Materials, Vol. II, International Atomic Energy Agency, Vienna, June 1969, p. 357.

[28] M. H. Wood and K. L. Kear, "On the In-Pile Nucleation and Growth of Grain-Boundary Bubbles," J. Nucl. Mater., 118 (1983) 320.

[29] H. Trinkaus and H. Ullmaier, "A Model for the High-Temperature Embrittlement of Metals Containing Helium," Philos. Mag. A, 39 (5), (1979) 563.

[30] R. Bullough, D. R. Harries and M. R. Hayns, "The Effect of Stress on the Growth of Gas Bubbles During Irradiation," J. Nucl. Mater., 88 (1980) 312.

[31] L. K. Mansur, W. A. Coghlan and A. D. Brailsford, "Swelling with Inhomogeneous Point Defect Production - a Cascade Diffusion Theory," J. Nucl. Mater., 85&86 (1979) 591.

[32] A. D. Marwick, "Fluctuations in Defect Concentrations due to Inhomogeneous Production of Point Defects by Collision Cascades," IBM Report RC9276 (#40786), (1982).

[33] C. P. Chou and N. M. Ghoniem, "The Effects of Collision Cascade Properties on the Diffusion of Point Defects in Irradiated Materials," to be pub. J. Nucl. Mater. (1985).

[34] N. M. Ghoniem and M. L. Takata, "A Rate Theory of Swelling Induced by Helium and Displacement Damage in Fusion Reactor Structural Materials," J. Nucl. Mater., 105 (1982) 276.

[35] D. Kaletta, "Growth of Gas-Bubbles In Solids Under Irradiation at Elevated Temperatures Around 0.5 T_m," Radiat. Eff., 78 (1983) 245.

[36] W. Jäger, R. Manzke, H. Trinkaus, G. Crecelius, R. Zeller, J. Fink and H. L. Bay, "Density and Pressure of Helium in Small Bubbles in Metals," J. Nucl. Mater., 111&112 (1982) 674.

[37] R. S. Nelson, "The Stability of Gas Bubbles in an Irradiation Environment," J. Nucl. Mater., 31 (1969) 153.

[38] K. C. Russell, "The Theory of Void Nucleation In Metals," Acta Metall., 26 (1978) 1615.

[39] S. Sharafat and N. M. Ghoniem, "Stability of Helium-Vacancy Clusters During Irradiation," J. Nucl. Mater., 122 (1984) 531.

[40] H. Trinkaus, "Energetics and Formation Kinetics of Helium Bubbles in Metals," Radiat. Eff., 78 (1983) 189.

[41] L. K. Mansur, "Theoretical Evaluation of a Mechanism of Precipitate-Enhanced Cavity Swelling During Irradiation," Philos. Mag. A, 44 (1981) 867.

[42] J. B. Gibson, A. N. Goland, M. Milgram and G. H. Vineyard, "Dynamics of Radiation Damage," Phys. Rev., 120 (1960) 1229.

[43] D. R. Olander, Fundamental Aspects of Nuclear Reactor Fuel Elements, NTIS TID-26711-P1 (Nat. Tech. Info. Serv., Springfield, VA, 1976) 208.

[44] R. Fastenau, "Diffusion Limited Reactions in Crystalline Solids," Ph.D. thesis, Delft University Press, 1982, p. 98.

[45] M. H. Wood and J. R. Matthews, Harwell Research Report TP806 (1979).

[46] M. H. Wood and J. R. Matthews, "A Simple Operational Gas Release and Swelling Model," J. Nucl. Mater., 56 (1980) 439.

[47] A. D. Brailsford and R. Bullough, "The Theory of Sink Strengths," Philos. Trans. R. Soc. London, Ser. A, 302 (1465), (1981) 87.

[48] G. Ayrault, H. A. Hoff, F. V. Nolfi, Jr. and A. P. L Turner, "Influence of Helium Injection Rate on the Microstructure of Dual-Ion Irradiated Type 316 Stainless Steel," J. Nucl. Mater., 103&104 (1981) 1035.

[49] P. Chou and N. M. Ghoniem, "An Approximate Calculation of Precipitate Dissolution Using a Diffusion-Slowing Down Theory for Charged Particles," accepted for publication, Nucl. Instrum. Methods B (1985).

[50] P. Maziasz and M. L. Grossbeck, "Swelling, Microstructural Development and Helium Effects in Type 316 Stainless Steel Irradiated in HFIR and EBR-II," J. Nucl. Mater., 103&104 (1981) 987.

CHAPTER V

THEORY OF CAVITY NUCLEATION AT GRAIN BOUNDARIES DUE TO HELIUM

It is a well established fact that voids are nucleated at grain boundaries even in the absence of irradiation during high temperature creep conditions. This has been attributed to the concentration of stress at particles and triple-point junctions, as already described in detail in Chapter III. However, under irradiation at high temperature, it has been observed [1-5] that the population of voids at grain boundaries is typically 4 to 5 orders of magnitude higher than unirradiated creep-tested specimens. This has been attributed to the presence of helium at such boundaries. In the previous chapter, the flux of single helium atoms to grain boundaries has been estimated through a series of rate equations which describe single gas atom motion and various VHCs (vacancy-helium clusters). A net flux of interstitial helium atoms will end up at grain boundaries resulting in cavity nucleation. It was recently suggested, but not implemented by Trinkaus [6], that, in principle, the bubble structure developing at grain boundaries can be estimated in the same way as has been done for the grain interior: i.e., through a series of rate equations to describe single helium atoms, trapped at grain boundaries, motion, and clustering. In this chapter an implementation of this idea is carried out with the added modification that single helium atoms can escape the grain boundary through dynamic re-solution. That is, helium atoms which are trapped can be displaced through collision cascades or direct collisions with

the primary particle (neutron or ion). Such a displacement will send the helium atoms back into the grain interior.

Details of the theory are shown in the next section. The results of calculations are presented in Section 2. These are followed by conclusions.

1. THEORY OF HELIUM CLUSTERING AT GRAIN BOUNDARIES

As was previously mentioned, helium production at the grain boundary is achieved through single, interstitial helium escaping the interior grain traps. Since the interior grain traps change with irradiation, the production of helium at the grain boundary is time dependent. Vacancies at grain boundaries are assumed readily available to trap helium interstitials. Once this vacancy-helium complex is formed on the grain boundary, it can accept the newly arrived gas atom to form higher order complexes on the grain boundary. Once a tri-helium complex is formed with some vacancies (need not be determined) a bubble is born on the grain boundaries.

1.1. Rate Equations

In this section, four equations are written for the following species: (1) single helium complex C_g^{gb}, (2) di-helium complex (also a bubble nuclei) containing 2 helium atoms C_{2g}^{gb}, and (3) large bubbles containing m helium atoms C_b^{gb}. An equation that describes the average number of helium atoms in a bubble is also presented. In the next chapter, the growth of the grain boundary bubbles is investigated.

1. Single Helium Complex.

$$\frac{dC_g^{gb}}{dt} = Q_{gb} - 2R_{g,g}^{gb}\, C_g^{gb\,2} - R_{g,2g}^{gb}\, C_g^{gb}\, C_{2g}^{gb} - R_{g,b}^{gb}\, C_g^{gb}\, C_b^{gb}$$

$$- bGC_g^{gb} - R_{g,bppt}^{gb}\, C_g^{gb}\, C_{bppt}^{gb} \quad . \tag{1}$$

2. Di-Helium Complex.

$$\frac{dC_{2g}^{gb}}{dt} = R_{g,g}^{gb}\, C_g^{gb\,2} - 2bGC_{2g}^{gb} - R_{g,2g}^{gb}\, C_g^{gb}\, C_{2g}^{gb} \quad . \tag{2}$$

3. Grain Boundary Bubble Concentration.

$$\frac{dC_b^{gb}}{dt} = \frac{3}{m_b^{gb}} R_{g,2g}^{gb}\, C_g^{gb}\, C_{2g}^{gb} \quad . \tag{3}$$

4. Average Number of Gas Atoms in a Bubble.

$$\frac{dm_b^{gb}}{dt} = R_{g,b}^{gb}\, C_g^{gb} - bGm_b^{gb} \quad . \tag{4}$$

1.2. Reaction Rates

A basic frequency is introduced to describe the clustering systems at the grain boundary η. η can be defined as:

$$\eta = 46\, \nu_g^{gb} \exp\left(-\frac{E_{He}^{GB}}{kT}\right) \quad , \qquad s^{-1} \quad . \tag{5}$$

The combinatorial factor for bubbles at the grain boundary will be described in the same way as in the matrix. This is,

$$\varepsilon = \frac{4\pi}{48} \left(\frac{R}{a}\right) \quad . \tag{6}$$

1.3. Gas Reactions

$$R^{gb}_{g,g} = 2\eta \quad , \tag{7}$$

$$R^{gb}_{g,2g} = 2\eta \quad , \tag{8}$$

$$R^{gb}_{g,b} = \varepsilon_{GB}\eta \quad . \tag{9}$$

Now the previous set of equations can be re-written in the following form:

$$\frac{dC^{gb}_g}{dt} = Q_{gb} - 4\eta {C^{gb}_g}^2 - 4\eta C^{gb}_g C^{gb}_{2g} - \varepsilon_{GB}\eta C^{gb}_g C^{gb}_b - \varepsilon^{ppt}_{GB}\eta C^{gb}_g C^{gb}_{bppt} - \delta C^{gb}_g \quad , \tag{10}$$

$$\frac{dC^{gb}_{2g}}{dt} = 2\eta {C^{gb}_g}^2 - 2\eta C^{gb}_g C^{gb}_{2g} - 2\delta C^{gb}_g \quad . \tag{11}$$

$$\frac{dC^{gb}_b}{dt} = \frac{6\eta}{m_b} C^{gb}_g C^{gb}_{2g} \quad . \tag{12}$$

$$\frac{dm^{gb}_g}{dt} = \varepsilon_{GB}\eta C^{gb}_g - \delta m^{gb}_b \quad . \tag{13}$$

The interbubble half spacing L can now be determined by using

$$L = 1/\sqrt{\pi C^{gb}_b} \quad , \tag{14}$$

2. RESULTS OF CALCULATIONS

The rate of clustering of helium at grain boundaries is only influenced by the effective migration energy of the single helium atom comple. The effective migration energy of helium in the matrix has been studied in detail by Ghoniem et al. [7]. However, very little is known about its value at grain boundaries.

It is generally believed that helium atoms introduced at grain boundaries reside in a substitutional position since the supply of vacancies at grain boundaries is inexhaustible. Figure 1 illustrates the sensitivity of the effective helium migration energy on the grain boundary bubble density. The irradiation conditions simulated in the figure are that of dual ion-beam irradiation which are conducted at 625°C on type 316 stainless steel. The displacement rate is 3×10^{-3} dpa/sec and the helium to dpa ratio is 5. Increasing the effective migration energy results in enhanced nucleation. A migration energy of 1.5 to 2.0 eV results in a bubble density consistent with those observed experimentally [1-5].

Another key parameter which indirectly influences the boundary clustering conditions is the bias factor Z_i. In principle, Z_i should affect the grain boundary sink strength by controlling the supply of vacancies in the matrix and hence the average bubble size. The larger the bubble size, the less single interstitial helium atoms are able to escape the matrix to the grain boundary. The exact value of Z_i is not well known. Figure 2 nicely illustrates that the bias factor, which controls the clustering picture in the matrix, does not have a large influence on the amount of helium arriving at the grain boundary and does not affect its bubble structure. The irradiation conditions used

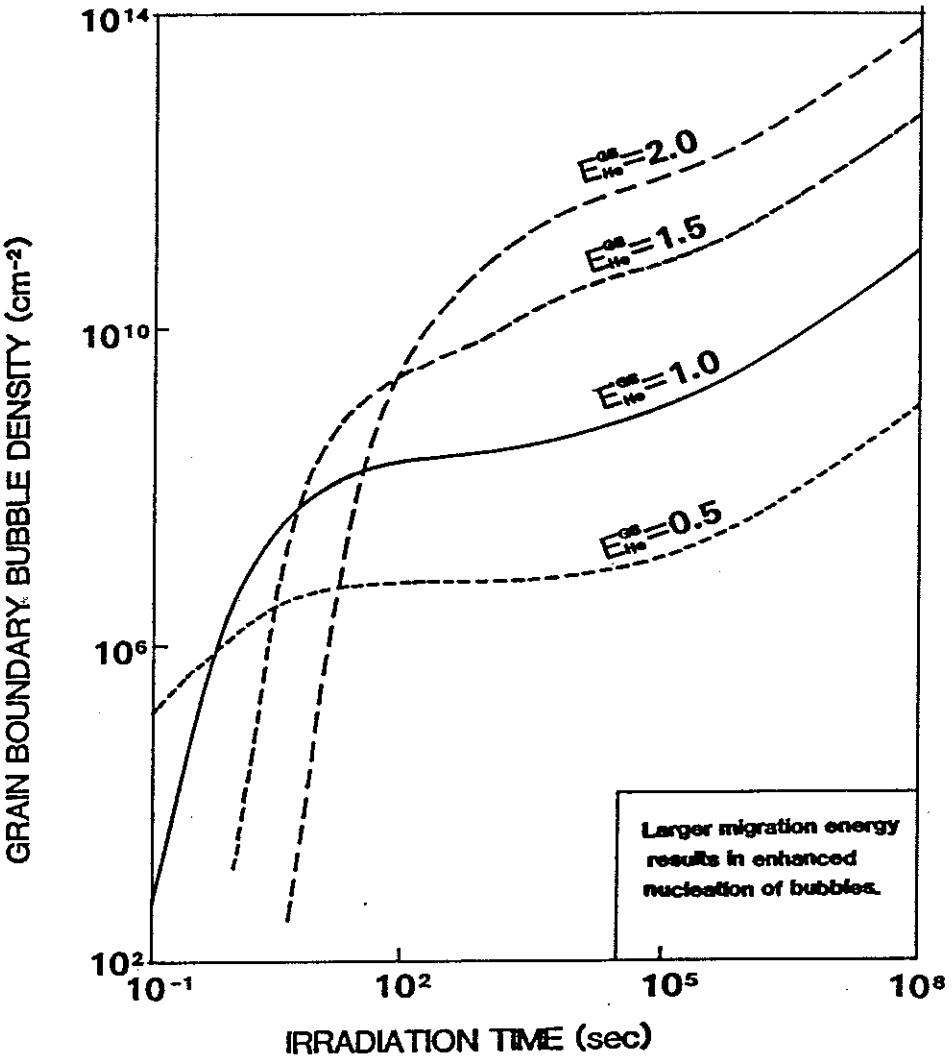

Figure 1. The effect of the grain boundary migration energy on the grain boundary bubble density.

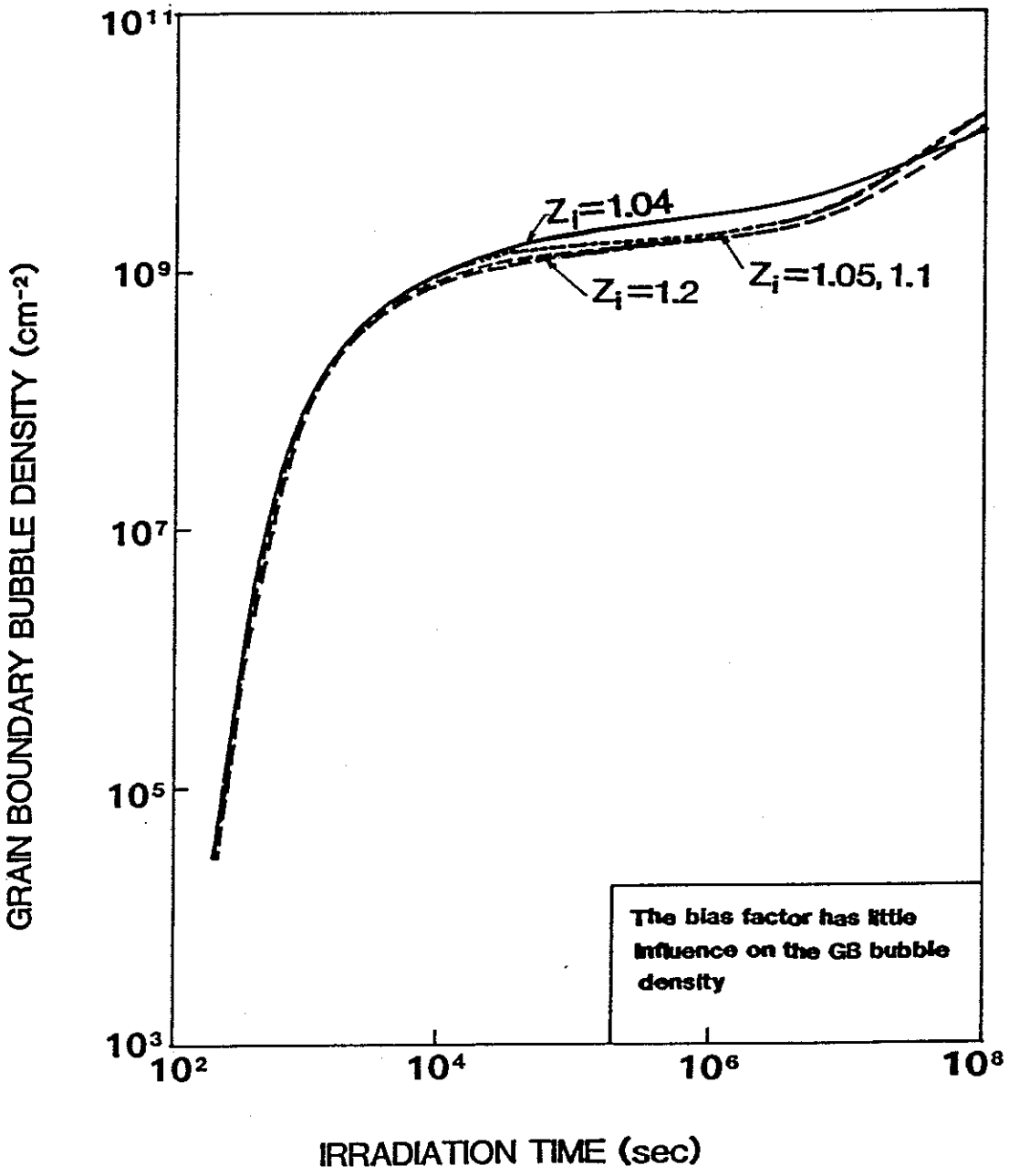

Figure 2. The influence of the bias factor on the bubble density at the grain boundary for HFIR condition at 470°C.

for the calculations are that of HFIR at 470°C on type 316 stainless steel. The displacement rate is 10^{-6} dpa/sec and the helium (appm)/dpa is 69.

2.1. Comparison with Experiments

There are many experiments which reported cavitation due to helium (e.g., [1]-[5],[8]-[10]). However, many failed to report the exact irradiation conditions. This has made it difficult to test the strength of the theory over a wide range of irradiation conditions. However, the theory gives a reasonable account of the extent of clustering in comparison with the two experiments. Figure 3 is intended to simulate the grain boundary bubble nucleation experiment conducted by Lane and Goodhew [4]. It shows the bubble densities as a function of implantation rate. The experiments were carried out at 600°C. The helium (appm) to dpa ratio is 1.6×10^4. The figure clearly shows that the bubble density increases with increasing implantation rate. The model successfully shows the correct trends as those observed experimentally. The figure also illustrates that increasing the grain boundary helium migration energy enhances the nucleation of bubbles.

Figure 4 simulates a very recent grain boundary bubble nucleation experiment conducted by Batfalsky and Schroeder [2]. The helium (appm) to dpa ratio is 10^4. The helium implantation rate is 100 appm/hr and it is done at 750°C. The simulation clearly shows that the effective migration energy is approximately the same as that for self diffusion. A self-diffusion energy of 1.9 eV has been reported by Smith and Gibbs [11]. The figure also shows that the helium clustering rate is extremely large in the beginning of irradiation and it slows down as the

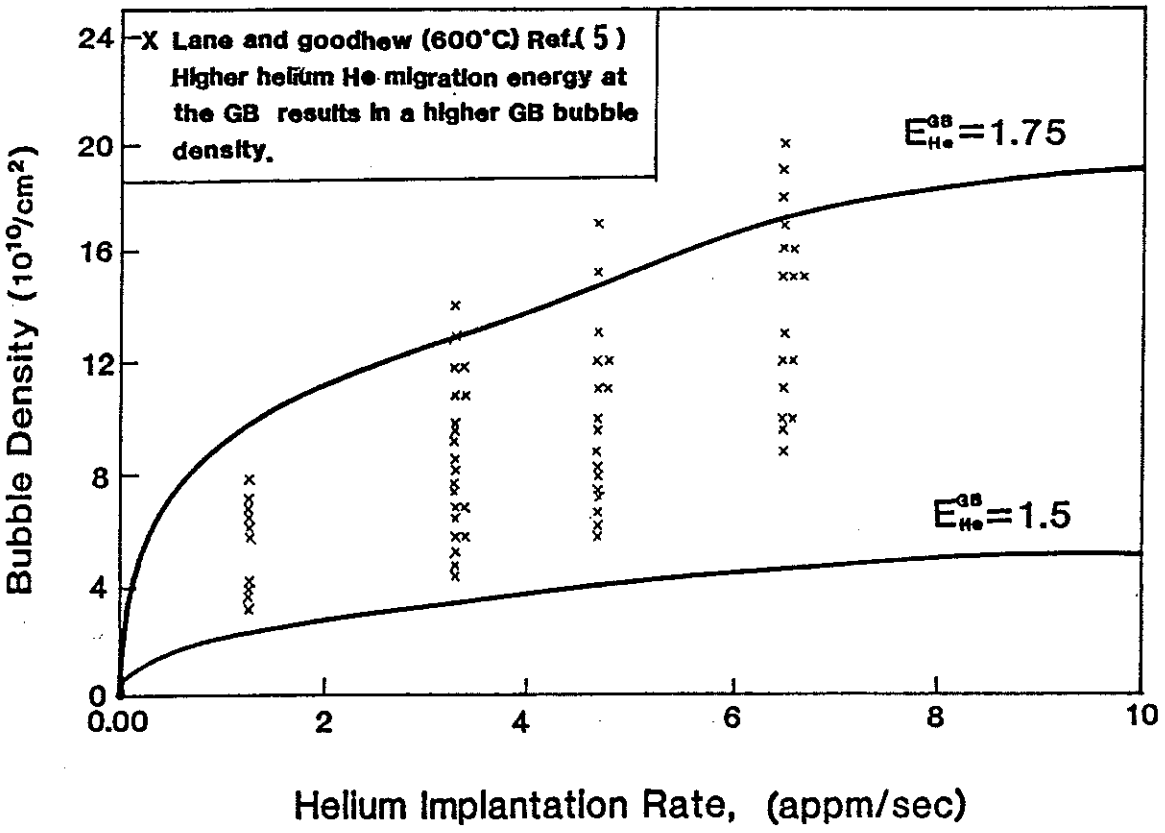

Figure 3. The influence of the He migration energy on the grain boundary bubble density. The total injected He is 5600 appm. (Data from ref.[5])

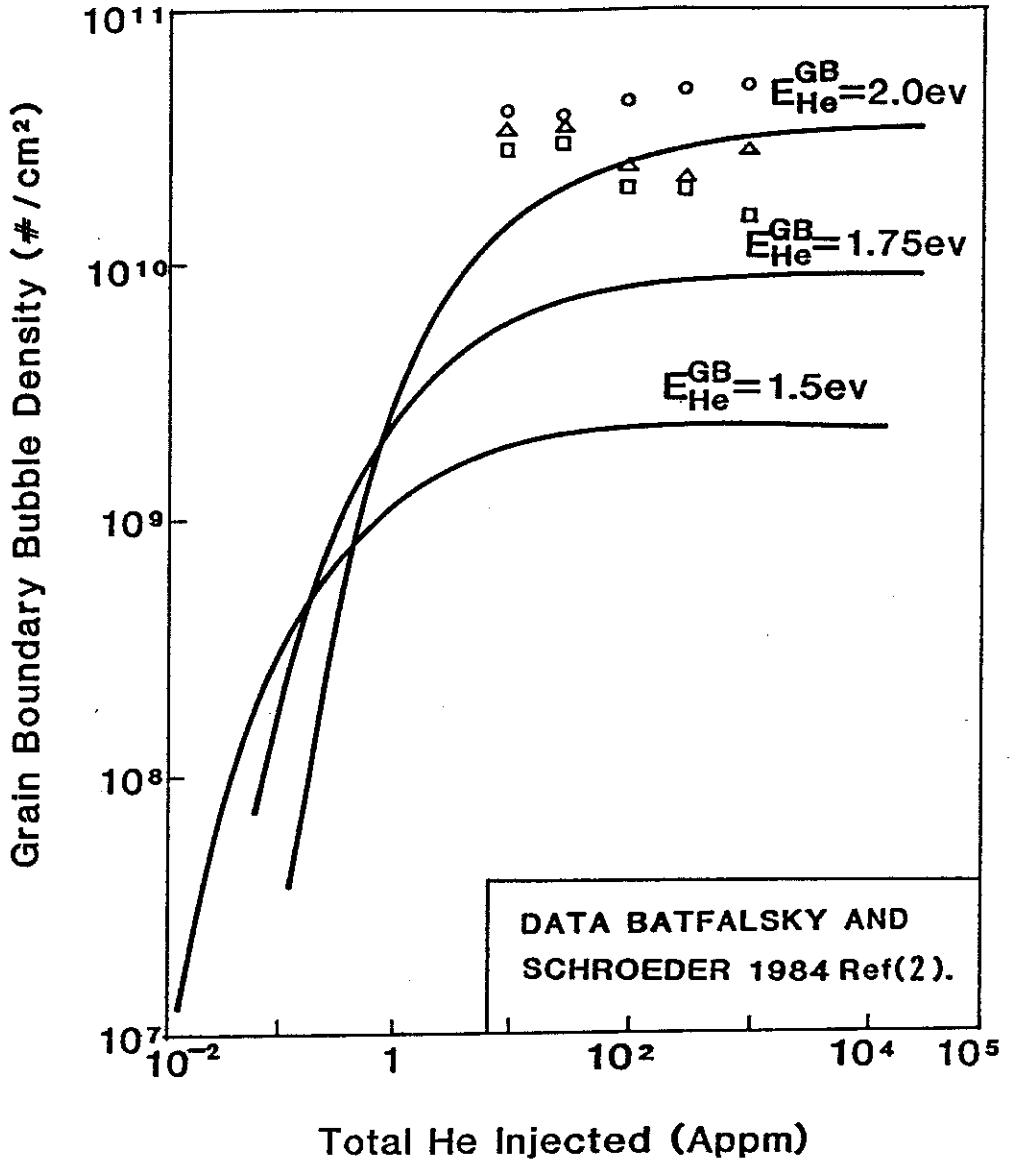

Figure 4. Grain boundary bubble density as a function of the helium concentration. (Data from ref.[2])

amount of helium arriving at the grain boundary balances that which leaves it by re-solution.

3. CONCLUSIONS

1. Rate theory can be successfully used to study the clustering behavior of helium at grain boundaries.

2. The clustering behavior of helium at grain boundaries is insensitive to variations in the bias factor which influences the matrix clustering system.

3. The effective migration energy of helium at grain boundaries is approximately that of self diffusion.

4. The model confirms experimental observations that the bubble density, due to irradiation, forms orders of magnitude larger than the cavity population observed in creep experiments in the absence of irradiation.

5. Higher helium implantation rates result in a higher grain boundary bubble density, even though the total amount of helium injected remains constant.

6. Even if the total injected helium is as little as one (appm), it can result in a grain boundary bubble density as high as 10^9 cm^{-2} and thus drastically deteriorates the grain boundary resistance to fracture.

7. The grain boundary bubble density reaches a steady state at large amounts of injected helium ($\sim$ 10 appm).

NOMENCLATURE

Symbol	Description	Units
C_g^{gb}	Single helium atom concentration (at grain boundary)	(at/at)
C_{2g}^{gb}	Di-helium complex concentration	(at/at)
C_b^{gb}	Grain boundary bubble concentration	(at/at)
m_b^{gb}	Average number of gas atoms in a bubble	
Q_{g_b}	Flux of helium to the grain boundary	(at/at/sec)
b	Re-solution parameter	(~ 1)
E_{He}^{GB}	Effective helium migration energy	(eV)
η	Frequency factor	(1/sec)
δ	Re-solution frequency	(1/sec)
T	Temperature	(°K)
k	Boltzmann's constant	(eV/°K)
t	Time	(sec)
ε_{GB}	Diffusional-control combinatorial factor for bubbles	(1/sec)
$R_{g,g}^{gb}$	Reaction rate between single helium complexes	(1/sec)
$R_{g,2g}^{gb}$	Reaction rate between single and di-helium clusters	(1/sec)
$R_{g,b}^{gb}$	Reaction rate between single helium and bubbles	(1/sec)
ν_{g_b}	Helium vibration frequency	(1/sec)

REFERENCES

[1] A. F. Rowcliffe, G. J. C. Carpenter, H. F. Merrick and R. B. Nicholson, "An Electron Microscope Investigation of the High Temperature Embrittlement of Irradiated Stainless Steels," Effects of Radiation on Structural Metals, ASTM-STP-426, (Am. Soc. Testing Mater., 1967) pp. 161-199.

[2] P. Batfalsky and H. Schroeder, "Helium Bubble Microstructure in Stainless Steel Implanted Under Various Conditions," J. Nucl. Mater., 122&123 (1984) 1475.

[3] J. I. Bennetch and W. A. Jesser, "Microstructural Aspects of He Embrittlement in Type 316 Stainless Steel," J. Nucl. Mater., 103&104 (1981) 809.

[4] P. L. Lane, J. H. Evans and P. J. Goodhew, "Helium Bubble Formation During Dual Ion Beam Irradiation," J. Nucl. Mater., 120 (1984) 342.

[5] P. L. Lane and P. J. Goodhew, "Helium Bubble Nucleation at Grain Boundaries," Philos. Mag. A, 48 (1983) 965.

[6] H. Trinkaus, "On the Modeling of the High-Temperature Embrittlement of Metals Containing Helium," J. Nucl. Mater., 118 (1983) 39.

[7] N. M. Ghoniem, S. Sharafat, J. M. Williams and L. K. Mansur, "Theory of Helium Transport and Clustering in Materials Under Irradiation," J. Nucl. Mater., 117 (1983) 96.

[8] T. M. Williams and K. Gott, "The Effects of Initial Boron Content and Distribution on Helium Bubble Population and the Stress-Rupture Properties Exhibited by Irradiated Type 316 Austenitic Steel," J. Nucl. Mater., 95 (1980) 265.

[9] D. Kramer, H. R. Brager, C. G. Rhodes and A. G. Pard, "Helium Embrittlement in Type 304 Stainless Steel," J. Nucl. Mater., 25 (1968) 121.

[10] G. J. C. Carpenter and R. B. Nicholson, "High Temperature Embrittlement of Metals by Rare Gas Bubbles," in Proc. Conf. on Radiation Damage in Reactor Materials, Vol. II, International Atomic Energy Agency, Vienna, June 1969, pp. 383-400.

[11] A. F. Smith and G. B. Gibbs, "Volume and Grain-Boundary Diffusion of Iron in 20 Cr/25 Ni/Nb Stainless Steel," Met. Sci. J., 2 (1968) 47.

CHAPTER VI

RESULTS ON THE EFFECTS OF HELIUM ON CREEP RUPTURE

Numerous models have been proposed (e.g., [1-11]) to explain the observed time-to-rupture in creep experiments. All existing cavity growth models assume that cavity growth, rather than the other stages such as nucleation and interlinkage, is the dominant stage in determining creep fracture life. In the present model, the two stages of helium-driven cavity nucleation and cavity growth are combined together in our model.

Grain boundary cavity growth is a process which involves the presence of vacancies in ample quantities. Many cavity growth models [1-4,7] always assumed that boundaries can supply such vacancies without limitation. Such models actually ignored the physical nature of grain boundaries in their ability to supply vacancies. In this chapter, a review is given of the basic concepts behind grain boundaries as vacancy sources. This is followed by a review of the basic growth models. In Section 4, calculations and results of the combined nucleation/growth model developed by us are given. This is accomplished by comparing the theoretical model to experimental data on creep rupture.

1. GRAIN BOUNDARIES AS A VACANCY SOURCE

1.1. Experimental Evidence

Chronologically, the first method for demonstrating that grain boundaries act as a vacancy source was devised by Barnes et al. [12,13]. Helium atoms were injected into metals by bombardment with

alpha particles. On subsequent heating helium atoms have a tendency to precipitate within the metal in the form of large gas bubbles by capturing vacancies. This blanket of bubbles forms in the vicinity of high angle grain boundaries which act as a vacancy source. The specimens which were not heated showed no bubbles.

Similar experimental results obtained in studies of precipitation processes (of both point defect precipitation and solute precipitates) at grain boundaries supply evidence for grain boundaries as point defect sinks/sources. When a pure metal is quenched from high temperatures and/or irradiated with high energy particles, a supersaturation of point defects may be obtained. These point defects may condense in the form of dislocation loops and voids which may be observed by transmission electron microscopy. The condensation process is heterogeneous in polycrystalline specimens in the sense that denuded zones exist near grain boundaries [14,15]. As the condensation occurs by nucleation and growth processes, a certain supersaturation of point defects is required. Hence the observation of denuded zones suggests a lower point defect supersaturation in the denuded zones in the vicinity of grain boundaries than in the perfect lattice. This is attributed to the annihilation of point defects at the boundaries.

1.2. Diffusional Creep

Indirect evidence for the creation/annihilation of point defects at grain boundaries comes from observation on diffusional creep (high temperature creep, Nabarro-Herring creep). Diffusional creep of polycrystalline materials is known to occur by the stress-motivated diffusion of vacancies through the lattice and along grain boundaries.

Hence, diffusional creep requires the emission and absorption of vacancies from grain boundaries to occur. In the case of pure metals, the theory of Nabarro-Herring creep [16,17] (excellently supported by the experiments [18]) indicates that most grain boundaries in polycrystalline specimens act as perfect vacancy sources and sinks even at vacancy chemical potentials as low as 10^{-5} eV. However, detailed measurements [19,20] have shown the existence of threshold effects for the creation/annihilation of vacancies at specific grain boundaries. In order to correlate the existence of threshold stresses and the source/sink efficiency of a grain boundary with the intrinsic boundary structure, the vacancy source efficiency of different types of boundaries has been measured by means of diffusional creep experiments [21], using copper specimens with a bamboo-type structure. It was found that the boundaries of low efficiency are the low energy grain boundaries whereas high energy boundaries readily emit vacancies. The different behavior of both types of boundaries may be understood in terms of the boundary structure. The emission of a vacancy from a boundary requires a local rearrangement of the atoms in the boundary. In the case of a low energy boundary, e.g., a coherent twin boundary, such a rearrangement requires a relatively large energy because it results in a local distortion of the low energy boundary structure. In the case of high energy boundaries, a distortion of the boundary structure is not required. Hence high energy grain boundaries may be expected to act as more efficient sources or sinks for vacancies than low energy boundaries. The conclusion is that non-special boundaries were found to act as ideal sources whereas special boundaries, corresponding to Σ = 3, 5, 7, 9, 11, and 15

misorientations (Σ characterizes the inverse coincidence site density), did not operate at all at chemical potentials smaller than 2×10^{-5} eV.

1.3. The Role of Grain Boundary Dislocations in Point Defect Absorption/Emission

Any high angle grain boundary can be represented as an array of closely spaced lattice dislocations [primary grain boundary dislocations (PGBDs)]. However, if non-uniformities are periodically present in the array of PGBDs, they may always be described as secondary grain boundary dislocations (SGBDs). The geometry and Burgers vectors of SGBDs have been discussed in detail elsewhere [22].

All dislocation models of high angle grain boundaries as point defect sources/sinks (e.g., [23-25]) are based on the assumption that the point defects are created/annihilated by the climb of dislocations in the boundary. The basic feature of the source/sink models based on the climb of boundary dislocations may be understood by considering the two limiting cases: (1) boundaries containing only PGBD (exact coincidence boundaries) and (2) boundaries containing both PGBD and SGBD (off-coincidence boundaries). Boundaries of the exact coincidence type, Fig. 1(a), may operate as source/sink by the climb of a segement of a PGBD [26] as illustrated in Fig. 1(b). Such a process introduces a non-uniformity into the PGBD array which may further grow into a loop by the addition of new point defects. In order to overcome the nucleation barrier of the loop, an appreciable point defect chemical potential is required which is experimentally evidenced by a threshold stress or threshold supersaturation of point defects [19,20]. In this case, the boundary efficiency as a source/sink depends on the density of climbed

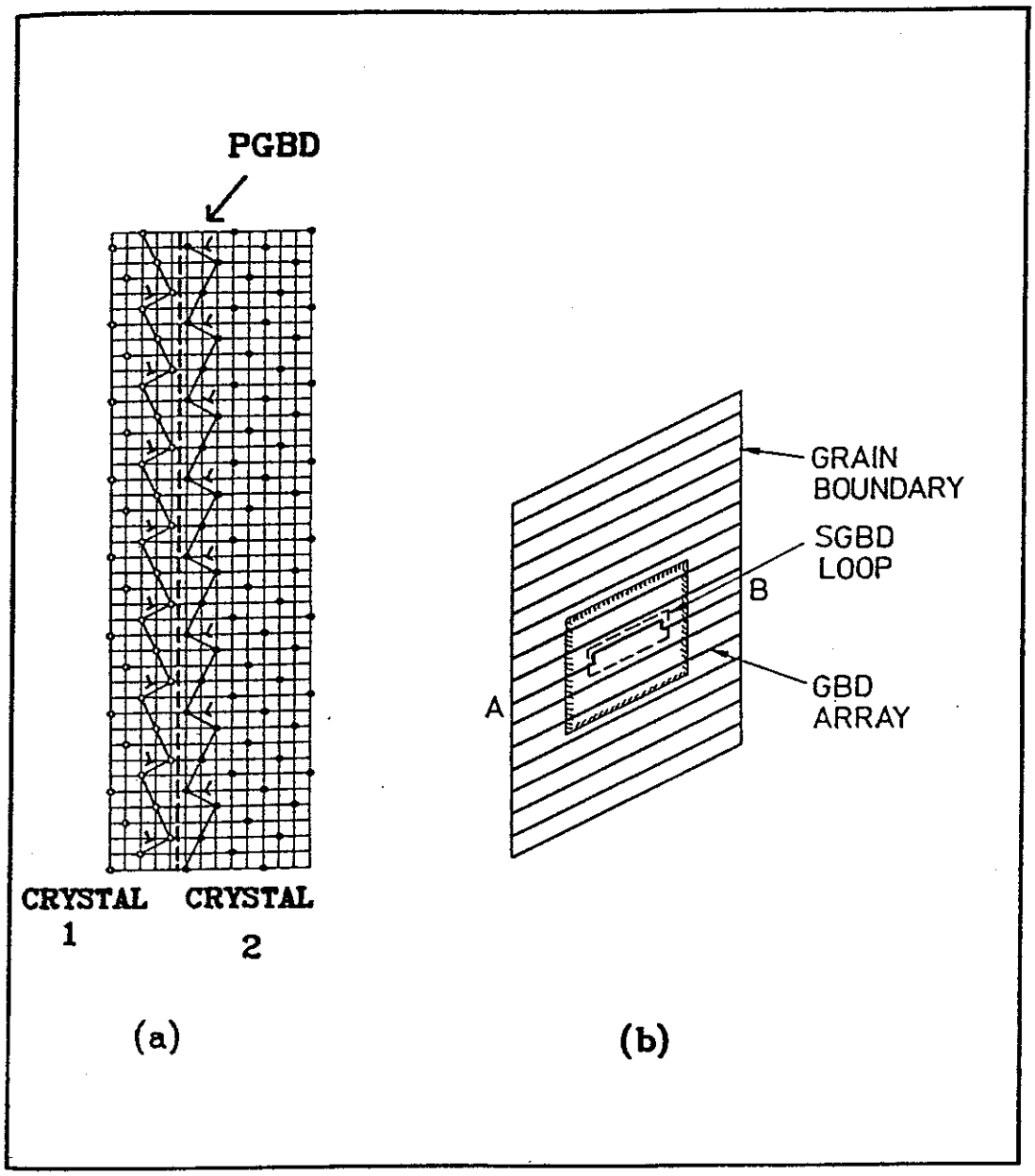

Figure 1. (a) A schematic illustration of a typical grain boundary. (b) Dislocation arrangement during point defect absorption/ creation. The dislocation AB has absorbed point defects resulting in a jog. This jog can be described as a loop of a secondary grain boundary dislocation (broken line).

segments per unit area of the boundary. Boundaries of the exact coincidence type may contain SGBDs which are not part of the equilibrium structure, e.g., lattice dislocations which have impinged on the boundary. Such (extrinsic) SGBDs can climb in the boundary and wrap themselves into dislocation spirals [24,27]. The presence of such SGBD loops inhibits the nucleation of SGBD and substantially reduces the chemical potential of the point defects to drive the source/sink action. However, there may still be a threshold effect when the critical radius of curvature of the spiral approaches the grain size.

Off-coincidence boundaries can act as a source/sink by the climb of a SGBD segment similarly to the process shown in Figs. 1(b) and 2. Boundaries of this type may act as sources/sinks basically analogous to the exact-coincidence boundaries.

The description of the creation/annihilation of point defects given in terms of PGBDs and SGBDs may represent an over simplification of reality. The model seems applicable to boundaries where well-defined SGBDs are known to exist. However the total number of such boundaries revealed is still small [28], and it may not be evident that such dislocations are responsible for the creation/annihilation of point defects.

1.4. Control of Vacancy Creation/Annihilation in Boundaries by Lattice Dislocations

According to the formal theory of crystalline interfaces, which has been developed by Bollmann [29], it is always geometrically possible for a lattice dislocation that impinges on a grain boundary to enter the grain boundary. Such dislocations may dissociate into two or more grain boundary dislocations while conserving the total Burgers vector [30-33].

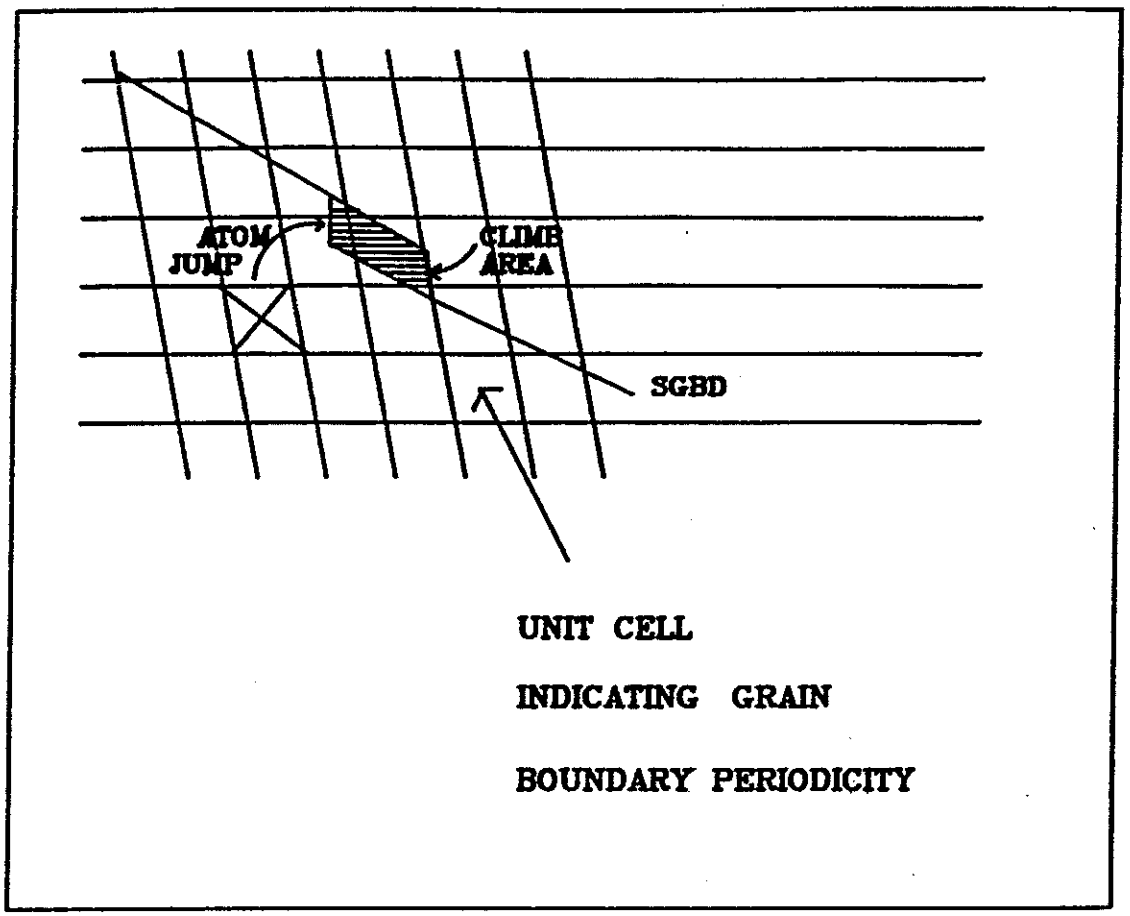

Figure 2. Diagram illustrating the climb of a SGBD by atom absorption.

It was asserted by Dingley et al. [32] that grain boundaries do not offer substantial resistance to oppose the entry of a crystal dislocation into them. However, a second dislocation approaching the boundary on the same slip plane as the first will be opposed, to a greater or lesser extent, by the first dislocatons trapped there. The magnitude of the repulsive force will depend on the mobility of the first dislocation in the boundary, since it is possible that such dislocations become trapped at grain boundary ledges, etc., which will result in a large repulsive force preventing any additional dislocations from entering the boundary in nearby slip planes. However, trapped lattice dislocations can leave the boundary once a favorable exit slip plane is encountered. This process is illustrated schematically in Fig. 3. The model illustrated in Fig. 3 is a very general representation which includes the possibilities that lattice dislocations may enter or leave the boundary and climb in both the lattice and the boundary, and that they may actually control vacancy creation and annihilation in the boundaries. The mode of vacancy creation is essentially the climb process of these dislocations in the boundary plane. This model has already been quantified by Beere [9] and will be discussed in detail later in this chapter.

2. THEORETICAL TREATMENT OF CREEP CAVITY GROWTH

Many cavity growth mechanisms have been proposed to explain the observed time-to-rupture during creep rupture experiments. Some of these mechanisms compete with each other so that the fastest mechanism determines the growth rate of grain boundary cavities. In other cases, the slowest of a group of mechanisms control the overall rate of cavity

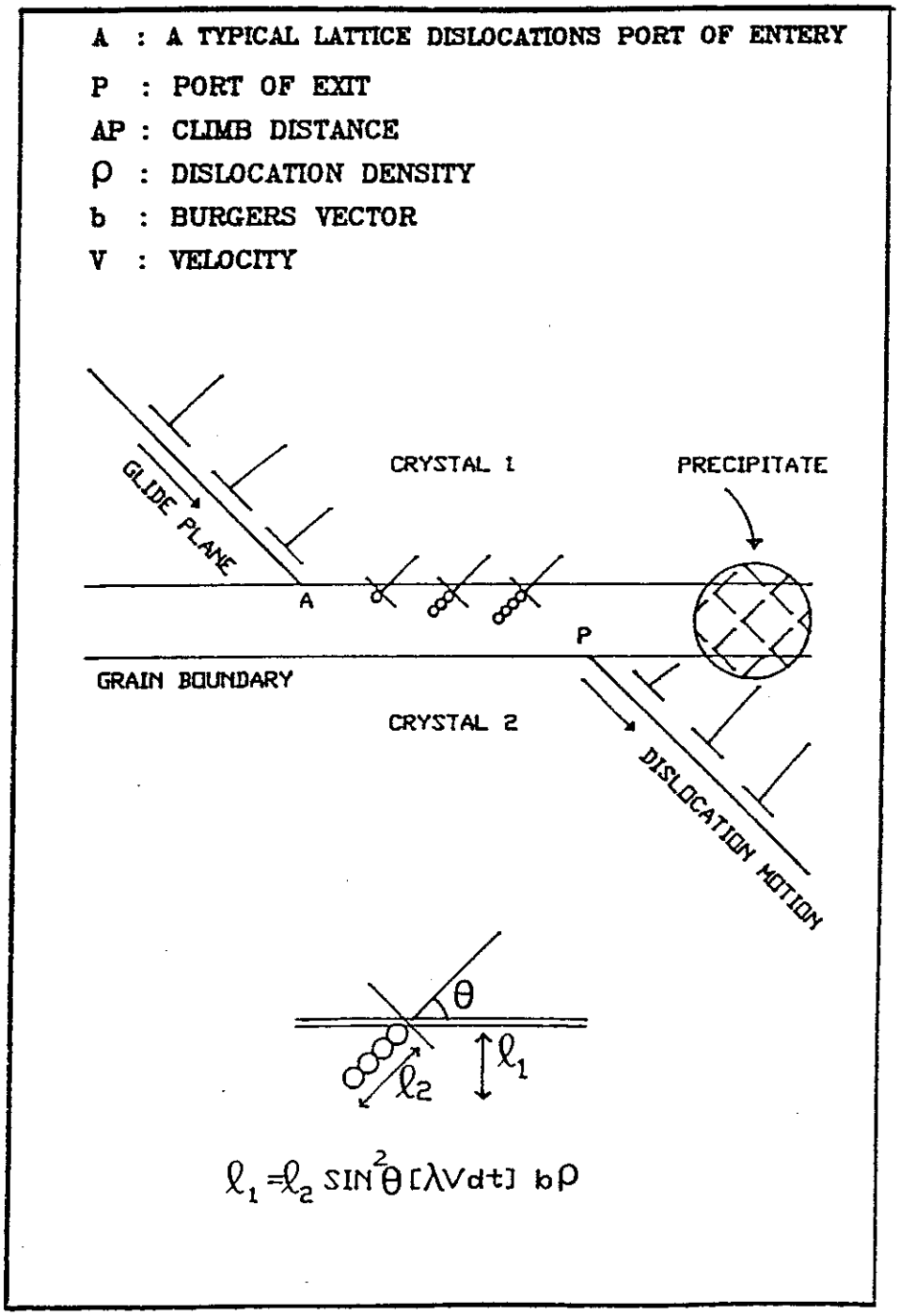

Figure 3. A schematic illustration of lattice dislocations interaction with grain boundaries.

growth. Beere [34] has suggested that the actual growth rate can be computed by considering that various growth mechanisms share mixed sequential/independent relationships to each other. For instance, grain boundary diffusion can act independently of the plastic cavity growth mechanism. The relationships between the mechanisms are illustrated in Fig. 4. Independent mechanisms are represented by parallel circuits and sequential mechanisms by series circuits. In the approach of Beere [34] the reciprocal growth rate of a particular mechanism is treated as an impedance, and the impedance of a given series circuit is obtained by summing the impedances of the mechanisms in the circuit. The overall growth rate is then obtained by summing the reciprocal impedances of the circuits in parallel.

Adopting the approach outlined above, and denoting grain boundary diffusion by BD, dislocation creep growth by DC, and source control of vacancies by SC and also realizing that surface diffusion is rapid at high temperature and not rate controlling, the overall volumetric cavity growth rate $\dot{V}$ is then given by:

$$\dot{V} = \dot{V}_{DC} + \frac{\dot{V}_{BD}\dot{V}_{SC}}{\dot{V}_{BD} + \dot{V}_{SC}} \quad , \tag{1}$$

where $\dot{V}_{DC}$, $\dot{V}_{BD}$, and $\dot{V}_{SC}$ are the volumetric cavity growth rates from the three mechanisms individually.

Before performing the computation indicated by Eq. (1), the details of the various mechanisms will be presented which will also include our modification to account for the lenticular cavity shape.

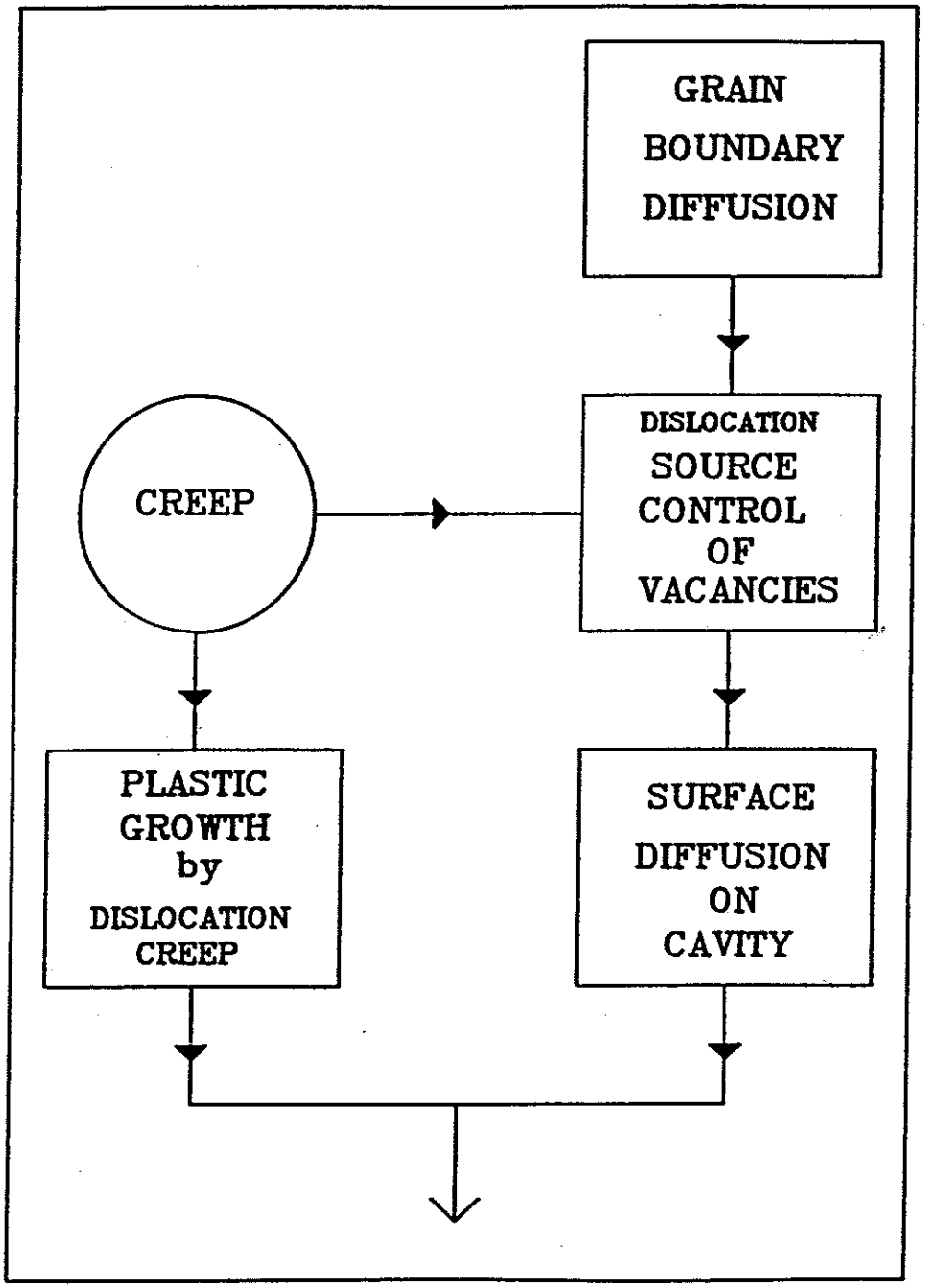

Figure 4. Diagram to illustrate the competing and interacting cavity growth mechanisms.

2.1. Grain Boundary Diffusion Growth Model

It is now more than a quarter of a century since Hull and Rimmer [1] published their classic paper on the stress-induced growth of grain boundary voids. Their work was based on the Balluffi and Seigle [35] findings that vacancies could be produced at grain boundaries in sufficient numbers to allow cavity growth. The cavities were placed on an idealized square grid in the grain boundary plane. However, the combination of circular and square geometries in the Hull-and-Rimmer treatment led to an inconvenient form for the growth rate. Since then, many authors have recalculated the growth rate assuming circular geometry in the boundary plane for both the cavity and the collection area of vacancies [2-4,7]. The quantitative model of Speight and Harris [7] of the growth of grain boundary voids under stress follows.

Speight and Harris [7] assume that N_{gb} voids of radius R_o have been nucleated per unit area of grain boundary transverse to the tensile stress. The void population is divided into a series of identical unit cells, each with a central void surrounded by the associated grain boundary area. Figure 5 shows a typical unit cell with the void at some stage of the growth process and the radius has increased to R. The extent of grain boundary from which the void draws its vacancies is determined by

$$L = 1/\sqrt{\pi N_{gb}} \quad , \tag{2}$$

where N_{gb} is the areal void density at grain boundaries.

It is also assumed that vacancies are created uniformly at a rate of S per atom site per sec in the annular disk $R < r < L$ surrounding each void. The vacancies created in the annulus diffuse to the void

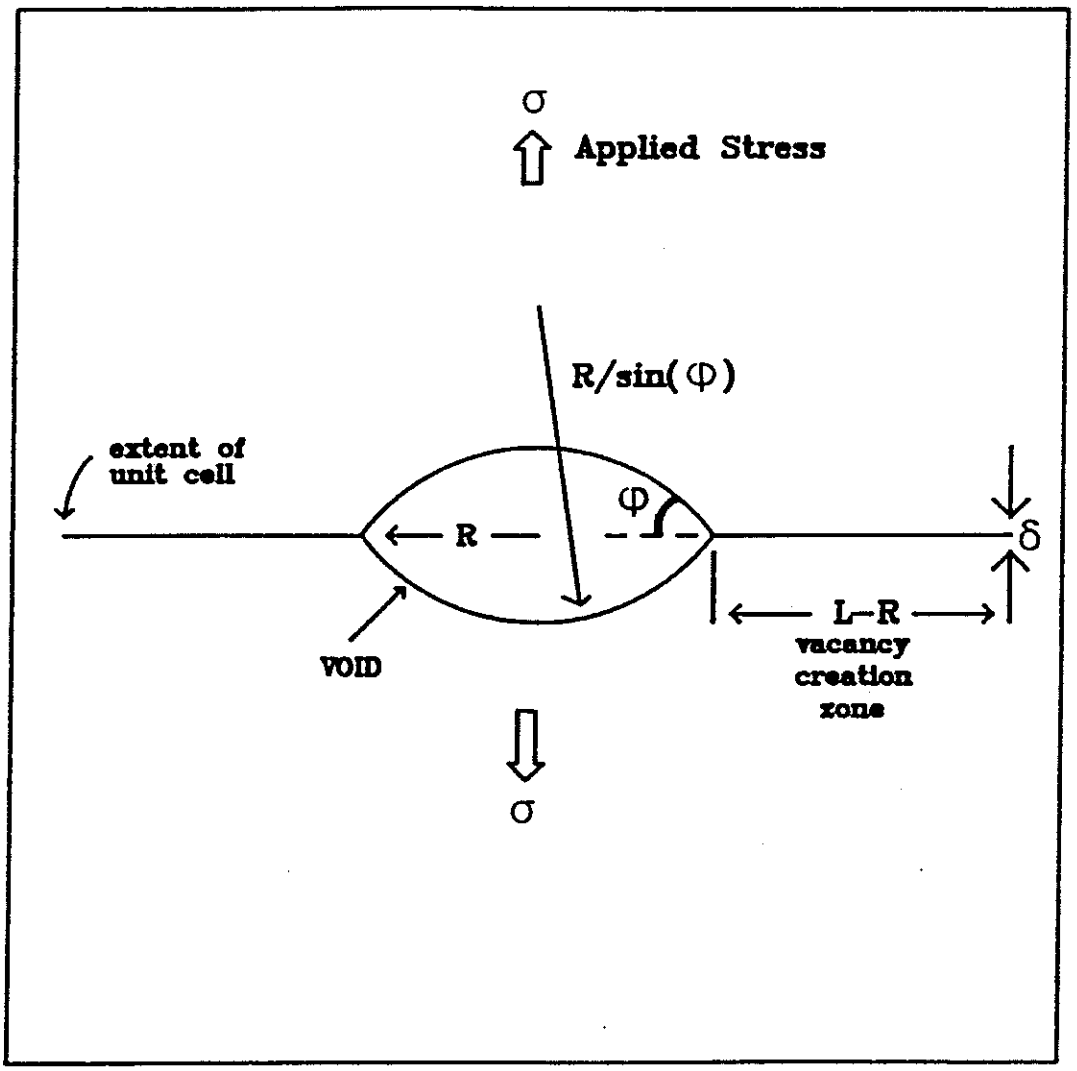

Figure 5. A model for the growth of voids on grain boundaries during creep by diffusion of vacancies in the grain boundary.

causing them to grow. The vacancy-diffusion equation in the annulus region surrounding each void is

$$D_{vgb} \frac{1}{r} \frac{d}{dr}\left(r \frac{dC_v}{dr}\right) + S = 0 \quad , \tag{3}$$

where D_{vgb} is the diffusion coefficient of vacancies in the grain boundary, C_v is the volumetric concentration of vacancies, and S is the vacancy creation rate. The appropriate boundary conditions

$$C_v(R) = C_v^{eq} \exp\left[\left(P - \frac{2\gamma \sin\phi}{R}\right) \Omega/kT\right] \quad , \tag{3a}$$

$$C_v(L) = C_v^{eq} \exp\left(\frac{\sigma\Omega}{kT}\right) \quad , \tag{3b}$$

where C_v^{eq} is the thermal equilibrium vacancy concentration. An additional boundary condition can be obtained by realizing that an individual void is supplied with vacancies from its associated grain boundary cell; this demands that

$$\left[\frac{dC_v}{dr}\right]_{r=L} = 0 \quad . \tag{3c}$$

The solution of Eq. (3), utilizing the boundary conditions given by Eqs. (3a) - (3c), is

$$C_v(r) = C_v^{eq} \exp\left(\frac{2\gamma \sin\phi}{R} \frac{\Omega}{kT}\right)$$

$$+ \frac{SL^2}{2D_{vgb}} \left[\ln\left(\frac{r}{L}\right) - \left(\frac{1}{2} \frac{r^2 - R^2}{L^2}\right)\right] \quad . \tag{4}$$

The vacancy creation rate S can be determined by applying Eq. (3b). Now, the time rate of change of the volume of the void can be determined by applying the conservation equation

$$\frac{dV}{dt} = (2\pi R\delta)D_{vgb}\left(\frac{dC_v}{dr}\right)_R \Omega \quad . \tag{5}$$

The cavity volume is defined as a function of R and ϕ by [36]

$$V = R^3 F_v/[\sin(\phi)]^3 \quad , \tag{6}$$

where F_v is given by

$$F_v = \frac{2\pi}{3}(2 - 3\cos\phi + \cos^3\phi) \quad , \tag{7}$$

as derived earlier in Chapter III. Combining Eqs. (5) and (6) yields

$$\frac{dR}{dt} = \frac{[\sin(\phi)]^3}{3 F_v R} 2\pi\delta D_{vgb} \left(\frac{dC_v}{dr}\right) \Omega \quad . \tag{8}$$

The gradient at the void surface is obtained using Eq. (4); and S is eliminated by the use of Eq. (3c). The product $D_{vgb} C_v^{eq} \Omega$ is identified with the grain boundary self-diffusion coefficient. Because of the arguments of the exponentials in Eqs. (3a) and (3b) are small, e^x is approximated by 1 + x. Equation (8) then yields

$$\frac{dR}{dt} = \frac{4\pi}{3} \frac{[\sin(\phi)]^3}{F_v} \frac{\delta D_{gb} \Omega}{L^2 kT} \left(P + \sigma - \frac{2\gamma \sin\phi}{R}\right)$$

$$\times \left[\frac{(L/R)^2 - 1}{2\ell n(L/R) - 1 + (R/L)^2}\right] \quad , \tag{9}$$

where D_{gb} is the grain boundary self-diffusion coefficient.

2.2. Model for Dislocation Source Control of Vacancies

The source of vacancies at grain boundaries has been discussed in detail in the previous section. The model depicted by Fig. 3 is widely accepted [9,32-33,37]. The principle of the model is that cavitation may be controlled by dislocation creep. Dislocations moving in the matrix were considered to enter the boundary and migrate in the boundary by a combination of climb and glide. Vacancies are created during climb and migrate to the cavities. If grain boundary diffusion is sufficiently rapid, cavity growth can be controlled by the supply of dislocations. Beere [9] has quantified this model by assuming dislocations to climb on the average a distance equal to the inter-precipitate spacing before re-entering the lattice. Beere's model [9] is equally applicable to the situation shown in Fig. 3. In the following, we discuss Beere's model for dislocation source control, and apply it as a part of our comprehensive creep rupture analysis.

Consider a block of material containing dislocations having their glide plane parallel to the x axis as shown in Fig. 6. During creep dislocation, glide is responsible for the bulk of the plastic deformation. If the dislocation density in the square block $x'y'$ is ρ, each

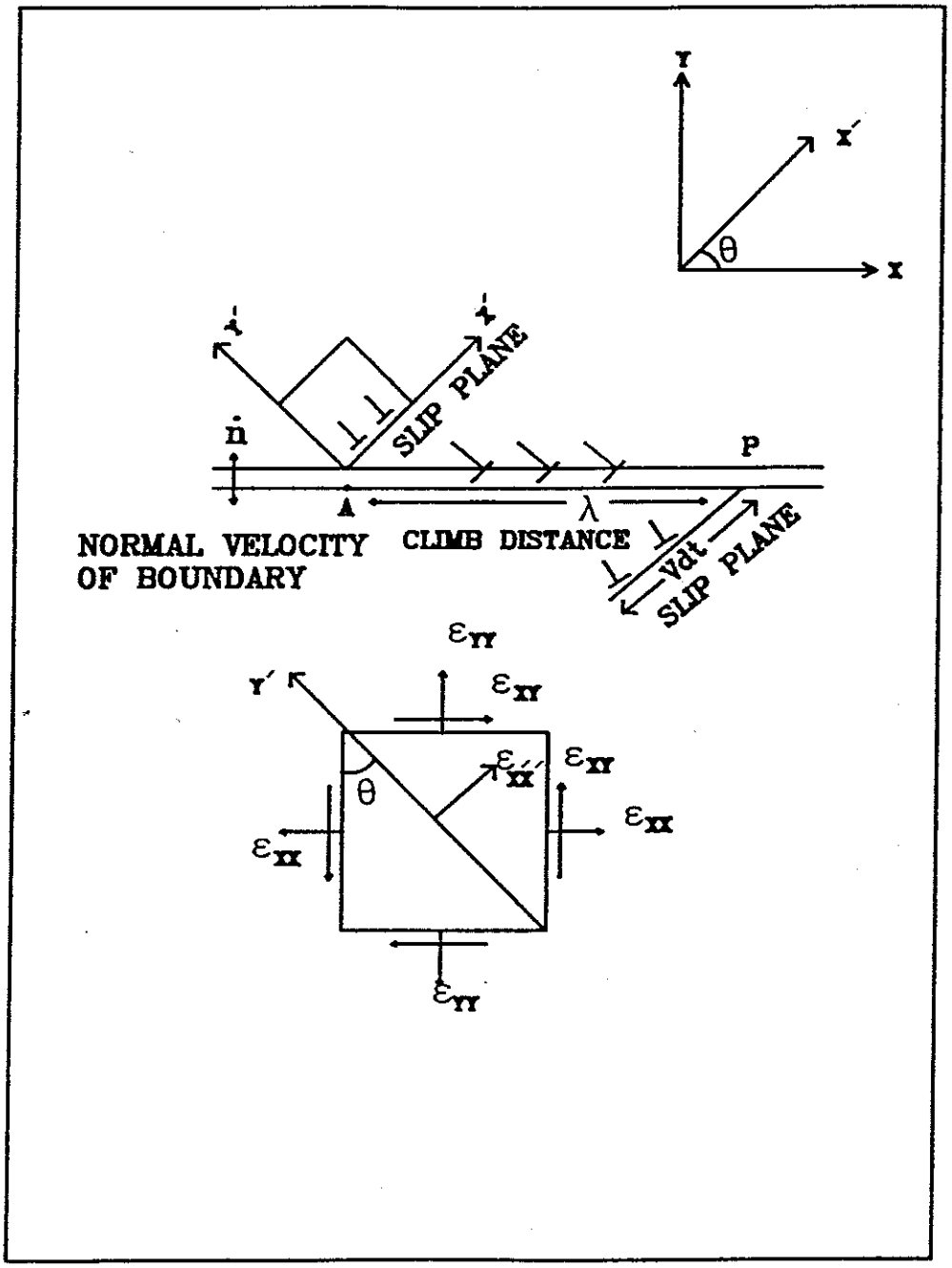

Figure 6. Dislocations in the matrix enter the boundary during the course of creep. In the boundary the dislocations climb a distanse λ before being re-emitted into the matrix (After Beere [24]).

with Burger's vector b, moving at an average velocity V, the strain rate will be given by [38]

$$\dot{\varepsilon}_{x'y'} = \rho V b \quad . \tag{10}$$

If the block is oriented at an angle θ to the specimen axes, the specimen strains are given by

$$\varepsilon_{xx} = \varepsilon_{x'y'} \sin\theta \cos\theta \quad , \tag{11a}$$

$$\varepsilon_{yy} = -\varepsilon_{x'y'} \sin\theta \cos\theta \quad , \tag{11b}$$

$$\varepsilon_{xy} = \varepsilon_{x'y'}(\cos^2\theta - \sin^2\theta) \quad . \tag{11c}$$

The material will have more than one operative glide plane. The model essentially applies for a typical glide system in which one or two families of slip planes dominate. The system shown in Figs. 3 and 6 represent a typical glide system composed of two independent glide systems.

Dislocations entering the boundary climb a distance λ before being re-emitted. The climb motion of these dislocations results in a normal motion of the boundary by interstitial absorption during climb. Examining a typical point at the grain boundary, say point p in time dt, half the dislocations in the parallelogram of sides λ and Vdt (Fig. 6) will pass through it. The other half share the same glide plane but move in the opposite direction. Since an equal number enter the boundary from above and the absorption of interstitials occurs along the dislocation axis, the normal motion of the boundary at the point p is

$$\dot{n}(\theta) = \rho|V|b\lambda \sin^2\theta \quad , \tag{12}$$

as shown in Fig. 3.

The positive value of V is taken to account correctly for the contribution from different climb directions in the boundary. The resolved shear stress on the dislocations is given by

$$\sigma_{x'y'} = (\sigma_{yy} - \sigma_{xx})\sin\theta\cos\theta + \sigma_{xy}(\cos^2\theta - \sin^2\theta) \quad . \tag{13}$$

For uniaxial deformation, Eq. (13) reduces to

$$\sigma_{yy} = \sigma_{applied} \quad , \tag{14a}$$

$$\sigma_{xx} = \sigma_{xy} = 0 \quad , \tag{14b}$$

$$\sigma_{x'y'} = \sigma_{yy} \sin\theta \sin\theta \quad . \tag{14c}$$

In this case V is positive in the interval $0 < \theta < \pi/2$ and negative in the interval $\pi/2 < \theta < \pi$. Equations (11) and (12) may be simplified by taking average values for the angles of the glide planes. In the case of uniaxial strain, the velocity V changes sign as discussed above and hence

$$\dot{\epsilon}_{yy} = \frac{2}{\pi}\int_0^{\pi/2} \rho b V \sin\theta\cos\theta \, d\theta \quad , \tag{15}$$

$$\dot{n} = \frac{2}{\pi}\int_0^{\pi/2} \rho b V \lambda \sin^2\theta \, d\theta \quad . \tag{16}$$

Performing the integrations we can end up with

$$\dot{\varepsilon}_{yy} = \frac{2}{\pi} \rho b V \quad , \tag{17}$$

$$\dot{n} = \frac{1}{2} \rho b V \lambda \quad . \tag{18}$$

Putting $\dot{\varepsilon}_{yy} = \dot{\varepsilon}_{\ell}$, the strain rate immediately above the boundary, the normal motion of the boundary is given by

$$\dot{n} = \frac{\pi}{4} \dot{\varepsilon}_{\ell} \lambda \quad . \tag{19}$$

This normal motion of the boundary as a result of dislocation climb is also responsible for the creation of vacancies. It has been assumed [9] that matrix dislocations entering the boundaryy climb on average a distance equal to the precipitate half spacing before being re-emitted. We will check the validity of this assumption by comparing the model with the experiments.

The rate of increase in volume of cavities $\dot{V}_{SC}$ is given by the change in volume associated with an area of the boundary πL^2, where L is the cavity half spacing

$$\dot{V}_{SC} = \pi L^2 \dot{n} \quad , \tag{20a}$$

$$\dot{V}_{SC} = \frac{\pi^2}{4} L^2 \lambda \dot{\varepsilon}_{\ell} \quad . \tag{20b}$$

The creep rate required in Eq. (20b) $\dot{\varepsilon}_{\ell}$, is the local to the boundary. It will differ from the far field creep rate $\dot{\varepsilon}$ due to the effect of porosity (e.g., [10]). If we define n as the creep exponent for power law creep, we have

$$\dot{V}_{SC} = \frac{\pi^2}{4} L^2 \lambda \dot{\varepsilon} \left(\frac{1 - 2\gamma \sin\phi/R\sigma + P/\sigma}{1 - R^2/L^2} \right)^n \quad , \tag{21a}$$

where P is the pressure of any gas in the bubble. The cavity growth rate is therefore given by:

$$\frac{dR}{dt} = \frac{\sin^3\phi}{3R^2 F_V} \frac{\pi^2}{4} L^2 \lambda \dot{\varepsilon} \left[\frac{1 - (2\gamma \sin\phi/R\sigma) + (P/\sigma)}{1 - R^2/L^2} \right]^n \quad . \tag{21b}$$

2.3. Plastic Growth by Dislocation Creep

At sufficiently high values of the applied tensile stress, it is possible that part of the cavity growth can be accommodated by plastic deformation of the grains. The problem of cavity growth by combined vacancy diffusion along the grain boundary and plastic deformation has already been treated by Beere and Speight [4], but the solution is rather cumbersome. In the extreme case of no vacancy creation and cavity growth occurs solely by plastic deformation, the cavity growth rate has been given by Hancock [39] as

$$\frac{dR}{dt} = R\dot{\varepsilon} \left[\frac{1 - (2\gamma \sin\phi/R\sigma) + (P/\sigma)}{1 - R^2/L^2} \right]^n \quad , \tag{22a}$$

and hence

$$\frac{dV_{DC}}{dt} = \frac{3R^3 F_v}{\sin^3\phi} \dot{\varepsilon} \left[\frac{1 - (2\gamma \sin\phi/R\sigma) + (P/\sigma)}{1 - (R^2/L^2)} \right]^n \quad . \tag{22b}$$

Equation (1) is solved numerically using the growth equations, i.e., Eqs. (9), (21b) and (22a) to determine the time-to-rupture which can be

defined as the time taken for the cavity to grow to a particular value of F = R/L where L is the cavity half spacing. A value of F ~ 0.6 has been adopted in the literature [40-42] as the point as the point at which the boundary will not be able to support any additional load and failure occurs. We will investigate the validity of this assumption in our combined model in Section 4.

3. PROPOSED COMPREHENSIVE MODEL FOR THE HIGH TEMPERATURE FRACTURE OF FERRITIC/MARTENSITIC AND AUSTENITIC STEELS

As was discussed in Chapter II, ferritic/martensitic steels exhibit a lower susceptibility to high temperature helium embrittlement over austenitic alloys (e.g., [43]). The only attempt to explain this phenomenon is recently due to Wassilew [44]. Experimental evidence [44] has shown that grain boundary cavity growth rate is much smaller in martensitics than austenitics; hence cavities are significantly smaller in martensitic steels. This results in a significant amount of ductile deformation in martensitics before fracture. However, in austenitics, cavities grow relatively faster and fracture appears to be brittle in nature.

At this stage, it seems appropriate to present Wassilew's explanation [44] of the fracture behavior of martensitic and austenitic steels.

3.1. Wassilew's Explanation [44]

Experimental observations of austenitics have shown that junctions of grain boundaries and coherent twin boundaries are preferred sites of the initial cavity nucleation and growth. With time, cavity nucleation and subsequent growth spread from these junctions along grain boundaries

perpendicular to the applied stress axis. However, in martensitics, cavities remained uniformly small along the fracture zone.

Wassilew [44] examined the interaction of dislocations with twin planes and high angle grain boundaries. It is argued that dislocation motion across twin boundaries is not possible, as it would imply the destruction of the cubic close-packed structure along the slip plane. In the twin plane, many vacancies are formed through dislocation jogs. As dislocations move away from the jog at the coherent twin plane, the vacancies created are trapped in the twin plane because of the high binding energy of vacancies to twin planes. They migrate along the twin plane toward the high angle grain boundaries where they are absorbed by helium bubbles.

In martensitics, twinning doesn't take place and hence the suggested vacancy source is blocked and results in a slowed-down bubble growth rate.

3.2. Our Grain Boundary Cavitation Model for Martensitic and Austenitic Alloys

Although the principles of twin planes as vacancy sources seem reasonable, the number of twin planes available are not sufficient to result in a marked difference from martensitics. It seems that if Wassilew's proposed explanation is valid, it will only result in a few large cavities at twin plane junctions and the cavitated grain boundary area should not be affected significantly.

As was shown in Chapter III, grain boundary obstacles are preferential sites for cavity nucleation. The junctions of twin planes and grain boundaries are actually ideal nucleation sites since they can be

the source of high stress concentration. This can explain the observed cavities at these junctions. The rupture behavior discrepancy between martensitics and austenitics can be explained by examining the slip and slip systems of the two steels. The principal means by which plastic deformation occurs in crystalline solids is slip. Face-centered cubic (FCC) metals such as austenitics have 12 possible slip systems. However, body-centered cubic (BCC) metals such as martensitics have 48 possible slip systems [49]. In our model, we implement Beere's concept [6] which states that dislocations entering the boundary are actually the source of vacancies and the efficiency of the boundary is determined by the climb distance at the boundary of these dislocations. In addition, these dislocations leave the boundary once precipitates are encountered. We propose the following scenario for grain boundary cavitation.

1. The creep rate is dependent upon the number of dislocations which are able to glide when a specific stress system is applied. The larger number of slip planes in martensitics as compared to austenitics readily explains the higher creep rates and the higher plastic deformation observed at rupture in martensitics.

2. Dislocations entering the grain boundary will climb a shorter distance in irradiated martensitics as compared to irradiated austenitics. This can be rationalized by taking bubbles to act as obstacles to dislocations motion. Therefore, in martensitics, the large number of slip systems will cause

dislocations to exit the boundary readily, thus limiting the vacancy supply source needed for cavity growth. While in austenitics, although bubbles can act as obstacles to dislocation motion, the number of possible slip systems is significantly lower; hence dislocations remain in the boundary and climb until precipitates are encountered which are usually associated with slip planes [45] and can provide a suitable exit.

In conclusion, dislocations climb in the boundary a significantly larger distance in austenitics as compared to martensitics; thus they provide a larger supply of vacancies needed for growth.

4. NUMERICAL CALCULATIONS AND RESULTS

4.1. Assumptions, Method, and Input Parameters

1. Grain boundary precipitates are perfect sites for cavity nucleation and cavitation occurs readily, as compared to cavity growth, upon the application of creep stress at high temperatures. It was shown in Chapter III that stress-controlled cavity nucleation is quite fast.

2. The grain boundary bubble concentration, not necessarily associated with precipitates, is determined from the helium clustering model discussed in Chapters IV and V.

3. Grain boundary bubbles and precipitates can act as obstacles to the SGBD climb process. This limits the growth of bubbles since SGBDs are the primary source of vacancies.

4. As a result of irradiation (a secondary vacancy source), bubble nuclei are larger than the ones which can be swept by SGBDs during their climb process.

5. The growth behavior of grain boundary cavities and bubbles is determined by utilizing Eqs. (1), (9), (21a) and (22b).

6. The equations are integrated simultaneously using Gear's method [46].

7. The interbubble distance is determined from Eq. (14) in Chapter V.

8. The creep rates used in solving the growth equations, taken directly from rupture experiments, are given in Table 1.

9. The cavity radius at failure, as a fraction of cavity half-spacing is taken to be 0.6 [41,42]. The validity of this assumption will be checked later. The lenticular angle that the cavity makes with the boundary is taken to be 15 deg [36]. This is consistent with that used in the nucleation calculation in Chapter III. The surface energy is taken to be 1 J/m^2 and the vacancy migration energy is taken to be 1.4 eV, which is consistent with that used in Chapter IV.

TABLE 1. The experimental creep rates utilized[a] in the theoretical model. (The applied stress σ is in MPa.)

Stainless Steel Type	Temp (°K)	$\dot{\varepsilon}$ (1/sec)	Remarks
1.4914	873	$3.23 \times 10^{-34}\ \sigma^{11}$	Unirradiated [47]
1.4914	873	$2.31 \times 10^{-18}\ \sigma^{5}$	In-pile [48]
1.4914	873	$3.24 \times 10^{-33}\ \sigma^{11}$	Out of pile, 90 appm He [47]
1.4914	923	$7.4 \times 10^{-24}\ \sigma^{7}$	Out of pile, 90 appm He [47]
1.4914	923	$2.1 \times 10^{-16}\ \sigma^{4}$	Out of pile, 90 appm He [47]
1.4914	1023	$6.18 \times 10^{-13}\ \sigma^{4}$	Out of pile, 90 appm He [47]
1.4970	973	$2.65 \times 10^{-56}\ \sigma^{20}$	Unirradiated[b] [47]
1.4970	923	$8.6 \times 10^{-27}\ \sigma^{7}$	Out of pile, 90 appm He [47]
1.4970	973	$2.31 \times 10^{-14}\ \sigma^{2}$	Out of pile, 90 appm He[c] [47]
1.4970	973	$1.86 \times 10^{-54}\ \sigma^{20}$	Out of pile, 90 appm He[b] [47]
1.4970	973	$3.26 \times 10^{-14}\ \sigma^{2}$	Out of pile, 140 appm[c] [47]
1.4970	973	$4.81 \times 10^{-54}\ \sigma^{20}$	Out of pile, 140 appm[b] [47]
1.4962	973	$3.44 \times 10^{-14}\ \sigma^{2}$	Out of pile, 140 appm[c] [47]
1.4962	973	$8.6 \times 10^{-54}\ \sigma^{20}$	Out of pile, 140 appm[b] [47]

[a] The experimentally observed creep rates is used in the theoretical model for accuracy.

[b] $\sigma > 150$ MPa.

[c] $\sigma < 150$ MPa.

10. The numerical calculations are aimed at finding the rupture times at a given stress. Once theoretical rupture times are obtained, the data are fitted by linear regression methods. The correlation coefficient for linear regression analysis on a log-log scale has been close to unity.

11. For out-of-pile calculations, it is assumed here that during irradiation, the grain boundary vacancy flux is large enough to enable bubbles to grow to ~ 500 Å; hence they are at equilibrium. This is taken as the initial bubble radius. A lower stable initial bubble radius was found not to alter the results significantly.

12. The climb distance of dislocations in martensitics is limited by the interbubble half spacing, while in austenitics it is limited to the interparticle half distance.

4.2. Out-of-Pile Results

4.2.1. Martensitic Stainless Steels. Numerous out-of-pile rupture data are obtained from the work of Wassilew [44] and Wassilew et al. [47]. The creep rupture data shown in Fig. 7 is for 1.4914 steel (similar to ferritics). Two sets of data are treated together in the figure. The first comes from creep rupture experiments on unirradiated steels; the second from similar experiments on pre-irradiated steels. In Fig. 7, the experimental and calculated results of the time-to-rupture for stresses up to ~ 300 MPa at 873°K are compared. The calculated times-to-rupture are in good agreement with the experimental results over the

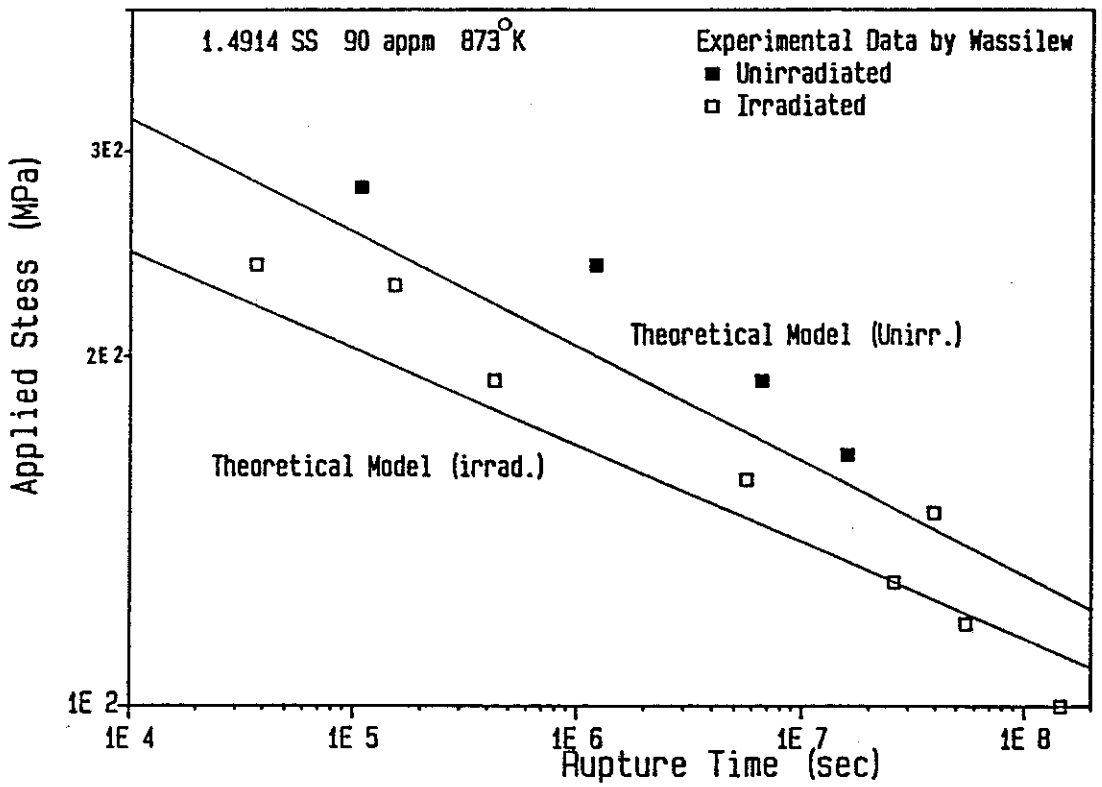

Figure 7. A comparison of calculated and experimental Time-to-Rupture for martensitic stainless steel (Data ref. [47]).

entire stress range. The figure also shows that the rupture times can be reduced by up to one order of magnitude due to pre-irradiation and a helium content of 90 appm.

Before proceeding, it is appropriate to check the validity of the assumption that fracture occurs when the cavity radius is 60% of the cavity half spacing. Figure 8 examines the fracture of martensitic stainless steel at 873°K under an applied stress of 150 MPa. The figure shows that once the ratio of cavity radius to cavity half spacing reaches 0.5 to 0.6, the growth rate is quite large and fracture occurs readily after that. If diffusion controls the growth process, this ratio could be as high as 0.8. Therefore, choosing a ratio of 0.6 is a reasonable cutoff region for fracture since source control is dominant in our calculation. This is in good agreement with other theoretical models (e.g., [41]). In addition, the figure shows that the time-to-rupture is under predicted by orders of magnitude if the vacancy supply is unexhaustible as is assumed by the diffusion growth models (e.g., Hull and Rimmer [1,4,7]).

Figure 9 shows a wider range of experimental data. The theoretical model is again in good agreement with the experimental results over very wide stress and temperature ranges. The figure clearly illustrates that the rupture time decreases rapidly as temperature increases. Figure 10 isolates the data at 973°K to show the importance of modeling. This figure contains data from experiments which are in progress. The model is in fair agreement with the time-to-fracture of these specimens.

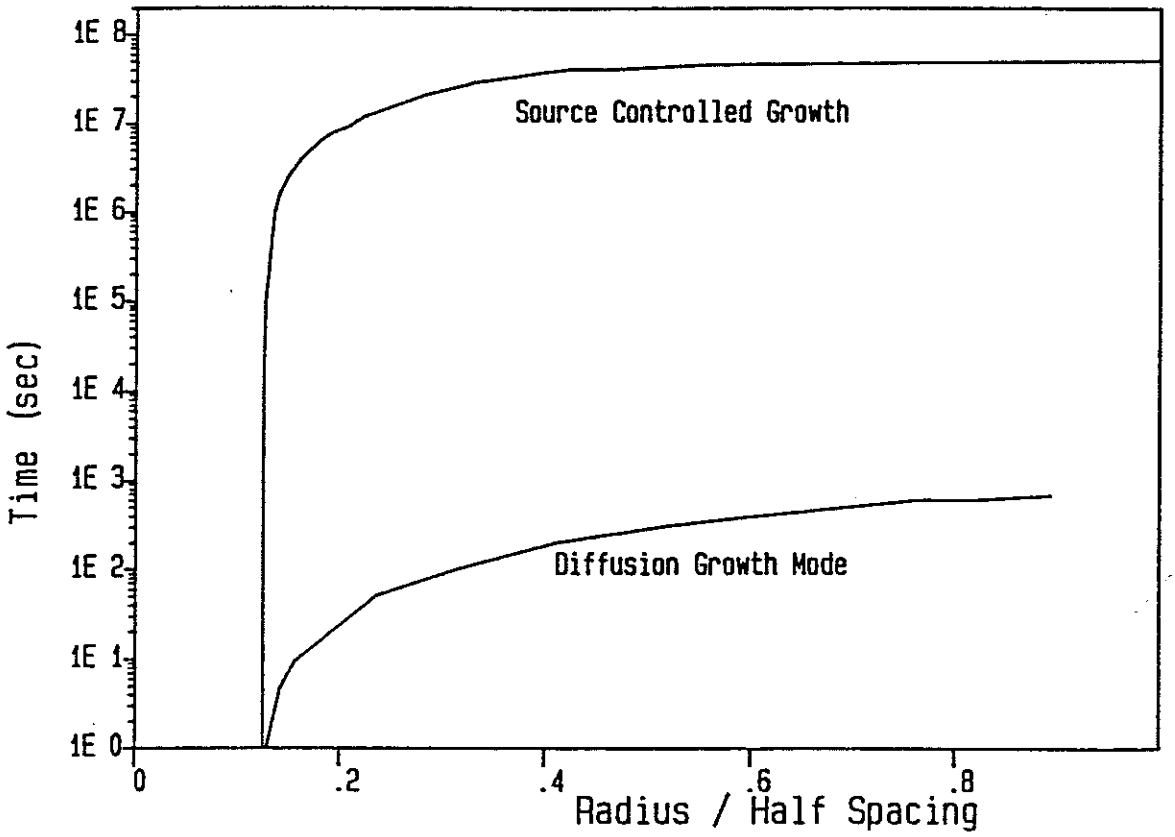

Figure 8. A typical growth behaviour of cavities. Theoretical modelling of martensitic stainless steel ,pre-injected with 90 appm He, under an applied stress of 150 MPa at 873°K.

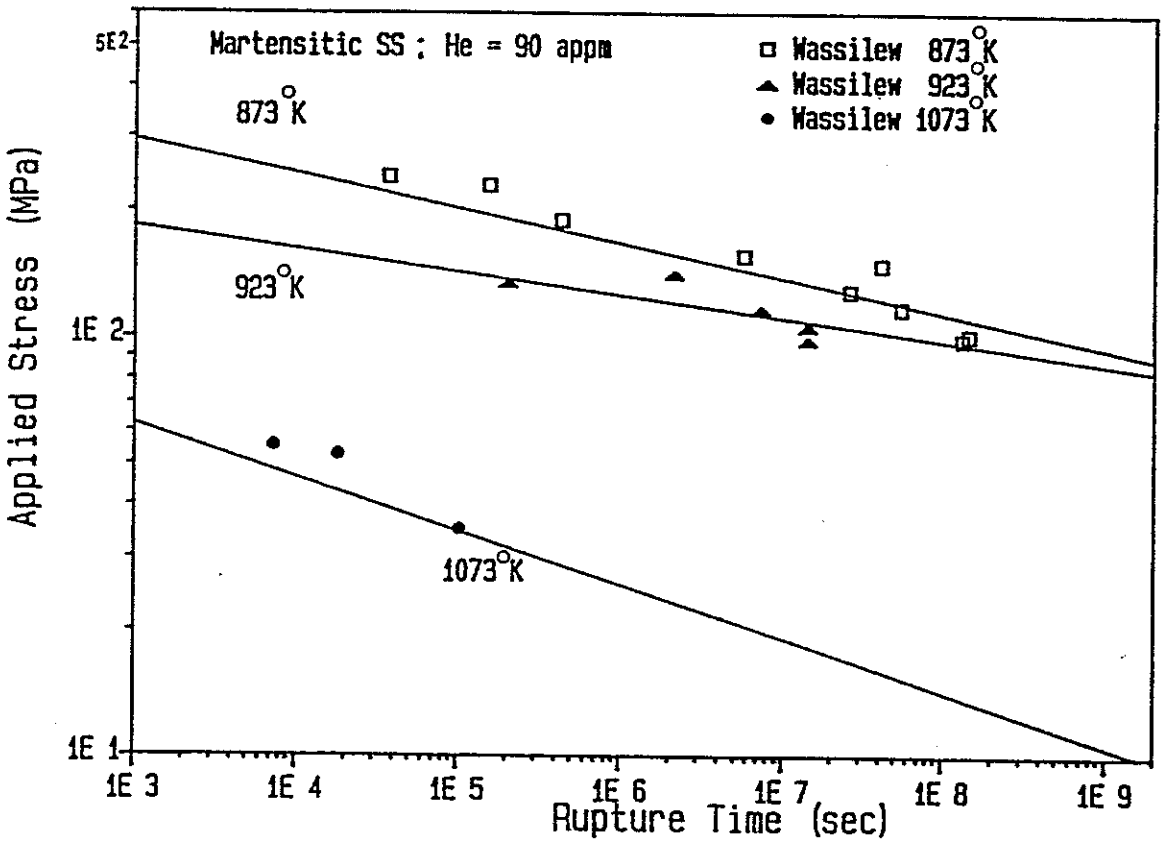

Figure 9. A comparison of calculated and experimental Time-to-Rupture for pre-irradiated martensitic stainless steel at various temperatures (Data ref. [47]).

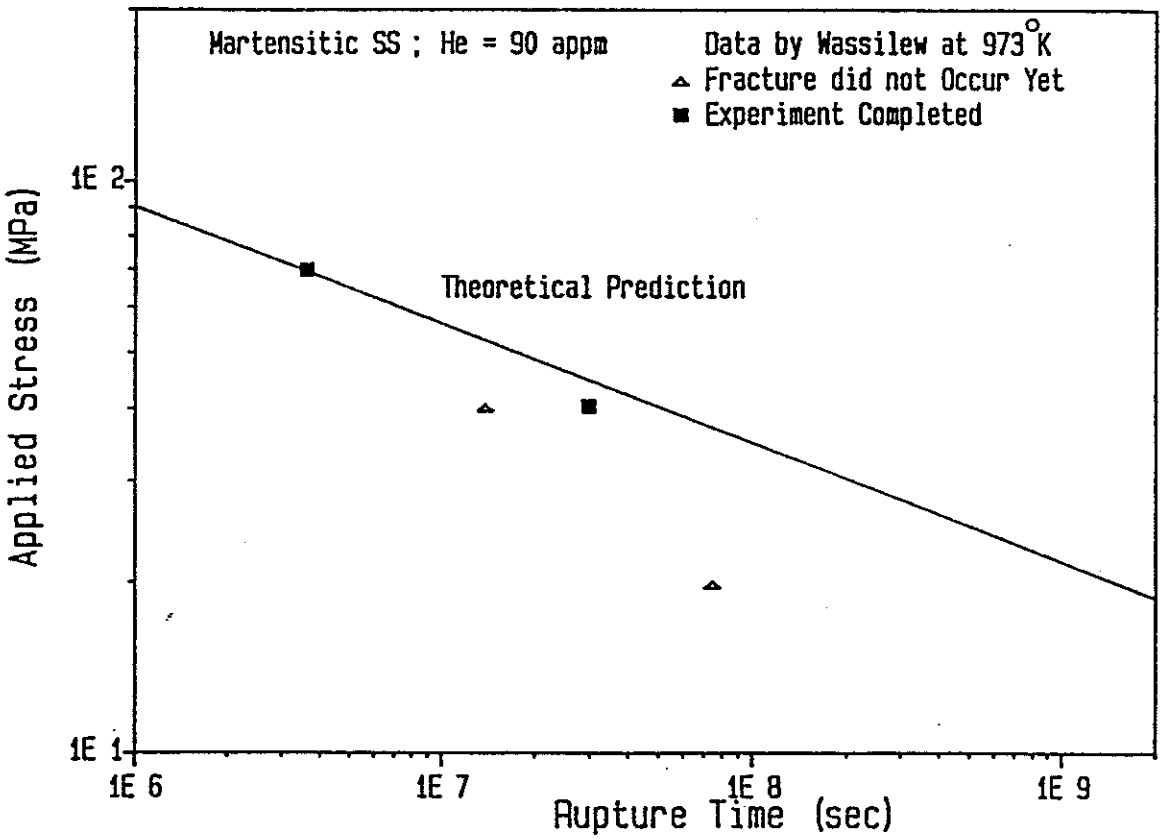

Figure 10. A comparison of calculated and experimental Time-to-Rupture for pre-irradiated martensitic stainless steel at 973°K (Data ref. [47]).

4.2.2. Austenitic Stainless Steels. Two types of austenitic stainless steels were employed in the tests conducted by Wassilew [44, 47], 1.4970 and 1.4962. The creep rate stress dependence of both types of steel are identical for the unirradiated and the irradiated material. However, two ranges of extremely different stress dependences of creep rate after irradiation can be identified:

1. In the high stress range ($\sigma > 150$ MPa) the stress dependence of creep rate is extremely high and similar for both steels, before and after irradiation ($n \approx 20$).

2. In the low stress range ($\sigma < 150$) the stress dependence of creep rate is proportional to the square of the applied stress.

Figure 11 compares the theoretical model with experimental data for 1.4970 stainless steel tested at high stressed ($n \approx 20$). The climb distance utilized in the theoretical model is limited by the inter-particle half spacing. The theoretical model is in reasonable agreement with the experimental data. The figure indicates again that irradiation can result in a reduction in the time-to-rupture by about one order of magnitude. Figure 12 compares the theoretical with the experimental data at lower stresses ($n \approx 2$). The calculated times-to-rupture for high and lower stresses are in good agreement with the experimental results.

Figures 13 and 14 compare the theoretical and experimental rupture data at high and low stresses ($n \approx 20$ and $n \approx 2$, respectively). The pre-irradiated steels contain 140 appm helium. The theoretical model is in

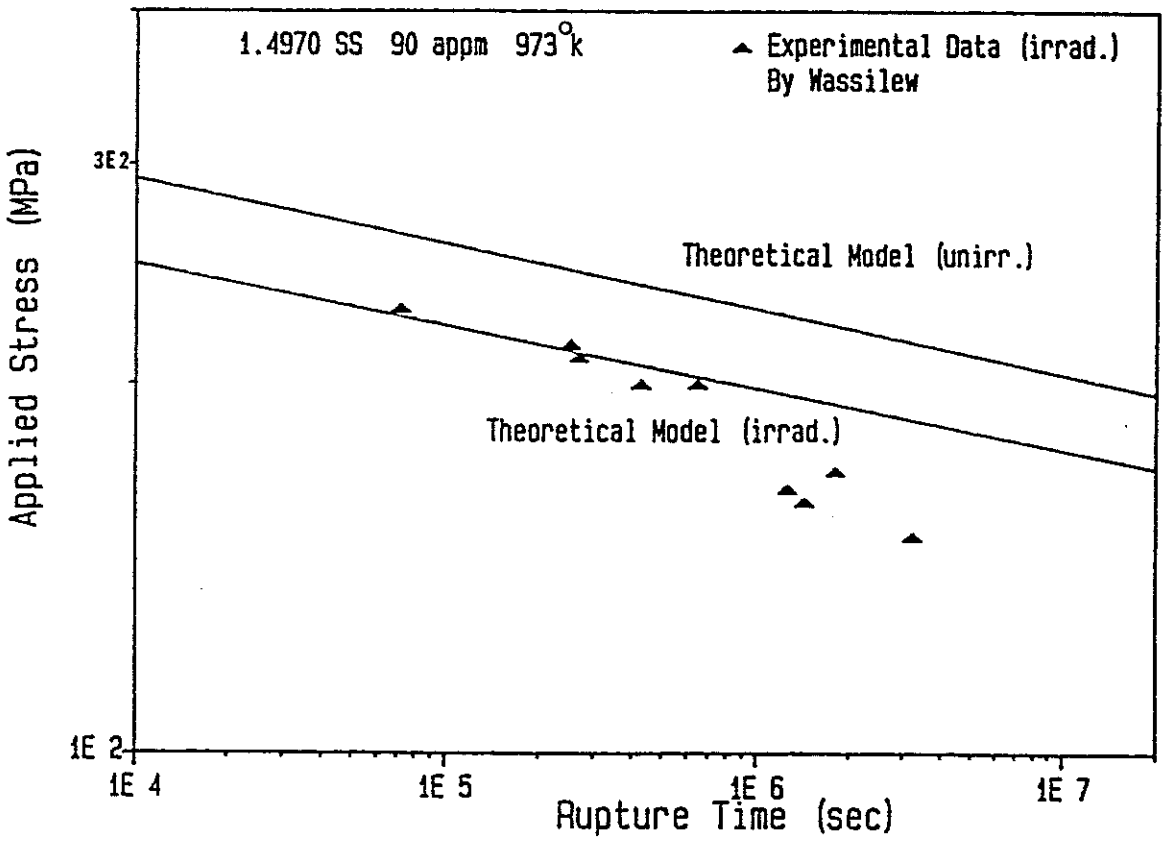

Figure 11. A comparison of calculated and experimental Time-to-Rupture for austenitic stainless steel at 973°K (Data ref. [47]). (σ>150 MPa , He=90 appm)

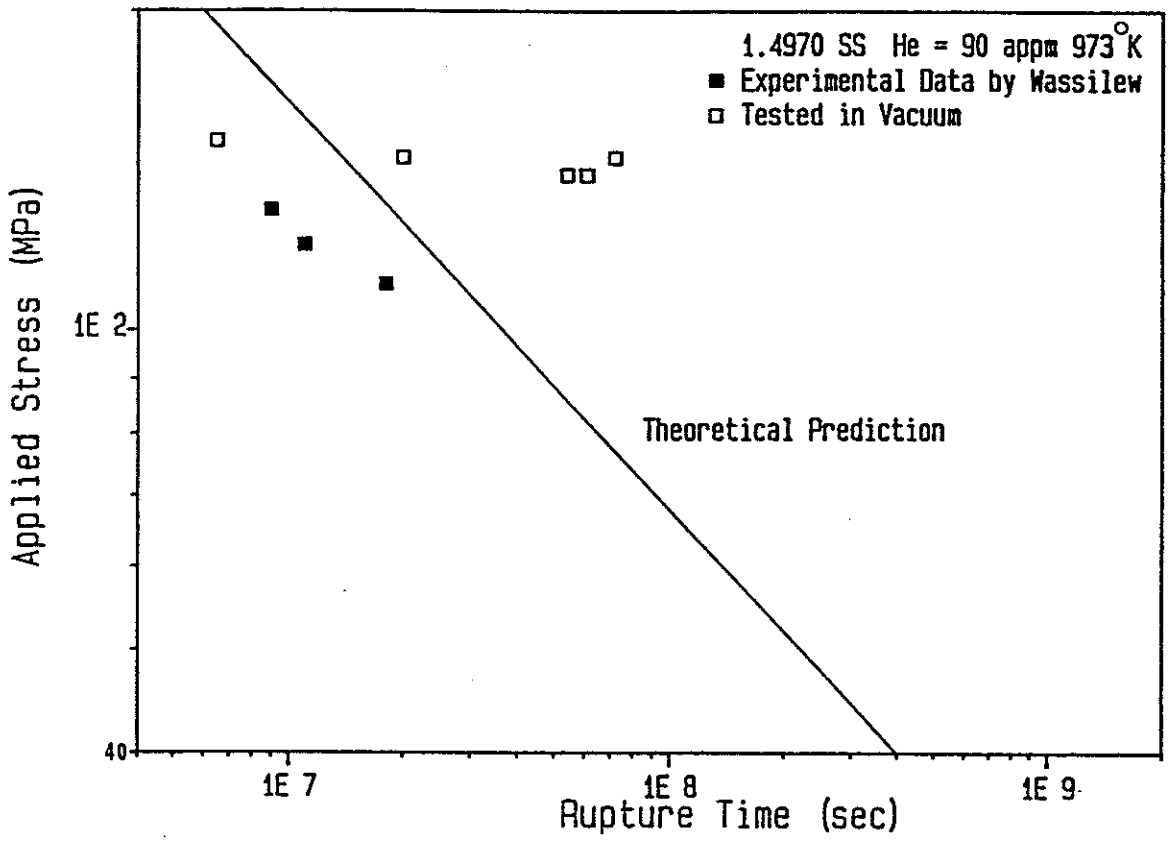

Figure 12. A comparison of calculated and experimental Time-to-Rupture for pre-irradiated austenitic stainless steel at 973°K (Data ref.[47]) (σ<150 MPa , He=90 appm)

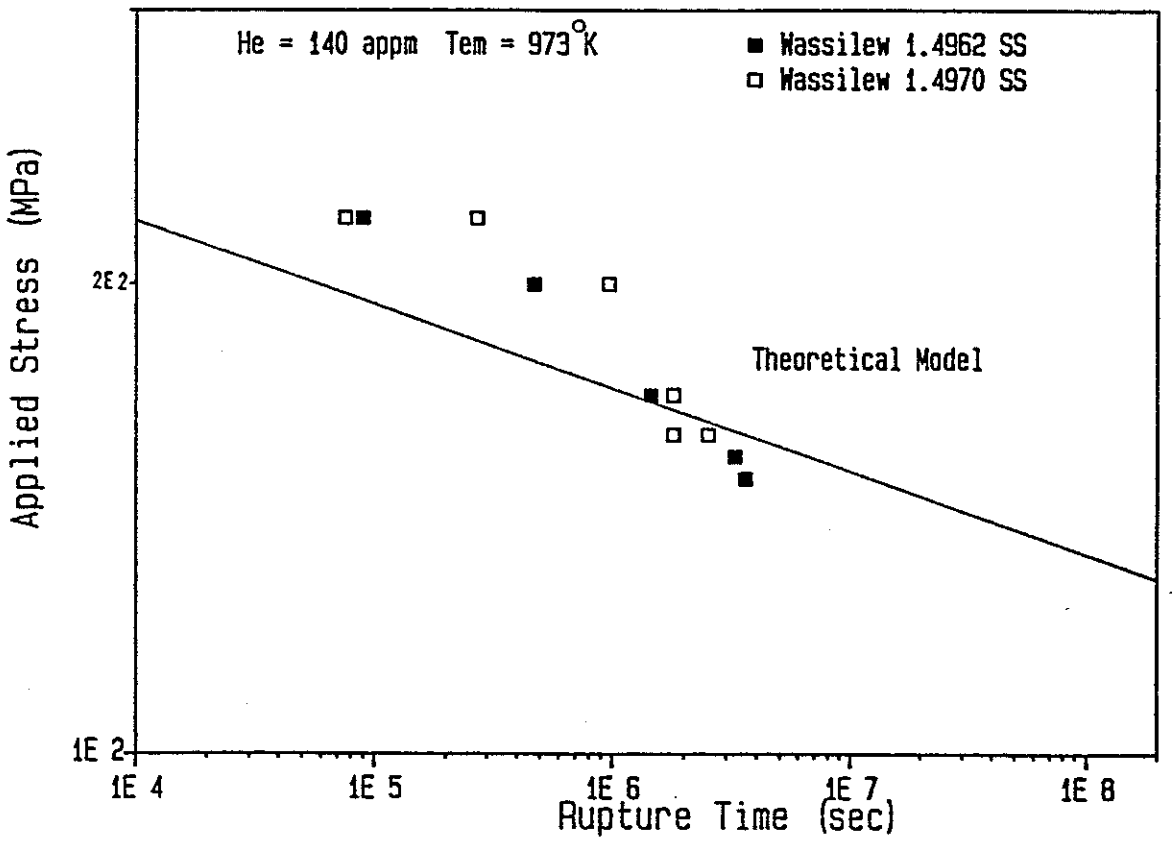

Figure 13. A comparison of calculated and experimental Time-to-Rupture for pre-irradiated austenitic stainless steel at 973°K (Data ref.[47]). (σ>150 MPa , He=140 appm)

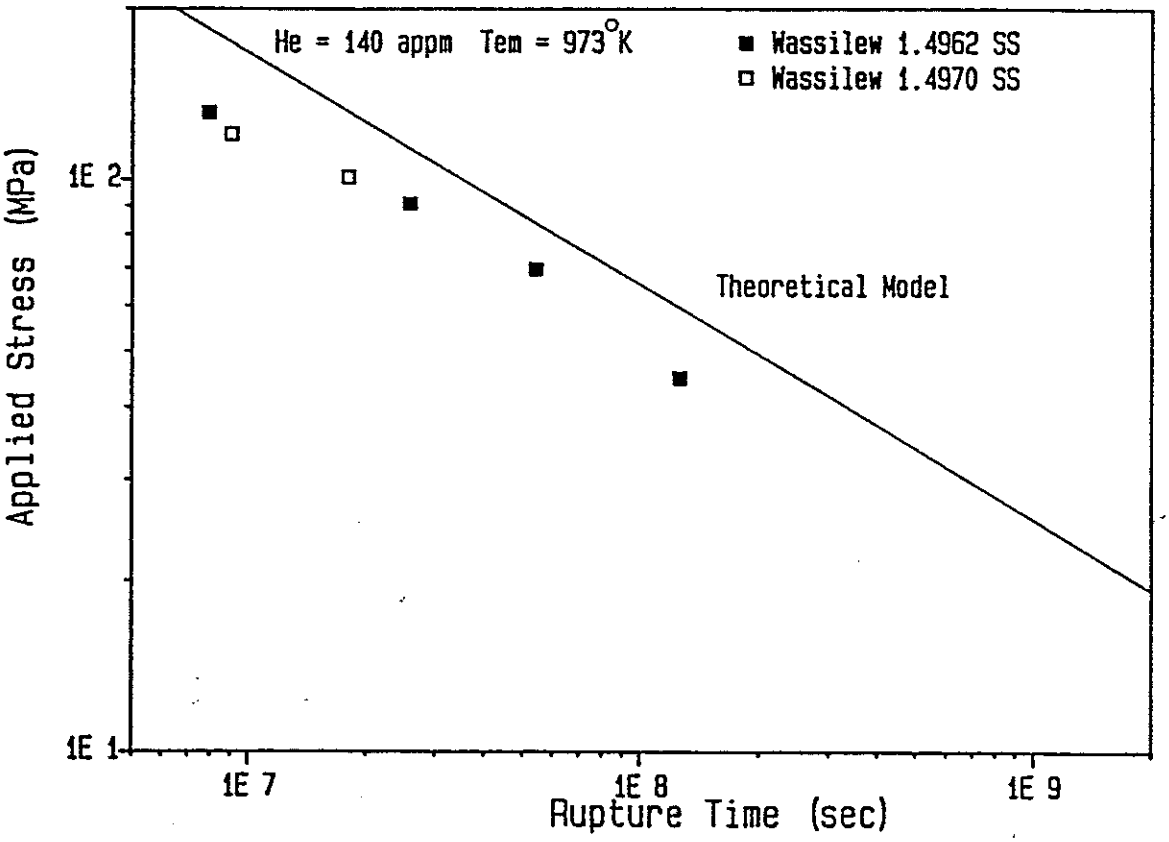

Figure 14. A comparison of calculated and experimental Time-to-Rupture for pre-irradiated austenitic stainless steel at 973°K (Data ref.[47]). (σ<150 MPa , He=140 appm)

close agreement with the experimental data. If we examine Figs. 11 and 13, a cutoff stress of about 150 MPa should have been utilized and lower stress data points are actually part of a transition zone between the high and low stress regions. An additional note to mention is that, increasing the helium from 90 appm to 140 appm does not affect the bubble density significantly to alter the fracture times, but rather it affects the creep rate and hence the growth rate of these cavities.

4.2.3. Martensitics Versus Austenitics. The experimental data as well as the theoretical model shown in Fig. 15 indicate that the rupture properties of austenitics are favored over martensitics even after the helium injected reaches 90 appm. If we examine the creep rates provided in Table 1, it is obvious that the creep rate is much higher in martensitics than in austenitics. This results in a marked difference in the ductility behavior between the two steels. At rupture, although the time-to-rupture in austenitics is much larger than ferritics, martensitics provide a larger amount of deformation than austenitics, provided that the primary and tertiary creep regimes are included.

4.3. In-Pile Results

Figure 16 represents the theoretical findings of in-pile rupture simulation of martensitic stainless steel. The figure clearly shows a severe reduction in the time-to-rupture in in-pile specimens as a result of the helium embrittling effect. As expected, the reduction in the rupture time from unirradiated specimen is more severe in in-pile tests as compared to out-of-pile tests. This can be attributed to the fact that the in-pile creep rate is significantly higher [48]. A higher

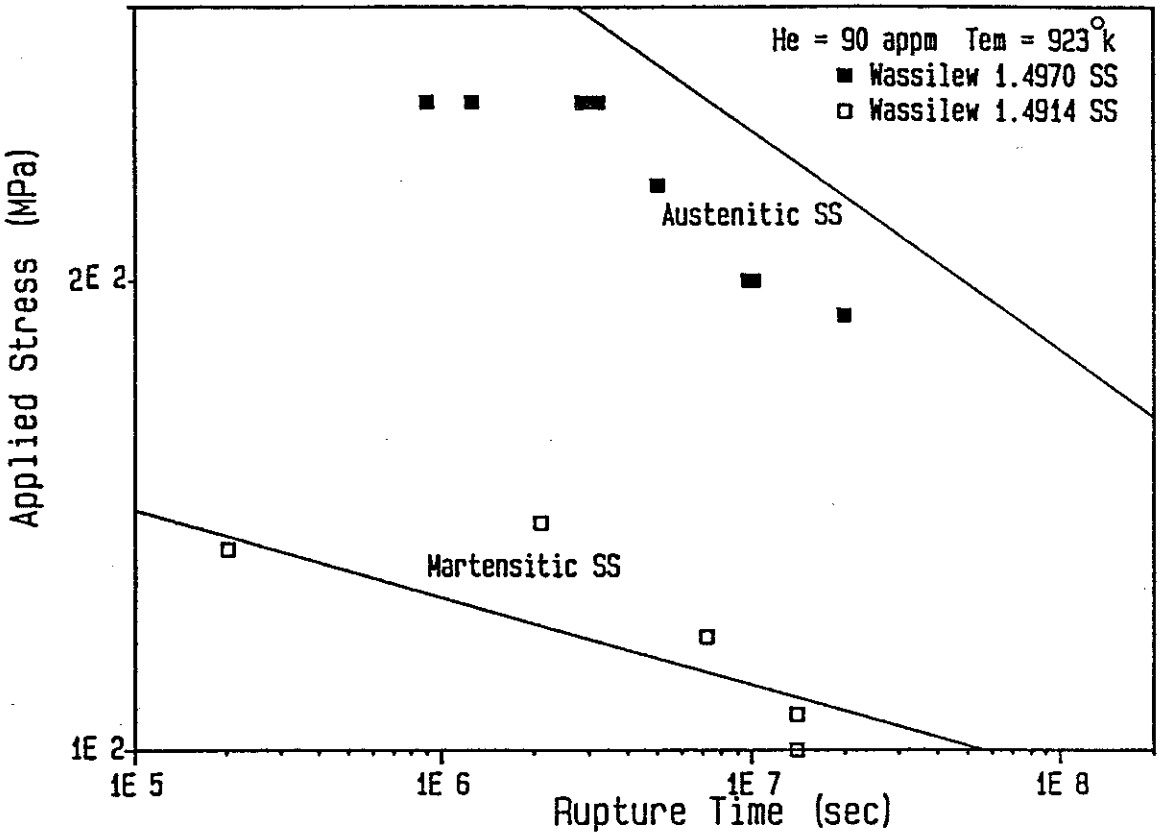

Figure 15. A comparison of calculated and experimental Time-to-Rupture for pre-irradiated austenitic and martensitic stainless steels at 923°K (Data ref.[47]).

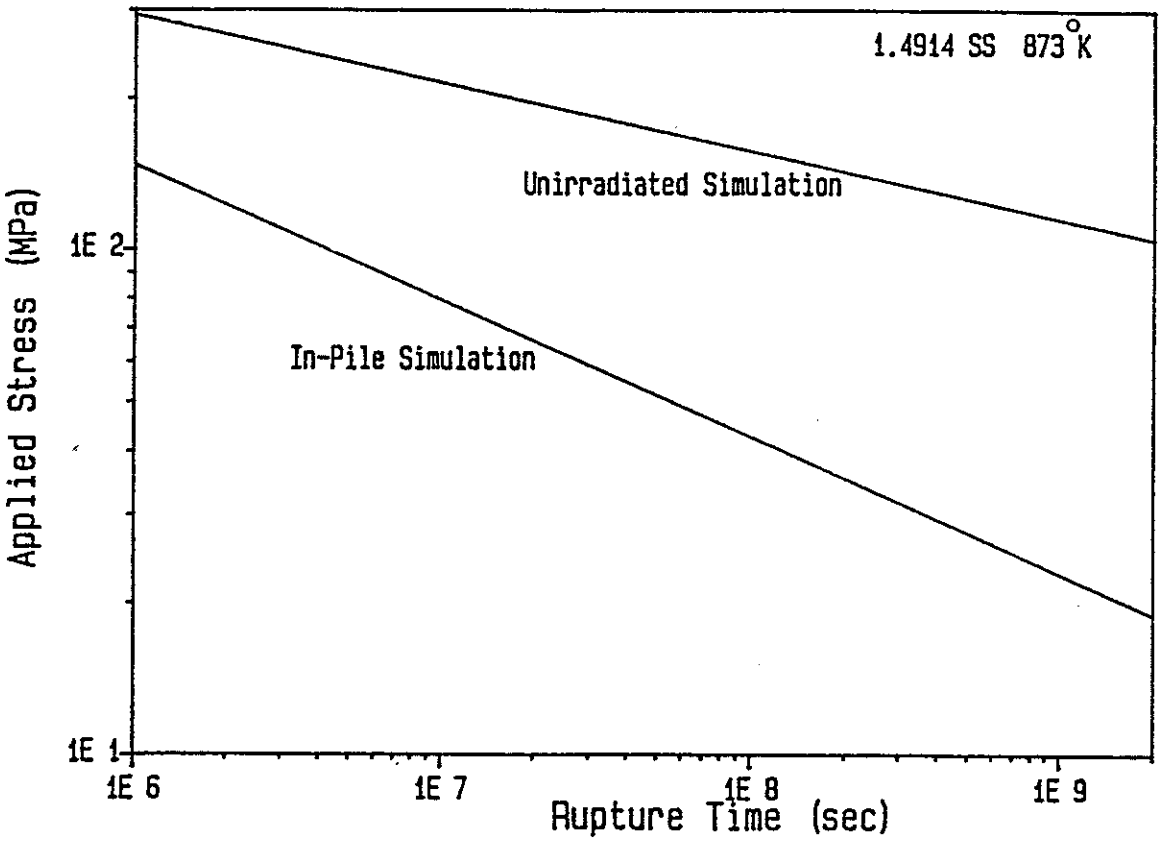

Figure 16. A theoretical comparison of the stress rupture dependence of the Time-to-Rupture of unirradiated and inpile tested martensitic stainless steel at 873°K.

creep rate results in enhanced bubble growth by creep deformation and an enhanced supply of vacancies from dislocation entering the boundary. In addition, the bubble structure at grain boundaries is established during the early stages of irradiation, as discussed in Chapter V. However, continuous irradiation results in the accumulation of helium atoms in existing bubbles as shown in Fig. 17. This drives the pressure to increase significantly as shown in Fig. 18. The increase in the internal pressure causes the bubble to enlarge to the size that satisfies the stability criterion. However, a sharp drop in the pressure occurs once the bubble starts to grow by the excess vacancy flux. This is shown in Fig. 18. This confirms that the growth of grain boundary bubbles under in-pile condition is an instability as was suggested by Brailsford and Bullough [49].

Bullough, Harries and Hayns [51] utilized the Brailsford and Bullough Model [50] to describe the creep rupture during irradiation. The basic difference between our results and theirs is that we calculate the number of helium atoms arriving to the grain boundary bubbles as a function of time from our comprehensive model. In the work of Bullough et al. [51], the total amount of helium generated was assumed to be absorbed by bubbles without any time dependence. In addition, no distinction between matrix and grain boundary bubbles was made.

5. CONCLUSIONS

1. Grain boundary bubbles and cavities are lenticular in shape with a dihedral angle of at most 17 deg.

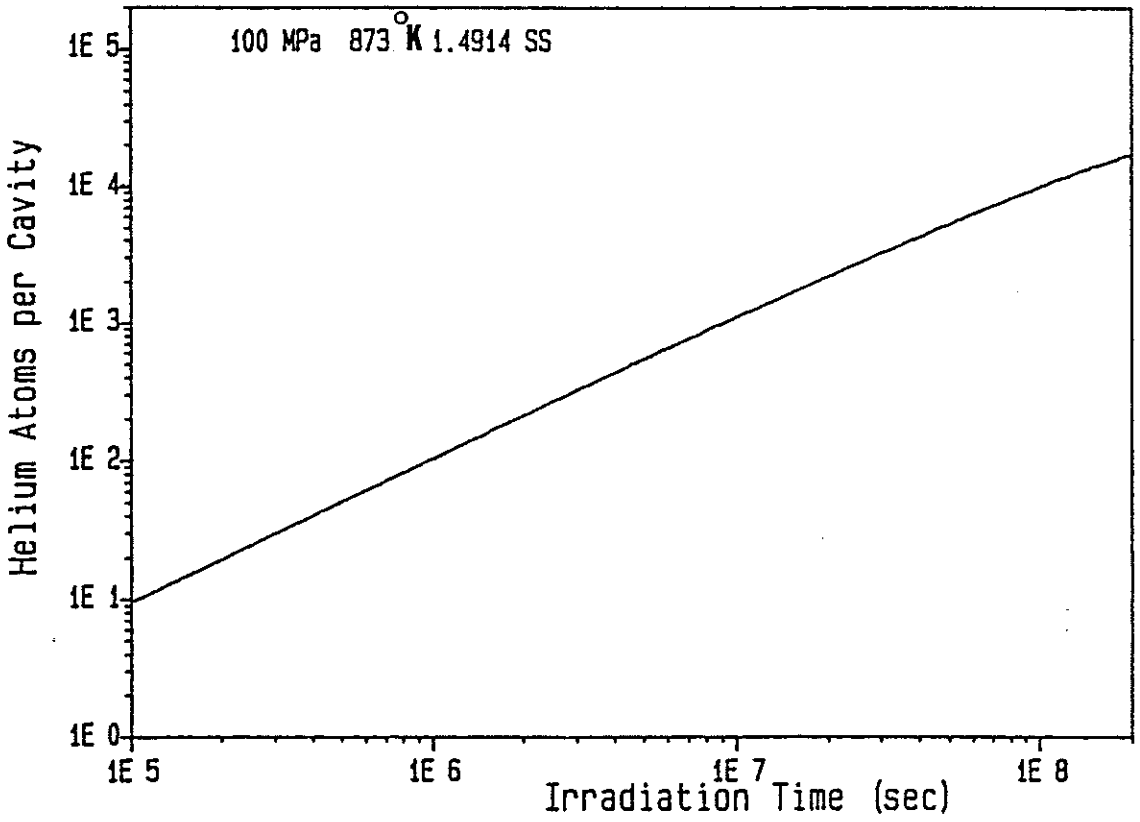

Figure 17. A typical helium atoms accumlation at grain boundary buubbles as a result of continuous irradiation.

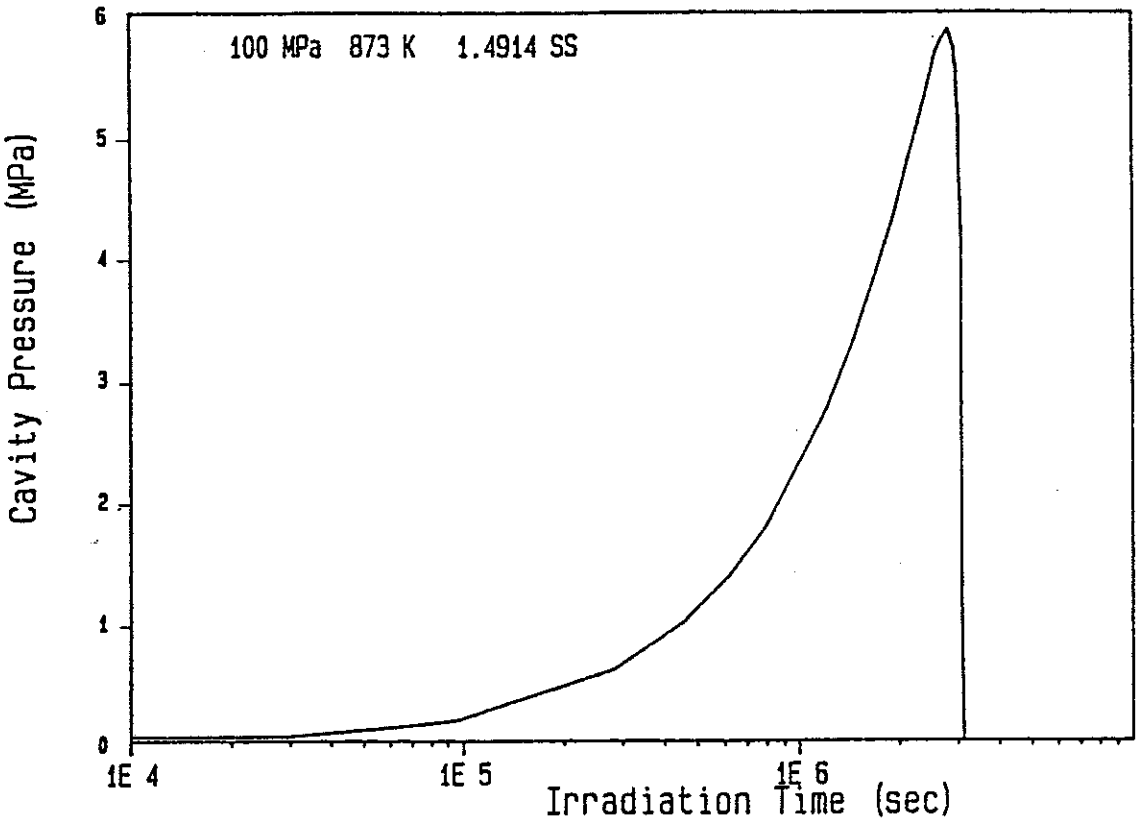

Figure 18. Pressure build-up in grain boundary bubbles as a result of helium atoms accumlation.This results in an instability in the bubble growth.

2. In the absence of irradiation, precipitates at sliding boundaries are preferential sites for cavity nucleation. In their absence, creep fracture by grain boundary cavitation does not occur.

3. The nucleation process of grain boundary bubbles and cavities is quite fast and the time-to-rupture is controlled primarily by the growth rate of void nuclei.

4. Helium gas re-solution due to the interaction of displacement damage with gas-filled cavities in a process of prime importance to matrix cavity re-nucleation. Increasing the bubble density in the matrix can result in a reduction in the amount of helium reaching grain boundaries. This will delay the occurrance of grain boundary cavity instability and hence a better resistance to helium embrittlement.

5. Irradiation results in a significant enhancement of the boundary cavity population.

6. Higher helium implantation rates result in a higher grain boundary bubble density.

7. The grain boundary bubble density reaches a steady state at large amounts of injected helium (~ 10 appm).

8. Although the model predicts absolute time-to-rupture values, it clearly shows that the rupture times determined from

post-irradiation creep tests is significantly different from those of in-pile experiments.

9. Post-irradiation tests do not accurately describe the in-reactor behavior. To promote the understanding of helium embrittlement, in-pile experiments should be conducted.

10. The model provides an explanation of the creep rupture properties of ferritic/martensitic and austenitic stainless steels. The new explanation states that dislocation climb in austenitics at grain boundaries is limited by precipitates while it is limited to the interbubble spacing in martensitics. This is due to much larger possible slip systems in martensitics. Therefore, secondary grain boundary dislocation motion impeded by bubbles can leave the boundary in martensitics while it is less likely to leave the boundary in austenitics as a result of the reduced possible slip systems in austenitics. This translates into a reduced vacancy source in martensitics.

11. Implementing the new explanation of the rupture properties of martensitics in the model has yielded an excellent description of the stress and temperature dependence of the measured rupture times.

12. The time-to-rupture decreases significantly at a given stress with an increase in temperature for austenitics as well as martensitics.

13. Grain boundary bubble growth rate can be reduced by limiting dislocation climb in the boundary. This can be done by increasing precipitate density at grain boundaries.

14. Grain boundary bubble growth can also be reduced by reducing the creep rate. This limits bubble growth by creep deformation as well as reduces the vacancy supply by dislocations entering the boundary. This has also been recently suggested by Kesternich [52].

15. An increase in the bubble surface energy will cause the instability to occur at higher pressures for in-pile tests and hence improve the rupture times.

16. An increase in the matrix precipitate density can result in a reduction in the amount of helium reaching grain boundaries, as suggested in Chapter IV. This will delay the occurrance of grain boundary cavity instability, and will result in a better resistance to the helium embrittling effect. Recent experimental investigations [53,54] support this theoretical finding.

REFERENCES

[1] D. Hull and D. E. Rimmer, "The Growth of Grain Boundary Voids Under Stress," Philos. Mag., 4 (1959) 673.

[2] J. Weertman, "Hull-Rimmer Grain Boundary Void Growth Theory - A Correction," Scripta Metall., 7 (1973) 1129.

[3] M. V. Speight and W. Beere, "Vacancy Potential and Void Growth on Grain Boundaries," Met. Sci. J., 9 (1975) 190.

[4] W. Beere and M. V. Speight, "Creep Cavitation by Vacancy Diffusion in Plastically Deforming Solid," Met. Sci. J., 12 (1978) 593.

[5] I. G. Crossland and J. E. Harris, "Influence of Intergranular Precipitates on Diffusional Growth of Creep Voids," Met. Sci. J., 13 (1979) 55.

[6] W. Beere, "Models for Constrained Cavity Growth in Polycrystals," Acta Metall., 28 (1980) 143.

[7] M. V. Speight and J. E. Harris, "The Kinetics of Stress-Induced Growth of Grain-Boundary Voids," Met. Sci. J., 1 (1967) 83.

[8] W. Beere, "Star-Shaped Unstable Growth of Grain Boundary Cavities," Philos. Mag., 38 (1978) 691.

[9] W. Beere, "Inhibition of Intergranular Cavity Growth in Precipitate Hardened Materials," J. Mater. Sci., 15 (1980) 657.

[10] B. F. Dyson, "Constraints on Diffusional Cavity Growth Rates," Met. Sci. J., 10 (1976) 349.

[11] F. H. Vitovec, "Cavity Growth and Creep Rate Taking into Account the Change of Net Stress," J. Mater. Sci., 7 (1972) 615.

[12] R. S. Barnes, G. B. Redding and A. H. Cottrell, "The Observation of Vacancy Sources in Metals," Philos. Mag., 3 (1958) 97.

[13] R. S. Barnes, "The Generation of Vacancies in Metals," Philos. Mag., 5 (1960) 635.

[14] P. B. Hirsch, J. Silicos, R. E. Smallman and K. H. Westmacott, "Dislocation Loops in Quenched Aluminum," Philos. Mag., 3 (1958) 897.

[15] R. L. Segall, "Coherent Annealing Twin Boundaries as Vacancy Sinks," Acta Metall., 12 (1964) 117.

[16] C. Herring, "Diffusional Viscosity of a Polycrystalline Solid," J. Appl. Phys., 21 (1950) 437.

[17] F. R. N. Nabarro, Rept. of Conf. on Strength of Solids (Phys. Soc., London, 1948) 75.

[18] H. Jones, "A Comparison of Theory with Experiment for Diffusion Creep in Metal Foils and Wires," Mater. Sci. and Eng., 4 (1969) 106.

[19] B. Burton and G. L. Reynolds, "The Diffusional Creep of Uranium Dioxide: Its Limitations by Interfacial Processes," Acta Metall., 21 (1973) 1073.

[20] J. H. Gittus, "On the Possibility that Boundary Dislocations and Steps are a Source of a Threshold Stress for Diffusion Creep and Superelastic Flow," Scripta Metall., 10 (1976) 551.

[21] W. Jager and H. Gleiter, "Grain Boundaries as Vacancy Sources in Diffusional Creep," Scripta Metall., 12 (1978) 675.

[22] R. W. Balluffi, "Grain Boundary Structure and Segregation," in Interfacial Segregation, W. C. Johnson and J. M. Blakely, Eds. (ASM, Metals Park, OH, 1979) 193.

[23] G. W. Greenwood, "Grain Boundaries as Vacancy Sources and Sinks," in Vacancies '76 (The Metals Society, London, 1977) 141.

[24] B. Burton, "Interface Reaction Controlled Diffusional Creep: A Consideration of Grain Boundary Dislocation Climb Sources," Mater. Sci. and Eng., 10 (1972) 9.

[25] M. F. Ashby, "On Interface-Reaction Control of Nabarro-Herring Creep and Sintering," Scripta Metall., 3 (1969) 837.

[26] H. Gleiter, "Grain Boundaries as Point Defect Sources or Sinks - Diffusional Creep," Acta Metall., 27 (1979) 187.

[27] J. Bardeen and C. Herring, in Imperfections in Nearly Perfect Crystals, W. Shockley, Ed. (Wiley, New York, 1952) 279.

[28] P. Goodhew, "The Relationship Between Grain-Boundary Structure and Energy," in Proc. Sem. on Grain-Boundary Structure and Kinetics, ASM Materials Science, Sept. 15-16, 1979, Milwaukee, WI (ASM, Metals Park, OH, 1980).

[29] W. Bollmann, Crystal Defects and Crystalline Interfaces, (Springer-Verlag, Berlin-New York, 1970).

[30] R. C. Pond and D. A. Smith, "On the Absorption of Dislocations by Grain Boundaries," Philos. Mag. A., 36 (2), (1977) 353.

[31] T. P. Darby, R. Schindler and R. W. Balluffi, "On the Interaction of Lattice Dislocations with Grain Boundaries," Philos. Mag. A., 37 (2), (1978) 245.

[32] D. J. Dingley and R. C. Pond, "On the Interaction of Crystal Dislocations with Grain Boundaries," Acta Metall., 27 (1979) 667.

[33] W. A. T. Clark and D. A. Smith, "Interaction of Lattice Dislocations with Periodic Grain Boundary Structures," J. Mater. Sci., 14 (1979) 776.

[34] W. Beere, "Theoretical Treatment of Creep Cavity Growth with Application to Embrittlement by Inert Gas," Res Mechanica, 2 (1981) 189.

[35] R. W. Balluffi and L. L. Seigle, "Effect of Grain Boundaries Upon Pore Formation and Dimensional Changes During Diffusion," Acta Metall., 3 (1955) 170.

[36] P. J. Clemm and J. C. Fisher, "The Influence of Grain Boundaries on the Nucleation of Secondary Phase," Acta Metall., 3 (1955) 70.

[37] Y. Ishida and D. McLean, "The Formation and Growth of Cavities in Creep," Met. Sci. J., 1 (1967) 171.

[38] D. R. Olander, Fundamental Aspects of Nuclear Reactor Fuel Elements, NTIS TID-26711-P1 (Nat. Tech. Info. Serv., Springfield, VA, 1976) 92.

[39] J. W. Hancock, "Creep Cavitation Without a Vacancy Flux," Met. Sci. J., 10 (1976) 319.

[40] K. L. Kear and M. H. Wood, "An Analysis of Grain Boundary Failure in Austenitic Stainless Steel," AERE Harwell Report AERE-R 10907 (1983).

[41] H. Trinkaus and H. Ullmaier, "A Model for the High-Temperature Embrittlement of Metals Containing Helium," Philos. Mag., 39 (1979) 563.

[42] V. Sklenička, I. Saxl and J. Čadek, "Time to Fracture and Cavity Growth Mechanisms in Creep," Res Mechanica, 4 (1982) 225.

[43] R. G. Faulkner and K. Anderko, "High Temperature Ductility of Irradiated Ferritic and Austenitic Steels," J. Nucl. Mater., 113 (1983) 168.

[44] C. Wassilew, "Influence of Helium Embrittlement on Post-Irradiation Creep Rupture Behaviour of Austenitic and Martensitic Stainless Steels," in Proc. Inter. Conf. on Mechanical Behaviour and Nucl. Applications of Stainless Steel at Elevated Temperatures, The Metals Society, Varese, Italy, 1981, p. 172.

[45] A. A. Abu Zahara and H. Schroeder, "The Influence of Thermomechanical Treatment on the Creep Behaviour of DIN 1.4970 Austenitic Stainless Steel at 973°K," Institut für Festkörperforschung, Kernforschungesanlage Jülich Jül-Spez-109 (April 1981) D-5170, Jülich, W. Germany.

[46] G. W. Gear, Numerical Initial Value Problems in Ordinary Differential Equations (Prentice-Hall, Englewood Cliffs, NJ, 1971).

[47] C. Wassilew, W. Kunischand and B. Ritter, "Vergleich der Zeitstand- und Kriecheigen-schaften austenitischer Stähle ...," Institut für Material- und Festkörperforschung II, Kernforschungszentrum PSB-Ber. 2035 (Kl.III) (October 1981) Karlsruhe, W. Germany.

[48] K. Herschbach, "In-Pile Creep of the Martensite 1.4914: Some Fundamental Observations," J. Nucl. Mater., 127 (1985) 239.

[49] I. LeMay, Principles of Mechanical Metallurgy (Elsevier North Holland, Inc., New York, 1981).

[50] A. D. Brailsford and R. Bullough, "The Stress Dependence of High Temperature Swelling," J. Nucl. Mater., 48 (1973) 87.

[51] R. Bullough, D. R. Harries and M. R. Nayns, "The Effect of Stress on the Growth of Gas Bubbles During Irradiation," J. Nucl. Mater., 88 (1980) 312.

[52] W. Kesternich, "A Possible Solution of the Problem of Helium Embrittlement," J. Nucl. Mater., 127 (1985) 153.

[53] W. Kesternich and J. Rothaut, "Reduction of Helium Embrittlement in Stainless Steel by Finely Dispersed TiC Precipitates," J. Nucl. Mater., 103&104 (1981) 845.

[54] W. Kesternich, M. K. Matta and J. Rothaut, "Influence of Ti-Precipitation in Austenitic Stainless Steel on the Strength, Ductility and Helium Embrittlement," J. Nucl. Mater., 122&123 (1984) 130.